Dissertation

submitted to the
Combined Faculty of Mathematics, Engineering and Natural Sciences
of Heidelberg University, Germany
for the degree of
Doctor of Natural Sciences

Put forward by
Eva Marcella Rückert, M. Sc.
born in Heidelberg
Oral examination: 24th July 2024

Interhemispheric Deep Water Exchange Revealed by Authigenic Neodymium Isotopes in the Southern Atlantic Ocean During the Last One Million Years

Referees:

Prof. Dr. Norbert Frank

Prof. Dr. André Butz

Abstract

The deep Southern Ocean circulation is of major significance for our understanding of the ocean's impact on Earth's climate as uptake and release of CO_2 strongly depend on the redistribution of well and poorly ventilated water masses. Authigenic neodymium isotopes (εNd) preserved in deep sea sediment have proven useful to study the deep ocean circulation and water mass provenance and are of special interest over major climate changes such as the Mid Pleistocene Transition (MPT). In this thesis, the authigenic Nd isotopic composition of two Atlantic sediment sites south of the Polar Front were investigated. The record at site ODP 1093 spans the last 1 Ma in millennial resolution, while ODP 1094 covers terminations I, II, V and the MPT. The results yield the first 1 Ma εNd benchmark in the southern Atlantic Ocean, which shows a variable behavior synchronous with climate. Based on the strong correlation with climate in ODP 1093, an age model was developed. The observed εNd point to an interplay of advective and diffusive processes influencing the εNd signatures preserved in the authigenic coating. The interhemispheric εNd gradient was discussed, to investigate circulation strength changes across the Atlantic Ocean in the past 1 Ma. The gradient observations indicate a potential bi-stability of the circulation starting during the MPT with the occurrence of the first strong decrease in circulation strength.

Zusammenfassung

Die Tiefenzirkulation des Südlichen Ozeans hat einen großen Einfluss auf das Klima der Erde, da die Aufnahme und Abgabe von CO_2 stark von der Verteilung der Wassermassen abhängt. Mit Hilfe der authigenen Neodym Isotope (εNd) in Tiefseesedimenten kann die Zirkulation im Ozean und die Herkunft von Wassermassen während großer Klimaänderungen wie dem mittelpleistozänen Übergang (MPT) untersucht werden. In dieser Arbeit wurde authigenesεNd in Sediment an zwei Orten südlich der Polarfront im Atlantik analysiert. ODP 1093 deckt die letzten 1 Mio. Jahre ab und ist mit dem Klima synchronisiert. Damit bildet dieser den ersten εNd Datensatz im südlichen Atlantik über diese Zeitspanne. Die εNd Daten in ODP 1094 decken die Klimaübergänge I, II, V und den MPT ab. Auf Basis der starken Korrelation mit dem Klima in ODP 1093 wurde ein Altersmodell entwickelt. Der beobachtete εNd Verlauf deutet auf ein Zusammenspiel von advektiven und diffusiven Prozessen hin, die die authigenen εNd Signaturen beeinflussen. Um die Veränderungen der Zirkulationsstärke im Atlantik in den letzten 1 Mio. Jahren zu untersuchen, wurde der interhemisphärische εNd Gradient diskutiert. Die Beobachtungen dessen deuten auf eine mögliche Bi-Stabilität der Zirkulation hin, die während des MPT mit dem Auftreten der ersten starken Abnahme der Zirkulationsstärke begann.

Contents

1. Introduction

The global climate of the Earth changed dramatically in the past and will change in the future. Reconstructing past climate conditions is a challenging task, yet crucial to understand the complexity of the Earth's climate system. Depending on the time frame, climate follows various patterns. The modern climate is dominated by seasonal and multi-decadal variability and the well confirmed anthropogenic climate change (Lee et al., 2023). On millennial timescales the global climate of the past 11.7 ka was rather constant. However, in the last 1 Ma multiple alternating warm and cold periods in line with the periodicity of orbital parameters have been reconstructed (e.g. Bereiter et al., 2015; Hasenfratz et al., 2019; Howe and Piotrowski, 2017; Link, 2021; Lisiecki and Raymo, 2005; Petit et al., 1999).

Climate variability is the result of the complex coupling of all compartments of the climate system and their response to external forcing. The main components of the system are the atmosphere, the biosphere, the hydrosphere, the cryosphere and the lithosphere. Each component has its individual time scale, over which significant changes occur. These range from days to weeks to seasons in the atmosphere to geological time scales in the lithosphere. Consequently, within the same time span some parts of the climate system vary strongly, while others remain seemingly constant. However, it is of great interest, how the different compartments act to the climate change induced by humans. Thus, it is of crucial importance to best constrain the past climate to gain insights in the complex interaction, sub-system interaction and stability on natural forcing and timescales far beyond observations. Of particular interest are the systems transitions from a cold to a warm state and vice versa (e.g. Huybers and Langmuir, 2009; Paillard et al., 1996; Raymo et al., 2006)

The global ocean circulation, as part of the hydrosphere, is mainly driven by density gradients caused by temperature and salinity changes. The so called thermohaline circulation is a fundamental component in the Earth's climate system, as it stores and re-distributes heat and matter such as carbon, oxygen and nutrients on the planet (Broecker, 1987; Roy-Barman and Jeandel, 2016; Jeandel, 2016). Hereby, the Atlantic Meridional Overturning Circulation (AMOC) and Southern Ocean carbon storage play a major role in connecting the ocean-atmosphere interface with the deep

ocean. It is hypothesized, that the AMOC forms a key element in the response of the ocean to climate changes, which can act as an amplifier of climate changes (Henry et al., 2016; Lenton et al., 2008; Lynch-Stieglitz, 2017).

Paleooceanographic studies aim for insights in the ocean circulation states and its response to climate changes in the ancient past. The direct reconstruction of temperature and salinity in the past ocean is not possible since they are not preserved over time. Thus, circulation reconstructions are made, based on various climate proxies, which indirectly trace such changes at variable precision and accuracy.

Since its first use in the late 70's, neodymium isotopic compositions (εNd) have proven useful as tracer for water mass provenance and became indispensable in paleooceanography (Martin and Haley, 2000; Piepgras et al., 1979; Rutberg et al., 2000; van de Flierdt et al., 2006). Countless studies used Nd isotopes in various climate archives across all oceanto explore past ocean dynamics (e.g. Colin et al., 2010; Frank, 2002; van de Flierdt et al., 2010; Pena and Goldstein, 2014; Piotrowski et al., 2004; Rutberg et al., 2000). Local processes at the water-sediment or water-rock interface, which alter the εNd signature, are well admitted. However, the details of these Nd fluxes in the ocean still remain highly debated (e.g. Abbott et al., 2022; Haley et al., 2017; Lacan and Jeandel, 2005; Stichel et al., 2018; Tachikawa et al., 2017). Consequently, besides reconstructions derived from εNd, it is crucial to extend the understanding of the processes modifying the Nd isotopic compositions in climate archives.

While the last glacial cycle was extensively studied using εNd isotopes e.g. in deep sea sediments, the data is sparse for the past 1 Ma and rarely of millennial resolution. Moreover, there is an additional bias toward studies in the North Atlantic. In fact, only two εNd records from sediments in the North Atlantic reach as far back as 1 Ma. The record at site IODP U1313/DSPD 607 is mainly of glacial-interglacial resolution and was extensively studied as key to understand North Atlantic Deep Water (NADW) trough time (Jaume-Seguí et al., 2021; Kim et al., 2021; Lang et al., 2016; Lippold et al., 2016; Pöppelmeier et al., 2021a; Yehudai et al., 2021). At site ODP 1063 a εNd record of millenial resolution has been debated as representing NADW due to recurring local overprints (Böhm et al., 2015; Gutjahr and Lippold, 2011; Jaume-Seguí et al., 2021; Link, 2021; Lippold et al., 2019; Roberts et al., 2010). In the southern Atlantic Ocean there is no εNd record published yet, which extends 150 ka.

The aim of this study was to investigate the water mass Nd isotopic composition

preserved in the deep sea sediments at sites ODP 1093 and 1094, which are located in the southern Atlantic Ocean south of the Polar Front (PF). To reach this goal, a millennial resolution εNd record at site ODP 1093 was obtained, spanning the past 1 Ma until the late Mid Pleistocene Transition (MPT). The new record sets the εNd benchmark for the southern Atlantic Ocean. ODP 1094 was analyzed in four smaller timespans with focus on rapid climate transitions. The εNd data emphasizes the local Nd fluxes from sediments and volcanism in the global ocean. Additional multielement analysis of the sediment leachates provided insights into the ability of the data to reflect water mass signatures.

In chapter 2 the background of this work regarding the ancient climate, modern and past ocean circulation and Nd isotopic composition as water mass provenance tracer, is presented. Chapter 3 is dedicated to the investigated sediment sites and the sample treatment. Further, the measurement technique and the data treatment are described. A discussion on the measurement quality and the results of the multielement measurements are presented prior to the εNd records at site ODP 1093 and 1094 in chapter 4. The main discussion of this thesis is split in four parts (chapters 5-8). Firstly, the development of an age model for site ODP 1093 is described (chapter 5). Secondly, the origin of the εNd isotopic signatures at both investigated sites and the implications for the Southern Ocean carbon storage are discussed (chapter 6). The interhemispheric gradient $\Delta\varepsilon$Nd is further introduced to predict εNd signatures across the Atlantic and explore changes of the AMOC in the past (chapter 7). In the last chapter of the discussion, the circulation changes derived from εNd south of the PF over the MPT (chapter 8) are presented. At the end of the thesis a brief summary on the findings and an outlook on future challenges is given (chapter 9).

2. Background

2.1. Climate of the Past

The global climate of the Earth changed dramatically over time. On geological timescales the most recent history of the Earth spans the Pleistocene (2.6 Ma until 11.7 ka BP) and the Holocene (from 11.7 ka BP until the pre-industrial). The climate of these epochs is characterized by the alternation of cold and warm climate stages. Their variable climate conditions are reflected in many different climate proxies. A selection of climate records for the past 1.4 Ma are displayed in Fig. 2.1. The oxygen isotopes of benthic foraminifera in deep sea sediments across all ocean basins provide an excellent climate archive spanning over 5 Ma of the Earth's history (LR04) (Lisiecki and Raymo, 2005). The oxygen isotopic composition is normalized to a respective reference standard and calculated as follows:

$$\delta^{18}\mathrm{O} = \left[\frac{(^{18}\mathrm{O}/\mathrm{O})_{\mathrm{sample}}}{(^{18}\mathrm{O}/^{16}\mathrm{O})_{\mathrm{reference}}} - 1 \right] \cdot 10^3 \tag{2.1}$$

The variations of the δ^{18}O correspond to changes of the global ice volume and the deep ocean temperature. Based on the LR04 stack so called Marine Isotope Stages (MIS) were defined (Fig. 2.1 b). High benthic δ^{18}O values correspond to a larger global ice volume and lower temperatures. These periods are labelled glacials and are indicated by even numbered MIS. The warm periods are called interglacials are indicated by odd numbered MIS.

Orbital forcing is considered as the main driving force of the glacial-interglacial cycles during the Pleistocene (Milankovitch, 1941; Laskar et al., 2011). The solar insolation follows the orbital parameters of precession (T∼26ka), the obliquity (T∼41ka) and the eccentricity (T∼100ka) (Fig. 2.1 a). In the early Pleistocene the frequency of the glacial-interglacial cycles was obliquity driven. In the phase from 1250 ka to 700 ka BP the frequency changed such as glacial-interglacial cycles followed the 100 ka frequency of the eccentricity, but obliquitiy is still well recognised. This transition from a 41 ka world to the 100 ka world is called the Mid Pleistocene

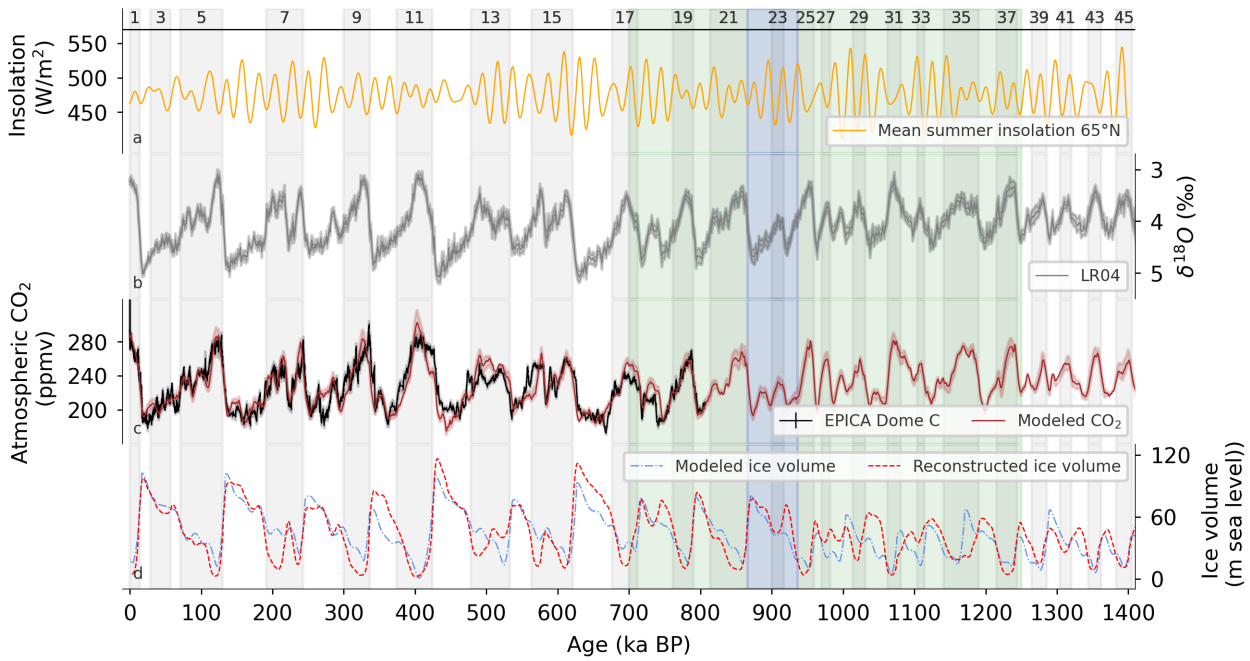

Figure 2.1.: Climate records of the past 1.4 Ma. Marine isotope Stages are marked in grey, the Mid Pleistocene Transition in green and the 900 ka event in blue. **(a)** Mean 65°N summer insolation (Laskar et al., 2011). **(b)** LR04 benthic δ^{18}O stack (Lisiecki and Raymo, 2005). **(c)** Atmospheric CO_2 reconstructed from EPICA Dome C (Bereiter et al., 2015) and modeled CO_2 (Berends et al., 2021). **(d)** Ice volume modeled (Legrain et al., 2023) and reconstructed from EPICA Dome C (Bereiter et al., 2015).

Transition (MPT) (Clark et al., 2006; Elderfield et al., 2012). With the transition of the glacial-interglacial cyclicity, the characteristics especially of the glacials changed significantly. In the 100 ka world glacials are characterized by higher δ^{18}O values indicating pronounced ice covers and lower global temperatures, while in interglacials similar δ^{18}O values are recorded as before the MPT. The glacials usually end abruptly with a sharp decline in δ^{18}O through melting and release of freshwater, marking the start of the warmer period with less ice volume and higher global temperatures. The trend toward higher δ^{18}O values during interglacials indicates a gradual glaciation of the planet until the next glacial maximum with following termination is reached. Together, this yields the typical sawtooth pattern of the climate of the past ∼1 Ma. In the earlier Pleistocene the glacials were less pronounced and their δ^{18}O signatures show a more symmetrical behavior.

There are many different drivers for the MPT proposed and associated events were observed on both hemispheres in various climate archives with different proxies (e.g. Hönisch et al., 2009; Kim et al., 2021; Lisiecki and Raymo, 2005; Willeit et al., 2019; Yehudai et al., 2021). The exact timing of the MPT and the origin of the global

cooling trend, however, are still highly debated. While several studies propose a gradual transition (e.g. Clark et al., 2006; Ford et al., 2016; Legrain et al., 2023), others assume a rather abrupt timing of the MPT, with the first occurrence of a strong glaciation, called the 900 ka event, spanning MIS 24-22 (Clark et al., 2006; Elderfield et al., 2012). This event is characterized by a global temperature minimum, the abrupt drop of the sea level and a dramatic rise in global ice volume (Bereiter et al., 2015; Elderfield et al., 2012; Legrain et al., 2023).

Over the MPT, there is no exceptional change in the main orbital forcing observed (Clark et al., 2006; Lisiecki, 2010), which could have led to a switch in the dominating frequency of the glacial-interglacial cyclicity and bifurcation of the systems states. Since the external forcing of the climate oscillations did not change, internal feedbacks in the Earth's climate system are proposed to explain the transition from a low amplitude 41 ka to the high amplitude 100 ka world with an enhanced global ice volume (e.g. Huybers and Tziperman, 2008). The atmospheric CO_2 is assumed to decrease progressively over the MPT (Hönisch et al., 2009; Raymo et al., 1997; Willeit et al., 2019). This would have led to the Earth's cooling eventually crossing a threshold, such that glacial ice sheets remained stable after the 41 ka (Clark et al., 2006).

Other studies propose the removal of regolith layers beneath ice sheets, mainly on the Northern Hemisphere, as a cause of the MPT (e.g. Clark and Pollard, 1998; Clark et al., 2006; Willeit et al., 2019). The low-friction regolith layer in the 41 ka world is thought to inhibit the built-up of large ice sheets. Hence, so called *pancake ice sheets* have been invoked for the Northern Hemisphere. The removal of the regolith layer exposed the underlying high-friction bedrock as basis for thicker and longer lasting ice sheets (Clark et al., 2006; Raymo et al., 1997; Willeit et al., 2019). Better ice sheet models invoke the combination of the drawdown in CO_2 and the regolith removal as essential to trigger the MPT (Legrain et al., 2023; Willeit et al., 2019).

Larger ice coverage of the Earth's surface in turn reduce the Earth's albedo, which further amplifies the cooling process. Somewhat counter-intuitive, the resulting ice sheet growth is assumed to reach a critical threshold size, which then results in a rapid deglaciation (Raymo et al., 1997). Recent modelling studies conclude, that both a gradual CO_2 decline and removal of regolith is necessary to control the MPT (Berends et al., 2021; Bereiter et al., 2015; Legrain et al., 2023; Willeit et al., 2019). Chalk et al. (2017) further explain the lower atmospheric CO_2 concentrations by a more effective carbon pump in the ocean. The glacial Southern Ocean stratification from the 900 ka event on, was suggested to be the physical mechanism supporting

an enhanced carbon storage in the deep ocean (Hasenfratz et al., 2019). However, atmospheric CO_2 reconstructions are sparse over the MPT and a substantial CO_2 decrease is only found when comparing the minimum values at the end of glacials (Chalk et al., 2017; Hönisch et al., 2009; Yamamoto et al., 2022).

Changes in atmospheric CO_2 and ice sheet dynamics in turn influence the Atlantic Meridional Overturning Circulation (AMOC) (e.g. Broecker, 1991; Farmer et al., 2019; Hasenfratz et al., 2019; Pena and Goldstein, 2014; Yehudai et al., 2021). In the North, changes in sea ice (e.g. Lear et al., 2016) and deep water dynamics due to the closure of the Bering Strait are hypothesized (Detlef et al., 2018; Kender et al., 2018). In the South, the Antarctic ice sheet and increased sea ice are proposed to influence deep water production and export from the Antarctic bordering Ocean (Lawrence et al., 2010; Raymo et al., 2006).

In summary, multiple studies show, that the interconnected reactions of the Earth's atmosphere, cryosphere, biosphere and the global ocean together led to the climate system's transition during the Mid Pleistocene. However, it is a complex task to robustly reveal their causal relation with each other.

2.2. Global Ocean Circulation

The global ocean circulation or as Wallace Broecker named it: *the great ocean conveyer belt* (Fig. 2.2) is a fundamental part of the Earth's climate, as it stores and re-distributes heat and matter such as carbon, oxygen and nutrients on the planet (Broecker, 1987, 1991; Roy-Barman and Jeandel, 2016).

2.2.1. Present Ocean Circulation

The modern ocean circulation is mainly driven by two mechanisms - wind stress at the surface and density gradients in the ocean's interior driving deep reaching convection. The winds at the atmosphere-ocean interface induce surface currents in the upper ocean ($\sim$100 m), the Ekman layer. The net transport within the Ekman layer is perpendicular to the wind direction due to the balance of the Coriolis force and the wind stress acting on the oceans surface. These surface currents lead to convergence and divergence of the sea surface and thus down and upwelling in the ocean. This results in a constant exchange of atmosphere and surface to mid-depth ocean on timescales of decades and centuries (Roy-Barman and Jeandel, 2016).

The second mechanism is called the thermohaline circulation. It is driven by

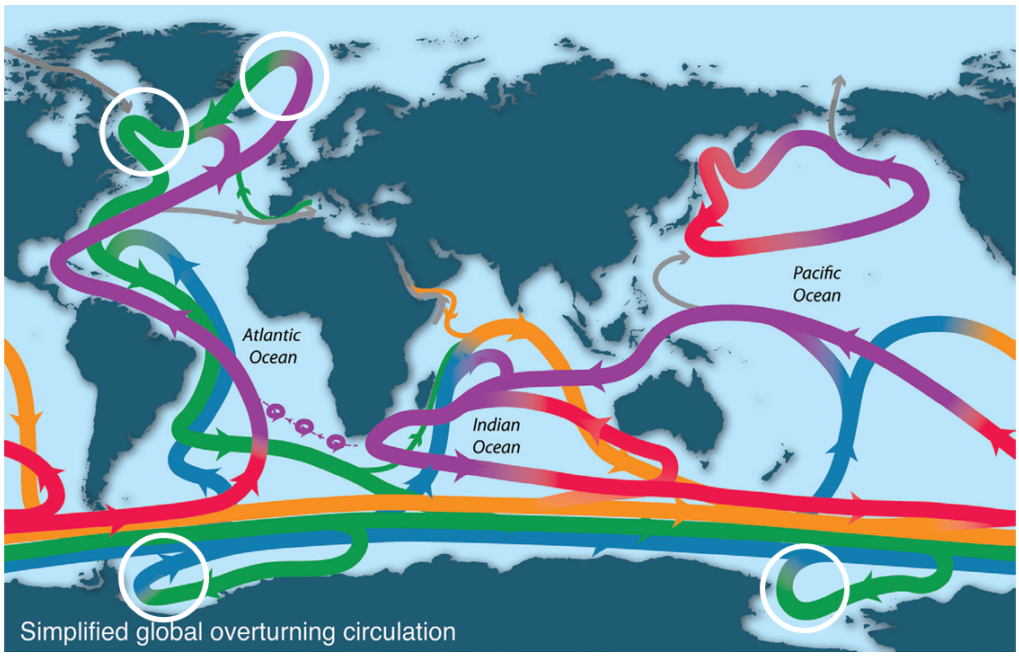

Figure 2.2.: Schematic of the global ocean circulation. Purple: upper ocean and thermocline. Red: denser thermocline and intermediate water. Orange: Indian Deep Water and Pacific Deep Water. Green: North Atlantic Deep Water. Blue: Antarctic Bottom Water. Grey: Bering Strait components and Mediterranean and Red Sea inflows. White circles: deep water formation areas. Adapted from Talley (2013).

changes in salinity and temperature of the ocean, which in turn lead to density gradients forcing advection (Rahmstorf, 2006). Processes influencing the temperature are surface heating, mainly at the equator, and cooling near the poles. Salinity is higher in areas of sea ice formation or evaporation and lower, when fresh water from rivers or ice melting enters the ocean (Fig. 2.3).

In combination, both mechanisms drive the meridional overturning circulation. This global circulation can be divided into two loops, the Atlantic Meridional Overturning Circulation (AMOC) and the Southern Meridional Overturning Circulation (SMOC). The latter connects all Ocean basins via worlds strongest current the Antarctic Circumpolar Current (ACC) in the Southern Ocean and is a crucial part in the overturning circulation (Marshall and Speer, 2012).

In the AMOC, warm and salty surface waters are transported from low latitudes to high latitudes, where sufficient cooling leads to a rise in density and less stratified water masses. Eventually the density is high enough, so the water mass sinks down and feeds deep water production. Today, this process only takes place in specific areas in the North Atlantic, forming North Atlantic Deep Water (NADW), and around Antarctica, forming Antarctic Bottom Water (AABW) (Fig. 2.2). NADW is exported to the Southern Ocean, where wind driven upwelling brings NADW to the

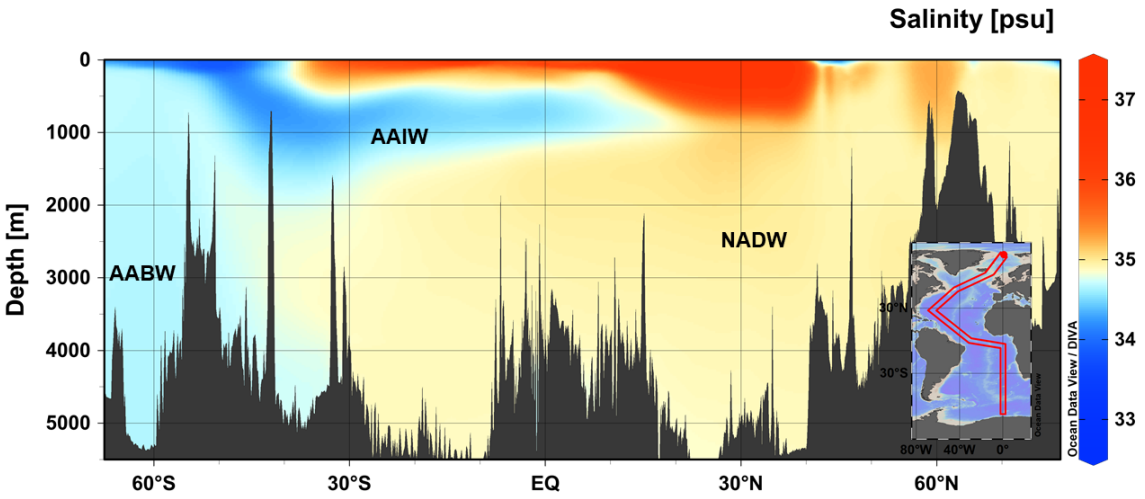

Figure 2.3.: Salinity across the Atlantic Ocean characterizing the water masses of AABW, AAIW and NADW in the Atlantic. Visualization with Ocean Data View (Schlitzer, 2019).

surface. It either feeds the AABW production or is mixed within the ACC. AABW itself is mixed in the Circumpolar Deep Water (CDW) or exported from the Southern Ocean to all ocean basins (Talley, 2013).

In contrast to the Atlantic Ocean, the Pacific and Indian Ocean do not show a meridional overturning circulation. Low salinity in northern Pacific and tropical conditions in the northern Indian Ocean inhibit sufficient deep water formation (Roy-Barman and Jeandel, 2016). Diffusive processes, however, lead to weak deep water formation in the Pacific and Indian Ocean, which is exported to the Southern Ocean. The crucial difference in the properties of water masses originating from the main ocean basins are imprinted from the sources feeding the respective deep waters. Since NADW is mostly supplied from the surface layer, ocean tracers indicate a young water mass age. This is reflected in high oxygen concentrations and low nutrient contents of NADW. The Pacific and Indian deep waters (PDW and IDW) are mostly sourced from bottom waters, resulting in higher water mass ages. Such water massed are characterized by low oxygen concentrations but high nutrient concentrations. Diapycnal upwelling of PDW and IDW in the Pacific and Indian Ocean are crucial to close the global overturning loop (Talley, 2013). Upwelling of waters from the deep Pacific and Indian Ocean takes also place in the Southern Ocean. Due to PDW and IDW being lighter than NADW, they are upwelled above and more northern than NADW (Talley, 2013). They partly feed Antarctic Intermediate Water (AAIW), which is characterized by a low salinity (Fig. 2.3).

2.2.2. Past Ocean Circulation

On glacial-interglacial timescales the ocean circulation is assumed to have changed drastically with climate. The circulation during interglacials is supposed to be rather similar to todays circulation. In contrast, the glacial ocean, even during the LGM is still not fully understood yet. During glacial the heat supply to the ocean was strongly reduced. Thus, the glacial ocean circulation is assumed a haline circulation (Adkins, 2013). However, the exact geometry of the ocean circulation remains debated. Various studies reconstructing the glacial AMOC, show glacial NADW export to be shallower and Southern Sourced Waters (SSW) dominating the glacial Atlantic Ocean (Jaume-Seguí et al., 2021; Kim et al., 2021; Lippold et al., 2012; Pena and Goldstein, 2014; Pöppelmeier et al., 2020; Rahmstorf, 2002, 2006; Yehudai et al., 2021). However, many studies point to similar deep water exchange during glacials compared to interglacials with a glacial NADW shoaling only during peak glacial maxima (Böhm et al., 2015; Rahmstorf, 2002). There is a strong bias toward studies in Northern Hemisphere regarding ocean circulation reconstructions, which do not draw a coherent picture yet.

In the Southern Hemisphere, recent studies showed less AABW export (Huang et al., 2020) and weaker ACC (Lamy et al., 2024; Toyos et al., 2020) during glacials of the past. The augmented sea ice cover during glacials lead to a northward shift of the westerly winds (Jochum and Eden, 2015; Sigman et al., 2010), which is not aligned with the Drake passage anymore (Marshall and Speer, 2012). As a consequence, the ACC was weaker, upwelling was shifted to the North, the meridional outflow from the Southern Ocean was likely reduced (Lamy et al., 2024; Marshall and Speer, 2012; Toggweiler et al., 2006; Toyos et al., 2020). These processes inhibited a strong interaction of the atmosphere with the deep ocean. Thus, the outgassing of CO_2 from the glacial Southern Ocean into the atmosphere was likely reduced. A sluggish circulation, strongly reduced export of AABW and the possible shoaling of glacial NADW provoke the ageing of a large volume of deep water occupying the deep Southern Ocean (Skinner et al., 2013). These processes allow for the accumulation of stored carbon in the deep southern Atlantic Ocean. This is further associated with reduced oxygen concentrations and thus increased alkalinity in the deep ocean (Yu et al., 2020).

How ocean circulation changes act as a trigger for such climate changes of the past, amplify various atmospheric or cryospheric changes or whether the ocean simply responds to climate, is the subject of recent paleooceanographic studies.

2.3. Nd as Water Mass Provenance Tracer

Neodymium is a lanthanoid of the atomic number Z=60. It naturally occurs in seven isotopes and has a mean mass of 142.242 u. Nd is considered as one of the 17 Rare Earth Elements (REE), which are mainly found in the Earth's lithosphere. REE are very similar in their chemical properties and thus in their particle reactive behavior in the environment.

The Nd isotopes of primary interest for this work are ^{143}Nd and ^{144}Nd, both of which are considered practically stable. Both originate from an α-decay of the respective mother isotopes ^{147}Sm and ^{148}Sm. With a half life of $\sim 10^{16}$ a ^{148}Sm is considered stable on geological timescales and thus also ^{144}Nd is assumed to be stable on these timescales. In contrast, ^{147}Sm has a half life of $\sim 10^{10}$ a and thus leads to measurable differences on geological timescales (O'nions et al., 1979). Due to a fractionation process during melting and crystallization within the Earth's mantle, Nd and Sm are differently abundant within the partial melt of the mantle. Nd is less compatible for mineral formation than Sm and is therefore enriched in the partial melt. As a consequence, the Sm/Nd ratio within the mantle is higher, than in continental crust, which in turn was formed by the partial melt. Over time the mantle and subsequent formed younger rocks are enriched in the radiogenic isotope ^{143}Nd originating from the continuous Sm decay. Hence, the Sm/Nd and especially ^{143}Nd/^{144}Nd ratios change in dependence of the lithology and time of the rock formation and thus contain valuable information of the age and the origin of rock material (O'nions et al., 1979; Tachikawa et al., 2020).

Since the variations in the ^{143}Nd/^{144}Nd ratios are in the range of hundred parts per million (ppm), the isotopic ratios are normalized to the Chondritic Uniform Reservoir (CHUR) (^{143}Nd/^{144}Nd = 0.512638) (Hamilton et al., 1983; Jacobsen and Wasserburg, 1980) and the epsilon notation (2.2) is used. Hereby, more positive/negative values are called radiogenic/unradiogenic and refer to the signature of younger rocks/older crust.

$$\varepsilon\mathrm{Nd} = \left[\frac{(^{143}\mathrm{Nd}/^{144}\mathrm{Nd})_{\mathrm{sample}}}{(^{143}\mathrm{Nd}/^{144}\mathrm{Nd})_{\mathrm{CHUR}}} - 1 \right] \cdot 10^4 \tag{2.2}$$

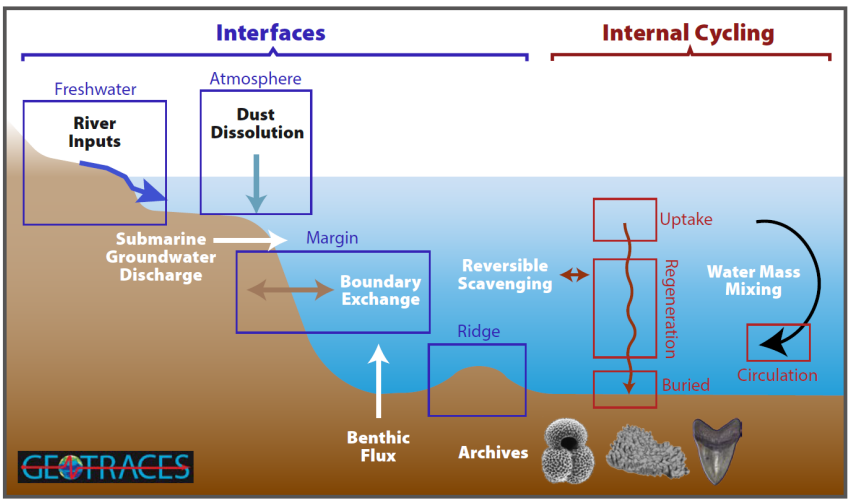

Figure 2.4.: Sources of Nd in the ocean and processes influencing its concentration and isotopic compositions. Figure from Tachikawa et al. (2020) based on GEOTRACES data.

2.3.1. Nd in the Ocean

There are several ways how Nd is transferred from the continents and recycled within the Ocean (Fig. 2.4). River runoff and dust input resulting from weathering processes serve as main sources of Nd in the ocean (Frank, 2002; Jeandel, 2016; Lacan and Jeandel, 2005; Tachikawa et al., 1999). Nd is not essential for biological processes but particle reactive and thus occurs in the ocean in dissolved or particulate form (Tachikawa, 2003). It has a mean concentration of approximately 10-50 pmol/g in the modern ocean, with higher concentrations in the bottom water due to its particle reactive nature (Lacan et al., 2012).

On its way into the ocean no significant Nd isotopic fractionation process takes place (Goldstein et al., 1984). The residence time of Nd in the ocean is in the same order of several hundreds to a thousand years as the ocean overturning time (Rempfer et al., 2011; Tachikawa, 2003). Thus, the residence time of Nd is sufficiently long to imprint water masses with the geographically distinct Nd isotopic composition of its deep water formation region (Fig. 2.5). The mean ocean circulation time is short enough to prevent the εNd signatures from equilibrating in the global ocean. Hence, variations of the sea water Nd isotopic composition are assumed to be mainly caused by advection and mixing of water masses on their way in the ocean. This quasi-conservative behavior forms the foundation of ocean circulation reconstruction with Nd isotopic compositions and is confirmed by observations in the modern ocean (Frank, 2002; Piepgras et al., 1979; Stichel et al., 2012; Tachikawa et al., 2017, 2020; van de Flierdt et al., 2016; Wu et al., 2022).

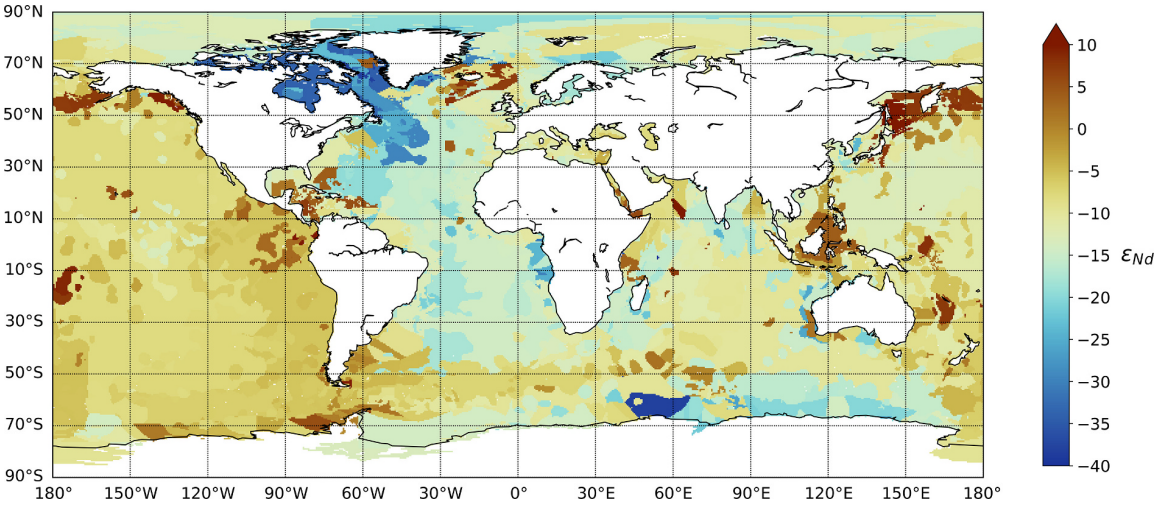

Figure 2.5.: Nd isotope signature of the global sediment-water interface from Robinson et al. (2021). The εNd data is extrapolated from the combination of the εNd signatures of the seafloor and continental margins.

When Nd gets recycled within the ocean, both Nd concentration and isotopic composition of the water masses may change in non-conservative processes, e.g. exchange with sediments and continental margins (Lacan and Jeandel, 2005; Tachikawa, 2003; Wang et al., 2022). The benthic flux was proposed as one underlying mechanism, which changes the Nd isotopic composition at the surrounding sediment-water interface via sedimentary pore fluids as source of Nd in the ocean (Abbott et al., 2015a,b; Haley et al., 2004). However, the contribution to the Nd budget and thus the Nd isotopic composition of the ocean are strongly dependent on the region, the flow dynamics and the oceans geochemistry (Abbott et al., 2022; Haley et al., 2017). Hence, to date no absolute value can be attributed to the change in εNd of a certain water mass due to local exchange processes.

2.3.2. Climate Archives of Nd Isotopes

The Nd isotopic signature of the present and past ocean is preserved in various climate archives and have been proven useful as a tracer for water mass provenance. Ideally, these archives have a robust age model, the knowledge on the past Nd sources and εNd signatures of deep water masses is sufficient and extraction methods for the Nd are available.

In the course of this work, the Nd isotopic composition of a distinct water mass produced by deep water formation will be defined as the water mass εNd endmember and is assumed to be constant over time. Further, the water mass, which interacts with an entire ocean basin originates often from a mixture of different water masses, like NSW or SSW. It will be referred to as ocean basin εNd endmember and may

show variable εNd signatures depended on the processes influencing its εNd signature.

There are several different archives available, which preserve the εNd signature of the ambient water mass. All different archives span various time and water depth ranges. Needless to say, all climate archives have their own advantages and limitations. The following enumeration does not aim for completion but rather provides an overview of the variety of εNd archives and studies using them.

Fish teeth and foraminifera are the most reliable archive for Nd isotopes and thus the reconstruction of deep water mass provenance (Roberts et al., 2012; Tachikawa et al., 2014). Fish teeth contain high amounts of Nd, which are mostly incorporated post mortem and thus reflect the sea water Nd isotopic composition (Martin and Haley, 2000). Although fish teeth globally occur in sediments, not every sample with in a sediment core contains fish teeth, thus rarely a continuous εNd record can be generated (Frank, 2002). Planktic and benthic foraminifera are single-celled organisms, which scavenge Nd in their $CaCO_3$ skeleton as they sink to the seafloor. Core top foraminifera Nd isotopic signatures are in great agreement with surrounding sea water εNd signatures and thus are used for reconstructing past seawater εNd values. However, when using only foraminifera from the sediment generating a continuous high resolution εNd record can be challenging depending on the site. This is on the one hand due to the huge number of foraminifera, which have to be picked from the bulk sediment to get a sufficient Nd concentration in the sample. On the other hand, their abundance may be low in carbonate poor sediments below the lysocline or in Antarctic polar waters, where opal dominates the sediment composition.

Cold water corals serve as excellent archives for the εNd signature of the ambient intermediate depth water Nd isotopic composition (Colin et al., 2010; Copard et al., 2010, 2012; Robinson et al., 2014; van de Flierdt et al., 2010). Since Nd is not involved in biological processes yet particle reactive, Nd is incorporated from the sea water into the $CaCO_3$ skeleton of corals. Cold water corals are further assumed to be free of sedimentary inputs. Their occurrence is widely spread in the global oceans and their age can be determined directly via Th-U dating (e.g. Frank and Hemsing, 2021). However, their temporal occurrence is variable and Nd concentrations can be very low (Copard et al., 2010; van de Flierdt et al., 2010). Thus, a well resolved and continuous εNd record is difficult to obtain from cold water corals.

Ferromanganese crusts and nodules but also authigenic coatings of sediment particles preserve the particle reactive REEs and thus Nd isotopic composition of the overlying water mass. Hereby, the REE scavenge onto reactive Fe and Mn oxides dur-

ing colloid formation, which are in exchange with the water column. During advection processes these colloids thus reflect the ambient sea water Nd isotopic composition. Finally, they precipitate either as nodules and crusts or onto sediment particles as Fe-Mn coatings. Nodules and crusts grow slowly and thus integrate the εNd signature over several hundred thousand years (Frank, 2002). Depending on the size of the nodule water mass εNd signatures over many millions of years can thus be reconstructed, however in a low temporal resolution.

The authigenic coating of particles in deep sea sediments offers the great opportunity to obtain continuous εNd record mostly in a high resolution depending on the sedimentations rate. Thus, the reconstruction of circulation patterns on glacial-interglacial time scales is possible (Frank, 2002; Piotrowski et al., 2004, 2005; Rutberg et al., 2000). Deep sea sediments accumulate on the sea floor via precipitation of sediment particles such as dust, biogenic material e.g. foraminifera or small Fe-Mn particles. The coating of the particles is assumed to reflect εNd signature of the bottom water mass, which was present at the time of sedimentation. Depending on the region, the sedimentation rates can reach up to tens of centimetres per thousand years. Another benefit from authigenic sediments coatings it the generally high Nd concentration in processed samples. Since sedimentation is unlikely interrupted, the authigenic coating of deep sea sediments form a continuous archive. Together with a suitable age model, ideally obtained from foraminiferal δ^{18}O values, a high temporal resolution can be achieved.

Sedimentary authigenic Nd also has its disadvantages, which mainly stem from the various local sources mentioned in chapter 2.3.1, which can influence the Nd budget of the Fe-Mn coating after the burial. The bulk sediment composition depends strongly on the area in the ocean. It contains various phases besides ferromanganese coatings and foraminifera also diatoms, volcanic ash, Ice Rafted Debris (IRD), terrigenous inputs and dust. Depending on the flow dynamics and the ocean's geochemistry these phases can exchange εNd signatures with the pore waters and therefore likely also the lowest bottom water layer (Abbott et al., 2022, 2015a; Lacan and Jeandel, 2005; Tachikawa et al., 2017).
The influences on the preserved Nd signature can only be estimated indirectly via determining the εNd signature of the different phases of the sediment independent from each other. Ideally, pore water Nd isotopic compositions give insights on the exchange of the sediment phases with each other (Abbott et al., 2015a; Haley et al., 2017). In summary, the total Nd budget in the authigenic sediment coating is initially driven by Nd originating from the water mass and after burial its Nd isotopic signature is modified under certain conditions to various extents. However, the exact

influence on the authigenic Nd isotopic composition from other sources remain elusive. Not only the Nd isotopic composition but also the absolute Nd concentration, which contribute to the Nd budget of the authigenic coating in the past are difficult to reconstruct.

Multiple studies showed a great agreement of εNd signatures of the core-top authigenic coating with the ambient deep water mass across ocean basins (Blaser et al., 2019, 2016; Howe et al., 2016a; Martin and Haley, 2000; Noble et al., 2012; Tachikawa et al., 2014; Williams et al., 2021). This observation usually is a measure for the applicability of authigenic coatings as recorders of past water mass signatures. Additionally, the εNd signature of foraminifera and the authigenic coating from the bulk sediment were shown to be identical (Martin et al., 2010; Tachikawa et al., 2017), which provides further evidence for reliable water mass reconstructions through the authigenic Nd isotopic composition. Discrepancies in the εNd of foraminifera and the authigenic coating are also known in particular regions (Roberts et al., 2010). Besides different local conditions within the sediment, the applied method to extract the Nd from the coating of a bulk sediment bears the potential to influence the presumed authigenic signature with εNd from the bulk sediment material (Blaser et al., 2016; Gutjahr et al., 2007; Huang et al., 2021). This influence can be minimized when using the optimal chemical extraction procedure to extract the authigenic Nd from the bulk sediment.

To reliably interpret authigenic εNd signatures of deep sea sediments, the entire Nd budget, the flow dynamics and the extraction procedure are considered. Taking these into account, the authigenic coatings of deep sea sediments serves as excellent climate archive for past seawater Nd isotopic signatures.

2.4. The Southern Ocean - an Overview

The Southern Ocean plays a unique role in the global ocean circulation and thus the global climate. Due to the solitary position of the Antarctic continent, the Southern Ocean is the only place on Earth where water masses can cycle more or less undisturbed around the globe forming the Southern Meridional Overturning Circulation (SMOC). Wind driven upwelling and deep water formation due to strong cooling around Antarctica connects all water depth layers (Kuhlbrodt et al., 2007; Talley, 2013). The ACC is the strongest ocean current and interconnects the southward exported water masses from the Pacific, Atlantic and Indian Ocean (Marshall and Speer, 2012).

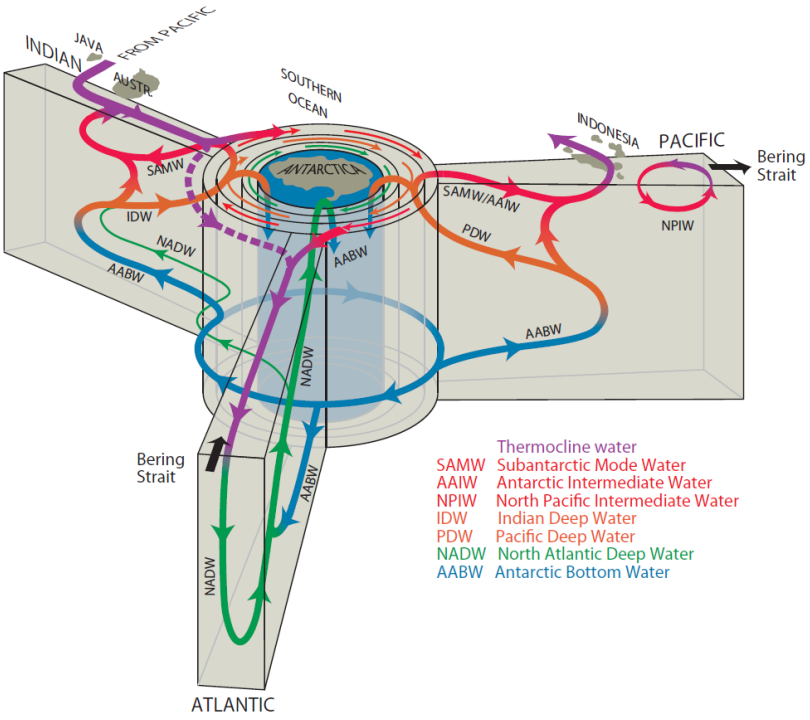

Figure 2.6.: Schematics of the overturning circulation from a Southern Ocean perspective (from Talley, 2013). Colors as in Fig. 2.2.

The position and the strength of the ACC are determined by wind stress from the vigorous westerly winds across the circumpolar belt, interaction with the bathymetry, and buoyancy forcing (Rintoul, 2018; Talley, 2013). The latter is controlled by freshwater inputs from ice melting in Antarctica and heat loss changing the density structure of the ocean (Rintoul, 2018).

The ACC is structured in three main oceanographic fronts, namely the Subantarctic Front (SAF), the Polar Front (PF), and the Southern ACC Front (SACCF) (Orsi et al., 1995). These coincide with the region of intense jets in the ocean current being responsible for the main geostrophic transport (Lamy et al., 2024; Orsi et al., 1995; Toyos et al., 2020). The position of the fronts change on seasonal to glacial-interglacial timescales (Gersonde et al., 2005; Kemp et al., 2010). The positions of the fronts within the ACC have a strong impact on the AMOC as they control the volume of the different water masses that enter the Drake Passage, and thus the southern Atlantic Ocean (Gordon, 1986). The topography of Drake Passage band around the globe (roughly 57° to 61°S, sill depth of about 2 km) and the westerly winds further cause diverging surface currents to the North and thus upwelling of deeper water masses, that in turn feed the repetitive formation of deep water (Talley, 2013).

The global ocean circulation from a Southern Ocean point of view is displayed in

Fig. 2.6. Within the ACC the high salinity North Atlantic Deep Water (NADW) lies beneath low oxygen Indian Ocean Deep Water (IDW) and Pacific Deep Water (PDW) today. All of these are exported via Southern Ocean upwelling to the sea surface to either form the dense Antarctic Bottom Water (AABW) (blue cylinder in Fig. 2.6) or feed the upper ocean waters and subtropical thermoclines flowing northward (Talley, 2013).

The layering of these deep water masses lead to IDW, PDW and the lighter fraction of NADW being more likely upwelled in ACC. After gaining buoyancy from fresh water due to sea ice melting they get exported northward in shallower depth as Subantarctic mode water or Antarctic Intermediate Water (AAIW) and again downwelled in the mid latitudes. The heavier fraction of NADW (75 %) is upwelled closer to the Antarctic margin to feed the AABW production or is mixed within the ACC forming the lighter CDW (Marshall and Speer, 2012). The AABW formation requires substantial fractions of IDW and PDW besides NADW (Talley, 2013). AABW is produced close to the Antarctic continent by brine rejection in the shallower water close to the continent or by strong cooling of waters in polynas and is exported to the deep North.

The variable interaction of the atmosphere and the ocean results in changes in ACC flow, that in turn impact the Antarctic cryosphere massively today and also in the past (Lamy et al., 2024; Noble et al., 2020; Shi et al., 2021). The strong and undisturbed westerly winds force the Southern Ocean's dynamic and induce a wide spread mesoscale eddy field in the ocean (Marshall and Speer, 2012). These enable effective transport of mass, heat and energy across the ACC but also the atmosphere-ocean interface (Hallberg and Gnanadesikan, 2006; Marshall and Speer, 2012). The close interaction between the atmosphere and the Southern Ocean further emphasizes the role of the ocean in the uptake and release of atmospheric CO_2 on glacial-interglacial timescales but also the recent anthropogenic climate change (Anderson et al., 2009; Brovkin et al., 2007; Burke and Robinson, 2012; Frölicher et al., 2015; Gottschalk et al., 2016; Sigman et al., 2010; Yu et al., 2020, 2022). In summary, the Southern Ocean and its flow dynamics are the key elements of inter ocean basin exchange and interactions between major components of the climate system, ocean, atmosphere and cryosphere, and impacts the marine biosphere. The Southern Ocean dynamic integrates over climate signals around the world and its response in turn affects the entire global climate.

All water masses are distinguishable by their physical properties such as salinity, temperature but also by nutrient and oxygen contents and by their εNd signatures.

The water masses that are of importance for this thesis are PDW, NADW, AABW and CDW, the mixture of all water masses present in the Southern Ocean.

As there is no sufficient buoyancy loss in the North Pacific to form deep water from the surface, PDW is almost entirely sourced from in the Pacific upwelled bottom waters originating from AABW (Talley, 2013). Hence, it is marked by tracers indicating much greater age through low oxygen and high nutrients. Due to the local Pacific Nd sources, PDW is the most radiogenic deep water mass (εNd ~ -2 to -4) (Hu and Piotrowski, 2018; Tachikawa et al., 2017) and contributes to the Upper CDW via export from the deep equatorial Pacific.

CDW is a mixture of all contributors, which is reflected in a mean εNd signature of approximately $\varepsilon\text{Nd} = -7.8 \pm 1.2$ (-7.9 ± 1.3) in the Pacific (Indian) Ocean (Tachikawa et al., 2017). Corals in the Atlantic sector of the Southern Ocean and the Drake Passage show modern CDW values of $\varepsilon\text{Nd} = -8.2 \pm 0.5$ and more variable glacial values in the range of $\varepsilon\text{Nd} = -5.9$ to -7.7 (Wilson et al., 2020).

NADW is a mixture of the deep water masses formed in the North Atlantic mainly in the Labrador Sea and the Nordic Seas. It has a characteristic signature of $\varepsilon\text{Nd} \sim -12.3 \pm 0.9$ (Tachikawa et al., 2017).

AABW can be considered as mainly recycled NADW and with additional Pacific and Indian Ocean sources. This yields an εNd signature of $\sim -8.6 \pm 0.6$ (Tachikawa et al., 2017).

3. Material and Methods

The reliable use of authigenic εNd signatures of deep sea sediments as a water mass provenance tracer requires an ultra clean sample processing and high precision measurements of the Nd isotopic signatures. The major steps in the processing procedure from dried sediment samples over chemical extraction of Nd to the εNd measurement and data treatment are displayed in Fig. 3.1.

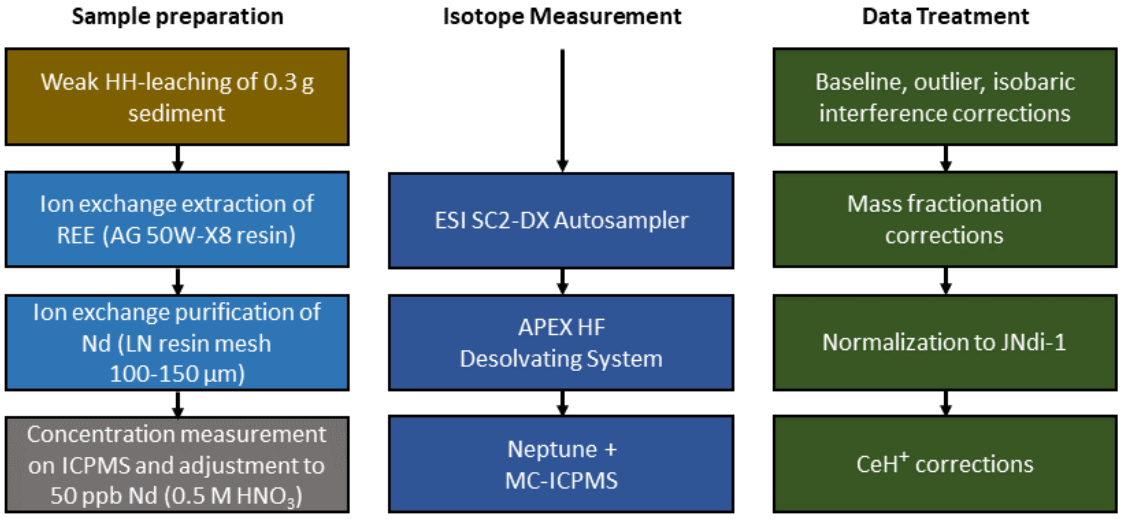

Figure 3.1.: Schematics on sample treatments, measurement and data evaluation. **Left**: Chemical sample preparation and concentration measurements. **Middle**: Measurement of the Nd isotopic compositions. **Right**: Procedure of the data evaluation.

3.1. Material and Sample Treatment

3.1.1. Sites ODP 1093 and 1094

Locations

ODP Site 1093 and 1094 were drilled during Ocean Drilling Program (ODP) Leg 177 in the southeast Atlantic sector of the Southern Ocean within the circum-Antarctic opal belt. Both sites are situated south of the modern PF and thus are within the bounds of the Antarctic Circumpolar Current (Fig. 3.2).

Site 1093 was drilled north of the Shona Ridge close to today's PF north of the average winter sea-ice edge at 49°58' S, 5°51'E in 3624 m water depth. It is located in the ACC exposed to Lower Circumpolar Deep Water. The area represents the southernmost influence of NADW as it mixes with CDW and becomes part of the ACC (Gersonde et al., 1999). The region is characterized by thick moderately laminated pelagic drift deposits and a high flux of biosiliceous ooze that accumulate with high sedimentation rates.

The sediment contains mainly diatom ooze from well preserved diatoms with varying abundances of foraminifera, nannofossils and siliciclastic mud. The extensive deposition of diatom mats leads to the overall high sedimentation rates at site ODP 1093 of more than 200 m/Ma. Calcium carbonate contents are generally highly variable between 0 to 53 wt%, opal averages 66 ± 13 wt%, and siliciclastics average 18 ± 12 wt%. The occurrence of foraminifera is highly variable, rather low for the upper ∼200 m of sediment and vanish almost completely during glacial intervals. Especially, the abundance and preservation of benthic foraminifera is overall poor. The occurrence of sand- to gravel sized siliciclastic material, mainly of volcanogenic origin, is minor however ubiquitous.

The obtained new data of ODP 1093 spans a total of 246.89 meters of sediment and was sampled in 525 different depths. It reaches 1081 ka back in time with an average temporal resolution of 2.06 ka. Thereby, major climate events such as the LGM (11.7 ka BP), MIS 11 (around 400 ka BP) and the end of the MPT with the 900 ka event in the Southern Atlantic Ocean around the polar frontal zone are recorded.

Site 1094 is located further to the South close to Bouvet Island and south of the PF at 53°10' S, 5°7'E in 2807 m water depth. It lies still within the ACC with its southern bound coinciding with today's average sea ice edge. However, Site ODP 1094 is assumed to be covered by sea ice during the Last Ice Age (Gersonde et al., 1999).

The sediment composition is quite similar to site ODP 1093, however pure diatom mats are less common yielding a lower sedimentation rate of around 100 m/Ma. Additionally, calcium carbonate contents are even smaller compared to site ODP 1093 varying between 0 to 30 wt%, whereas opal dominates with 50 to 95 wt% and siliciclastic ranges from 5 to 60 wt%. The abundance of foraminifera is lower for the first ∼80 m of sediment but generally higher compared to site ODP 1093, however benthic foaminifera occurrence is equally sparse. The shallower depth and lower sedimentation rates are assumed to positively influence the occurrence and preservation

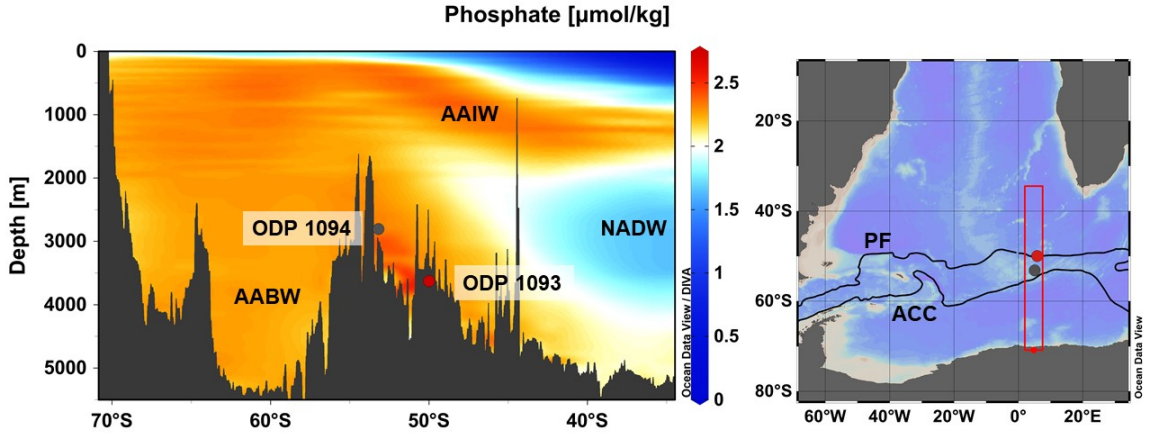

Figure 3.2.: Locations of the investigated sites ODP 1093 and 1094. **Left**: Dissolved phosphate content on a transect across the southern Atlantic Ocean. The phosphate concentration follows the main water masses. **Right**: Transect across the Polar Front (PF) and the Antarctic Circumpolar Current (ACC). Visualization with Ocean Data View (Schlitzer, 2019).

of foraminifera at this site (Gersonde et al., 1999). Besides the minor but persistent occurrence of vocanogenic sand- to gravel sized material, small volcanic dropstones are observed throughout that are likely deposited during glacial intervals.

The determined εNd record of site ODP 1094 consists of four time intervals with a total of 115 analysed depths. The record covers termination I and II, a full glacial-interglacial cycle from mid MIS 12 to mid MIS 8 and the time span around the 900 ka event from 850 to 1000 ka.

Age Models

The age-depth relation of both ODP sites were investigated in several studies. Kemp et al. (2010) used color reflectance data of both sites to correlate them with each other and assigned them to major climate events (Kemp et al., 2010). High color reflectance indicates high calcium carbonate content and can be tied to peak interglacial intervals, whereas lower reflectance corresponds to glacial periods (Gersonde et al., 1999). Additionally, the color reflectance data agrees well with the planktic δ^{18}O measurements in larger time intervals, especially in ODP 1094 (Kemp et al., 2010). ODP 1094 was used as a master site to compare ODP 1093 against. The sediment depth of ODP 1093 was tied to the depth of ODP 1094 via color reflectance data. In combination with earlier findings of studies on the timing of IRD occurrence in ODP 1094 (Kanfoush et al., 2002), paleomagnetic reversals in both ODP 1093 and ODP 1094 (Channell and Stoner, 2002) and δ^{18}O tie points and MIS boundaries (Kanfoush et al., 2002) an age model for both locations could be developed.

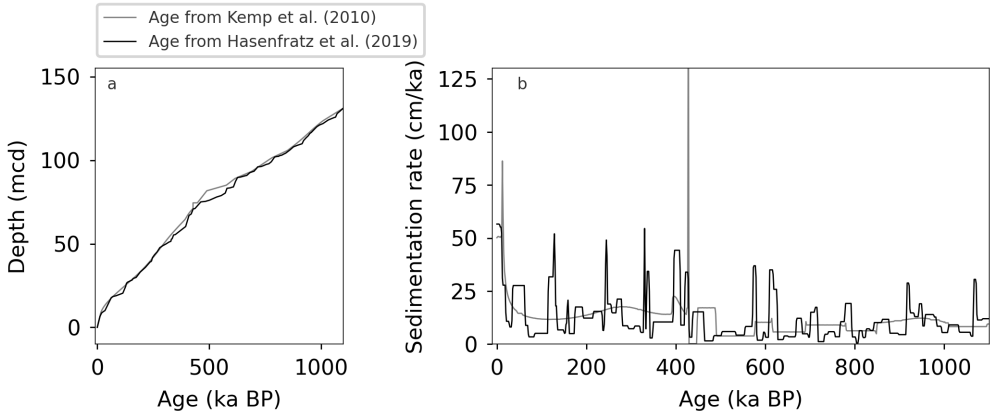

Figure 3.3.: Age model for site ODP 1094 from Kemp et al. (2010) and Hasenfratz et al. (2019) in comparison. **a**: Age-depth relation. **b**: Sedimentation rates in the past 1 Ma for both age models.

It is common to use the benthic δ^{18}O compilation LR04 (Lisiecki and Raymo, 2005) as a reference stack for δ^{18}O records of individual sediment sites. This method requires sufficient and continuous occurrence of benthic foraminifera species within the sediment. Hasenfratz et al. (2019) developed a new age model for ODP 1094 by extending existing δ^{18}O record with further data points from planktic foraminifera. Additionally, determined benthic δ^{18}O values are highly correlated with the planktic δ^{18}O record (Hasenfratz et al., 2019). These records were tuned to the benthic δ^{18}O compilation LR04 (Lisiecki and Raymo, 2005). Both age models for ODP 1094 agree very well with each other (Fig. 3.3).

Due to the total lack of benthic and the sparse occurrence of planktic foraminifera in ODP 1093 there is no age model published based on δ^{18}O values. Furthermore, during the work of this project, complications with the existing age model of Kemp et al. (2010) occurred. Since sedimentation rates of ODP 1093 are significantly higher compared to ODP 1094, the precise assignment of sediments depth across sites is difficult. Therefore, the age tie points for ODP 1093 are likely less reliable. To overcome this problem two different solutions were found. For the last 150 ka an age model was determined via tuning the existing planktic δ^{18}O record to the close by Vostok ice core data. For the older sediment sections of the site where oxygen isotope measurements are sporadic, abrupt transitions in εNd itself were tuned to the climate record of LR04 (Lisiecki and Raymo, 2005). Both methods are part of this work and are discussed in detail in chapter 5.

3.1.2. Sample Treatment

To reliably extract εNd signals from sediment coating the leaching technique of Blaser et al. (2016) was applied. The general procedure follows the scematics displayed in 3.1. Firstly, 0.25-0.3 g of dried sediment were rinsed with high purity water (MiliQ). Afterwards the ferromanganese hydroxide coatings were dissolved using a weak leaching solution. The leaching solution consists of 1.5% (0.26 M) acetic acid, 0.005 M hydroxylamine hydrochloride (HH), 0.003 M Na-EDTA and was buffered to a pH of 4 using NH_3. The samples were then centrifuged to separate the dissolved coatings from the remaining sediment particles. The total exposure time to the leaching solution did not extend 60 minutes to ensure minimal influences of the detrital material as recommended for carbonate depleted sediments (Huang et al., 2021).

Afterwards the solution was decanted, dried and solved for taking aliquots for future matrix element samples. The aliquots were diluted 20 times for storage and from that additional 250 times for the multi element measurements.

The Nd fraction of the remaining samples was separated via two ion exchange chromatography columns (Blaser et al., 2016; Gutjahr et al., 2007; Pin et al., 1994). Firstly, the REE fraction was separated using AG 50W-X8 (200-400 mesh, BioRad). Secondly, Nd was purified with LN-B50A resin (100-150 µm, Triskem). The final samples mainly contain purified Nd (∼45% of the initial Nd content) and are essentially Sm free however small residual amounts of Ce (∼7% of the initial Ce content) remain within the sample.

Prior to the εNd measurement the remaining concentrations of calcium and the Rare Earth Elements were determined with the ICAP Q mass spectrometer to assess the quality of the chemical separation of Nd. A successful chemical treatment is characterized by a low remaining calcium fraction, ideally lower than 1 ppm, and more importantly a low Ce concentration in comparison to the Nd fraction. The optimally achievable Ce/Nd ratios for sediment samples are smaller than five. Samples with much higher Ce concentrations were repeated. Additionally, the concentrations of the total procedural blanks were checked to be in the same order as the measurement blanks. Following the concentration measurements all samples with Nd concentrations higher than 50 ppb were diluted to 50 ppb to obtain optimal measurement conditions for the isotope measurements.

3.2. Measurements and Data Evaluation

Both the εNd signatures and the multielement concentrations are measured on mass spectrometer. For the εNd measurements a High Resolution Multi Collector Inductively Coupled Plasma Mass Spectrometer (HR MC ICPMS) is used. To measure the element concentrations a Quadrupole Inductively Coupled Plasma Mass Spectrometer (Q ICPMS) is sufficient.

3.2.1. Mass Spectrometry - an Overview

In general, all mass spectrometers work after the same physical principle of generating ions of the analyte's atoms or molecules by any suitable method. To separate these ions by their mass to charge ratio and to detect them based on their ratio and abundance in the sample. The analyte can be ionized e.g. thermally, by electric fields or via a plasma.

Ion separation requires ions of the same velocity and then takes place in a magnetic field in which the Lorentz force directs charged particles on circular paths of different radii depending of their mass to charge ratio. To simplify the separation and detection process, it is the convention to create single charged cations resulting in a radius dependency of only the mass of the particle. To detect the ions different detection systems can be used, while Secondary Electron Multipliers (SEM) or Faraday cups are the most common technique. Inductively Coupled Plasma sourced Mass Spectrometry (ICPMS) allows for a precise detection of various elements. Mass spectrometers of this type, as used in this work, consist in the main of three modules and a preconnected inlet system (Fig. 3.4). The inlet system varies depending on the elements that are measured. However, its main purpose is to convert the liquid sample to an aerosol and lead the sample from the laboratory environment into the Inductively Coupled Plasma (ICP) module.

The ICP module forms the interface from atmospheric pressure to high vacuum conditions. The load coil with the plasma torch is located in the ICP module. The $\sim$8000 °K plasma is ignited with an initial spark,in an argon gas flow under low vacuum conditions. Auxiliary gas flows stabilize the plasma while the sample is introduced in an argon nitrogen mixed gas flow. Within the plasma the sample atoms get ideally single ionized. The resulting ion beam passed two orifices, sample and skimmer cone, into the high vacuum of the Electrostatic Analyzer (ESA) module.

The ESA module consists of a configuration of different transfer lenses which serve to extract the ions from the gas flow and accelerate them on a velocity of $\sim$5 KeV.

The ion beam gets additional acceleration and isobaric ions get filtered out by another set of lenses. After shaping the beam, it perfectly fits through the entrance slit of the magnetic sector. The magnetic field of up to 1.2 T separates the ion beam into multiple beams depending on their mass to charge ratio. However, since all higher ionised ions were filtered out, the radii only depend on the respective mass of the ions.

The beams of mass differences of one atomic unit pass the focus lens system in order to optimize their detection. A multicollector module facilitates the detection of different elements simultaneously with accurately placed Faraday cups with connected amplifiers. Finally, the resulting signal can be converted in concentrations via calibration measurements since it is proportional to the incoming amount of the detected ions. This detection method is used in high precision multicollector mass spectrometers.

For faster, however less precise, analysis an SEM is used. The detection is achieved by adjusting the deflection of the ions such that only the mass range of one element hits the detector. Via scanning the whole mass range, a quasi simultaneous analysis of the concentrations of elements in a sample can be achieved.

Since its first appearance Inductively Coupled Plasma sourced Mass Spectrometry has thus become the leading technique for the analysis of trace elements in e.g. climate archives (Gray and Date, 1983; Houk et al., 1980). Together with a suitable inlet system the measurement of samples placed in an environment of atmospheric pressure is possible. In conclusion, ICPMS allows for the determination of isotopic compositions with a high sensitivity, good precision and effective sample throughput. ICPMS has the advantage of being less time consuming and also applicable for a broader range of elements even with high ionization energy such as hafnium and wolfram compared to its predecessor the Thermal Ionization Mass Spectrometry (TIMS) (Luais et al., 1997).

3.2.2. Multielement Measurements of the Leachates

Measurement Setup

The multielement measurements of the leachates have been carried out on an ICAP Q ICPMS (Thermo Fisher Scientific) at the Institute of Environmental Physics of Heidelberg University. For sample uptake and desolvation the combination of an SC2-DX Autosampler (ESI) and an APEX HF (ESI) desolvating system was used.

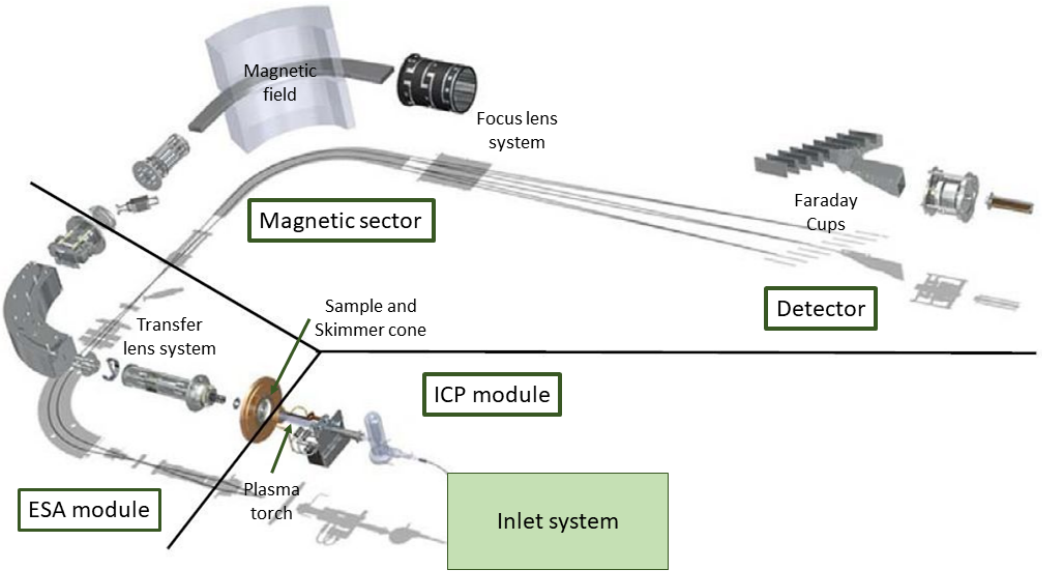

Figure 3.4.: Scematic setup of the Neptune Plus Mass spectrometer. Modified from Thermo Fisher Scientific (2009).

The measurement and evaluation protocol closely follows the used method of P. Blaser (Blaser et al., 2016; Blaser, 2017). All multielement measurements were conducted in Kinetic Energy Discrimination (KED) mode. Hereby, a collision cell in the path of the ion beam is filled with helium gas. The gas interacts with the ions deflecting light ions and molecules. Thus, the transmission efficiency of the less abundant heavier isotopes within the matrix element samples is improved. The overall measurement setup was optimized to accurately analyse low concentrations of REE and other elements such as aluminium, strontium and calcium. To calibrate the mass spectrometer, an accurately mixed multielement standard in different concentrations was measured with rising concentrations before every measurement.

The measurement reproducibility was assured by measuring several replicates and the sea water standard SPSSW2 throughout the measurement sequence. Repeatedly, a drift standard is measured, to correct for the internal drift of the machine. An additional oxide solution is analyzed, to correct for interference of barium and cerium on europium and gadolinium. Both standard and sample measurements consist of five consecutive measurements.

Data Evaluation

The raw intensity measurement data was partly evaluated by the Qtegra program that comes with the mass spectrometer. From the intensity average and its standard deviation, the concentration and its uncertainty are calculated using the determined

calibration curve. The data is additionally corrected for the blank and the drift of the machine. The concentration of Eu and Gd are adjusted regarding the interference on the respective masses of Ba and Ce in the oxide drift. Finally, the results are recalculated with respect to prior dilutions and the initially weighted sediment samples.

The results are used to investigate element and REE ratios. The REE ratios are defined and based on their abundance relative to the reference standard Post Archaean Australian Shale (PAAS) (Martin and Scher, 2004; Nance and Taylor, 1976). The ratios are calculated as follows with square brackets indicating element concentrations and horizontal bars stand for the arithmetic mean.

Ce anomaly:	$Ce/Ce^* = [Ce]/\overline{[La],[Pr]}$	(3.1)
Europium anomaly:	$Eu/Eu^* = [Eu]/\overline{[Sm],[Gd]}$	(3.2)
Light REEs:	$LREE = \overline{[La],[Pr],[Nd]}$	(3.3)
Middle REEs:	$MREE = \overline{[Gd],[Tb],[Dy]}$	(3.4)
Heavy REEs:	$HREE = \overline{[Tm],[Yb],[Lu]}$	(3.5)
REE slope:	$HREE/LREE$	(3.6)
MREE bulge:	$MREE/MREE^* = MREE/\overline{LREE, HREE}$	(3.7)

3.2.3. Nd Isotopic Composition Measurements

MC-ICPMS Setup

All analytical tests and Nd isotopic composition sample measurements reported here have been carried out on a Neptune Plus multicollector ICPMS (Thermo Fisher Scientific) at the Institute of Environmental Physics of Heidelberg University. For sample uptake an SC2-DX Autosampler (ESI) was used. The APEX HF (ESI) desolvating system has emerged as the most suitable for the measurement of Nd isotopes because it provided the most stable conditions in terms of signal intensity per concentration and mass discrimination while other desolvating systems connected to the used setup did cause more variable mass discrimination in particular during individual runs. Such unstable conditions would inhibit the use of standard-sample bracketing for normalization of isotope ratios.

The described analytical procedures follow the schematics shown in Fig. 3.1. Typical measurement parameters are displayed in Tab. 3.2. The measurement was conducted in a static mode on eight Faraday cups (Tab. 3.1). Six Nd isotopes and ^{142}Sm are measured on cups connected with 10^{11} Ω amplifiers to guarantee the same order

Table 3.1.: Cup configuration for Nd isotope measurements for the setup at the Institute for Environmental Physics in Heidelberg.

Cup	L4	L3	L2	L1	CC	H1	H2	H3
Isotope	^{140}Ce	^{142}Nd	^{143}Nd	^{144}Nd	^{145}Nd	^{146}Nd	^{147}Sm	^{148}Nd
Amplifier (Ω])	10^{10}	10^{11}	10^{11}	10^{11}	10^{11}	10^{11}	10^{11}	10^{11}

of magnitude of the respective signals. ^{140}Ce can be detected using a 10^{10} Ω amplifier, since its concentration may be up to five times higher than the Nd concentration in the samples. The measured mass of 143 u on the L1 cup is not only influenced by the ^{143}Nd isotope, but also by Ce hydrates ^{142}CeH, which thus requires a corresponding correction.

Before the actual measurement, a several hours long pre-measurement ensures a stabilized signal intensity, the magnet adjustment and the ion beam properties. The adjustment of the mass spectrometer is monitored by the analysis of internal standards to evaluate drift and reproducibility of the measurements. The measurement conditions are reevaluated regularly and if necessary re-optimized prior to the continuation of the measurement. All measurements were conducted with 0.5 M HNO_3 as solvent.

A Ni-Jet sample cone and a Ni skimmer cone were used together with a conventional glass torch. The complete setup was optimized for stable isotope fractionation, low oxide production, and optimal signal per injected concentration, usually yielding a ^{145}Nd signal of 2.5-3.5 V for a 50 ppb Nd solution and a mean baseline of 0.008 V for the 0.5 M HNO_3 blank solution. All measurement sequences used the method settings displayed in Tab. 3.2 and followed a classical standard-sample bracketing approach with either identical sample concentration level or increasing concentration level to avoid memory effects. Each measurement sequence consist of an array of multiple measurement blocks, that in turn always have the following configuration: Blank – Bracketing standard – Blank – Nd solution. While the bracketing standard remains the same during a measurement session, the Nd solution is usually one of the following: Sediment sample, reference sample, CeH^+ correction standard or a secondary in-house standard.

The neodymium isotopic ratios of the Nd solutions is determined from the average of 60 consecutive measurements of 4.194 s integration time per measurement cycle. Depending on the Nd concentration of the sample, a 50 ppb solution has proven optimal for sedimentary εNd measurements (Rückert, 2020). For a background cor-

Table 3.2.: Typical instrumental parameters of the Neptune Plus MC-ICPMS.

Inlet system	Cool gas	16 l/min
	Auxiliary gas	0.8 l/min
	Sample gas	0.84 l/min
	RF Power	1200 V
APEX HF	N_2 flow	On
	Heater/chiller	120 °C/2 °C
Source lenses	Extraction	-2000 V
	Focus	−600 V
	X-Defl.	−3.35 V
	Y-Defl.	−4.06 V
	Shape	240 V
Zoom Optics	Focus Quad	4.9 V
	Dispersion Quad	−1.8 V

rection, the 0.5 M HNO_3 blank solution was measured before every Nd solution.

The precision of measurements is referred to as internal error and was assessed by the doubled standard deviation from the mean (2SD) of the 60 consecutive measurements. The external reproducibility is derived from the average deviation of respective mean εNd values of different secondary in-house standards.

Reference Material

The internal precision and accuracy of MC-ICPMS Nd isotope measurements is tested using the bracketing standard JNdi-1 (Tanaka et al., 2000) as well as four different in-house reference standards i.e. the certified isotopy standard GSB 04-3258-2015 (Li et al., 2017), a VWR Nd concentration reference solution and sample-like Nd solutions (HeiNdS, Sith) from former sediment samples. To determine the full analytical repeatability per analytical session and over time scales of years, frequent measurements of replicates of samples, the above mentioned standards, and reference materials Nod-P-1 (Flanagan and Gottfried, 1980) were conducted. The latter has undergone full chemical treatment of sample aliquots. To perform tests of isobaric interference corrections, the VWR standard at 50 ppb Nd was prepared at different levels of Ce contamination ranging from 10 ppb Ce to 100 ppb Ce. These CeH^+ correction standards are measured with rising Ce concentration at the end of a sequence of samples and occasionally within the measurement sequence.

Data Evaluation

The raw measurement data was evaluated following the schematics given in Fig. 3.1. Instrumental blanks are removed from the respective isotope signals, followed by isobaric interference corrections of ^{142}Ce and ^{144}Sm. Mass fractionation was corrected using the ^{146}Nd/^{144}Nd ratio of 0.7219 (O'nions et al., 1977) by applying an exponential mass bias law (Vance and Thirlwall, 2002). The isotopic ratios were determined from the average of the conducted scans per solution after outlier removal (2σ test). The obtained data was then normalized to the JNdi-1 bracketing standard with ^{143}Nd/^{144}Nd = 0.512115 ± 0.000007 (Tanaka et al., 2000) measured after every Nd sample-blank combination. Since Ce further impacts through the formation of hydrides, the Ce doped standards were used to determine the influence of CeH^+ on ^{143}Nd. All processed Nd isotope data is expressed in the epsilon notation as displayed in equation 2.2 with $^{143}Nd/^{144}Nd_{CHUR} = 0.512638$ (Hamilton et al., 1983; Jacobsen and Wasserburg, 1980). The internal precision of measurements is referred to as internal error and was assessed by the 2σ standard deviation from the mean (2SD) of the 60 consecutive measurements if not declared differently.

4. Results

4.1. Quality Control of Nd Isotopic Compositions

A total of 554 samples of ODP 1093 and 122 samples of ODP 1094 (including replicates) were analysed firstly regarding their elemental concentrations and secondly for the authigenic Nd isotopic composition.

The median leached Nd sample concentration of ODP 1093 is 55.92 parts per billion (ppb) and thus slightly higher than the median Nd concentration of the ODP 1094 samples with 42.45 ppb. The median of the Nd concentrations of the 45 total procedural blanks since 2020 is 0.14 ppb. The Nd contamination by the total processing procedure to a sample is 0.2 % and consequently negligible small.

To evaluate the quality of the sample treatment and measurement procedure different aspects were considered. The Ce correction was assessed to gain insights in the successful chemistry procedure and the correction for the influence of the remaining cerium fraction. Furthermore, the reproducibility of the sample processing and the measurement itself were assessed.

4.1.1. Cerium Separation and Correction

The Ce separation during the LN column chemistry is crucial for a successful Nd measurement. A higher Ce concentration in a sample leads to vigorous Ce hydride CeH^+ formation, that interfere with isobaric ^{143}Nd ions. Samples with higher Ce/Nd ratios require a greater Ce correction. For the measurement routine in Heidelberg, the Ce/Nd ratio of the samples should be smaller than five to ensure a robust Ce correction. The Ce correction factor γ is determined such as, the deviation of the Ce-doped standards εNd values from each other and the pure standard is minimal. It yields values of $\sim$0.06. The final correction is calculated as follows:

$$\varepsilon\mathrm{Nd} = \varepsilon\mathrm{Nd}_{\mathrm{uncorr}} - \gamma \cdot (^{140}\mathrm{Ce}/^{144}\mathrm{Nd})_{\mathrm{sample}} \tag{4.1}$$

Hence, the strong correlation of the separately measured Ce/Nd concentration ratio with the Ce correction is visible (Fig. 4.1) for every measurement, proving

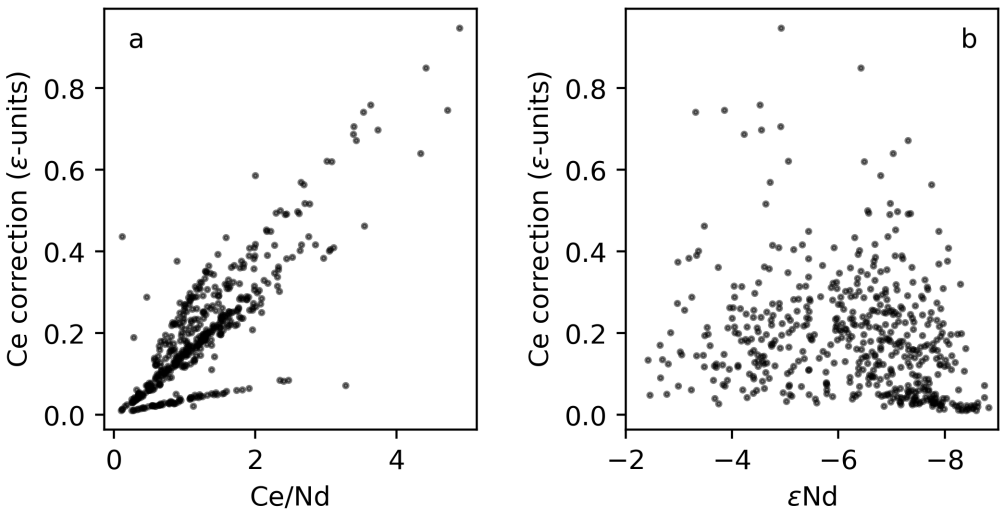

Figure 4.1.: Ce correction values and Ce/Nd in context with εNd. **(a)**: Ce/Nd ratio against Ce correction in ε-units. For each measurement session the Ce correction is linearly dependent in the Ce/Nd ratio. **(b)**: The εNd values show no correlations with the applied Ce correction.

the correction as efficient. There is no correlation observed between εNd and the Ce correction value, showing that glacial or interglacial sedimentation conditions do neither influence the Ce separation in the chemical sample treatment nor the quality of the correction itself. With that we are able to correct for CeH^+ formation of natural samples efficiently and without affecting the Nd isotope analysis.

4.1.2. Measurement Reproducibility

The overall measurement reproducibility is given by the standard error of the deviations from the respective mean εNd value of four different secondary in-house standards (Fig. 4.2). Within every measurement session two pure Nd solutions and two solutions from sediment material were measured multiple times. The pure Nd solutions are the certified Nd isotopic composition reference material GSB 04-3258-2015 (GSB) (Li et al., 2017) and the VWR Nd concentration solution (VWR International). The sediment solutions (HeiNdS, Sith) are from former sediment samples and thus contain a remaining element matrix similar to the measured samples of ODP 1093 and ODP 1094. A total of 257 secondary standards were measured during this work, yielding a measurement reproducibility of 19 ppm (2SD).

4.1.3. Sample Replicates

To maintain the quality of the chemical sample treatment, two different types of replicates were regularly made. For interlaboratory comparability the USGS Nod-P-1 standard (Flanagan and Gottfried, 1980) reference material was processed 14 times

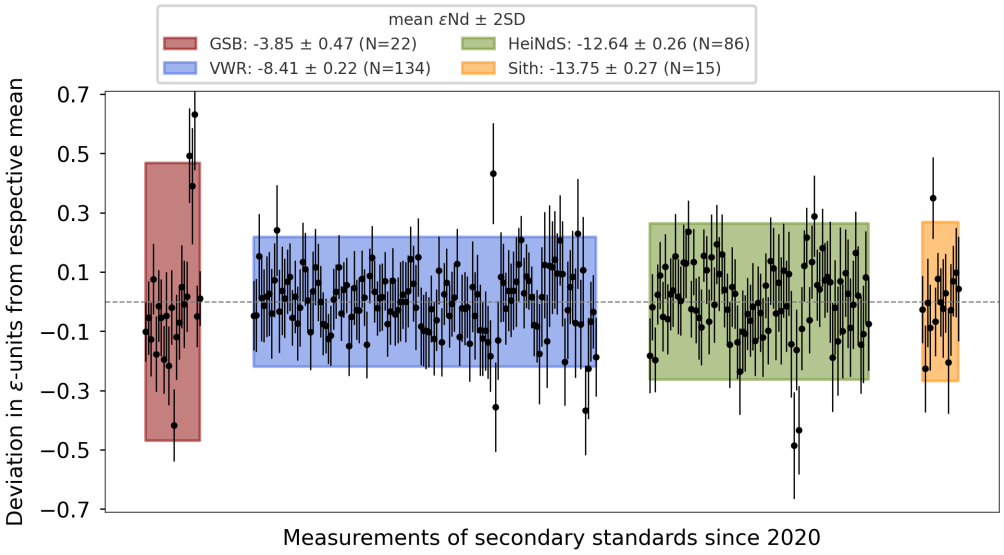

Figure 4.2.: Deviation of the secondary standard measurements of their respective mean εNd value. The mean values are displayed in the legend of the figure. The data contains all secondary standards measured since since October 2020.

since 2020. It originates from ferromanganese nodules from Deep Sea Ventures at a depth of 4300 m in the Pacific Ocean. Additionally, a total of 80 replicate samples of both sites were made, to ensure the reproducibility of the respective sediment εNd measurements. All εNd values for the Nod-P-1 reference material are displayed in Fig. 4.3. Individual values can be found in table B.1. The mean isotopic composition of the Nod-P-1 reference material is $\varepsilon\text{Nd} = -3.83 \pm 0.26$ (2SD). This is in line with published laser ablation data of $\varepsilon\text{Nd} = -4.25 \pm 0.43$ (2SD) (Foster and Vance, 2006), $\varepsilon\text{Nd} = -3.57 \pm 3.71$ (2SD) (Xu et al., 2018) and with leached material data of $\varepsilon\text{Nd} = -3.88 \pm 0.31$ (2SD) (Gutjahr et al., 2010). Thus, the quality of the sample analysis in Heidelberg is in excellent agreement with the literature.

The sediment replicates were processed twice, except for two samples, that were processed three times. The deviation from the respective mean values and the internal measurement error of the εNd values for both sites are displayed in Fig. 4.4. Overall, the replicates are in good agreement. The individual data points scatter around their respective mean εNd with a 2σ standard deviation of 0.13 ε-units, representing the external sample reproducibility. The accuracy of the εNd measurements is determined from the standard deviation of the 60 consecutive measurements of the respective sample. The mean sample accuracy of all samples is 0.14 ε-units and thus close to the external sample reproducibilty of the Nod-P-1 reference material of 0.13 ε-units. The overall measurement reproducibility since 2020 is 19 ppm is slightly larger, since it includes long term drifts over a measurement day and the past years. This proves the used method to produce precisely repeatable measurements of sediment samples.

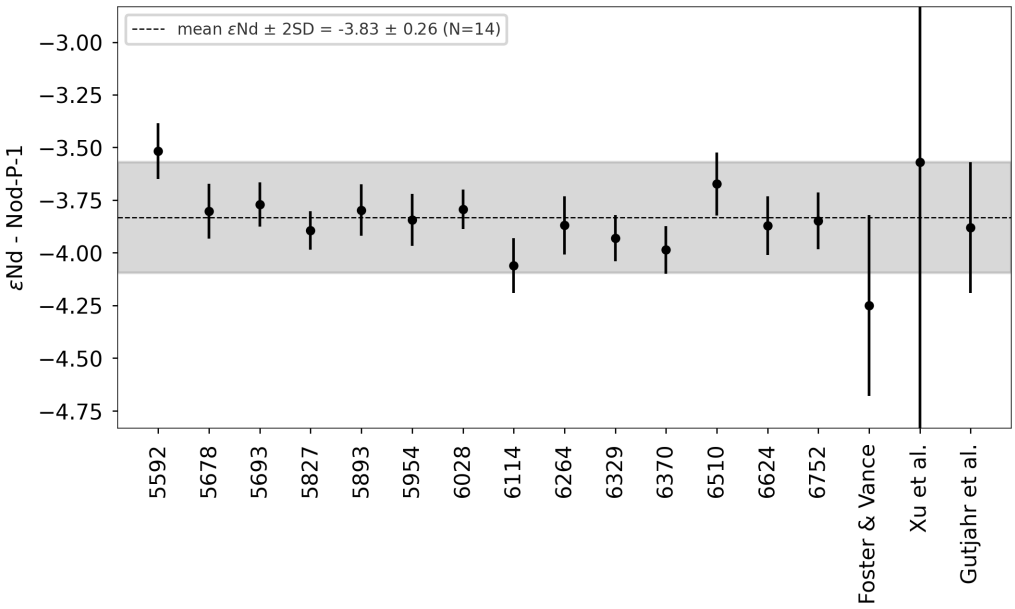

Figure 4.3.: εNd values of the reference material Nod-P-1 (Flanagan and Gottfried, 1980) measured during this work in comparison with the data from Foster and Vance (2006); Gutjahr et al. (2010); Xu et al. (2018). The dashed line marks the mean εNd value of -3.83 ± 0.26 (2SD), obtained from the processed material during this work. The data can be found in Tab. B.1

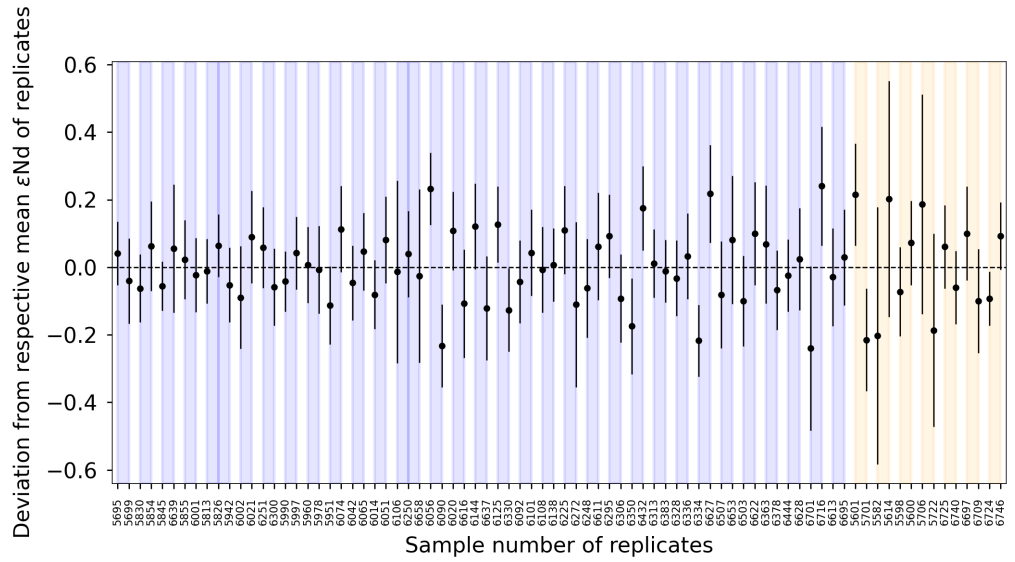

Figure 4.4.: Deviation of the total procedural sample replicates of ODP 1093 (blue) and 1094 (orange) from their respective mean εNd values. The colored bars mark the two or three εNd replicates from the same sediment sample.

4.2. REE Ratios and Element Ratios

The multielement measurements were conducted for a selection of 232 samples from ODP 1093 and 73 samples from ODP 1094 spanning last 450 ka. Together both datasets form the first multielement measurements on leachates from the southern Atlantic Ocean. The resulting REE and element ratios are displayed in Fig. 4.5. These results are used to study the chemical composition of leached sediment fraction and to qualitatively infer the origin of the resulting εNd signatures. The reliability of the measurements was ensured with multiple SPSSW2 measurements and error estimations were similar to the results from P. Blaser Blaser (2017). Thus, the uncertainty for REE ratios and Sr/Ca lies at approximately 3 % and at approximately 16 % for Al/Nd ratios.

In the leachates of ODP 1093 Al/Nd, Sr/Ca, Ce/Ce* and the $CaCO_3$ content show climate dependent behaviors, whereas REE slope, bulge and Eu/Eu* are rather constant with single extreme values over time (Fig. 4.5). The leachates of ODP 1094 record a similar pattern, however the extreme values for Al/Nd and Eu/Eu* are almost twice as large as the values of ODP 1093. The higher Al/Nd ratios occur throughout the whole data set and thus likely display an specific artefact of the leaching process from Southern Ocean sediments. In contrast, the Eu/Eu* outliers only occur in the first 30 ka and later show values scattering around 1. The samples within the first 30 ka were part of the re-establishment phase of the measurement method, after which especially the Eu measurements were adjusted. Thus, the Eu/Eu* values from these samples are rather an artefact of the not optimal measurement conditions than of the leachates. For further discussion, all investigated element and REE ratios are set in context with the respective εNd values and colour coded for glacial and interglacial samples (Fig. 4.6). Additionally, Sr/Ca, HREE/LREE and Ce/Ce* are displayed in context with the respective calcium carbonate content.

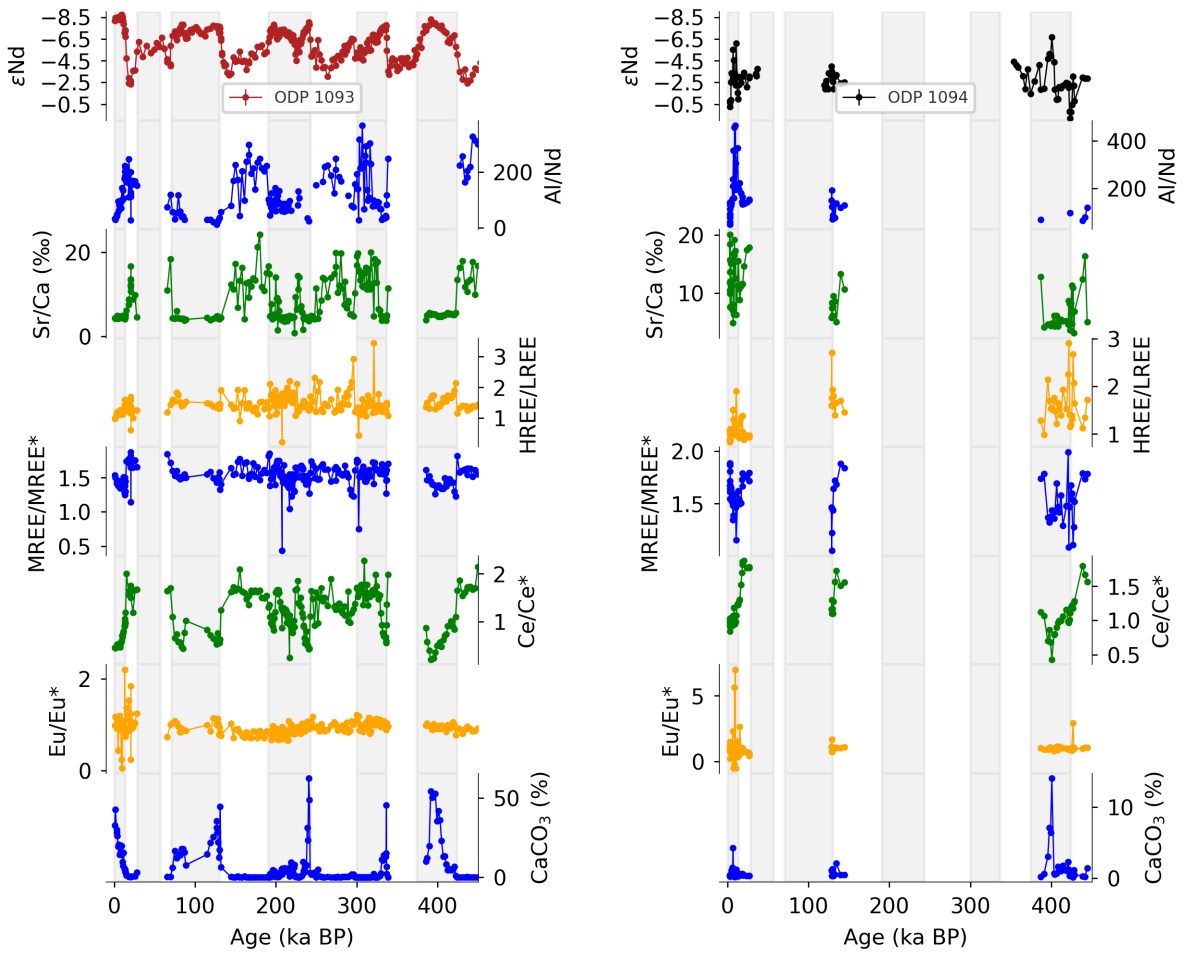

(a) ODP 1093 **(b)** ODP 1094

Figure 4.5.: Element and REE ratios of the leachates of ODP 1093 and ODP 1094 in comparison with the respective εNd values for the past 450 ka. All values are calculated as described in 4.2. The $CaCO_3$ content is obtained from the measured Ca concentration in the leachates. Grey shaded areas mark the MIS. The data can be found in Tab. C.2 and C.4.

4.3. εNd at Sites ODP 1093 and 1094

The εNd data of ODP 1093 and ODP 1094 (this study and Hallmaier et al. (2023a)) is displayed in Fig. 4.7 in comparison with the LR04 climate record of benthic $\delta^{18}O$ values (Lisiecki and Raymo, 2005). The dataset of ODP 1093 forms the first authigenic εNd record South of the PF of a millenial resolution over the past 1 million years. Interglacials are marked by odd MIS numbers and grey shaded areas. Terminations are indicated by roman numbers. A Kernel Density Estimation (KDE) analysis of the εNd distribution of both records is displayed in Fig. 4.8.

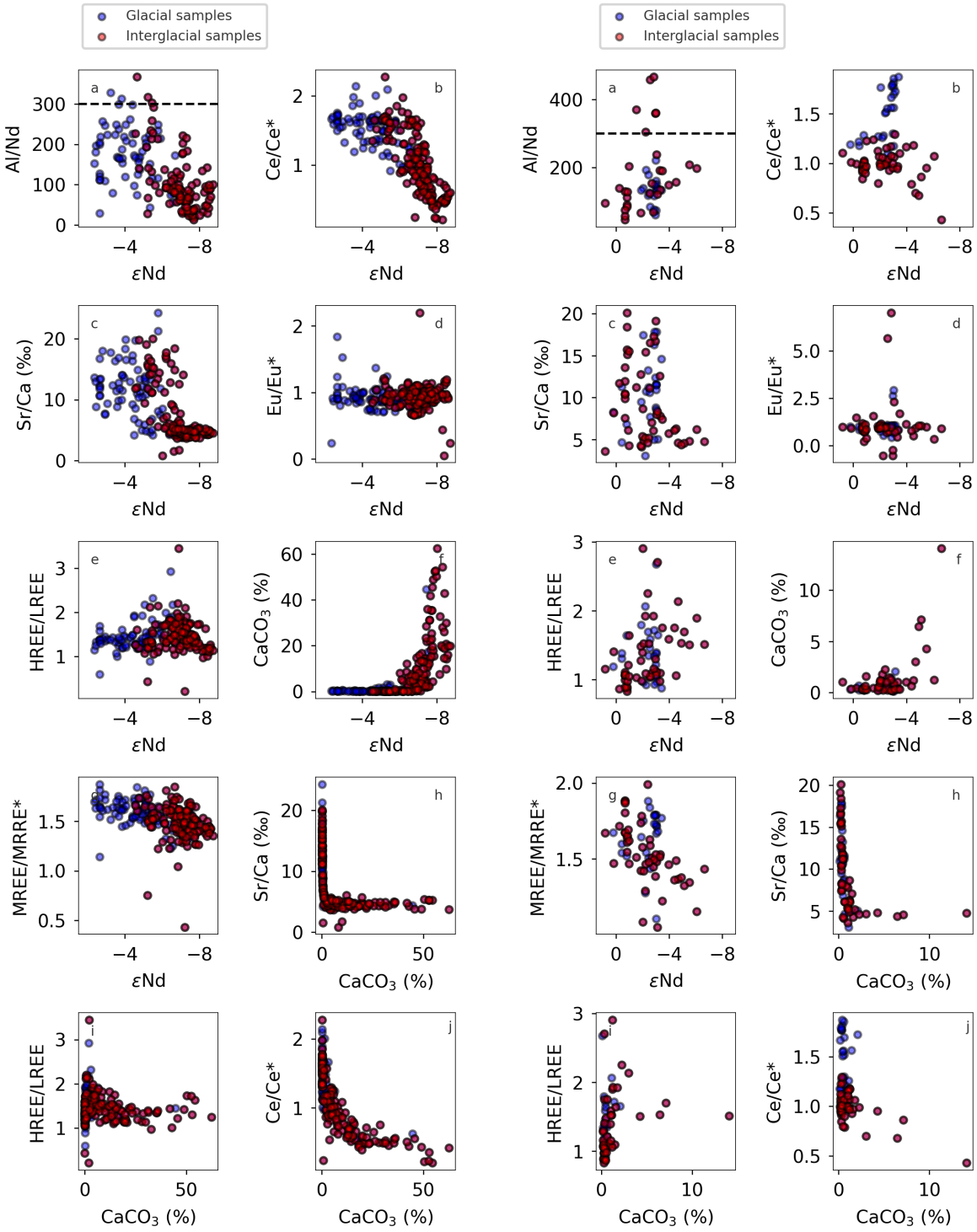

(a) ODP 1093 **(b)** ODP 1094

Figure 4.6.: Element and REE ratios against εNd and $CaCO_3$ context in the leachates of ODP 1093 and 1094. Blue/red dots are associated with glacial/interglacial MIS in the past 450 ka. The Al/Nd limit of 300 is indicated by a black dashed line.

4.3.1. Site ODP 1093

The εNd record of ODP 1093 covers the timespan from approximately 1 Ma BP until the Holocene continuously. The εNd values span a range of 6.39 ε-units from εNd = -8.74 to -2.35. The KDE analysis of the distribution shows two dominant modes with a focus around εNd = -7 and around εNd = -4.5. Both modes are within the bounds of modern water mass εNd values. The more radiogenic glacial mode is less pronounced due to the smaller sedimentation rate during glacial time and the chosen equal depth sample spacing.

The overall εNd signature of ODP 1093 varies on orbital time scales. Interglacial and glacial extreme εNd values are additionally highlighted with green/blue in Fig. 4.7. The MPT period is characterized by less pronounced differences between glacials and interglacials. The εNd variability during that time is approximately half of the overall range of the εNd record. The majority of the interglacials of the past 1 Ma are characterized by unradiogenic values around εNd = -8. MIS 23 and 3 stand out as more radiogenic interglacials. MIS 24 is the first strongly radiogenic glacial, followed by the weaker interglacial MIS 23. Together this glacial-interglacial cycle around 900 ka BP marks the change from the 41 ka world to the 100 ka glacial-interglacial cyclicity. In the post MPT period the 100 ka cyclicity dominates the record and the range in εNd values is the largest. All glacials show strongly radiogenic values around εNd = -4 except for MIS 14. Small scale variations of the εNd record are clearly recognizable within the climate record LR04 (Lisiecki and Raymo, 2005). The climate terminations during post MPT times are reflected in the εNd values as abrupt changes from radiogenic to unradiogenic values.

4.3.2. Site ODP 1094

The εNd record of ODP 1094 covers the time around 900 ka and three shorter time intervals around termination I and II and MIS 11. The εNd values span a range of 7.45 ε-units from εNd = -6.65 to $+0.8$. The KDE analysis yields three, however weak, modes. Two prominent modes centered around εNd = -5 and εNd = -3 are within the bounds of modern water mass εNd signatures (Tachikawa et al., 2017). In contrast the most radiogenic mode around εNd = -1 is far more radiogenic than modern day water masses. Moreover, the different modes in ODP 1094 cannot directly be associated with glacial or interglacial times since there is no correlation between εNd signature and climate.

During the MPT, the variations of the εNd signal is smaller than in the post MPT intervals. Additionally, a trend towards more radiogenic values with time is visible

until the higher amplitude behavior starts around termination X. The variations of the εNd signature in the post MPT are much stronger and characterized by sudden excursions to strongly radiogenic or unradiogenic values.

In total the εNd signature at site ODP 1093 is always an unradiogenic boundary for the fluctuating signal at site ODP 1094. The only exception of this happens around 900 ka BP, where both records are practically aligned. To conclude, the εNd signature of site ODP 1094 does neither show a pattern similar to the climate record nor similarities to the εNd signature of the close by site ODP 1093.

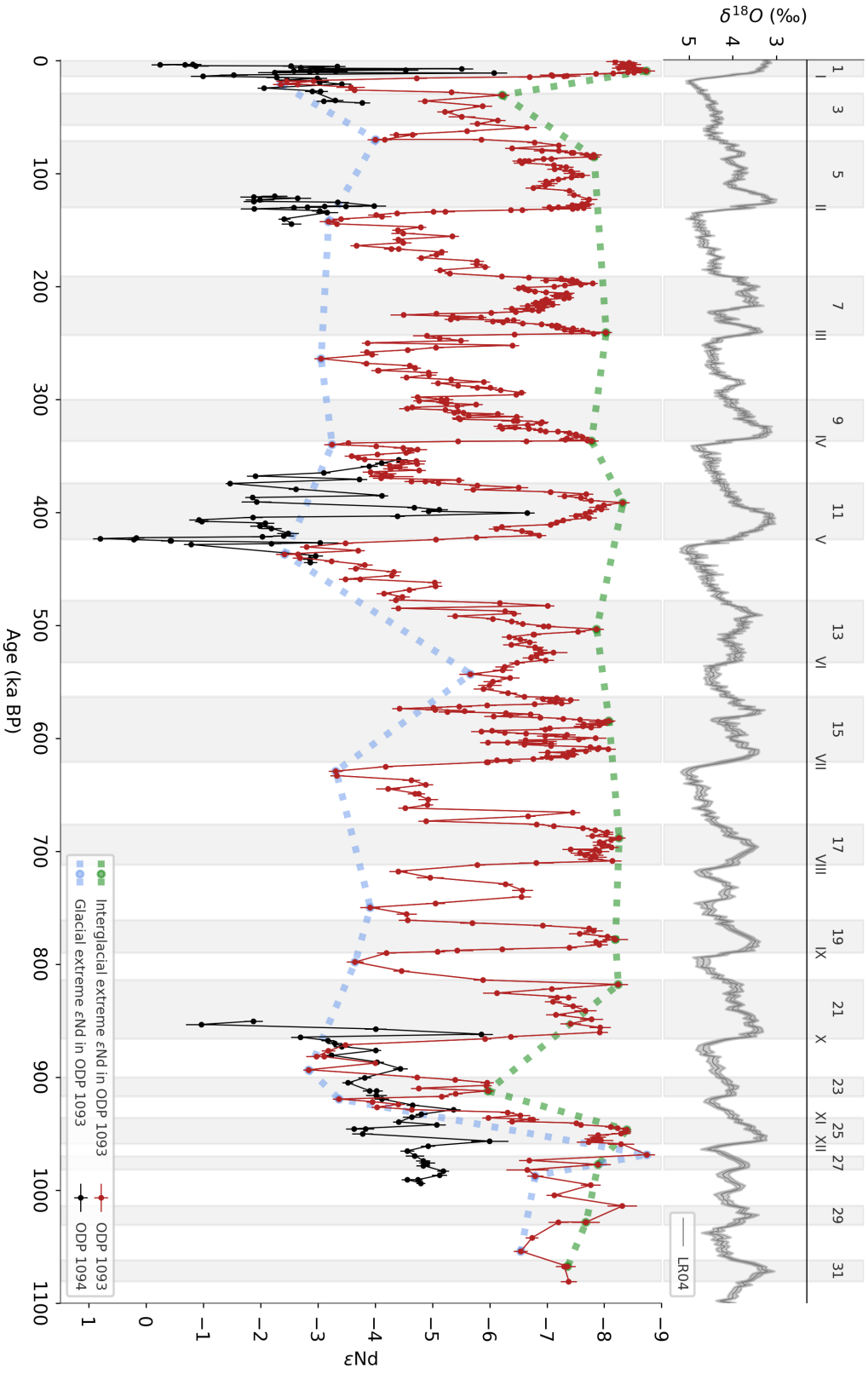

Figure 4.7.: Authigenic εNd signatures of ODP 1093 (red) and 1094 (black) (this study and Hallmaier et al. (2023a)) in comparision with the benthic δ^{18}O LRO4 record (Lisiecki and Raymo, 2005). Glacial and interglacial εNd extreme values are marked with the blue and green dashed line. Gray shaded areas mark the MIS. Interglacials and terminations are indicated above. The data can be found in Tab. C.1 and C.3.

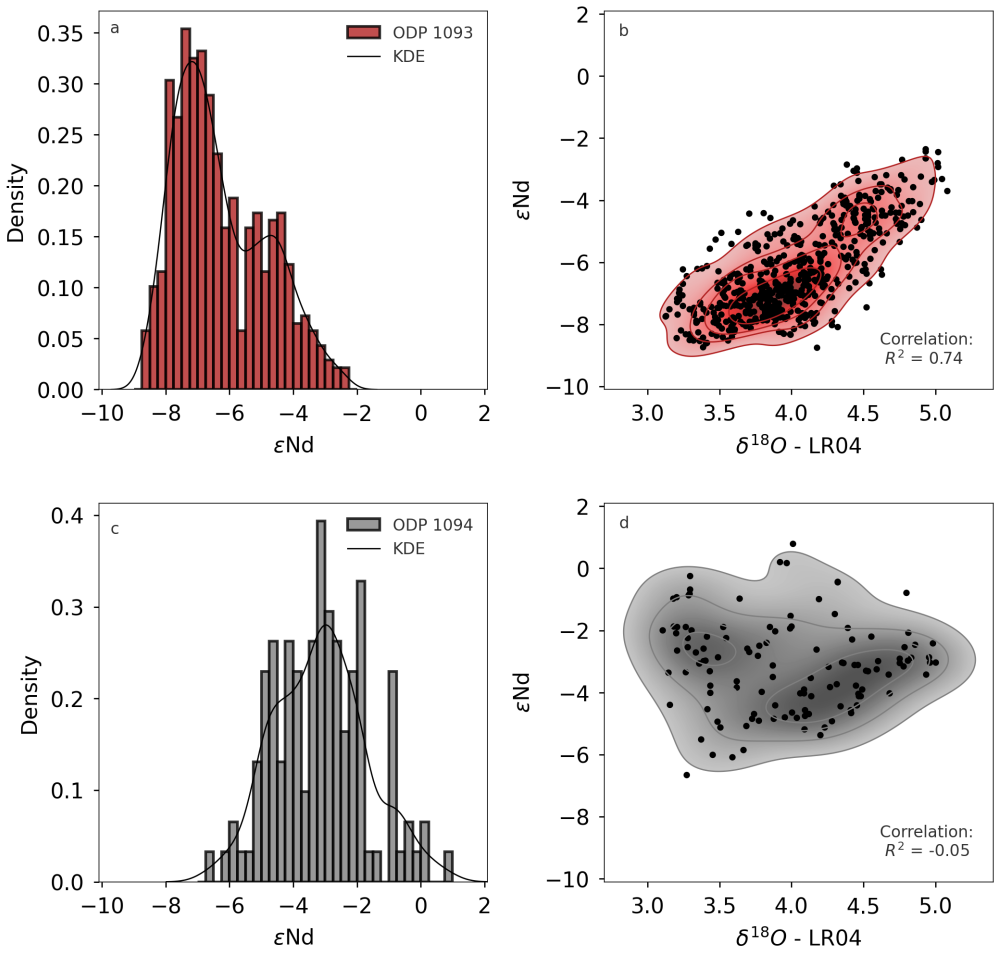

Figure 4.8.: Left: Distribution of εNd values in ODP 1093 (red) and 1094 (grey). (a) The εNd distribution of ODP 1093 consists of two clearly distinguishable modes. (c) The εNd distribution of ODP 1094 yields two strong and one weaker highly unradiogenic mode. **Right**: Correlation of the εNd values with the LR04 climate record (Lisiecki and Raymo, 2005). There is a strong correlation visible for ODP 1093 (b) and no correlation for ODP 1094 (d).

5. Age Model Development of ODP 1093

To overcome the already addressed issue of finding a suitable age model at site ODP 1093 a new approach is investigated. The possible influences on εNd are discussed in chapter 6 and lead to the assumption that the driving mechanisms of εNd variations south of the PF do not change during the past 1 Ma. Based on this, for the new age model the rapid εNd transitions were tuned to the observed terminations in the LR04 record of benthic δ^{18}O (Lisiecki and Raymo, 2005). The reliability of the resulting age model was further tested with various independent age tie points.

5.1. Age Assignment at Site ODP 1093

To investigate the authigenic εNd over time, a total of 246.89 m of sediment at site ODP 1093 were analysed. To interpret this data properly, a suitable age model is needed. As already indicated, the initial hopes of the Shipboard Party to develop an age model using foraminiferal δ^{18}O data were dashed by the low and sparse occurrence of foraminifera especially during glacials (Gersonde et al., 1999; Hodell and Venz, 2003).

For site ODP 1093 the age model from a previous study by Kemp et al. (2010) is the only published age model reaching back to 1 Ma, which is available to date. The new age model is introduced in the following discussion. Considering the continuous εNd record of high resolution with the new age model and comparing it to the LR04 climate record (Lisiecki and Raymo, 2005), doubts are arising on the reliability of this age model (Fig. 5.2).

Kemp et al. (2010) tried to overcome the lack of foraminifera by using site ODP 1094 as a master site to tune the colour reflectance data of site ODP 1093 to site ODP 1094. In a second step, the timing of certain geological events, visible in the colour reflectance data, was assigned to a respective sediment depth (Kemp et al., 2010). This method was previously used for the past 400 ka by Schneider-Mor et al. (2008). For ODP 1094, a detailed age model using δ^{18}O of planktic foraminifera

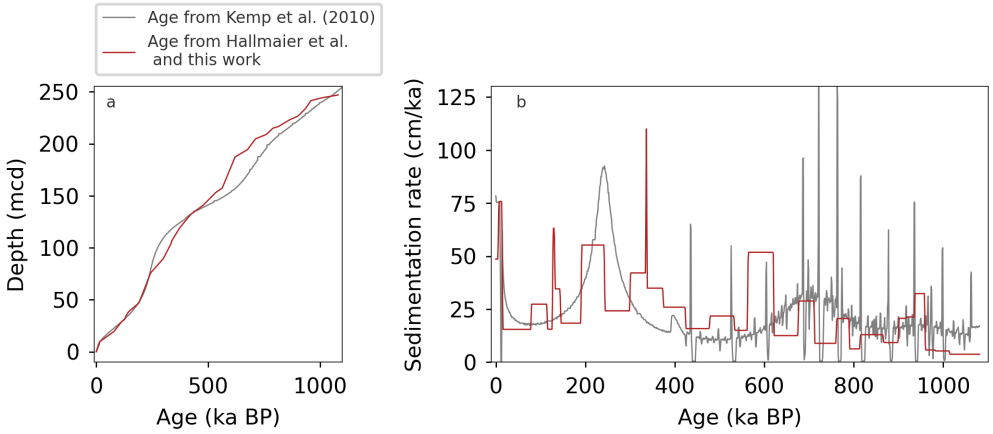

Figure 5.1.: Age model for site ODP 1093 from Kemp et al. (2010) and the combination of this study and Hallmaier et al. (2023a) in comparison. **a**: Age-depth relation. **b**: Sedimentation rates in the past 1 Ma for both age models.

tuned to the LR04 was later developed by Hasenfratz et al. (2019). Both age models and the resulting sedimentation rates for site ODP 1094 are compared in Fig. 3.3. They agree well with each other over the past 1 Ma except for the time between 400 and 600 ka. While the sedimentation rates in this time interval remain similar, there is an offset of several thousand years in their age ties. Additionally, the more recent age model has significantly less tie points compared to the age model by Kemp et al. (2010) (see Fig. 5.1). Nevertheless, the method of using a continuous δ^{18}O record from planktic foraminifera to tie to a climate record has proven to yield reliable results in foraminiferal Mg/Ca and Mn/Ca data obtained from ODP 1094 (Hasenfratz et al., 2019).

As already described in chapter 4.3, the authigenic Nd composition at site ODP 1093 shows regularly occurring abrupt changes from radiogenic to unradiogenic values. It is notable, that unradiogenic values coincide with higher calcium carbonate content in the sediment and low or no available $CaCO_3$ values correspond to phases of significantly more radiogenic εNd values (Fig. 4.5a). Higher $CaCO_3$ contents usually occur during interglacial warm periods, reflecting less $CaCO_3$ undersaturated waters due to the interglacial southward movement of the PF. The shift of the PF suggests that the abrupt changes in εNd signatures should coincide with the climate terminations. When using the age model of Kemp et al. (2010), it becomes visible that these εNd changes occasionally do not match the terminations marked by the LR04 benthic δ^{18}O stack (Fig. 5.2). While for termination I-III and V the discrepancy is rather small (0-10 ka), it increases up to ~50 ka in termination IV and X. These growing discrepancies between εNd and the LR04 δ^{18}O can be an artefact of the age model or could point to an unknown driver or a strongly variable response to climate changes

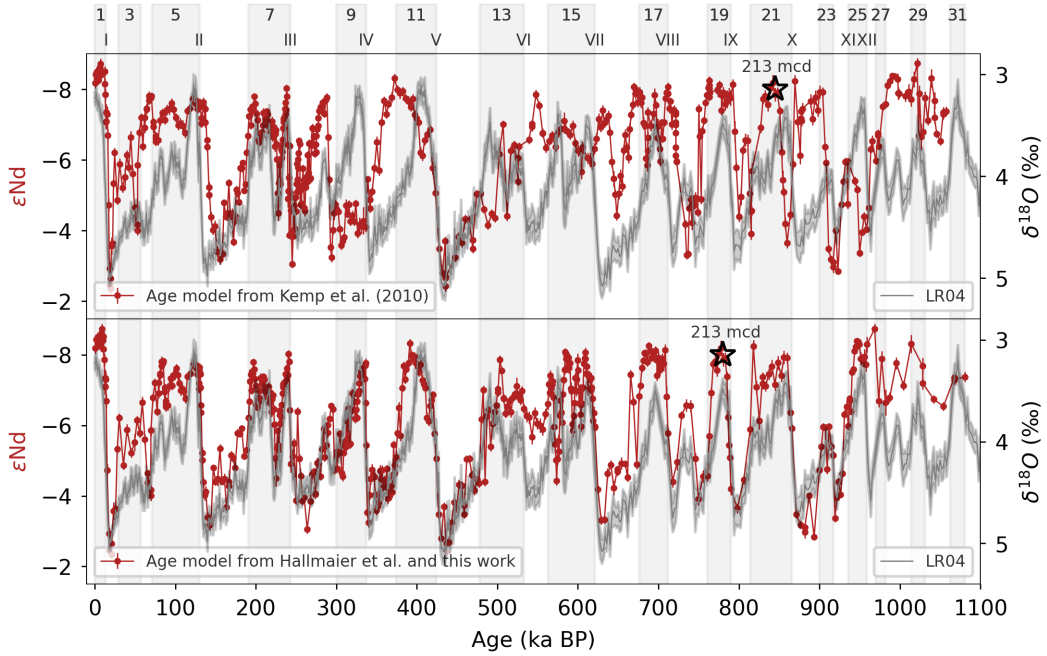

Figure 5.2.: Age model comparison for ODP 1093 of Kemp et al. (2010) and the new age model developed in this study and Hallmaier et al. (2023a) in context with the LR04 record (Lisiecki and Raymo, 2005). The black star marks 213 mcd, which is the depth associated with the Brunhes-Matuyama boundary in the new age model.

in εNd at site ODP 1093 and probably the whole Southern Atlantic Ocean. However, it seems more likely that the discrepancies result from the assigning of the age tie points themselves, since especially the first 150 ka closely align with the benthic δ^{18}O stack (Lisiecki and Raymo, 2005).

The sedimentation rate in ODP 1093 is almost twice as high as in ODP 1094. This yields a depth marking 1 Ma of ∼250 mcd for ODP 1093 and ∼130 mcd for ODP 1094 (Gersonde et al., 1999). Consequently, the same timespan covers a larger part of the sediment at site ODP 1093 compared to ODP 1094. Hence, single events likely span a broader section within the sediment at site ODP 1093 compared to ODP 1094. Thus, the precise assignment of the respective sediment depth to the exact timing of a climate transition is more difficult in ODP 1094 and bears the potential for offsets of several meters in the selection of tie points. Here, an alternative age model based on planktic foraminifera for the past 150 ka at site ODP 1093 and the corresponding εNd variations is proposed (Hallmaier et al., 2023a). In deeper sediment depth than 40 mcd, the abundance of foraminifera becomes increasingly sparse, thus, another admittedly unconventional approach for an age model was needed.

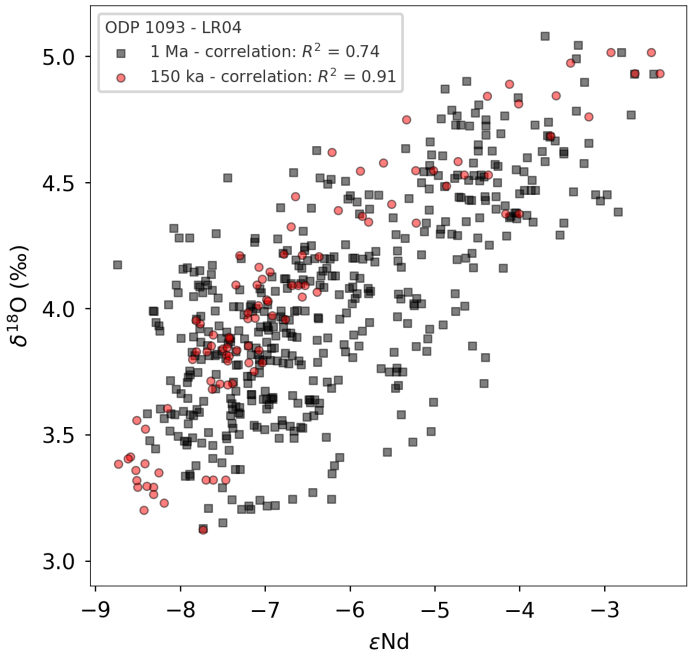

Figure 5.3.: Correlation of authigenic εNd of ODP 1093 and δ^{18}O of LR04 (Lisiecki and Raymo, 2005) with the new age model. εNd of the last 150 ka is marked in red and the extension to 1 Ma in grey.

5.2. Age Model for the Past 150 ka

For the past 150 ka, the age model for ODP 1093 was developed in a similar way as by Lal et al. (2006) and in studies of the close by sites PS1768-8 (Huang et al., 2020) and ODP 1094 (Hasenfratz et al., 2019). It was assumed, that the surface δ^{18}O recorded by planktic foraminifera is closely reflected in the ice from the Antarctic Ice Sheet. The δ^{18}O record of planktic foraminifera (*N. Pachyderma*) in ODP 1093 (Gersonde et al., 1999; Hodell and Venz, 2003) was aligned to the δD data from Vostok ice core (Petit et al., 1999). The advantage of the age model of ice cores is its precise determination by layer counting of differently dense packed snow or ice layers throughout the ice core. Tie points were found by allocating similar patterns in the sedimentary δ^{18}O record to the δD ice core record. Hereby, phases of extreme gradients were used instead of extreme values within the records (Hallmaier et al., 2023a). This technique ensures, that the timing of actual climate relative events is tied to one another instead of supposedly matching wiggles within the record. Finally, this method guarantees the independent assignment of sediment depth to a certain age. With this new age model, the εNd record highly correlates with the LR04 δ^{18}O stack (Lisiecki and Raymo, 2005) (R^2=0.91, Fig. 5.3) .

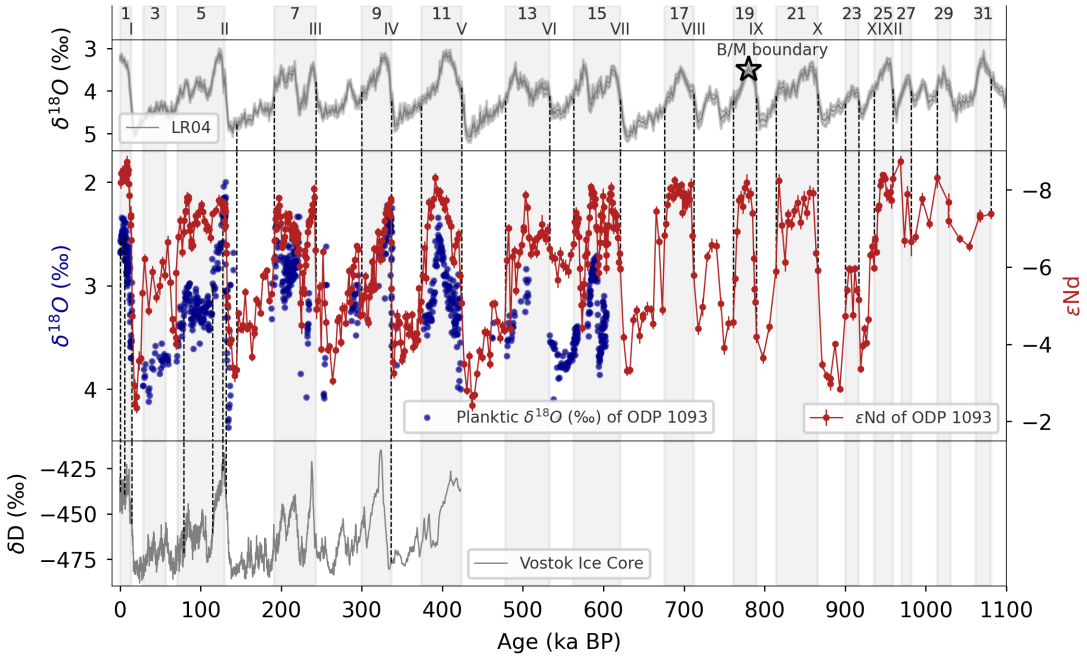

Figure 5.4.: Age model ties for ODP 1093 (this study and Hallmaier et al. (2023a)). For the last 150 ka the δ^{18}O values (blue) (Hodell and Venz, 2003) were tuned to the δD values of the Vostok ice core (Petit et al., 1999). For the extension the abrupt changes in the authigenic εNd signature were assigned to terminations and deglaciations in the LR04 climate record (Lisiecki and Raymo, 2005). Tie points are indicated by black vertical dashed lines and are listed in Tab. B.2. The black star marks the timing of the B/M boundary.

5.3. Age Model Extension to 1 Ma

Under the assumption, that the authigenic Nd isotopic signal in ODP 1093 is climatically controlled, the age model of the past 1 Ma was investigated and developed. The foraminifera occurrence in deeper depth than 40 mcd is patchier, as also reflected in the lack of calcium carbonate, yielding an increasingly disrupted δ^{18}O record (Hodell and Venz, 2003). As a result, the above used method to determine an age model is not feasible for a deeper depth or ages older than 150 ka. However, the periods of short continuous data can later be used to support the new age model during interglacials.

The εNd record of the last 150 ka at site ODP 1093 shows a close relation between εNd and the δ^{18}O of LR04 (Fig. 5.4). The REE and element ratios from the past 450 ka also show no conspicuous change for samples older than 150 ka. Hence, the measured εNd values are assumed to have the same authigenic origin in the past 450 ka and it seems unlikely to change for even older ages. Even if the mechanism influencing εNd values at site ODP 1093 changed abruptly at 150 ka, it remains elusive, why the pattern should not be aligned with climate records. Ocean circulation was

globally shown to change with glacial-interglacial conditions. Synchronous changes with climate are visible in dust inputs and sediment composition (Gersonde et al., 1999). In contrast, Nd from benthic flux and pore fluids can be considered climate independent (Abbott et al., 2022), or indirectly modulated by the ACC speed changes, which in turn correlate with climate for the past 5 Ma (Lamy et al., 2024; Toyos et al., 2020). If the unlikely case of a completely different mechanism drove the εNd signature, it is highly unlikely that this yet unknown process should not be climate controlled.

Since there is no reason for the driving force to be different before the penultimate termination, a similarly close alignment with the climate record can be expected for the time before 150 ka. Hence, due to the deficiency of an alternative suitable continuous climate related data set obtained at site ODP 1093, this study suggests to use the εNd record itself to align to the benthic δ^{18}O LR04 stack (Lisiecki and Raymo, 2005).

For this purpose, rapid changes from radiogenic to unradiogenic εNd values in the order of a minimum 4 ε-units were assigned to terminations. This procedure allowed constraining the timing of termination I-V and VII-X. Termination VI, at the end of MIS 14, remains difficult to determine and was therefore estimated by comparing the respective course of the available δ^{18}O record. The ambiguous behavior of the εNd record around MIS 14 points to the already proposed 'missing glacial' features of MIS 14 being visible also in the Southern Hemisphere (Hughes et al., 2020).

With only the terminations as tie points the sedimentation rate would be the same for every two MIS. Since it was shown that sedimentation in the Southern Ocean strongly varies between glacial and interglacial times (Charles et al., 1991), additional tie points were assigned during the more gradual glaciation. In between the new assigned tie points the age model was linearly extrapolated. From termination X onward, the εNd variability is much less pronounced and the temporal resolution is significantly smaller compared to the younger record. Consequently, the determination of earlier terminations is difficult. These less pronounced terminations, however, increase the uncertainty of the age model. Nevertheless, a similar approach as for the later terminations was applied here. Changes of around 2 ε-units were assumed to be sufficient to be considered as a termination. Additionally, as for MIS 14 the εNd record was closely compared to the LR04 δ^{18}O record (Lisiecki and Raymo, 2005).

Together, this leads to the following age model with the age tie points displayed in Fig. 5.4 and Tab. B.2 and the sedimentation rates visualized in Fig. 5.1. Regardless the significantly fewer tie points compared to the age model of Kemp et al. (2010),

even smaller structures of the LR04 stack align very well with the εNd data. The uncertainty for the new age model is estimated as 10 ka, which is the difference in the timing of the rapid εNd change associated with termination II compared to the age model of Kemp et al. (2010). Self-evidently, with this age model the εNd record at site ODP 1093 correlates with the climate record LR04 for the entire 1 Ma (R^2=0.74, Fig. 5.3).

To further evaluate the reliability of the new age model, the few existing δ^{18}O values are compared with the Vostok δD (Petit et al., 1999) and the δ^{18}O LR04 record (Lisiecki and Raymo, 2005). As far as it is possible to recognise a pattern within the ODP 1093 δ^{18}O data, it is in line with the data from both climate records (Fig. 5.4). Especially for the extreme interglacial times with low δ^{18}O and high δD values, both records show great similarity. However, during the gradual glaciation, the two data sets are less coherent, thus pointing to a higher uncertainty of the age model or regional influences on δ^{18}O during those times. There are two aspects, which might contribute to this fining. Firstly, both records show a higher variability during times of gradual deglaciations. And secondly, the lack of δ^{18}O data in ODP 1093 during glacials generally disables the possible correlation of glacial values.

The Brunhes-Matuyama boundary (B/M) at around 779±5 ka BP (Singer et al., 2019) was used as an external tie to check for the reliability of the age model. The B/M boundary marks the last full reversal of the Earth's magnetic field and is reflected in the intensity and inclination of the magnetization of sediment. Site ODP 1093 records the B/M boundary at the deepest core depth of all sites of expedition 177, however it has the poorest data quality compared to the other sites (Channell and Stoner, 2002). In the preliminary results of the Shipboard Party the depth of the B/M boundary was estimated to be within 205-210 mcd. From the magnetization data it is difficult to retrieve a sharp boundary, however it was determined to 198.6 ± 2 (Channell and Stoner, 2002). Since the overall magnetization signal is very noisy, colour reflectance data was additionally investigated. From the colour reflectance data, a clear peak around 213 mcd was determined to mark the B/M boundary (see Fig. 11 in Gersonde et al., 1999). With the age model of Kemp et al. (2010) the B/M boundary is pinpointed to 201 mcd, whereas the new age model yields a depth of 213 mcd. This leads to an offset in the data of approximately one cycle of radiogenic and unradiogenic εNd values (see black star in Fig. 5.2).

The 900 ka event depicts another possible tie point. It marks the first appearance of the 100 ka glacial-interglacial cyclicity. It is characterized by a higher δ^{18}O amplitude during terminations compared to the previously dominant 41 ka cyclicity with

less extreme ice sheets in the Northern Hemisphere. Depending on the age model, the transition from a low amplitude signal (2 ε-units) to a higher amplitude signal (6 ε-units) in the εNd record starts at different times. Presuming that the εNd record is driven by climate changes, this transition should align with the 900 ka event, more precisely the transition from MIS 23 to MIS 22. This tie point was implemented in the new age model, however, it was not reflected in the age model by Kemp et al. (2010).

In conclusion, finding an appropriate age model for ODP 1093 with lacking calcium carbonate content and thus δ^{18}O data is challenging. The high resolution εNd record opens up the possibility to be directly tied to the climate record. This is only possible, since the correlation of the two latter could be independently proved over two glacial-interglacial cycles in advance. With this approach an age model was developed, which is able to accurately hit two different major climate events in the past 1 Ma, namely the B/M boundary and the 900 ka event. When using this technique, it is needless to say, that statements on the more exact timing of certain events in εNd prior to 150 ka BP are limited due to the presumed εNd dependency on climate. In summary, with the construction of this age model for ODP 1093 the alternating pattern of radiogenic glacial and unradiogenic interglacial values can be discussed regarding their implication on the past climate.

6. Origin of the Nd Isotopic Signatures and Implications for the Carbon Cycle

The aim of determining the εNd signature of two sediment cores situated south of the modern Polar Front (PF) is to assess the southern εNd endmember. A water mass endmember is here defined as reflecting only one distinct water mass as e.g. North Atlantic Deep Water (NADW) or Antarctic Bottom Water (AABW). Since a mixture of water masses in high latitudes interacts with the whole ocean basin, the concept of an ocean basin endmember is introduced here. In the following, this ocean basin endmember is defined for the South as the signature of the mixed water mass, that is exported to the North and interacts with the entire Atlantic Ocean basin. This definition accounts also for the already proposed potential variations in εNd endmembers toward more radiogenic values (Gutjahr et al., 2008; Howe et al., 2016a; Skinner et al., 2013).

Up until now no continuous sedimentary εNd record south of the PF exists, that potentially records the Southern Ocean basin endmember. The investigated sites ODP 1093 and 1094 are nowadays located within the bounds of the Antarctic Circumpolar Current (ACC) and persistently bathed in Circumpolar Deep Water (CDW). CDW consists of a mixture of waters from all three main ocean basins and has a signature of approximately $\varepsilon\text{Nd} = -7.8 \pm 1.2$ in the Pacific and -7.9 ± 1.3 in the Indian Ocean (Tachikawa et al., 2017). Corals within the Drake Passage show modern CDW values of $\varepsilon\text{Nd} = -8.2 \pm 0.5$ and more variable glacial values in the range of $\varepsilon\text{Nd} = -5.9$ to -7.7 in the Atlantic sector of the Southern Ocean (Wilson et al., 2020). During glacial periods the PF moves northward as the sea ice extends and westerly winds are shifted accordingly (Jochum and Eden, 2015; Sigman et al., 2010). Consequently, both investigated sites are permanently within the influence of CDW and are expected to reflect its Nd isotopic signature through time. However, the records show a different behavior, albeit in different ways, both pointing to a more complex process than pure water mass mixing causing the signatures.

Parts of the findings of this chapter are summarised in the manuscripts *Glacial Southern Ocean Deep Water Nd Isotopic Composition Dominated by Benthic Modification* (Hallmaier, Rückert et al., in preparation) (former version published as preprint: Hallmaier et al. (2023b)) and *Small-scale AMOC Strength Variability Revealed by the Interhemispheric εNd Gradient of the Atlantic Ocean During the Last 150 ka* (in preparation).

6.1. Extraction of Authigenic Nd in Sediments South of the Polar Front

For this work the focus lies on the authigenic phase of the sediment, since it is assumed to reflect most likely the surrounding bottom water signature (Bayon et al., 2002; Blaser et al., 2016; Frank, 2002; Piotrowski et al., 2004; Rutberg et al., 2000). The analysis of the authigenic Nd isotopic composition of sediments is always hampered by the unknown concentration and isotopic composition of the Nd released from other sediment phases and the incorporated Nd in the authigenic phase. Thus, considering the overall sediment composition, it must be assessed how reliable the sediment phase of interest is extracted during the applied leaching procedure. Since the early use of Nd isotopes in paleooceanography, a variety of techniques were established to test for the contamination of the authigenic fraction from other leached sediment phases. These include the investigation of REE ratios and element ratios within the leachate of mainly carbonate rich sediments (Bayon et al., 2002, 2004; Blaser et al., 2016; Gutjahr et al., 2007; Rutberg et al., 2000). The respective results for ODP 1093 and ODP 1094 are displayed in Fig. 4.5 and Fig. 4.6.

Both investigated sites ODP 1093 and ODP 1094 have similar bulk sediment compositions. However, sediments from the Southern Ocean are very different from sediments in the North Atlantic, as described in chapter 3.1. The $CaCO_3$ content is only measurable during warm climate conditions, but rarely reaches up to 50 wt% after the Holocene (Gersonde et al., 1999). The main constituent is siliceous ooze, which dominates the sediment independently of the climate conditions (Janecek, 2001). Thus, the sediment composition is essentially driven by biogenic particles, on which Nd is efficiently scavenged in form of Fe-Mn coatings. Siliciclastic particles also contribute to the scavenging of Nd from seawater (Gersonde et al., 1999), but carry detrital Nd, which could be released to the leached fraction. Both sediments from sites ODP 1093 and ODP 1094 experience changes in overall particle composition (Gersonde et al., 1999). To minimize the contamination caused by the dissolution of detrital material a weak leaching procedure with a short exposure time was applied (Blaser et al., 2016;

Huang et al., 2021). Due to the bias toward REE studies on carbonate rich sediments mainly from the North Atlantic, the published limits for different values are not necessarily applicable on the here investigated sediment. Moreover, the combination of all results allows for a statement on the extracted phase throughout the entire set of sediment samples, but can not be used in order to identify contaminations in an individual sample (Blaser et al., 2016).

The Al/Nd ratios of the samples are tracers for non-hydrogenetic and especially detrital influences on the εNd signatures of the leachate (Blaser et al., 2016). Al/Nd ratios of carbonate rich sediments in the Atlantic, which are smaller than ∼100, indicate a lower probability of detrital contamination in presence of volcanic material (Blaser et al., 2016; Gutjahr et al., 2007). However, it was suggested that the limit for the Al/Nd ratios should be defined individually for the respective site or even the lithogenic units of the sediment (Blaser, 2017). The studied Al/Nd ratios of several samples from the past 450 ka at site ODP 1093 show that the Al/Nd ratio is <100 in presence of carbonates and increases to ∼300 for diatom ooze dominated carbonate free sediments, mainly from the glacial periods (Fig. 4.5a b, Fig. 4.6 a). Nevertheless, systematic climate driven changes in εNd are not always synchronous to changes of the Al/Nd ratio. MIS 9 stands out as an example for a time period with variable and higher Al/Nd ratios, while showing only slightly more radiogenic values compared to the most unradiogenic values of $\varepsilon\text{Nd} = -8$. Additionally, both samples from glacial and interglacial times span the whole range of detected Al/Nd ratios (Fig. 4.6 a). Sediments from the Southern Ocean, as ODP 1093, contain more biogenic silicates, which in turn contain large amounts of aluminium (Tian et al., 2022). In combination with the Al released from siliciclastic particles during the leaching procedure, this can increase the absolute amount of Al in leachates. A recent study from Huang et al. (2021) found Al/Nd ratios in a range of 50-500 for the 10 s and 30 min leaching method (Huang et al., 2021; Blaser et al., 2016) in southern Atlantic Ocean sediments. They further showed that, not only the leaching technique influences the respective εNd values and the Al/Nd ratios, but also the investigated site. This is in line with the suggestions from Blaser et al. (2016), to find individual limits for each site. Consequently, the samples of ODP 1093 with Al/Nd ratios smaller than ∼300 are assumed to reflect mainly the authigenic phase and associated εNd values are unlikely biased by more than 1 ε-unit. This behaviour remains similar throughout the entire investigated sediment of ODP 1093. The respective εNd values of samples with higher Al/Nd than 300 are excluded from further evaluations. Therefore, the conducted εNd measurements of ODP 1093 are assumed to mainly reflect the authigenic phase.

Since the sediment composition and the location of ODP 1094 is very similar to ODP 1093, the limit for the Al/Nd ratios is assumed to be the same. The Al/Nd ratios of ODP 1094 show extreme values up to 500 during the Holocene and no correlation of high Al/Nd ratios with the radiogenic εNd signatures. This points to a highly radiogenic source of Nd close to ODP 1094 and a significant contamination of the record by detrital, possibly volcanogenic material during the Holocene warm period. However, it should be kept in mind that the carbonate content of ODP 1094 is even smaller than the carbonate content of ODP 1093, possibly leading to naturally higher Al concentrations within the sediment.

Small Sr/Ca ratios of the leachates below 1 ‰ have been assumed to indicate contamination of the leachates by non-biogenetic carbonates e.g. from the detritus (Blaser et al., 2016; Blaser, 2017). All measured values of both sediment cores are above this limit, except for one sample of ODP 1093 with Sr/Ca = 0.8 (Fig. 4.5 a). The respective εNd value of this sample is excluded from further evaluations. The remaining Sr/Ca values range up to 24 ‰. Thus, the leachates are only insignificantly influenced by non-hydrogenetic carbonates. Nevertheless, the Sr concentration within the leachates is assumed to be tightly coupled to the calcium carbonate dissolution during the chemical treatment (Blaser et al., 2016). For the investigated sites they do not show a linear correlation (Fig. 4.6), but high Sr/Ca ratios only occur with the lowest $CaCO_3$ contents. Thus, an overall low Ca concentration leads to higher Sr/Ca values independent from the Sr concentrations within the sediment. Conclusively, the Sr/Ca ratios are difficult to clearly interpret as indicator for non-hydrogenetic carbonate in the samples of ODP 1093 and ODP 1094 due to low or absent calcium carbonate in the sediment.

The REE ratios can be used to further evaluate the source of the REE within the leachates (Bayon et al., 2002; Blaser et al., 2016; Martin et al., 2010). It was shown that REE slope values are usually within the range of 1 to 2 and MREE bulge values are rather constant with values of 1.6. Europium anomalies Eu/Eu* deviating from 1 have been interpreted as indicators of contamination by volcanic material (Blaser et al., 2016). The cerium anomaly Ce/Ce* reacts sensitively to the oxygen concentration within the sediment but provides less information on the quality of the leaching (Roberts et al., 2012). Nevertheless, the REE slope and Ce/Ce* values are also influenced by the sediment's carbonate content and the pH of the leach solution, which can limit their application for REE origin studies (Blaser, 2017). This is visible in the HREE/LREE outliers coinciding only with low carbonate contents (Fig. 4.6 i).

The obtained REE slope and bulge data from ODP 1093 and 1094 are in line with

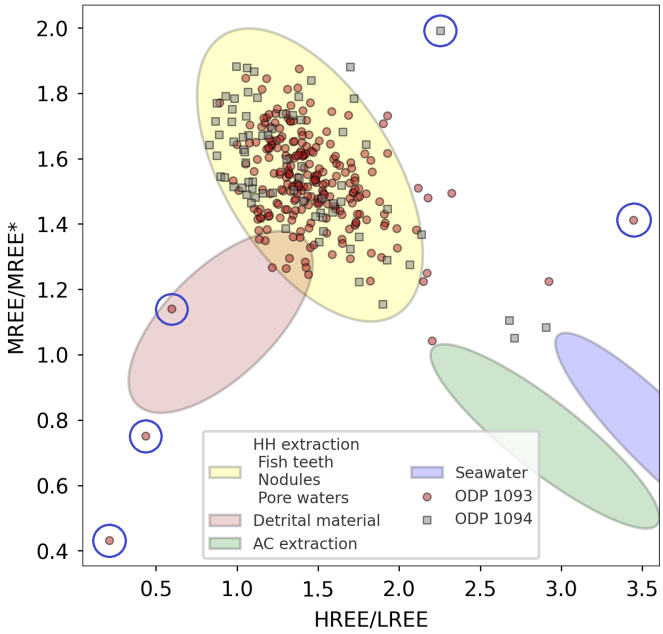

Figure 6.1.: HREE/LREE against MREE/MREE* of leachates from ODP 1093 (red) and 1094 (grey). Shaded areas (adapted from Martin et al. (2010) depict typical values of samples from hydroxylamine hydrochloride (HH) extraction (yellow), detrital material (red), acetic acid (AC) extraction (green) and seawater (blue). Blue circles indicate samples, of which the respective εNd is excluded.

the mentioned criteria apart from single outliers (Fig.4.5). In Fig. 6.1 the REE ratio results are compared with the results of several studies to gain insights in the origin of REE (Kraft et al., 2013; Martin et al., 2010; Molina-Kescher et al., 2014). Most of the displayed values of ODP 1093 and 1094 fall within the bound of typical HH-leached samples, indicating a similar interaction of the HH-leach with silicate rich samples compared to carbonate rich sediments. A small group of samples is shifted toward acetic acid (AC) extraction or sea water values. The five outliers toward detrital material or high elemental ratios are marked in Fig. 6.1. The respective εNd values are excluded from further evaluations. It should be kept in mind, that element and REE ratios can be highly sensitive to the concentration of different sediment components and thus always carry information regarding the sedimentary composition (Blaser et al., 2016; Blaser, 2017).

In summary, it is assumed, that the leachates and thus the εNd data of ODP 1093 and 1094 mainly reflect typical values found in samples from the same leaching technique. Thus, the used εNd extraction method is suitable for the carbonate depleted sediments. The respective εNd of the outliers from Al/Nd, Sr/Ca and HREE/LREE vs. MREE/MREE* are excluded from further evaluations of ODP 1093 and 1094. Conclusively, for all remaining εNd values it is very likely, that they reflect the au-

thigenic phase of the sediments of ODP 1093 and 1094 and do not record changes in the detrital sediment composition.

6.2. Origin of the Observed εNd Signature Change in ODP 1093

The authigenic Nd isotope record of site ODP 1093 near Bouvet Island in the Southern Atlantic shows a clear climate pattern in the isotopic signature (Fig. 6.2 b). During interglacials ODP 1093 is bathed in Lower CDW and its signature becomes the most unradiogenic with values of approximately -8.5 to -6.5. Such εNd values are in line with present day water signatures (Tachikawa et al., 2017). The most radiogenic εNd signatures are recorded during glacials, yielding values between -4 and even -2 in the LGM.

In contrast, the authigenic εNd signature of site ODP 1094 shows no systematic glacial-interglacial behavior throughout the past 1 Ma. In total, the εNd signature is more radiogenic than the signature of site ODP 1093. The record is characterized by abrupt radiogenic and unradiogenic spikes around a mean value of $\varepsilon\text{Nd} = -2 \pm 1$. These features point to a very local source of radiogenic Nd possibly entirely overprinting a water mass signal at this site, which is not visible in the multielement composition. The origin of the εNd signatures at site ODP 1094 are discussed separately in chapter 6.3.

South of the southern Atlantic Ocean's PF at site ODP 1093, synchronous climate induced changes of εNd imply massive increases of radiogenic Nd sources, most likely from volcanic reactive material replacing the Pacific-Atlantic intermittent εNd composition of the modern and last interglacial Southern Ocean. These changes need to be as abrupt and strong as the glacial-interglacial patterns or modulated with a climate related process. Via precipitation and sedimentation of neodymium onto particles, the radiogenic signature can be removed quickly from the water column. However, a sudden and persistent change of the dominant Nd source in the water column south of the PF asks for more than just the radiogenic Nd source but rather a mechanism allowing for the change in the entire Nd budget.

The matrix element analysis leads to the exclusion of leached detrital components as a cause for the changes in εNd in the investigated samples. According to a first order advection-diffusion model, two scenarios or a combination of both may cause the observed εNd signatures. Hereby, the Nd concentration [Nd] and the isotopic signa-

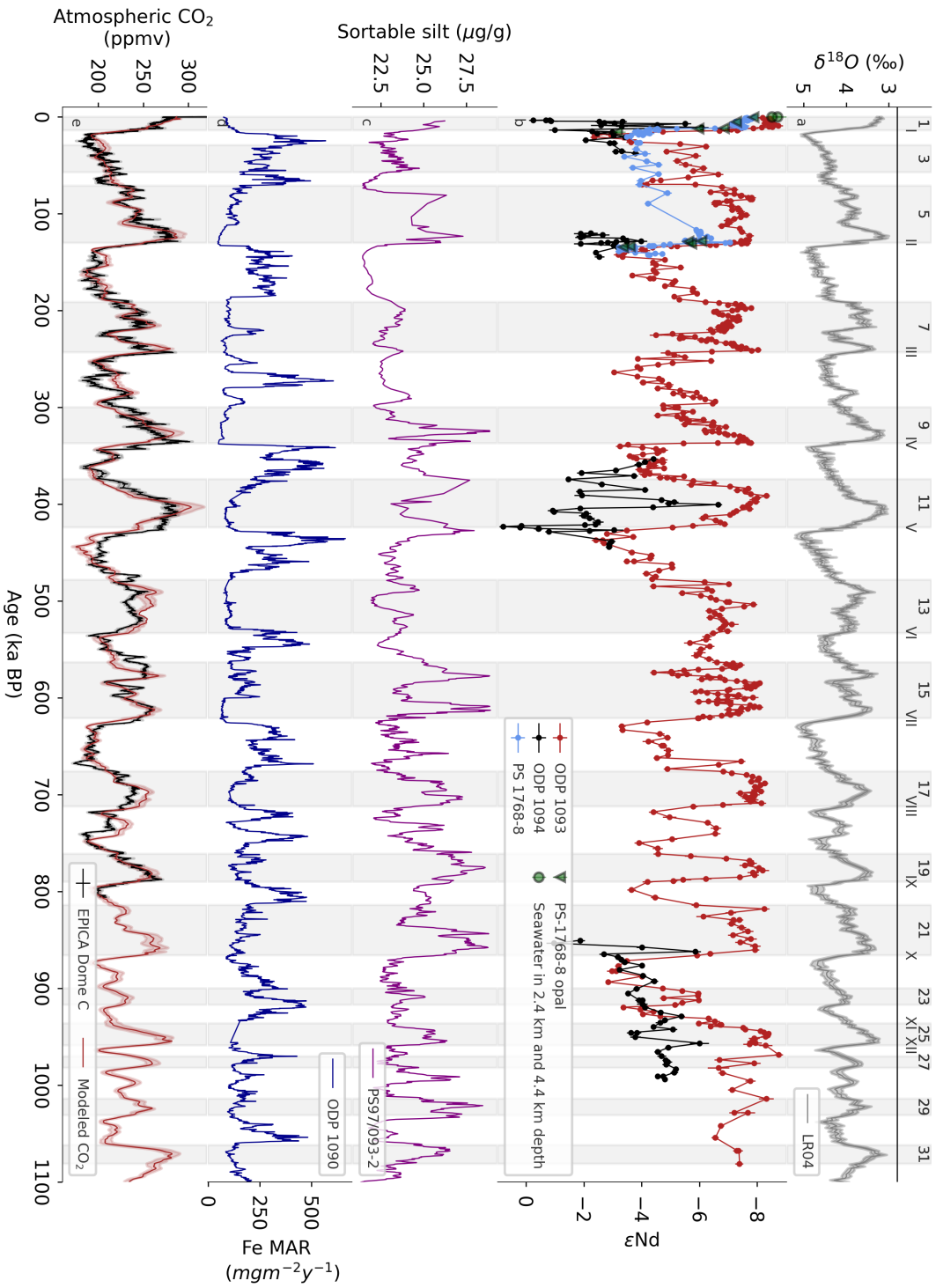

Figure 6.2.: εNd signatures of ODP 1093 and 1094 in context with other εNd data, sortable silt and iron supply in the Southern Ocean and atmospheric CO_2 in the past 1 Ma. **(a)** Benthic $\delta^{18}O$ stack, MIS and terminations (Lisiecki and Raymo, 2005). **(b)** εNd data of ODP 1093 and 1094 (this study and Hallmaier et al. (2023a), PS1768-8 (Hallmaier et al., 2023a; Huang et al., 2020), PS1768-8 opal (Huang et al., 2020) and nearby seawater (Stichel et al., 2012). **(c)** PS97/093-2 sortable silt from the Drake Passage (Toyos et al., 2020) as a measure for ACC strength. **(d)** Mass accumulation rate (MAR) of iron at site ODP 1090 (Martínez-García et al., 2014). **(e)** Atmospheric CO_2 reconstructed from EPICA Dome C (Bereiter et al., 2015) and modeled (Berends et al., 2021).

tures εNd of the sources have the potential to cause the changes in εNd and also [Nd] recorded in the authigenic coating of the sediment. Additionally, multiple advective or diffusive processes (diffusion coefficient D) may contribute to the change of the overall Nd budget. The advective-diffusive changes in the Nd budget $\partial_t(\varepsilon\mathrm{Nd}/[Nd])$ in a velocity field $\vec{v}$ can be described as follows:

$$\partial_t\left(\frac{\varepsilon\mathrm{Nd}}{[Nd]}\right) = \vec{v}\cdot\nabla\left(\frac{\varepsilon\mathrm{Nd}}{[Nd]}\right) - D\cdot\nabla^2\left(\frac{\varepsilon\mathrm{Nd}}{[Nd]}\right) \tag{6.1}$$

The three plausible scenarios, that are discussed regarding their potential to account for the authigenic εNd signatures south of PF, are the following:

(I) The εNd changes are of pure water mass origin, such that the diffusive second part of the equation 6.1 is zero. Glacial values are caused by a significant change in the circulation regime, allowing a most radiogenic water mass with potential central Pacific origin to enter the South Atlantic and sink down to the abyss.

(II) The εNd changes are the product of diagenetically altering processes, thus the advective first part of the equation 6.1 is zero.

(III) The εNd changes are caused by alternating dominance of the Nd budget of advective water mass influence during interglacials and the diffusive benthic fluxes during glacials driven by ACC flow speed changes.

Scenario (I) Assuming a pure water mass origin of the εNd signatures, the observations at site ODP 1093 likely result from changes in the export flux of those water masses. During interglacials the flow regime in the southern Atlantic Ocean at depth is dominated by AABW production and its export to lower latitudes in the abyss. Water mass mixing is persistent due to the influence of the ACC and AABW can efficiently be exported to site ODP 1093. Assuming an AABW signature of approximately -8.6 (Tachikawa et al., 2017), the Holocene εNd values at site ODP 1093 are very similar. The close by site PS 1768-8 records a similar pattern (Huang et al., 2020). Additionally, the data agrees with present day water mass signatures representing AABW like values near this site (Stichel et al., 2012). Therefore, it is suggested, that the authigenic εNd signatures at site ODP 1093 reflect seawater isotopic compositions of AABW during the Holocene and likely also the previous warm climate periods.

The glacial radiogenic signature must originate from a strongly radiogenic water mass, implying major changes in ocean circulation in the southern Atlantic Ocean.

Recent studies show a significant change in ocean dynamics during the last and penultimate glacial characterized by a strongly reduced AABW export from the Weddell Sea coupled to raising sea ice extent (Hallmaier et al., 2023b; Huang et al., 2020; Wu et al., 2021; Yu et al., 2020). Moreover, a weakening of the southward NADW influence during glacial times is suggested by several studies (Howe and Piotrowski, 2017). This allows the Nd budget south of the PF to be much more sensitive to inputs with extreme εNd signatures, such as Pacific Sourced Waters (PSW) within the ACC. Yet, the lack of AABW and less southward transport of NADW alone, are not sufficient to explain signatures of $\varepsilon\text{Nd} \sim -2$ in the South Atlantic. Interglacial-like PSW within CDW cannot account for the strong radiogenic εNd values. A significant PSW intrusion through the Drake Passage would be needed to increase Nd isotopic compositions in Southern Ocean bottom waters and thus at site ODP 1093. Presently, CDW is composed of mainly Atlantic and Antarctic water masses and their respective εNd fingerprints with little influence from the Pacific Nd reservoir.

Within the vast radiogenic Pacific Nd pool the most radiogenic water mass can be found at the equatorial eastern Pacific with a signature of approximately $\varepsilon\text{Nd} = -2$, reflecting Pacific Deep Water (PDW) (Frank, 2002). Several studies showed that the PDW flows southward along the eastern margin of the Pacific Ocean and potentially extends further south along the Patagonian margin into the ACC during glacials (Hu and Piotrowski, 2018; Yu et al., 2020; Well et al., 2003). Additionally, low carbonate ion concentrations were observed during glacials in the deep South Atlantic, which were nterpreted as an expansion of carbon-rich Pacific deep waters into the South Atlantic (Yu et al., 2020).

This scenario is known as the reversed flow or strong deep Pacific recirculation. Based on $^{231}\text{Pa}/^{230}\text{Th}$ of sediments from the deep Southern Ocean, evidences of a mid-depth water mass in the Pacific and stable carbon isotope observations have already been proposed (Roberts et al., 2010). However, stronger PSW export into the North Atlantic seems counter-intuitive due to today's salt deficit in the Pacific and the obvious lack of deep convection in the North Pacific, if compared to the North Atlantic or Weddell and Ross Sea at Antarctica. According to Adkins (2013), the density structure of the interior Atlantic during glacials reversed to a haline stratification. During these times PSW was shown to be as salty or even saltier than the water masses from the North Atlantic (Adkins et al., 2002), opening up the possibility for PSW to sink down to the depth of site ODP 1093. However, this flow path seems unlikely, considering the deep South Atlantic bathing in the densest water mass of all ocean basins during glacials (Adkins, 2013).

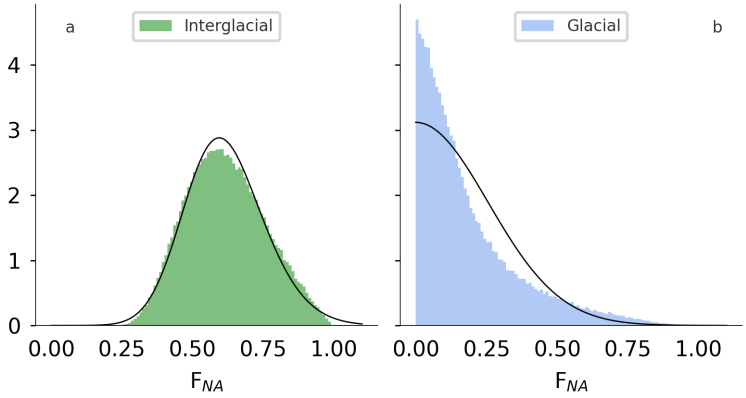

Figure 6.3.: Distribution of the fraction of deep water from the North Atlantic (F_{NA}) at site ODP 1093. The northern endmember range is set as εNd = −11 to −14. The southern endmember range is set as εNd = −3 to −5. **a**: During interglacials the mean εNd values from εNd = −7 to −9 can be explained by variable F_{NA} at site ODP 1093. **b**: During glacials the mean εNd values from εNd = −2.5 to −4.5 can only partly be explained by variable F_{NA} at site ODP 1093. The strong shift of the distributions toward F_{NA} = 0 demonstrates either a more radiogenic endmember or its variation during glacials. Model results after Yehudai et al. (2023).

To date, there are no further authigenic Nd records along the suggested flow path in the Pacific and the Southern Ocean, which could inform on the Nd isotopic composition of this water mass all the way to the core site ODP 1093. Several sites in the western Pacific (Basak et al., 2018; Molina-Kescher et al., 2014) measure the CDW further downstream as εNd ∼ −6. However, these sites are farther west and outside the assumed way of southward flowing PDW.

PSW intrusion must further be limited due to a weakening of the ACC strength during glacials, speaking against a dominating export of highly radiogenic PDW. Moreover, Howe and Piotrowski (2017) proposed a southern endmember of approximately εNd = −5.5, contradicting the here necessary εNd = −2. Further, the southern Pacific Ocean εNd over the past 60 Ma showed only low variability in the range of εNd = −5 to −3 (Frank, 2002). Applying the Bayesian statistic-based model of Yehudai et al. (2023) onto the ODP 1093 εNd data with an assumed mixed Pacific εNd signature of εNd = −3 to −5, the observed radiogenic values during glacials cannot be explained solely by a zero fraction of Northern Sourced Water (NSW) (Fig. 6.3). Thus, a dominant (even up to 100%) Pacific contribution cannot account for the total shift to more radiogenic εNd signatures south of the PF.

Therefore, despite recent studies supporting a PSW intrusion to the southern Atlantic Ocean during periods of reduced AMOC (Robinson and van de Flierdt, 2009; Struve et al., 2020b; Williams et al., 2021; Yu et al., 2020) PSW alone cannot account

for the observed εNd values in ODP 1093 and the process leading to a significant intrusion of PDW remains elusive.

Scenario (II) The εNd signatures are permanently altered by either diagenesis or benthic flux. On the one hand, diagenetic processes within the sediment and pore waters can lead to an interaction between the detrital and authigenic Nd resulting in the authigenic coatings no longer reflecting Nd scavenging from the overlying water mass. On the other hand, the benthic flux from pore waters can alter the bottom water itself at the sediment-water interface, which in turn will be reflected in the authigenic coating and foraminifera (Abbott et al., 2022, 2015a,b; Haley et al., 2017; Tachikawa et al., 2017). Moreover, diagenesis can influence the preserved Nd isotopic composition completely independent from the bottom water signature.

The εNd values match the expected present-day seawater composition of AABW (Fig. 6.2 b) (Stichel et al., 2012). Additionally, the εNd values of ODP 1093 are in line with Holocene and LGM foraminifera values of $\varepsilon\text{Nd} = -8.3$ and -4.5 of the nearby site TN057-13PC (Nielsen et al., 2007) and opal data from PS 1768-8 (Fig. 6.2 b) (Huang et al., 2020). Further, the data of PS 1768-8 from a close by site record similar glacial-interglacial εNd behavior in different water depth (Hallmaier et al., 2023a; Huang et al., 2020). Thus, the εNd signal likely records a regional water mass signature even during glacials and not only a local diagenetically altered sediment. A quantitative determination of the influence of diagenesis, however, is not possible, since there are few fish teeth or foraminifera within the investigated sediment and pore water samples are not available (Gersonde et al., 1999).

If the Nd budget in this region is predominantly influenced by a pore water or benthic Nd flux during all times the glacial-interglacial εNd variations must represent changes in the sediment composition and thus particles. In the southern Atlantic Ocean, local changes in particle fluxes are well admitted (Martínez-García et al., 2014; Shoenfelt et al., 2018; Struve et al., 2020a). Volcanogenic inputs, however, are very likely having an overall impact, best seen at site ODP 1094 situated close to the Bouvet triple junction (Nielsen et al., 2007). The glacial period is also known for higher dust fluxes from Patagonia carrying reactive volcanic particles, with highly radiogenic Nd signatures, to the South Atlantic (Shoenfelt et al., 2018). Additionally, the northward shift of the PF inhibits carbonate productivity, causes sea ice to thicken and to reach further northward (Abelmann et al., 2015; Sigman et al., 2010; Schneider-Mor et al., 2005; Wolff et al., 2006). Consequently, changes in particle chemistry and the southward admixture of North Atlantic waters during glacial

periods are induced, allowing for an increase of the regional influence on the isotopic composition of the Southern Ocean south of the PF. Additionally, such regional changes of particle fluxes and sediment composition coincide with the authigenic εNd changes at site ODP 1093 and thus likely the bottom waters (Fig. 6.2 b,d).

Recent studies have shown, that the dust deposit in the Southern Atlantic yield a higher Fe flux at site ODP 1090 during glacial times (Fig. 6.2 d) (Martínez-García et al., 2014; Shoenfelt et al., 2018). However, assuming the main dust contributions stemming from South America and Australia (Lamy et al., 2014; Struve et al., 2022; Weber et al., 2022), the dust εNd signature would be in the range of εNd = -3.7 to -5.3 (Struve et al., 2020a). There can also be glacial observed volcanic glass present with highly radiogenic signatures of εNd $\sim$+7 (Nielsen et al., 2007). Such material released Nd into the authigenic phase in nearby site ODP 1094. However, the dissolution of volcanic glass is difficult to quantify.

The impact of Nd originated from particles, such as dust and volcanic glass, was investigated in a binary mixing model (Fig. 6.4). Depending on the εNd signature of the particle sources, a change of the authigenic εNd is linearly dependent on the contributing Nd concentration ratio $F_{particle}$ between the ambient water mass (εNd = -8.6) and the particle. The mixing model yields, that more than 90% of the Nd concentration would need to be of dust origin to at least cause a bottom water signature shift to εNd = -4. Volcanic glass in turn only has to make up 30% of the Nd concentration to cause a similar εNd shift.

Furthermore, detrital values of εNd = -5.2 and -3.8 during the Holocene and LGM at site ODP 1093 were determined by Noble et al. (2012), confirming the strong Patagonian dust influence at the investigated site (Noble et al., 2012). Even if a combination of increased aeolian dust input and reduced North Atlantic water influence can partly explain the radiogenic εNd synchronously changing with climate, the purely radiogenic εNd values of up to -2 remain challenging to explain. Consequently, an additional source of radiogenic Nd is needed to explain the glacial observations.

Scenario (III) In the third scenario, the εNd signature of the authigenic coating is influenced by water mass provenance changes and local alterations, which are difficult to disentangle. It has been shown, that the impact of the benthic flux is highly dependent on the circulation strength (Abbott et al., 2019; Blaser et al., 2019; Du et al., 2016; Homoky et al., 2016; Howe et al., 2016a; Jaume-Seguí et al., 2021; Roberts

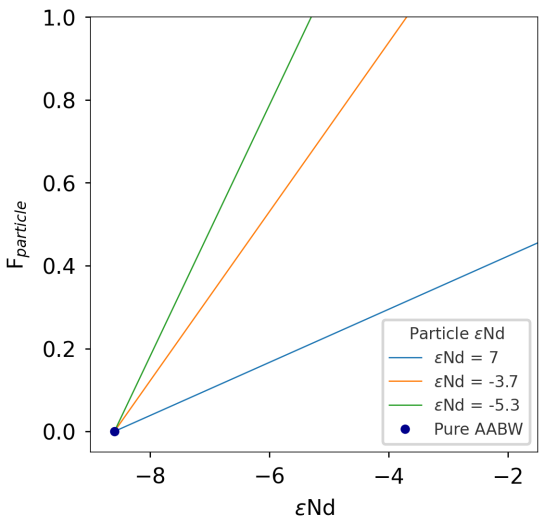

Figure 6.4.: Binary mixing model for particle contribution to εNd signatures in the ambient seawater of AABW (blue dot). The lines depict the change in εNd signature of the water mass by adding Nd from dust to the Nd budged in various fractions F_{dust}. The mixing model was applied with typical dust εNd signatures of Patagonian origin (Struve et al., 2020a, 2022) and volcanogenic glass (Nielsen et al., 2007). The model does not make any statements on the dissolution process of particles itself.

and Piotrowski, 2015; Vogt-Vincent et al., 2020). During times of a sluggish ACC the resulting exposure time of water masses around Patagonia increases compared to interglacial times (Lamy et al., 2024; Toyos et al., 2020; Wu et al., 2021), allowing diffusion of pore water Nd to become more relevant with respect to advection.

Lacking direct reconstructions of flow speed from ODP 1903, the reconstructed flow speed at site PS97/093-2 (Toyos et al., 2020) is presumed to be the same as at site ODP 1093 in a first approximation (Fig. 6.2 c). At ACC flow speeds of 10 cm/s in glacials to 20 cm/s in interglacials, the transport of water from site PS97/093-2 to sites ODP 1093 and 1094 occurs in less than a year, which is instantaneous compared to the millennial resolution of the εNd records. Thus, more sluggish ACC conditions lead to an overall longer exposure of the bottom water mass to possible sedimentary and volcanogenic influences in the investigated region. This becomes visible in a strong correlation of the ACC speed with the εNd signatures at site ODP 1093 during the first 150 ka (R^2=0.7, Fig. 6.5 a). For the entire 1 Ma the correlation is still imaginable, however, likely due to age model uncertainties of ODP 1093 only at R^2=0.38 (Fig. 6.5 a). The exact influence of the εNd modifying processes is not quantifiable due to the various mechanisms underlying the εNd signature change. For comparison, diffusive effects on the Nd budget in todays South Pacific are in the order of 1.4 ε-units and thus do not cover up completely the εNd water mass signal (Haley et al., 2021).

The fact that ACC conditions during glacials are quantitative, allows suggesting that the local change of the water mass εNd signature increases during glacials compared to interglacials. A lack of AABW export (Huang et al., 2020) and the possibly less southward reaching NADW during glacials (e.g. Farmer et al., 2019; Frank, 2002; Howe and Piotrowski, 2017; Pena and Goldstein, 2014) further facilitates the dominance of the regional volcanic Nd budget in the southern Atlantic Ocean by processes such as the benthic flux. Note that this scenario does not exclude any impact of PSW possibly contributing to the radiogenic Nd budget. The benthic modified Deep Water (bmDW) is assumed to be recorded in the authigenic coatings of the sediment at site ODP 1093. Its occurrence must be a more regional feature, since also at site PS 1768-8 a highly radiogenic signature of $\varepsilon\text{Nd} \sim -4$ is recorded (Huang et al., 2020).

These temporal and regional changes of the bottom water mass imply, that the quasi-conservative behavior of Nd isotope composition in the ocean is not maintained south of the PF in the southern Atlantic Ocean. A complex interaction of sediment composition, flow strength and water mass advection and mixing pathways allows a pore water flux to modify the bottom water εNd signature. These findings support the hypothesis of a switch to more non-conservative behavior of Nd during glacials with a more sluggish circulation (Pöppelmeier et al., 2022). However, the εNd modified water mass of bmDW interacts via the ocean circulation with the whole Atlantic Ocean basin, once it leaks the PF toward the North.

During interglacials the combination of advective ocean dynamics with higher ACC speeds and the pronounced AABW export diminishes the regional flux and causes a more advection-driven Nd budget. Thus, conservative water mass mixing between the latter is assumed to entirely account for the εNd signature of the authigenic coating. This is in line with similar interglacial εNd signatures at sites ODP 1093, PS 1768-8, the foraminifera, opal and sea water εNd data (Hallmaier et al., 2023a; Huang et al., 2020; Nielsen et al., 2007; Stichel et al., 2012). Solely ODP 1094 stands out, likely being to close to the source of volcanic particles and Nd release. A low to no benthic influence during interglacials is further constraint by the strongly different εNd values of the detritus and the authigenic coating (Noble et al., 2012).

In summary, the εNd record at site ODP 1093 is considered to predominantly reflect bottom water through interglacials. A reduction of ACC strength, AABW production and NADW import lead to a change in Nd flux density during glacial periods and a more significant contribution of regional diffusion of Nd from dust and volcanogenic particles. The resulting changes in Nd budget and the sluggish circulation could possibly allow for a PSW influence on the εNd signature. However, this

influence is not quantified at present, as it requires observations along the presumed advective pathways. Beyond this, the changes in ocean dynamics allow for local sedimentary sources, dust inputs and also volcanogenic impacts altering the bottom water εNd signature, yielding glacial bmDW. The spatial extent of bmDW over time remains elusive due to the lack of multiple further εNd records south of the PF. Only for the past 150 ka, the εNd recorded at site PS 1768-8 support the importance of a volcanic Nd flux during glacial (Huang et al., 2020). Obviously, a combination of the discussed processes can also account for the εNd variability at site ODP 1093.

In conclusion, the εNd signature of ODP 1093 depicts a variable southern Atlantic Ocean basin endmember changing synchronously with the climate. The εNd signature most likely accounts for advective and diffusive processes altering the Nd isotopic composition of the bottom water on climate timescales.

6.3. Local Influences Dominating the εNd Signature of ODP 1094

Compared to site ODP 1093 the εNd signal at site ODP 1094 does not record an entirely climate related signal at first glance. The εNd values during glacial periods are similar to the glacial values of ODP 1093 supporting the hypothesis, that the regional bottom water mass is altered toward radiogenic values during glacials. Nevertheless, sudden radiogenic spikes during interglacials cannot be explained by a climate related process. As already proposed, these signatures point to a strong radiogenic source in close vicinity of ODP 1094. Nowadays, the core site is located in vicinity to Bouvet triple junction (∼500 km), which is part of a complex submarine volcanic area and seaflor spreading center. In this area the South American Plate, the South African Plate and the Antarctic Plate diverge (Ligi et al., 1999). Due to continuous ridge formation the volcanic activity around this area is very high. However, the connected processes are unlikely to influence the Nd isotopic composition at site ODP 1094 in a different way than ODP 1093.

Site ODP 1094 is today located within a plume of dissolved Fe and Mn pointing to submarine hydrothermal activity (Klunder et al., 2011; Middag et al., 2011). The high Fe-Mn inputs from hydrothermal vents have the ability to alter the bottom water Nd budget by decreasing the Nd concentration due to direct scavenging of Nd onto Fe-Mn oxides. This process can lead to a strong shift in the seawater Nd budget and isotopic composition. Thus, the possible benthic flux influence on the εNd signatures preserved in authigenic coatings may be increased in close proximity to the

source (Jeandel et al., 2013). It was shown, that the ability of hydrothermal inputs to modify water mass εNd signatures on a larger scale is approximately +0.7 ε-units in the North Atlantic (Stichel et al., 2018). The observed hydrothermal plume expands along the zero meridian distinctly from ∼51°S to 56°S and ∼1.4 km to 2.8 km water depths (Middag et al., 2011). Assuming the plume to be neutrally buoyant, it gets strongly advected eastward within the strong ACC (German et al., 2016; Klunder et al., 2011; Middag et al., 2011). As site ODP 1094 is located within the center of the plume, the plume has a direct impact on the εNd signatures. In contrast, the deeper location of ODP 1093 is outside the plume and a direct influence of the hydrothermal activity is strongly reduced.

Besides the prominent radiogenic spikes, the εNd signature also shows single but remarkably unradiogenic spikes during interglacials. Comparing the two authigenic Nd isotope records of the neighbouring locations ODP 1093 and ODP 1094, the signature of the more northern location ODP 1093 envelops the highly variable signature of ODP 1094 and forms an unradiogenic limit to ODP 1094 (Fig. 6.2). The rare unradiogenic spikes during interglacials can be interpreted as short time periods where advective water mass signatures have the potential to dominate the Nd budget at site ODP 1094, maybe due to short interruptions in hydrothermal activity. Since all possibly modifying processes, such as e.g. volcanic activity, boundary exchange and dust dissolution, lead to more radiogenic εNd values, these excursions must stem from a localized overprinted water mass at that site. Additionally, hydrothermal activity is erratic and unlikely continuous. Thus, it is possible that radiogenic spikes of century long duration influence the record during interglacials. In glacials the sensitivity to these radiogenic influences vanishes as the surrounding bottom water becomes overall more radiogenic.

For a quantitative measure of the deviation of the ODP 1094 signature to the expected ODP 1093 signature, a comparison is made by calculating the difference in εNd over time and comparing it with the ACC strength (Toyos et al., 2020) (Fig. 6.5 b). For the period before the 900 ka event the difference in the εNd signatures is significantly lower and the εNd signature at site ODP 1094 less variable, which is discussed in detail in chapter 8.

The ACC flow strength is highly variable on glacial-interglacial time-scales (Lamy et al., 2024; Toyos et al., 2020). The ACC itself acts as a main mechanism transporting the hydrothermal plume, consequently it has the potential to modulate the impact of the plume on site ODP 1094. Thus, the calculated difference in εNd is set in context with ACC flow speed reconstructions via sortable silt measurements

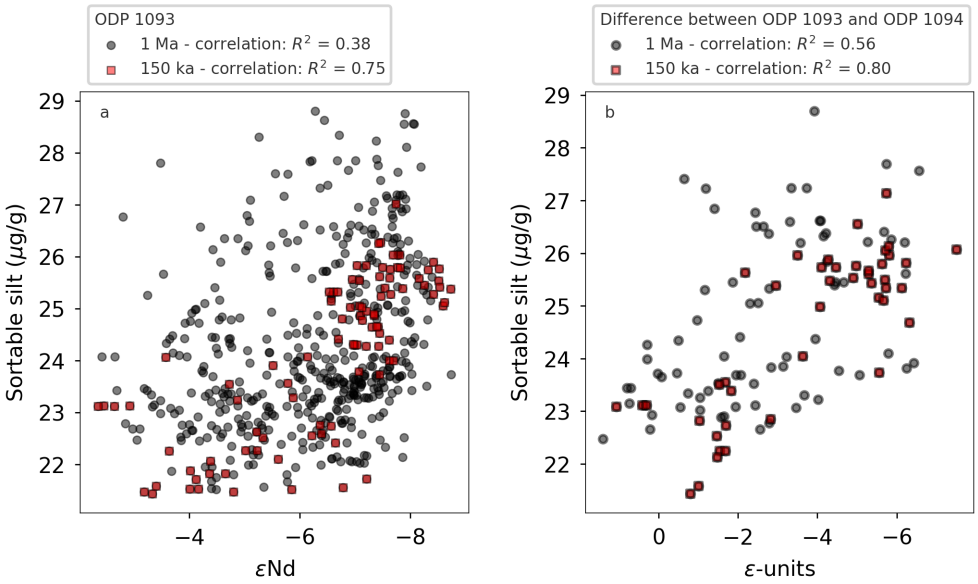

Figure 6.5.: a: Correlation of εNd of ODP 1093 with sortable silt measurements of PS97 093-2 from the Drake Passage as measure for ACC flow strength (Toyos et al., 2020). **b**: Correlation of the difference in ε-units of the εNd signatures from ODP 1094 to ODP 1093 with ACC strength.

($\overline{SS}$) at the entrance of the Drake Passage over the past 1 Ma (Toyos et al., 2020). The observed $\overline{SS}$ variations correspond to current speeds in a range of 15 to 18 cm/s (McCave et al., 2017) or 8 to 17 cm/s (Wu et al., 2019) depending on the used calibration. The correlation between the difference in εNd values of the locations and the respective $\overline{SS}$ measurement is especially strong for the last 150 ka (R^2=0.8). The correlation is still visible for the whole record even though less strong (R^2=0.56). The lower correlation is likely linked to the higher uncertainties in the age model of ODP 1093 for older ages and especially before the 900 ka event. In summary, large εNd offsets of ODP 1094 to ODP 1093 can be associated with higher ACC speeds and vice versa (Fig. 6.5 b). This suggests a hidden climate signal within the otherwise apparently random behavior of the εNd signature of ODP 1094.

These observations allow for the conclusion that ACC flow speeds are of crucial importance for the spreading of such variable εNd signatures at site ODP 1094 and likely the whole ocean. During times that are characterized by a more sluggish circulation such as glacials, the eastward advection of the hydrothermal plume is less pronounced. Thus, it is most likely that the plume does not reach site ODP 1094, leading to a weaker Nd scavenging and a more dominant signal from the surrounding bottom water. Additionally, as indicated by ODP 1093, the overall isotopic signature of the bottom water is more radiogenic and thus more similar to possible local effects. Consequently, still occurring local sedimentary processes may not dominate

as strongly as during interglacials.

In summary, the εNd record at site ODP 1094 reveals a coherence with ACC flow speeds, which is driven by climate. Current flow speeds within the ACC seem to play a major role in advection-diffusion pattern of εNd in the Atlantic Ocean south of the PF. The unique εNd pattern further emphasizes the importance of Nd isotope exchange processes through pore waters and volcanic activity.

6.4. Increased Carbon Storage in the Deep Southern Ocean During Glacials

During glacials, the deep oceans are stratified rather by salt instead of heat (Adkins, 2013), resulting in a more haline ocean circulation. The salinity pattern of global bottom waters was different during glacials: The saltiest waters are found in the southern Atlantic Ocean, contrasting with the freshest waters today (Adkins, 2013; Adkins et al., 2002; Kobayashi et al., 2015). This led to a decrease in vertical diffusivity of heat between the Atlantic and the Southern Ocean deep waters. The decrease in diapycnal mixing is suspected to create two distinct circulation cells separating the Southern Hemisphere from oceanic heat fluxes more efficiently (Adkins, 2013; Hines et al., 2019). This concept points toward a different vertical water mass structure in a more stratified glacial deep Atlantic, prohibiting a vertical exchange of water and thus ventilation of Southern Ocean waters.

The stronger influence of benthic flux in ODP 1093 during glacials is in line with the observations of a much less dynamic circulation regime in the southern Atlantic Ocean favouring an enhanced carbon storage. These processes combined lead to a carbon rich, benthic modified Deep Water occupying the glacial Atlantic Ocean south the PF. The εNd data supports the leading hypothesis of an aged and less ventilated water mass, increasing the glacial carbon storage in the Southern Ocean (Huang et al., 2020; Skinner et al., 2013; Struve et al., 2020b; Williams et al., 2021; Yu et al., 2020). This indicates a significant impact of the Southern Ocean on the carbon cycle during glacial-interglacial cycles. Note that due to PSW being old and carbon rich, the implications of this chapter would be similar, if only scenario (I) was true, instead of a combination of scenario (I) and (III).

The abrupt decrease in εNd during deglaciations points to the sudden change from a benthic flux dominated deep water to advection dominated AABW and CDW. In contrast, the glaciation is characterized by a more gradual establishment of bmDW,

reflected in a rise toward radiogenic εNd values. Furthermore, this strengthens the hypothesis of two different modes causing the εNd signatures, also reflected in the overall εNd distribution of site ODP 1093.

The onset of terminations is abrupt and is characterised by the sudden return to interglacial conditions regarding ACC strength, AABW and possible NADW export, reduced sea ice cover and the position of the PF (Ai et al., 2024). The high fresh water influxes from sea ice melting led to changes in the stratification regime and the westerlies shift back to the South. Altogether this yields to the reestablishment of upwelling processes and efficient export of the accumulated carbon rich water masses to the surface where outgassing takes place (Ai et al., 2024). Additionally, during deglaciations the AAIW export extends further to the North to feed the onset of NADW production and thus opens up the possibility for outgassing in the whole Atlantic (Yu et al., 2022).

In conclusion, the occurrence of a carbon rich, poorly ventilated water mass during glacials in the southern Atlantic Ocean bears the potential to contribute significantly to the abrupt climate changes in the past via upwelling and outgassing during deglaciations. This further highlights the importance of the complex interplay between atmosphere, cryosphere and the ocean in the Southern Hemisphere.

6.5. Conclusions

The εNd signature of ODP 1093 shows two distinct modes, which evolve synchronously with the LR04 benthic δ^{18}O record and thus ice volume changes (Lisiecki and Raymo, 2005). In contrast, the εNd signature of ODP 1094 is characterized by abrupt centennial changes in its isotopic composition with three modes, that are not correlated with climate. Here, the first multielement measurement of the carbonate depleted sediment leachates of ODP 1093 and 1094 point to a mainly authigenic source of the extracted Nd in both cases. Non-hydrogenetic and especially detrital influences on the authigenic εNd signatures were concluded for samples with higher Sr/Ca than 1 ‰ and Al/Nd below the limit of ∼300. Comparing the HREE/LREE and MREE/MREE* ratios, single samples outside the bounds of leached and seawater samples were observed by Martin et al. (2010). With this method a total of 15 samples and their respective εNd signatures were excluded from further evaluation.

The high εNd dynamic at both sites is unlikely entirely caused by water mass provenance changes. In fact, a combination of three different processes influences the Nd budget. These processes are: (I) advective water mass changes, (II) regionally

altering pore water flux of Nd and (III) modulation of the advection-diffusion balance by ACC volume and speeds.

Site ODP 1094 is situated close to an active volcanic and hydrothermal area. Thus, the surrounding bottom water is likely influenced by punctual scavenging of Nd and relabelling due to volcanic isotope exchange processes. Under specific conditions, these mechanisms have the possibility to dominate the Nd budget. Especially, ACC flow speed changes lead to recurring overprints of the water masses at site ODP 1094.

Furthermore, the unique variability of 6 ε-units observed at site ODP 1093 is caused by advection-diffusion processes, but due to the distance to the volcanic plume a direct influence of volcanism and hydrothermal impacts is missing. During interglacial periods with a strong ACC and persistent AABW export, the εNd signature is driven especially by the Nd from advective water mass flow. This is reflected in the AABW like εNd signature of approximately -8 during interglacials. During glacial times circulation conditions are more sluggish and AABW export is strongly decreased (Wu et al., 2021). However, considering the contributing water masses, this influence can only explain signatures of around $\varepsilon\text{Nd} = -5$. Within a sluggish ACC and without a strong AABW influence local benthic sources dominate the Nd budget within the bottom water, explaining the strongly radiogenic signature up to $\varepsilon\text{Nd} = -2$ ε-units during glacial periods. Altogether, this causes a major change in the Nd isotopic composition south of the PF.

Thus, the εNd signature at site ODP 1093 points to a regional modification of CDW, namely bmDW, due to more sluggish circulation conditions. This in turn supports the occurrence of a respired carbon rich, poorly ventilated water mass in the southern Atlantic Ocean. Conclusively, bmDW export bears the potential to contribute significantly to the abrupt climate changes in the past. The water masses with the radiogenic εNd signature, recorded at site ODP 1093, interact with the entire Atlantic Ocean via the frontal upwelling systems and potentially alter the Atlantic's Nd isotopic composition toward more radiogenic εNd values over time. Thus, ODP 1093 serves as the SSW εNd endmember in the Atlantic Ocean.

7. Interhemispheric εNd Gradient and Deep Ocean Circulation Strength

Throughout the past 1 Ma, sites in the North Atlantic show less radiogenic εNd signatures compared to the sites on the Southern Hemisphere. Several studies interpreted this phenomenon as the decreasing southward imprint of NADW on the water mass mixing balance on its way to the South, which is also visible in the benthic carbon isotopes of foraminifera tests (Howe and Piotrowski, 2017; Kim et al., 2021; Pena and Goldstein, 2014). Other studies have recently interpreted this gradient as a result of detrital particle composition and weathering release of Nd (Abbott et al., 2022; Zhao et al., 2019). In the South Atlantic a similar εNd behavior as across the Atlantic basin is observed. As already discussed in chapter 5 and 6, the εNd signature at site ODP 1093 does reflect signs for a change in water masses. The recorded SSW reflects the Southern Ocean basin endmember of the Atlantic Ocean interacting with the entire ocean basin and accounting for different processes altering the εNd signature of the regional bottom water.

The change of εNd signatures across the Atlantic Ocean over time can be quantified via the εNd gradient $\Delta\varepsilon$Nd. All relevant sites for this study are displayed in Fig. 7.1. The weakening of the AMOC during glacials proposed by several εNd studies in the past, is always based on the assumption of a constant Southern Atlantic Ocean basin endmember. The new findings of this study show on the one hand that this is not the case and on the other hand, open up the possibility to review proposed changes in the strength of deep ocean circulation with a variable εNd endmember.

The findings of this chapter summarize and extent the results of the manuscript *Small-scale AMOC Strength Variability Revealed by the Interhemispheric εNd Gradient of the Atlantic Ocean During the Last 150 ka* (in preparation).

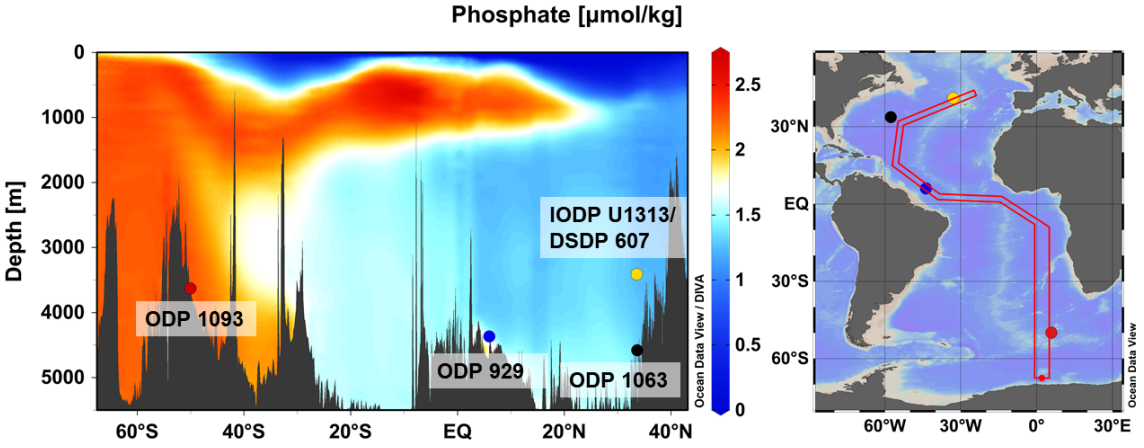

Figure 7.1.: Locations of various sites across the Atlantic considered in the interhemispheric gradient $\Delta\varepsilon$Nd discussion **Left**: Dissolved phosphate content on a transect across the Atlantic Ocean. The phosphate concentration follows the main water masses. **Right**: Transect across the Atlantic Ocean along the locations of the investigated sites. Color code as in Fig. 7.3. Visualization with Ocean Data View (Schlitzer, 2019).

7.1. Synchronous εNd Changes in the North and South Atlantic

To get a broader picture of the εNd evolution across the Atlantic Ocean several locations were set in context with each other. The exact location of the sites, the high temporal resolution of the εNd data and a time range of ideally 1 Ma were main criteria for the choice of data to compare with. Applying these criteria, the data coverage is sparse, in fact there are no published records at millennial resolution, that reach further back in time than 800 ka. In the North, the glacial-interglacial resolution record of IODP U1313/DSDP 607 and the mainly unpublished record of ODP 1063 with a high temporal resolution are considered. Site ODP 1093 marks the southern boundary. The respective εNd signatures over the past 1 Ma are displayed in Fig. 7.2 a.

Site ODP 1093 is located south of the PF and records the past 1 Ma εNd signature in a millennial resolution. It serves as the southern Atlantic Ocean basin endmember, which in turn interacts with the entire Atlantic, as already discussed in chapter 6 and 5. IODP U1313/DSDP 607 is located at the base of the upper western flank of the Mid-Atlantic Ridge and extensively studied as a key to understand NADW through time (Jaume-Seguí et al., 2021; Kim et al., 2021; Lang et al., 2016; Lippold et al., 2016; Pöppelmeier et al., 2021a; Yehudai et al., 2021). ODP 1063, located at the Bermuda rise, has been debated as representing NADW through time due to a recur-

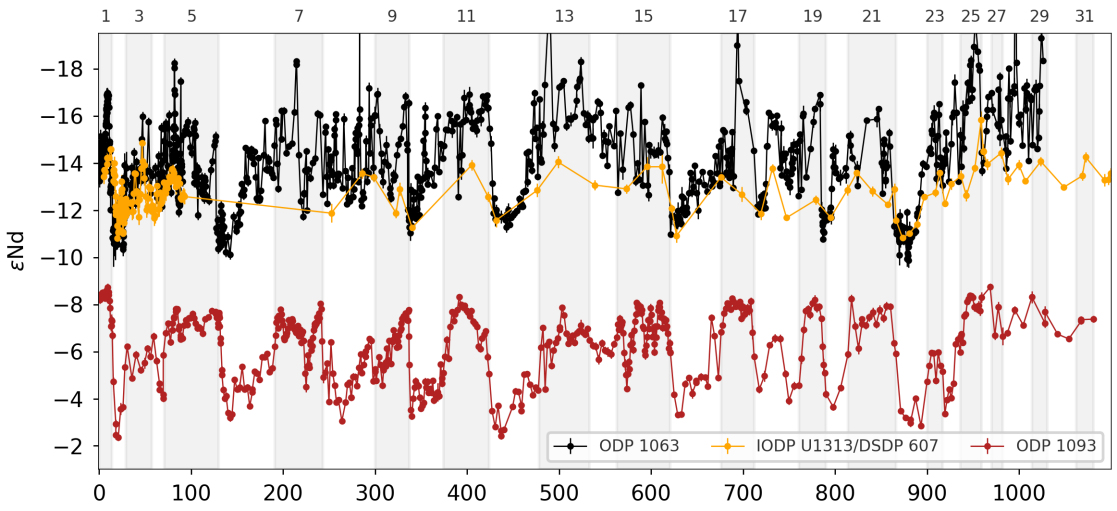

Figure 7.2.: εNd signatures in the North and South the Atlantic Ocean. εNd signatures at sites IODP U1313/DSDP 607 (Kim et al., 2021; Lang et al., 2016; Lippold et al., 2016; Pöppelmeier et al., 2021a), ODP 1063 (Böhm et al., 2015; Gutjahr and Lippold, 2011; Jaume-Seguí et al., 2021; Link, 2021; Lippold et al., 2019; Roberts et al., 2010) and ODP 1093 (this study and Hallmaier et al. (2023a)). Grey shaded areas and numbers above mark the MIS.

ring local unradiogenic overprint, which is disturbing the water mass exchange signal in more than 25 % of the observations during the past 150 ka (Böhm et al., 2015; Gutjahr and Lippold, 2011; Lippold et al., 2019; Roberts et al., 2010). Nevertheless, J.M. Link has shown the value of ODP 1063 by extending the εNd record to 1 Ma and demonstrating its ability to partly represent water mass signature despite local influences (Link, 2021).

The strong oscillation pattern of εNd in ODP 1093 is synchronous and in the same order of magnitude as εNd records in the North, like ODP 1063 or IODP U1313/DSDP 607, which is of lower temporal resolution (Fig. 7.3 a). The resolution in the first 150 ka of εNd at site IODP U1313/DSDP 607 is equally high as in the other records. Further, its signature is in a similar range as the εNd signature at site ODP 1063, however, shows less variability and no strongly unradiogenic excursions. The data from site IODP U1313/DSDP 607 has only glacial-interglacial resolution, making the comparison between the northern sites more difficult. In total, all three records show similar glacial-interglacial patterns. Compared to site ODP 1063 the εNd signature at site ODP 1093 has little millennial variability within single MIS. While the absolute values and the origin of Nd in both regions and under changing climate are completely independent from one another, the close temporal correlation and even similar amplitude is remarkable and advocates for a common driver. Both εNd signatures change synchronous with the benthic δ^{18}O record (Lisiecki and

Raymo, 2005), inferring that the oscillation is primarily driven by climate forcing and ice volume changes. Moreover, the forcing altering the εNd signature must be of similar strength, synchronized and thus basin wide, possibly even global.

One hypothesis to explain the strong connection could be a water mass endmember change, driven by the increase and decrease of Northern Hemisphere ice volume. The synchronous shift of 6 ε-units is dramatic and implies a major change of the Nd sources, as today the Pacific and Atlantic differ by only 8-10 ε-units (Tachikawa et al., 2017). Such a massive change would imply a modification of the entire Atlantic εNd composition towards more radiogenic values without changes in the actual water mass structure and flow strength, and thus interior ocean circulation patterns, respectively. To change the water mass endmembers' signature, deep water formation must take place in either an entire different region or the signature at the respective site must change on the same time scale. Additionally, the radiogenic εNd must be quickly removed from the water mass during deglaciations.

The here used northernmost sites ODP 1063 and IODP U1313/DSDP 607 are in large distance from today's deep water formation areas and thus cannot trace such changes directly. Additionally, there is no particular reason for the deep water formation to take place in a different region in the past compared to nowadays. Present-day deep water formation in the Atlantic occurs in the Norwegian, Greenland and Labrador Seas and in the Southern Ocean in the Weddell and Ross Sea. Each of these Seas have a strongly differing Nd isotopic composition (Foster et al., 2007; Howe et al., 2016a; Jaccard et al., 2013; Jaume-Seguí et al., 2021; Lippold et al., 2019; van de Flierdt et al., 2006). Denmark Strait Overflow Waters (DSOW) and Iceland Scotland Overflow Waters (ISOW) are far more radiogenic than Labrador Sea Waters (LSW) due to the influence of Nd from weathering of Icelandic volcanic material. This leads to an increase of the Nd isotope composition of NADW (εNd ~ -12.3, Tachikawa et al. (2017)) if compared to the Labrador Sea Water (LSW) (εNd ~ -16, Blaser et al. (2020)). Analysis of Fe-Mn crusts (Foster et al., 2007; Frank, 2002) and of cold-water corals (van de Flierdt et al., 2006) from the North Atlantic further suggest a constant NADW endmember Nd isotopic composition during the past ∼3 Ma. Also, the εNd composition of continental margins are assumed to be stable over geological time scales and especially independent from glacial-interglacial cycles.

The process of changing water mass endmembers in the North is therefore highly unlikely. However, the possibility of a variable NSW endmember is hereby not excluded, it only appears very unlikely. For the South the variability of the SSW

endmember value was shown in the previous chapters. CDW has no distinct formation area, but is rather a well mixed water mass of southward exported water masses from all ocean basins. Deep water formation in the southern Atlantic Ocean only takes place in the Weddell Sea and the resulting AABW is the most radiogenic deep water mass formed in the southern Atlantic Ocean today. Based on Pb and Nd isotopes it was shown that AABW εNd signatures remained constant (εNd ~ -8.6) over the last glacial period, but Weddell Sea deep convection almost vanished during the last glacial (Huang et al., 2020). The record of site ODP 1093 confirmed, that this process was recurring during all glacial periods within the past 1 Ma. Thus, a changing water mass εNd endmember of AABW is not only unlikely, but of rather minor importance for the radiogenic change in the εNd signature in the southern Atlantic Ocean due to its reduced occurrence during glacials.

Changes in ocean dynamics from larger to more local scales have the potential to cause the distinct εNd signatures. The northern sites do not to reflect a water mass endmember but rather the change of flow dynamics over time (Jaume-Seguí et al., 2021; Kim et al., 2021; Lang et al., 2016; Lippold et al., 2016; Pöppelmeier et al., 2021a; Yehudai et al., 2021). Thus, this location is considered as the Northern Atlantic Ocean basin endmember, which interacts with the entire ocean basin. However, very local effects have the ability to modify the εNd signatures in the North in a similar way compared to changes in the South. For ODP 1063 it was suggested, that the more radiogenic values were caused by a stronger export of SSW (Böhm et al., 2015). In contrast, the more unradiogenic values were caused by most localized influences from reactive sediments, possible diagenesis or benthic fluxes. These are documented in εNd < -16, which occurred at the end of the past two climate terminations (early interglacial overshoot) and frequently during earlier interglacials (MIS 11 and before), or during the slow transitions to glacial climate. The unradiogenic peaks have been explained as being caused by LSW (Lippold et al., 2019), abyssal unradiogenic sources (Howe et al., 2016b; Jaume-Seguí et al., 2021) or weathering of detrital material (Abbott et al., 2022). However, these inputs are not assumed to modify the Atlantic's regional bottom water Nd isotopic composition significantly. In addition, it was shown by ^{231}Pa/^{230}Th that the export of deep water solely vanished surrounding Heinrich events (Böhm et al., 2015). The overall circulation showed persistently strong overturning likely at shallower depth. Less NADW export coincides with more radiogenic Nd isotopic compositions (εNd ~ -10) at site ODP 1063 during these millennial events (Jaccard et al., 2013; Skinner et al., 2013). To conclude, ODP 1063 reflects a combination of water mass contributions and not yet quantifiable very local inputs in ODP 1063 (Böhm et al., 2015; Gutjahr and Lippold, 2011; Link, 2021; Lippold et al., 2019; Roberts et al., 2010). For further evaluation locally overprinted

εNd < -16 in ODP 1093 are excluded.

The strong mixing capacity of the ACC provides an εNd endmember south of the PF, which here reflects the southern Atlantic Ocean basin endmember. Its characteristic signature was shown to originate from the alternating impact of advective water masses and regionally pore water fluxes modifying the bottom water Nd isotopic composition during glacials (Chapter 6). To further quantify the North-South εNd changes through climate, the evolution of the difference in εNd signatures across the Atlantic is investigated.

7.2. Latitudinal εNd Gradient

The synchronous interhemispheric Nd isotope changes lead to the here defined neodymium isotope gradient $\Delta\varepsilon$Nd, which is given as the North-South difference in εNd per 10° latitude:

$$\Delta\varepsilon\mathrm{Nd} = \frac{\varepsilon\mathrm{Nd}_{\mathrm{South}} - \varepsilon\mathrm{Nd}_{\mathrm{North}}}{\text{latitudinal difference}/10^{\circ}}. \tag{7.1}$$

In this concept, the lower the gradient the more similar are the water masses. This can be the result of a strengthening NSW flow to the South or a complete reversal of the flow. Following this concept, the sensitivity of water masses to Nd isotope mixing is low, when the interhemispheric gradient is small and the circulation Φ strong. The absolute values of εNd point to the directions of flow. This concept does not include a possible impact of increasing NSW and SSW endmember volumes during glacials due to growing ice volume. This would result in dynamic changes of the mixing volume with climate, which would imply changes in the circulation Φ, while the recorded $\Delta\varepsilon$Nd value between the northern and southern sites remains similar. When the circulation collapses, water mass mixing of NSW and SSW is reduced and their difference in εNd at maximum. Thus, the gradient should be at the maximum value of $\Delta\varepsilon\mathrm{Nd}_{max} \simeq \frac{-3-(-15)}{8.6} \simeq 1.4$. In contrast, the circulation is assumed to be the strongest, when the difference in εNd of NSW and SSW is at minimum, yielding $\Delta\varepsilon\mathrm{Nd}_{min} \simeq \frac{-9-(-12)}{8.6} \simeq 0.4$. The here used εNd values for the maximum and minimum $\Delta\varepsilon$Nd are estimated from the εNd at the northern and southern locations of this study.

The underlying assumption that εNd changes linearly with the difference in latitude is a first order approximation, that only holds true for basin wide processes. It is

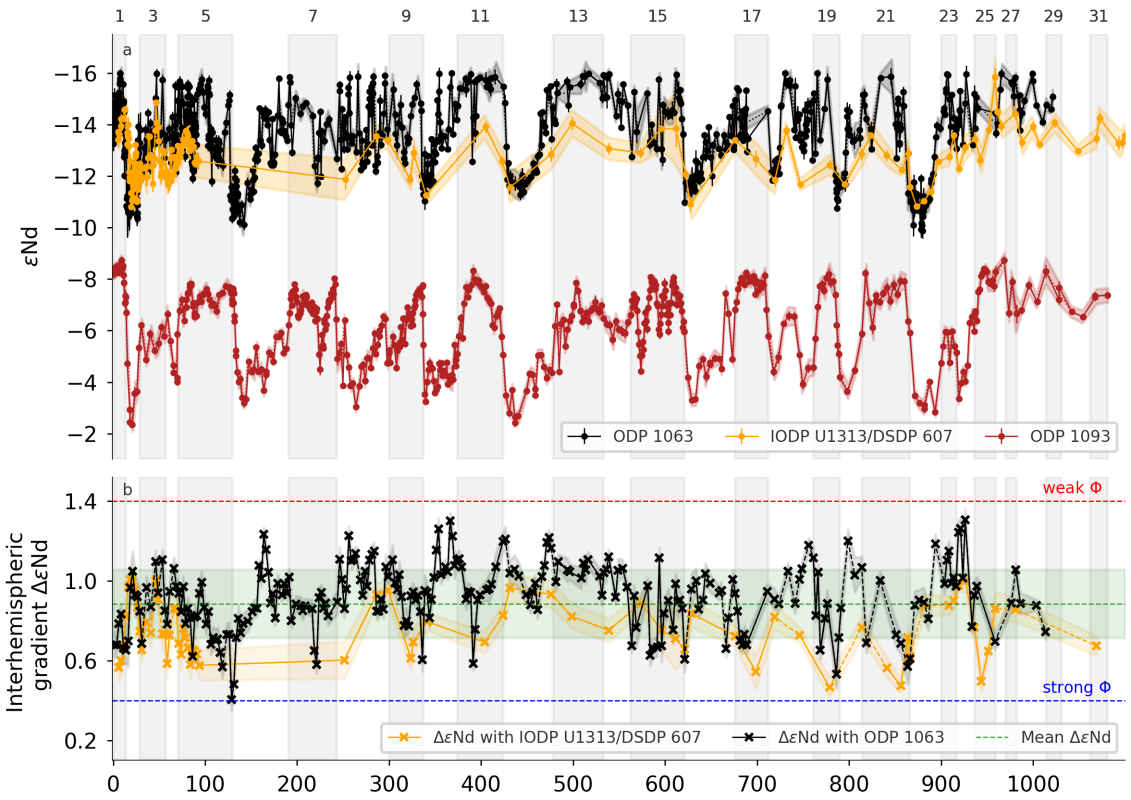

Figure 7.3.: εNd signatures in the North and South Atlantic Ocean and the resulting interhemispheric gradient ΔεNd. **(a)** εNd signatures at sites IODP U1313/DSDP 607 (Kim et al., 2021; Lang et al., 2016; Lippold et al., 2016; Pöppelmeier et al., 2021a), ODP 1063 (outliers excluded, Böhm et al., 2015; Gutjahr and Lippold, 2011; Jaume-Seguí et al., 2021; Link, 2021; Lippold et al., 2019; Roberts et al., 2010) and ODP 1093 (this study and Hallmaier et al. (2023a)). **(b)** The interhemispheric gradient ΔεNd calculated from IODP U1313/DSDP 607 and ODP 1063. The green dashed line and shaded area mark the mean ΔεNd (± SD). The red/blue dashed lines mark the maximum/minimum ΔεNd associated with a weak/strong circulation Φ.

based on the observation of the gradual change in εNd from North to South over the whole Atlantic Ocean. Potential influences of East-West gradients, frontal systems or very local processes are assumed to be averaged out along the dominant North-South pathway. In short distances high gradients are expected when crossing e.g. a frontal system. Further, it is assumed, that the Nd concentration has not changed dramatically over the averaged time span of 2.5 ka. Knowing this sensitivity to water mass exchange, an εNd prediction can be made, which is similar to the approach for modern seawater taken by Tachikawa (2003), who used an expectation value for the sediment Nd isotope composition, based on modern seawater as a predictor.

To calculate the gradient between εNd records of different resolution, a smoothed signal is obtained by forming the average εNd signature over a given time span for

the records. The time span is chosen to be 2.5 ka, as this time interval is close to the resolution of the εNd record, but large enough to average over very local processes. These smoothed εNd signatures thus reduce the effects on ΔεNd of single eventually locally dominated processes, regardless of their origin. In the following, the gradient ΔεNd was calculated using both Northern Hemisphere locations to ensure and compare the feasibility of the resulting ΔεNd. The obtained gradient ΔεNd with both Northern Hemisphere locations is displayed in Fig. 7.3 b. In the most recent past, where the data for IODP U1313/DSDP 607 is of equally high resolution as the data from ODP 1063, the ΔεNd records behave similarly. The obtained ΔεNd values are overall quite variable in a range from 0.41 to 1.31 ε-units per 10° latitude. Thus, they fall within the expected range for the gradient across the Atlantic. Further back in time the ΔεNd data is less variable due to the solely glacial-interglacial resolution of IODP U1313/DSDP 607. However, the overall variability of the gradient shows a noise-like behavior, which is especially uncorrelated with ice volume changes and thus the glacial-interglacial cycles.

On average the mean gradient of $\Delta\varepsilon\text{Nd} = 0.88 \pm 0.17$ ε-units per 10° latitude implies a moderately weaker circulation compared to the modern value of $\Delta\varepsilon\text{Nd} \simeq 0.5 \pm 0.1$ ε-units per 10° latitude, thus speaking for either a systematic offset or an overall weaker circulation. Given the assumption that the εNd signatures get more radiogenic further to the South, it is counter-intuitive, that the εNd data of IODP U1313/DSDP 607 always depicts more radiogenic values compared to ODP 1063. This behavior is assumed to be caused the low εNd data resolution of IODP U1313/DSDP 607 or the highly variable still unradiogenic signatures of ODP 1063, which were not excluded despite applying the filter of $\varepsilon\text{Nd} < -16$ to the data. This is reflected in the overall higher gradient values calculated from ODP 1063 compared to the ones calculated from IODP U1313/DSDP 607. In summary, neither of the εNd data sets are perfectly suitable for the gradient calculations due to low εNd resolution or local overprints of the water mass Nd isotopic composition.

There are numerous events standing out in their extreme sensitivity, that seem related to global climate change (Fig. 7.3 b). When ΔεNd approaches the maximum value of 1.4 ε-units per 10° latitude, the circulation seems at minimum, which occurs independent of the climate state. Lower εNd gradients always coincide with interglacials and advocate for a strong overturning. The unradiogenic εNd in the North and the South during theses times must reflect a North-South transport, as expected from northern deep convection. The lower ΔεNd, observed during the termination at the end of MIS 6, 10, 16 and 20 suggests, that the stronger export of AABW at the end of the glacial starts before the Northern Hemisphere circulation switches back to

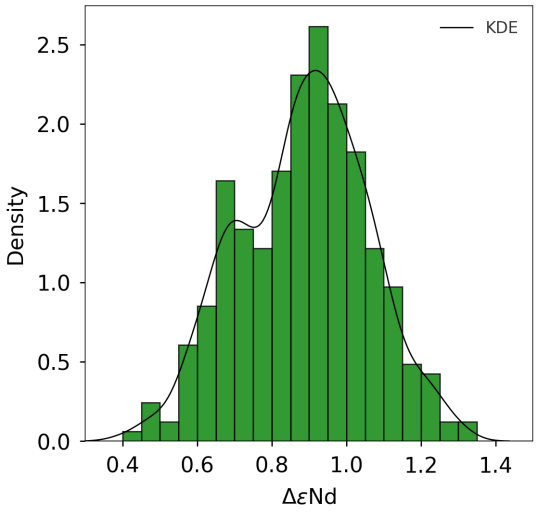

Figure 7.4.: Distribution of $\Delta\varepsilon$Nd values, obtained from both northern sites IODP U1313/DSDP 607 and ODP 1063 and the southern site ODP 1093.

the interglacial conditions. The Antarctic sea ice extent seems a plausible parameter, on which AABW export depends due to its impact on the sheer stress of the westerly winds and formation of polynas (Huang et al., 2020; Jochum and Eden, 2015; Sigman et al., 2010; Wilson et al., 2020). The different response of the hemispheres to the sudden change from glacials to interglacials accelerates the circulation temporarily, as also proposed in Friedrich et al. (2014). Conclusively, the climate stages favor certain patterns in the $\Delta\varepsilon$Nd behavior, however, both circulations stages may occur independent from climate. It cannot be fully excluded, that these punctual gradient variations may also be related to the age model uncertainty of ∼10 ka. Due to age uncertainties or different temporal resolutions both records may virtually appear more similar during terminations.

The distribution of the obtained $\Delta\varepsilon$Nd values from both northern locations points to two different circulation states (Fig. 7.4). The weaker circulation mode with $\Delta\varepsilon$Nd $\sim$ 0.9 ε-units per 10° latitude, is close to the mean gradient and more frequently observed. In contrast, the circulation is less often in the stronger mode with $\Delta\varepsilon$Nd $\sim$ 0.7 ε-units per 10° latitude. The broad distribution implies, that circulation strength was highly variable in the past 1 Ma, but even extreme circulation states did not persist for a long time. Note that the weaker mode may be observed more often due to the higher resolution and stronger variability of the εNd data at site ODP 1063. In summary, the findings could hint to a circulation bi-stability, but is also imply that the circulation state itself is not the cause of climate change.

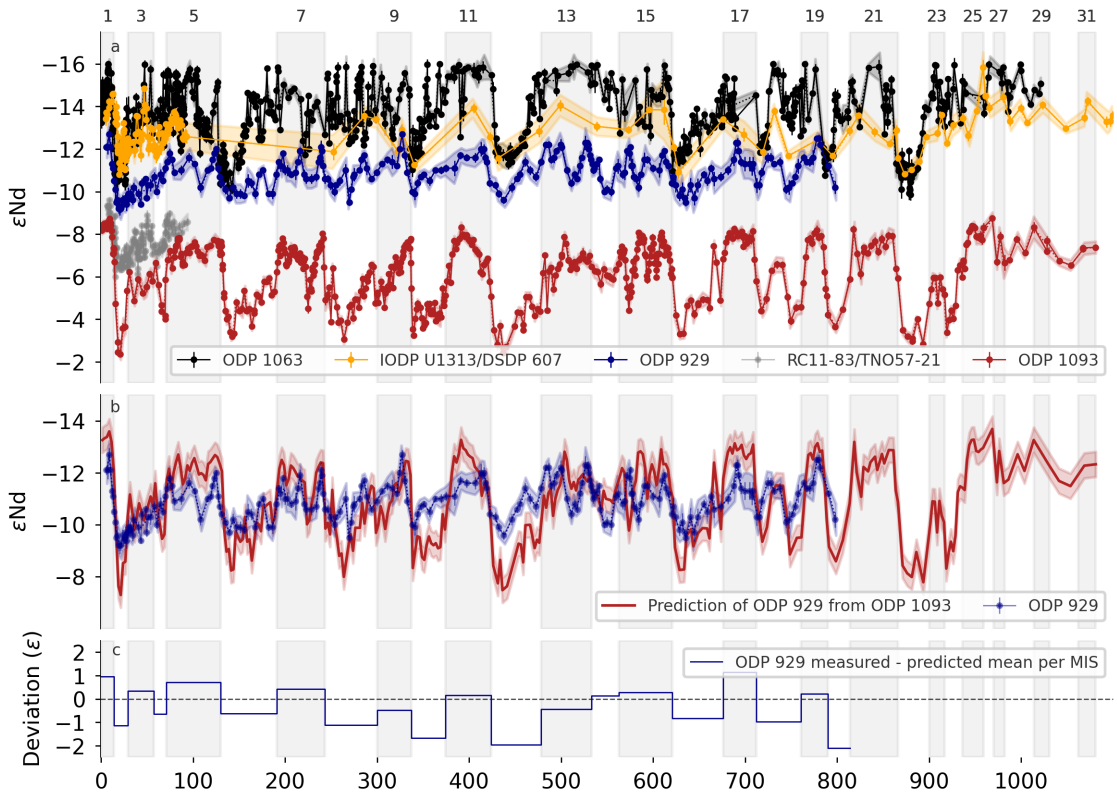

Figure 7.5.: εNd signatures across the Atlantic Ocean, the prediction of εNd signatures at site ODP 929 and their respective deviation from the measured εNd signatures. The grey shaded areas mark the MIS. **(a)** εNd signatures at sites IODP U1313/DSDP 607 (Kim et al., 2021; Lang et al., 2016; Lippold et al., 2016; Pöppelmeier et al., 2021a), ODP 1063 (Böhm et al., 2015; Gutjahr and Lippold, 2011; Jaume-Seguí et al., 2021; Link, 2021; Lippold et al., 2019; Roberts et al., 2010), ODP 929 (Howe and Piotrowski, 2017), the combined data of RC11-83 and TNO57-21 (Piotrowski et al., 2005) and ODP 1093 (this study and Hallmaier et al. (2023a)). **(b)** The prediction of the εNd signature of ODP 929 from the signature of ODP 1093 in comparison with the measurements of ODP 929.

7.3. Prediction of εNd Signatures in the Central Atlantic

Assuming a very consistent sensitivity to water mass changes over time, the mean gradient of $\Delta\varepsilon\text{Nd} = 0.88 \pm 0.17$ ε-units per 10° latitude is used for further estimations on εNd signatures across the Atlantic Ocean. Together with the εNd record at site ODP 1093 as southern boundary the neodymium isotopic signature of the Atlantic Ocean at any given site in between ODP 1093 and the chosen northern locations becomes predictable. The prediction is calculated as follows, with the error derived from the gradient's uncertainty and the mean uncertainty of the εNd measurements at site ODP 1093:

$$\varepsilon\mathrm{Nd}_{\mathrm{prediction}} = \varepsilon\mathrm{Nd}_{\mathrm{ODP\ 1093}} + \Delta\varepsilon\mathrm{Nd} \cdot (\text{latitudinal difference}/10°). \tag{7.2}$$

A resolution of the εNd data with at least one data point per 5 ka is favoured to compare the prediction and its accuracy with the respective measurement. The proposed method is applied and evaluated on the signature of ODP 929 at the Ceara Rise in the central Atlantic Ocean for which a quasi-millennial Nd isotope record exists (Howe and Piotrowski, 2017). The εNd record of site ODP 929 from the Central Atlantic reflects a glacial-interglacial pattern in a range between the εNd signatures of the northernmost sites and the southernmost site. It ranges from interglacial values of $\varepsilon\mathrm{Nd} = -12.5$ to more radiogenic values around $\varepsilon\mathrm{Nd} = -9.5$ during glacials (Fig. 7.5 a). Howe and Piotrowski (2017) state that the data reflects seawater εNd and is especially assumed to be free from modifications originating from i.e. benthic fluxes and particulate dissolution.

In Fig. 7.5 b the prediction and the measured εNd values of ODP 929 are displayed. The modelled εNd data is overall in coarse agreement with the measured signature of ODP 929. During all transitions between isotope stages the predicted and the measured signatures are similar within uncertainty. For a better comparison, the prediction with the measured εNd signature the deviation between both and its mean per MIS are calculated and displayed in Fig. 7.5 c. Positive values point to the actual values being more radiogenic than the prediction and vice versa. It becomes visible, that the measured signature during interglacials tends to be more radiogenic than the modelled prediction (positive deviation). During glacials the εNd signature of ODP 929 is more unradiogenic than the prediction (negative deviation), however MIS 14 forms the only exception to this.

The glacial behavior can be interpreted as a stronger NSW contribution at site ODP 929 during glacials than assumed from the model. Consequently, positive deviations of the measured ODP 929 εNd data from the model can be interpreted as a stronger influence of radiogenic SSW at site ODP 929 than predicted. This implies, that the SSW export is stronger during interglacials compared to the prediction. During glacials the opposite is observed. Consequently, SSW does not dominate the central Atlantic during glacials, which is in line with the findings of Friedrich et al. (2014) and a stable interhemispheric NSW and SSW export over glacial-interglacial cycles.

The sheer difference in size of the respective ocean basins must be considered when discussing the signature's evolution across the Atlantic. Due to the larger area of the

central Atlantic compared to the North and South Atlantic, the residence time and the travelled distance of water masses in the central Atlantic is much longer. Additionally, the high radiogenic predictions could also originate from an overestimation of the export of the benthic flux modified water mass into the central Atlantic. This would indicate that the regionally modified glacial bmDW still is stronger diluted when crossing the PF. The smoothed glacial signatures of the combined εNd record of sites RC11-83/TNO57-21 (Piotrowski et al., 2005) from the Cape Basin further support this finding (Fig. 7.5 a). Hence, glacial bmDW is less dominant in the vast basin of the central Atlantic during glacials. Thus, the strong variations in the Northern and the Southern Atlantic are smoothed out in the much larger central Atlantic basin explaining the two times smaller glacial-interglacial variations at site ODP 929 compared to the North and South. Considering the smoothing effects on the εNd signature within the basin, the prediction for the εNd signature at site ODP 929 is in line with the measured εNd record. This further emphasizes the balanced export of SSW and NSW through time.

7.4. Evaluation of Local Influences on ODP 1063

In the following, the mean εNd gradient is used to predict εNd signatures at site ODP 1063, following equation 7.2. The obtained record ideally reflects solely water mass changes and further can be used to evaluate the strongly unradiogenic εNd values. While the excursions to far more unradiogenic values than today's water masses can be associated with local influences quite easily, the less pronounced yet very variable signals are difficult to disentangle from the likely underlying water mass signal.

In Fig. 7.6 the prediction and the mean deviation from the measured εNd values of ODP 1063 are displayed. The predicted εNd data is overall in agreement with the measured signature of ODP 1063. The agreement is high for past 150 ka and also during the following glacial periods. Over this time interval less excursions toward unradiogenic Nd isotopic compositions are observed at site ODP 1063. The prediction from 150 to 560 ka is biased to more radiogenic values, especially during interglacials, where the previously described local effects on the εNd signatures occur. From 560 ka to 900 ka the unradiogenic excursions in the measured data are less visible, leading again to an agreement of ODP 1063 and its εNd prediction. During the time before the 900 ka event the prediction and the measured data show the highest difference. Three processes may cause strong deviations from the predicted values: Local unradiogenic overprints of authigenic εNd values, age model deviations and a non-linearity in the concept of the basin wide Nd isotope gradient.

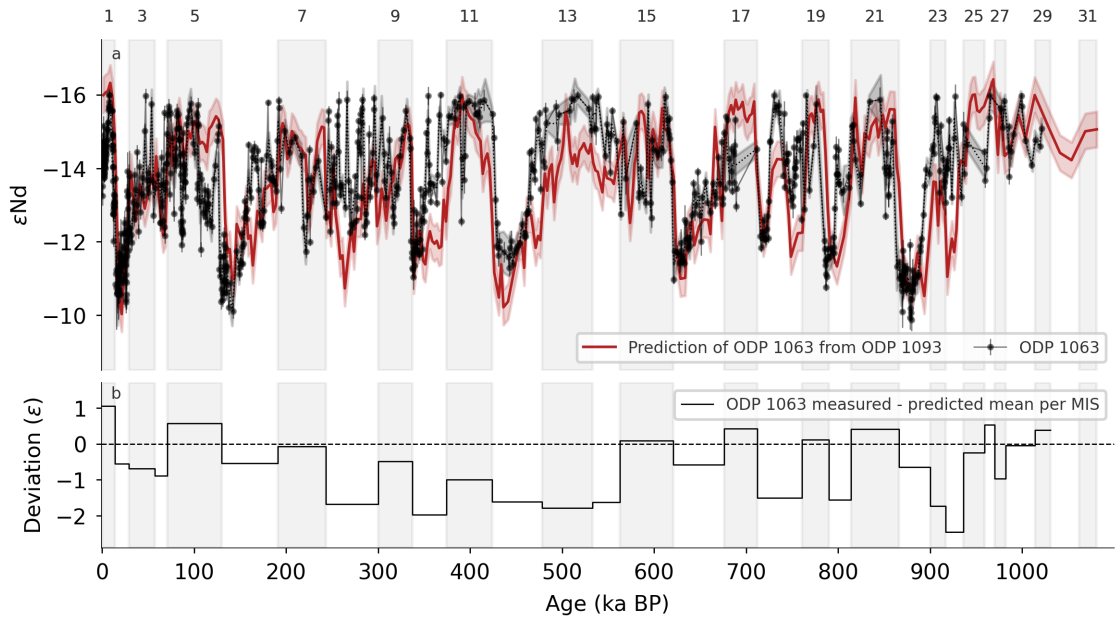

Figure 7.6.: The prediction of εNd signatures at site ODP 1063 and their respective deviation from the measured εNd signatures. **(a)** The prediction of the εNd signature of ODP 1063 (Böhm et al., 2015; Gutjahr and Lippold, 2011; Jaume-Seguí et al., 2021; Link, 2021; Lippold et al., 2019; Roberts et al., 2010), ODP 929 (Howe and Piotrowski, 2017) from the signature of ODP 1093 in comparison with the measurements of ODP 1063. **(b)** The mean deviation per MIS of the measurement from the prediction of ODP 1063.

The εNd origin at site ODP 1063 seems less variable during glacial times, which is here interpreted as dominant water mass origin. The interglacial predictions of ODP 1063 are assumed to be the result of water mass mixing, since the prediction for the central Atlantic was accurate and the εNd at site ODP 1093 is of water mass origin. Thus, especially for the past 150 ka and the timespan from 560 to 900 ka BP the prediction points to a strong and local overprint of the water mass signal at site ODP 1063. In contrast, the εNd signature in the timespan from 150 to 560 ka shows systematic differences between the prediction and the measurement, that cannot be caused solely by single unradiogenic excursions. In this time the interglacial values depict the most unradiogenic mean values pointing to a more comprehensive modification of the bottom water compared to the modern North Atlantic. However, the more unradiogenic baseline of the εNd signature and thus the stronger unradiogenic deviation from the prediction may also be caused by a stronger LSW or weaker SSW export during these times.

Similar to the prediction of site ODP 929, the difference between data and prediction of ODP 1063 can also originate from a dilution of the most radiogenic more regional southern signatures in the vast basin of the Atlantic Ocean, indicating non-

linear mixing due to e.g. Nd concentration gradients. Consequently, the highly radiogenic SSW signature gets stronger diluted across the whole Atlantic Ocean basin. Finally, the age model uncertainties of ODP 1093 cannot be ignored and may account for the deviations especially during terminations. In summary, these findings further support the ambiguous behavior of the εNd data at site ODP 1063, but they also strongly support the hypothesis of an underlying water mass signal that is partly veiled by dominating local effects at this site at least over the past 1 Ma.

7.5. Implications on Water Mass Export and Deep Ocean Circulation Strength

Circulation strength changes within the Atlantic and especially AMOC changes are of high research interest ever since. There are several other proxy and modelling studies used to reconstruct the AMOC over time, however, the focus is mainly on the LGM and the Holocene and within the central and North Atlantic. Thereby, a weakened export of NSW to the South, that inevitably goes along with a stronger export from SSW to the North, is interpreted as indicator for a weaker AMOC circulation.

These changes in water mass provenance are not only examined with Nd isotopic compositions but also by e.g. the nutrient based benthic stable carbon isotope proxy $\delta^{13}C$ (Duplessy et al., 1988; Lynch-Stieglitz, 2003; Pöppelmeier et al., 2023) or the particulate ratio of ^{231}Pa to ^{230}Th (Pa/Th), which is sensitive to changes in water mass advection at a given site and thus also allows for the reconstruction of circulation strength (Böhm et al., 2015; Lippold et al., 2012; Lynch-Stieglitz et al., 2007; Ng et al., 2018; Süfke et al., 2019). All these proxies have their own complex cycle and limitations when being interpreted regarding ocean dynamics. In fact, independent of observation or model-based reconstruction, the results do not yet draw a coherent picture on the changes in AMOC strength during the last climate cycle and some studies even contradict each other. The interpretations range from no significant AMOC change at all (Lynch-Stieglitz et al., 2007; Pöppelmeier et al., 2021b) to a differently pronounced weakening of the AMOC during the LGM (Böhm et al., 2015; Bradtmiller et al., 2014; Lippold et al., 2012; Pöppelmeier et al., 2021b; Süfke et al., 2019) or even a full collapse of the circulation (McManus et al., 2004). There are theories on the formation of two distinct circulation cells of the AMOC during glacials indicating an AMOC change mainly in mid-depths (Böhm et al., 2015; Hines et al., 2021).

The consideration of ODP 1093 as the southern basin endmember has wide impacts

on the overall interpretation of εNd signatures as indicator for circulation changes. Up until now for the SSW endmember a constant εNd signature was assumed (e.g. Howe and Piotrowski, 2017; Kim et al., 2021; Pena and Goldstein, 2014; Yehudai et al., 2021). This is based on the observation of the most radiogenic εNd values in the South Atlantic and less variable εNd signatures in the central Atlantic (Howe and Piotrowski, 2017). Before the here conducted work, no continuous εNd record south of the PF exceeding the penultimate glacial existed. However, a recent study indicates a variable southern εNd endmember south of the PF at least for the last 150 ka (Huang et al., 2020). In several former εNd studies on the central and North Atlantic, radiogenic glacial values are interpreted as a stronger SSW export into the deep North Atlantic and less or a shallower NADW export to the South (Farmer et al., 2019; Frank, 2002; Gutjahr et al., 2008; Howe and Piotrowski, 2017; Jaume-Seguí et al., 2021; Kim et al., 2021; Lang et al., 2016; Link, 2021; Lippold et al., 2016; Pena and Goldstein, 2014; Roberts and Piotrowski, 2015; Roberts et al., 2010; Tachikawa et al., 2017, 2021; Yehudai et al., 2021). Hence, a shoaling of the AMOC from the North was proposed.

Drawing conclusions for the whole AMOC with this proxy disregards changes in the shallower AMOC structures. The authigenic εNd records the characteristic deep water mass signature and has the ability to trace bottom water propagation, when neglecting benthic fluxes and other isotope exchange processes. Thus, changes in intermediate depth may not be reflected in the data. By implication, the εNd gradient rather reflects the deep ocean's circulation changes and may not entirely consider possible circulation changes in mid-depths and thus the AMOC as a whole. The findings of this study strongly contradict the assumption of a constant southern εNd endmember. It is characterized by a lower AABW export to the Atlantic and export of a stronger radiogenic water masses from the South Atlantic during glacials. Consequently, a similar export of SSW to the North Atlantic is able to cause a shift to more radiogenic northern values without a significant change in NSW export to the South or SSW export to the North. The observations in εNd signatures do not imply a significant change in NSW/SSW export over time, as also proposed by the εNd study of (Howe et al., 2016a). This is further supported by the results of proxy-model comparisons, which point to a similar volume of NSW in the LGM compared the Holocene (Gebbie, 2014). This in turn is reflected in a rather stable interhemispheric εNd gradient, which is in first order independent from glacial-interglacial climate variability.

While the variability is high and climate independent, there is no sign pointing to a persistent deep circulation weakening solely during glacial periods. Hence, stable Atlantic deep water dynamics are proposed for the past 1 Ma with a North-South

pathway being the leading but variable AMOC pattern. This is in line with the findings from several other studies and modern observations, that suggest a stable Atlantic deep water mass structure during the past 100 ka and a high present day variability (Du et al., 2016; Hines et al., 2021; Howe et al., 2016a; Latif et al., 2022; Pöppelmeier et al., 2020, 2021a). Nevertheless, when using authigenic Nd isotopes for water mass dynamic reconstructions, the residence time of Nd of ∼650 a and the εNd data resolution of a similar time span inhibits the recording of abrupt short-term changes. Especially, the glacial data of lower temporal resolution at site ODP 1093 and the few glacial-interglacial data points of IODP U1313/DSDP 607 may not reflect such changes. Additionally, the timescale for investigation of processes is restricted to the maximum resolution of the gradient of 2.5 ka. Note that a higher resolution of the time steps in the gradient calculation would lead to a higher uncertainty when using highly variable (ODP 1063) or εNd data of lower resolution (IODP U1313/DSDP 607).

The nutrient-based benthic stable carbon isotope proxy (δ^{13}C) in the North Atlantic records a similar story as the εNd records across the Atlantic with higher values during interglacials and lower values during glacials (Curry and Oppo, 2005; Keigwin, 2004; Keigwin and Swift, 2017). The δ^{13}C values of SSW are more depleted compared to NSW due to a larger sea ice extent (Marchitto and Broecker, 2006) and higher productivity from elevated dust fluxes (Jaccard et al., 2016). Thus, the lower carbon isotope values during glacials reflect SSW advances. However, lower δ^{13}C values may also be explained by increased remineralized carbon due to a more sluggish deep circulation (Hines et al., 2021; Howe et al., 2016a; Lynch-Stieglitz et al., 2007; Pöppelmeier et al., 2020). Furthermore, the change in carbon isotopic composition is assumed to additionally reflect an increase in carbon storage within the ocean (Tachikawa et al., 2021). This is in line with the proposed enhanced glacial carbon storage, as described in chapter 6.4. The findings from carbon isotopes suggest a pronounced glacial SSW expansion to the North Atlantic compared to today is not entirely necessary (Howe et al., 2016a; Pöppelmeier et al., 2020, 2021a). A possibly variable δ^{13}C northern and southern endmember has the potential to also account for carbon isotopic composition changes in the ocean. Similar as for εNd, carbon isotopes do not draw a coherent picture on the advance of SSW during glacials.

Studies of Pa/Th to reconstruct ocean circulation strength during the LGM record a more coherent story of a shoaling AMOC, yet to a variable extent (Gu et al., 2020; Lippold et al., 2012; Lynch-Stieglitz, 2017; Lynch-Stieglitz et al., 2007; Ng et al., 2018). The depth structure of Pa/Th data, however, supports the hypothesis of NSW being dominant in the North-Western Atlantic during the LGM rather than

SSW (Süfke et al., 2019). The data availability of Pa/Th is by far the sparsest and it is thus difficult to asses the circulation over the whole basin. Besides, the complex geochemical cycling of the mother element uranium of Pa and Th adds complications to the interpretation of Pa/Th. For example, particle fluxes and opal concentrations of sediments influence the respective Pa/Th ratios. Bradtmiller et al. (2014) filtered the data for both altering factors and came to the conclusion, that the data from the North Atlantic shows no significant circulation strength difference between the modern and LGM, although differences in depth and across the locations were apparent. In line with this, the possibility of a decoupling of the upper water masses and the deep ocean circulation was brought up from Pa/Th (Lynch-Stieglitz, 2017). This hypothesis of a depth dependent change in the circulation is further corroborated by combined εNd and δ^{13}C studies (Hines et al., 2021; Pöppelmeier et al., 2020) and sortable silt investigations (Spooner et al., 2018). This interpretation would also be consistent with the here recorded variable but climate independent deep ocean water mass export.

Yet, it still remains difficult to obtain a coherent picture from all the proxies but the results converge. Recent modelling studies tried to overcome this problem in a multi proxy model analysis to evaluate conflicting proxy evidence during the Holocene and LGM through direct model-data comparison (Gu et al., 2020; Pöppelmeier et al., 2023). As a result, the proxies' abilities to either reflect water mass provenance or circulation strength were determined yielding Pa/Th as best suiting tracer for circulation strength changes, δ^{13}C for water mass changes and εNd tracing both equally acceptable. Despite agreeing over the proxies's sensitivity to AMOC changes, both modelling studies are not in accordance with each other regarding circulation strength changes. However, these model studies are still based on a constant or less variable southern εNd basin endmember. It remains elusive how their would change with the knowledge of this work.

7.6. Conclusions

The here defined interhemispheric gradient $\Delta\varepsilon$Nd is a parameter of the sensitivity of water masses to Nd isotopic changes across the Atlantic Ocean over the past 1 Ma. The εNd variations in the North represented by sites ODP 1063 and IODP U1313/DSDP 607 and the southern Atlantic Ocean basin endmember ODP 1093 change in tandem with each other. The synchronous changes indicate a strong climate coupling of the εNd driving forces on the Northern and Southern Hemisphere. The gradient calculations yield a glacial-interglacial independent sensitivity over the past 1 Ma with a mean value of $\Delta\varepsilon\text{Nd} = 0.88 \pm 0.17$ ε-units/10° latitude. The ex-

pected maximum value is $\Delta\varepsilon\text{Nd}_{max} \simeq 1.4$, indicating the weakest circulation. The strongest circulation in reflected in a value of $\Delta\varepsilon\text{Nd}_{min} \simeq 0.4$. Lower $\Delta\varepsilon$Nd occur simultaneous to unradiogenic εNd in the Northern Hemisphere, which confirms the leading mode of deep convection. The observed variability stays within the expected ranges and is in first order climate independent, which is interpreted as only minor temporal variations in deep water exchange from the North and South. Thus, deep ocean circulation strength in between the investigated locations is assumed to be rather constant. Note, that the assumptions of a linear εNd change across the Atlantic and constant Nd concentrations over time were made here.

With this knowledge εNd signatures at central Atlantic site as ODP 929 become predictable. Taking the smoothing effects on the εNd signature within the basin into account, the prediction for central Atlantic signatures are in line with the measured εNd record. This further emphasizes the balanced export of SSW and NSW through time. With the prediction of the εNd signature at site OPD 1063, the veiled water mass signal could be further investigated and partly decoupled from the overlying erratic unradiogenic signal.

The observations of a stable mean εNd gradient holds true over the last 1 Ma and are likely a hint for the operation of the AMOC. Many studies on AMOC strength reconstructions do not yield conclusive results regarding strength and structure of the AMOC during glacial times. What is known, however, is the high internal variability and bi-stability of the AMOC regarding fresh water fluxes (Latif et al., 2022; Pöppelmeier et al., 2021b; Weijer et al., 2019). The use of εNd gradients to hint the AMOC strength variability cannot be fully exploited, due to the lack of chronological constraint and the solely two available 1 Ma records of millennial resolution. But the concept bears high potential to explore intra-basin deep circulation changes over such timespans. The results of this study advocate a balanced NSW and SSW export through climate changes with high internal dynamic over timescales of multiple millennia. Yet, the possible formation of two distinct circulation modes remains to be further investigated. The ongoing debate on AMOC changes, the discrepancies in the proxy and model results and the new southern εNd endmember give reason to further investigate the AMOC structure in mid-depths across the Atlantic Ocean basin in the past.

8. Mid Pleistocene Transition South of the Polar Front

In chapter 5 and 6 site ODP 1093 was identified as representative for the southern Atlantic Ocean basin εNd endmember. It turned out to be highly sensitive to critical climate parameters such as changes in ocean dynamics, ice coverage and atmospheric carbon dioxide. Consequently, the εNd record of 1 Ma has the potential to provide further information on the climatic changes during the late Mid Pleistocene Transition (MPT).

The εNd signature and its driving mechanism at site ODP 1094 reflect a special case. The change from lower to high variability in the εNd signature over the MPT points to linked changes in the cryosphere and seafloor volcanic activity.

8.1. εNd Signatures During the MPT South of the Polar Front

The MPT describes the change in climate cyclicity from 41 ka to 100 ka frequency. This change was gradual and took place within the timespan from approximately 1250-700 ka BP without any change in the orbital forcing (Fig. 8.1 a). However, the so called 900 ka event (Clark et al., 2006; Elderfield et al., 2012), accompanied by a proposed MPT-AMOC crisis (Pena and Goldstein, 2014), is rather abrupt and marked by the weak glacial-like interglacial MIS 23 and the first occurrence of the 100 ka cyclicity. The post-MPT phase describes the time from approximately 700 ka until today and the pre-MPT phase the time before 1250 ka BP. As described in chapter 2.1, there are multiple hypothesis that aim to explain the change in climate cyclicity.

Site ODP 1093 has a higher age model uncertainty and the lower resolution of a εNd data in the early phase of the MPT, thus, no absolute εNd values for individual MIS are discussed. The εNd data of ODP 1094 covers the 900 ka event and three shorter time intervals in post-MPT times. Despite the different origin of the εNd

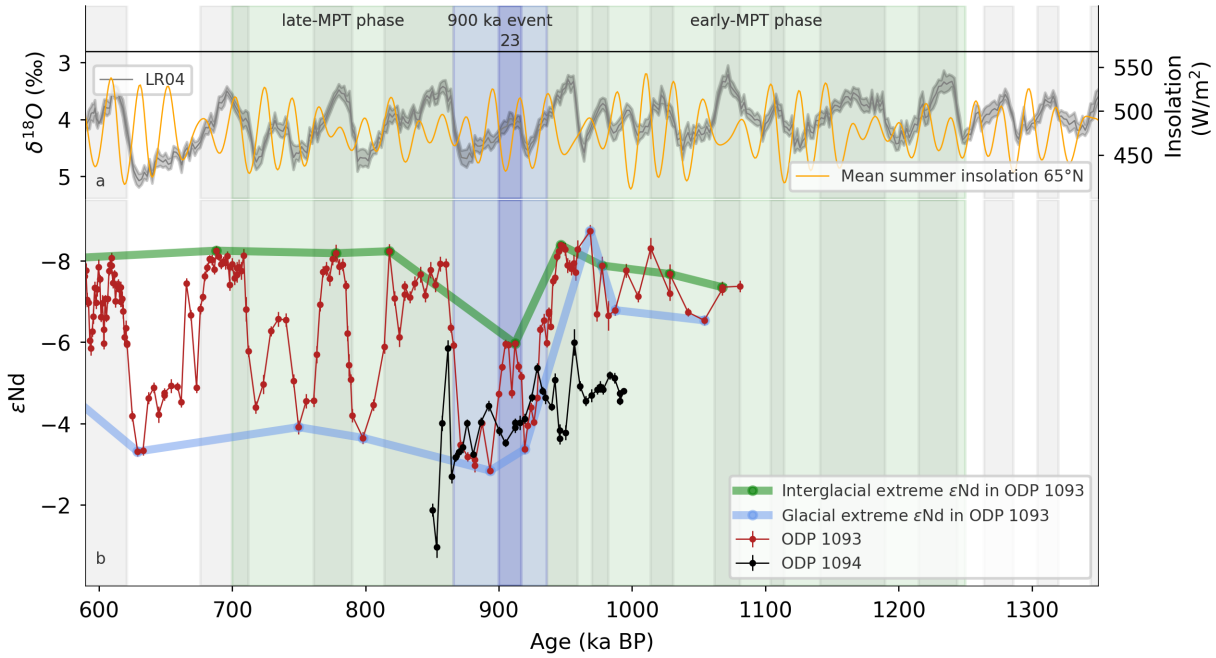

Figure 8.1.: εNd of site ODP 1093 and 1094 in context with solar insolation and the LR04 across the Mid Pleistocene Transition. The MPT is separated in the early and the later phase (green), the 900 ka event (lightblue) and MIS 23 (darkblue). **(a)** Benthic δ^{18}O stack (Lisiecki and Raymo, 2005) and mean 65°N summer insolation (Laskar et al., 2011). **(b)** εNd data of ODP 1093 and 1094 (this study and Hallmaier et al. (2023a)) with glacial (blue) and interglacial (green) extreme values (following Kim et al., 2021; Pena and Goldstein, 2014).

signatures at both sites, it is clearly visible that prior to the change in climate cyclicity the εNd variability was much smaller at both sites south of the PF (Fig. 8.1 b). In the early phase of the MPT at site ODP 1093 the difference between extreme climate conditions was approximately 2 ε-units, with εNd values between -8.5 and -6.5, thus in the range of modern AABW and CDW. Since water mass endmember εNd values unlikely change over the observed time (Frank, 2002), it is assumed that water mass mixing within the ACC took place in a similar way as in recent times. The low glacial-interglacial variability indicates that the origin of the εNd signature in the early phase of the MPT did not change drastically and was likely similar as in the Holocene. Thus, these observations point to a persistent AABW production even during glacials and no significant benthic overprint in the early-MPT phase.

In contrast, during the late-MPT phase, the glacial-interglacial variability in the εNd signature is more pronounced spanning approximately 6 ε-units. Thereby, the interglacial εNd signatures remain at the same level as in the early-MPT. The highly radiogenic εNd values at site ODP 1093 were first observed during the glacial MIS 24 and characterize all following glacials in the post-MPT. Hence, across the MPT a

significant change of the mechanisms dominating the Nd isotopic compositions south of the PF occurred. Moreover, at site ODP 1094, the 900 ka event is clearly marked too. The early-MPT is characterized by a low εNd variability with a trend toward radiogenic values of approximately $\varepsilon\text{Nd} = -4$. This behavior switches rather abruptly to the erratic system with random radiogenic excursions. The implications of the changes in Nd isotopic compositions at site ODP 1094 will be discussed separately at the end of this chapter. In summary, the observations at both sites support the leading hypothesis of a drastic change within the climate system around the 900 ka event, even visible south of the PF in the South Atlantic.

8.2. The 900 ka Event in the Southern Atlantic Ocean

The 900 ka event describes the first occurrence of a pronounced glacial (MIS 24) and the completed shift from the 41 ka to the 100 ka climate cyclicity observed in many different climate records. The interglacial MIS 23 is characterized by overall glacial-like conditions and together with the previous and following more pronounced glacials (MIS 24 and MIS 22) they form a glacial cycle similar to the glacial cycle of MIS 4,3 and 2 (Clark et al., 2006).The first occurrence of strongly radiogenic εNd values during the glacial MIS 24 is followed by the most radiogenic interglacial of MIS 23 at site ODP 1093 (Fig. 8.2 a). These radiogenic εNd values are untypical for previous and later interglacials. It is suggested, that these observations point to the first occurrence of a benthic flux dominating the bottom water in the southern Atlantic Ocean. This finding agrees with the low ACC speed reconstructions during the 900 ka event (Toyos et al., 2020). Especially MIS 23 stands out as an interglacial with exceptionally low ACC speeds similar to subsequent glacial times (Fig. 8.2 b).

In the early-MPT glacials the ACC strength at site PS97/093-2 is not significantly different compared to post-MPT (Toyos et al., 2020). In contrast, the late-MPT interglacials show somewhat higher $\overline{SS}$ data and are suggested to reflect a change in the position of the Southern Ocean fronts due to larger sea ice extent (Toyos et al., 2020). Lamy et al. (2024) reconstructed the ACC strength at multiple sites in the southern Pacific Ocean and observed a significant strengthening of the ACC during the post-MPT compared to pre-MPT times. Further, they came to the conclusion, that the link between a weaker ACC, equatorward shifted opal depositions and Southern Ocean fronts and glacial climate conditions with enhanced ocean carbon storage emerged for the first time over the MPT.

Following the discussion in chapter 6, the similar ACC strength reconstruction for glacials in pre and post-MPT times would imply a radiogenic εNd pattern in glacials

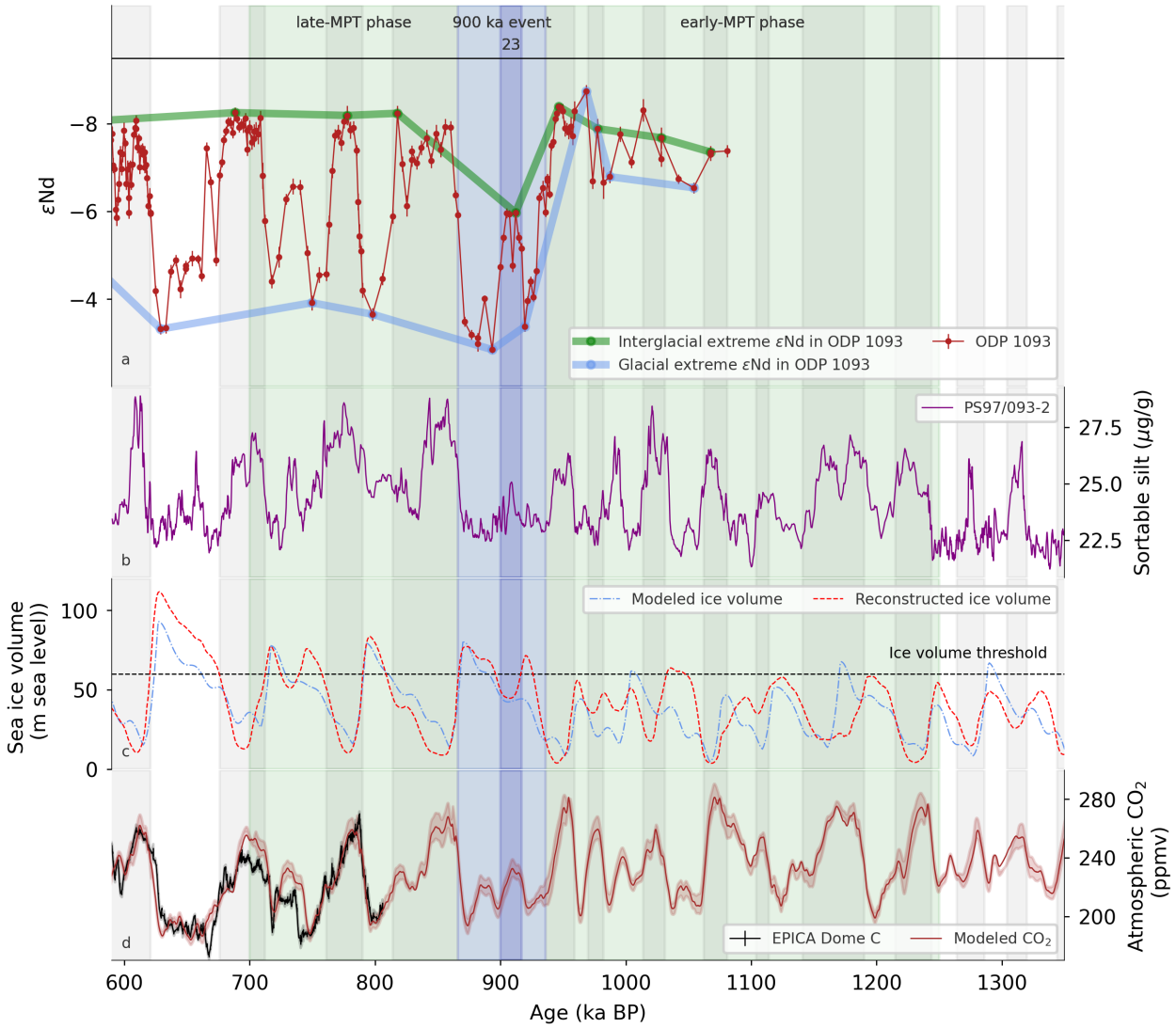

Figure 8.2.: εNd of site ODP 1093 and 1094 in context with various climate records across the Mid Pleistocene Transition. The MPT is separated in the early and the later phase (green), the 900 ka event (lightblue) and MIS 23 (darkblue). **(a)** εNd data of ODP 1093 and 1094 (this study and Hallmaier et al. (2023a)) with glacial (blue) and interglacial (green) extreme values (following Kim et al., 2021; Pena and Goldstein, 2014). **(b)** PS97/093-2 sortable silt from the Drake Passage (Toyos et al., 2020) as a measure for ACC strength. **(c)** Ice volume modeled (Legrain et al., 2023) and reconstructed from EPICA Dome C (Bereiter et al., 2015). **(d)** Atmospheric CO_2 reconstructed from EPICA Dome C (Bereiter et al., 2015) and modeled CO_2 (Berends et al., 2021).

of both early and late-MPT intervals. However, this behavior only emerged with the start of the 900 ka event at site ODP 1093. The discrepancy of expectation and data could indicate the possible shifts of the ACC fronts from the early-MPT to the post-MPT at site ODP 1093. The mitigation of the PF in the southern Atlantic Ocean was reconstructed from laminated diatom mat deposits at sites ODP 1094, 1093 and 1091, which recorded a shift from a more southern position in the early-MPT to a more northern position in the late-MPT (Kemp et al., 2010). Such process would lead to ODP 1093 being closer or farther from fronts such as the Polar Front, where flow speeds are generally higher (Orsi et al., 1995). These changes can not be recorded at site PS97/093-2, as it is within the center of flow in the Drake Passage (Toyos et al., 2020). Om shorter timescales the exact frontal shifts and ACC flow speed at site ODP 1093 remain elusive.

Following the interpretation of Huang et al. (2020) for the last glacial cycle, the radiogenic εNd values during the 900 ka event indicate, that AABW export was vanishing. The lack in AABW export during MIS 23 coincides with higher δ^{18}O values in LR04 (Lisiecki and Raymo, 2005) imlying more ice volume compared to other interglacials (Elderfield et al., 2012; Ford and Raymo, 2019; Kitamura and Kawagoe, 2006; Mudelsee and Schulz, 1997). This is in line with the low ACC speeds, which allow the build up of a high amount of sea ice (Lamy et al., 2024). Kim et al. (2021) identified MIS 38 and 23 as exceptionally radiogenic in the North Atlantic (Kim et al., 2021). During MIS 38 the size of the continental ice sheets in the Northern Hemisphere crossed a threshold, by reaching the coastlines and interacting with the ocean (Birner et al., 2016). The εNd data of ODP 1093 and the observations for MIS 23 across the Atlantic suggest that the 900 ka event was the time interval where such a threshold for the Southern Ocean was finally crossed. Recent model reconstructions of the global ice volume across the MPT, support this interpretation by showing a persistent ice sheet coverage over MIS 24, 23 and 22 with only low ice volume change in MIS 23 (Berends et al., 2021; Legrain et al., 2023). MIS 24 is the first glacial, in which the ice volume exceeded the maxima from early MPT times. Here, the maximum value in ice volume prior to the 900 ka event is considered as the threshold, which allows for the build up of even larger ice sheets in the following glacials. The interglacial MIS 23 is characterized by an ice volume comparable to the previous glacials. Thus, typical interglacial features were not fully developed, which is also reflected in the response of εNd to the change in ice volume cyclicity. Therefore, the observations for MIS 23 and 24 show the first time where continental ice sheets did not retreat within the 41 ka cyclicity as shown during the early MPT phase and before.

As discussed in chapter 6, sea ice cover and a weaker ACC promote a well stratified ocean. This slowed down the deep-to-surface circulation in the southern Atlantic Ocean shown in foraminiferal $\delta^{18}O$ data from the nearby site ODP 1094 over the MPT (Hasenfratz et al., 2019). The consequence is the first prolonged carbon storage in the ocean. Modelled and reconstructed global atmospheric CO_2 drawdown during the 900 ka event support this concept (Berends et al., 2021; Hönisch et al., 2009) (Fig. 8.2 c,d). The observations made here regarding the fist radiogenic εNd during the 900 ka event at site ODP 1093 can be interpreted as the first extended sea ice cover around Antarctica diminishing AABW production and export from the Weddell Sea.

8.3. Deep Water Exchange During the MPT

The interhemispheric εNd gradient across the Atlantic shows no particular climate variability during the past 1 Ma. Following the $\Delta\varepsilon$Nd concept as a hint to deep ocean circulation strength, an increase in the gradient would indicate a lower circulation strength and vice versa, respectively.

The gradient calculated from IODP U1313/DSDP 607 shows moderately higher values during the 900 ka event associated with MIS 22-24, if compared to the periods immediately before and after (Fig. 8.3 b). When using the gradient calculated from ODP 1063, $\Delta\varepsilon$Nd values across MIS 22-24 are very high up to $\Delta\varepsilon$Nd $\sim$ 1.2. This observations point to a very first AMOC reduction, but possibly not a full collapse, during MIS 22-24. The higher gradient values stem from the early rise in εNd values at site ODP 1093, which indicates, that a response to the MPT or its trigger likely originates on the Southern Hemisphere. At site ODP 1093 there is no data available for pre-MPT times, thus, it is not possible to evaluate the deep water circulation strength based on $\Delta\varepsilon$Nd before 1.1 Ma. In summary, the gradient $\Delta\varepsilon$Nd indicates the first significant decrease in circulation strength during the 900 ka event followed by the first occurrence of a significantly stronger circulation mode at the end of the 900 ka event.

The findings of this study do not directly support the leading hypothesis of several εNd studies across the Atlantic Ocean, that propose a significant weakening of the AMOC strength during glacials from the MPT onward. However, the first occurrence of more radiogenic εNd values compared to their respective early MPT values coincide with the 900 ka event at all investigated sites (Kim et al., 2021; Pena and Goldstein, 2014; Tachikawa et al., 2021; Yehudai et al., 2021) (Fig. 8.3 a). The radiogenic glacial values were interpreted as a stronger SSW export into the deep

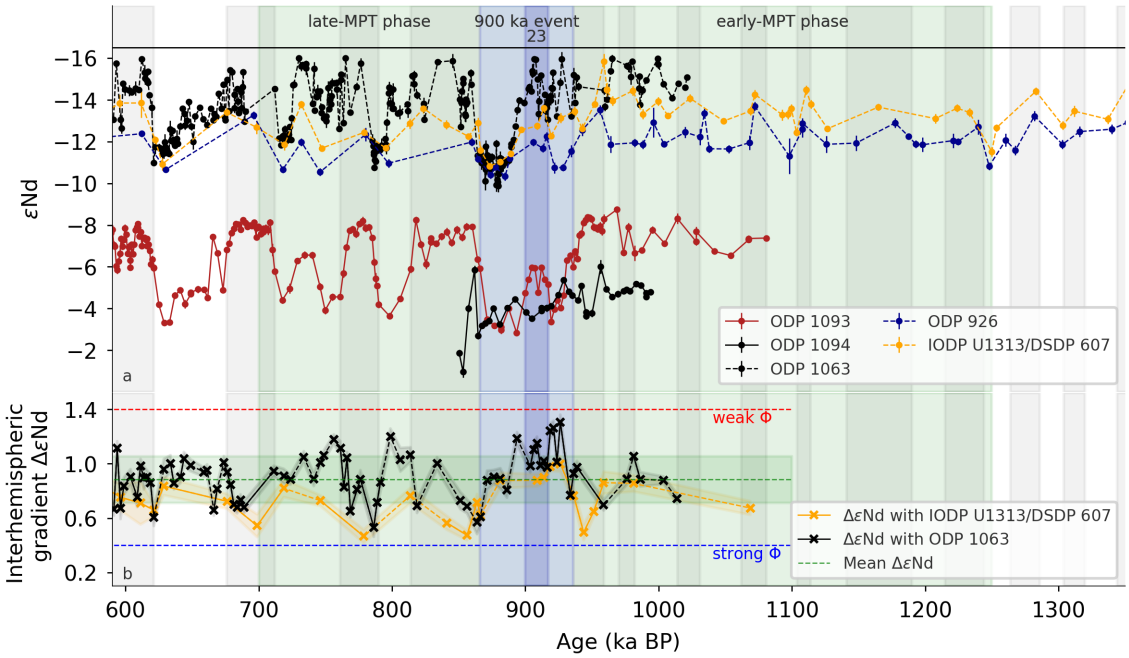

Figure 8.3.: εNd signatures across the Atlantic ocean in context with the $\Delta\varepsilon$Nd. **(a)** εNd signatures across the Atlantic from North to South: sites IODP U1313/DSDP 607 (Kim et al., 2021; Lang et al., 2016; Lippold et al., 2016; Pöppelmeier et al., 2021a), ODP 1063 (Böhm et al., 2015; Gutjahr and Lippold, 2011; Jaume-Seguí et al., 2021; Link, 2021; Lippold et al., 2019; Roberts et al., 2010), ODP 926 (Yehudai et al., 2021), the combined data of RC11-83 and TNO57-21 (Piotrowski et al., 2005) and ODP 1093 and 1094 (this study and Hallmaier et al. (2023a)). **(b)** The interhemispheric gradient $\Delta\varepsilon$Nd calculated from IODP U1313/DSDP 607 and ODP 1063. The green dashed line and shaded area mark the mean $\Delta\varepsilon$Nd ($\pm$ SD). The red/blue dashed lines mark the maximum/minimum $\Delta\varepsilon$Nd associated with a weak/strong circulation Φ.

North Atlantic and vice versa for unradiogenic interglacial times (Howe et al., 2016a; Kim et al., 2021; Pena and Goldstein, 2014; Pöppelmeier et al., 2021a). The 900 ka event indicates a collapse of the AMOC, labelled as the MPT-AMOC-crisis (Pena and Goldstein, 2014), leading to a weaker AMOC strength during glacials since the MPT (Kim et al., 2021; Pena and Goldstein, 2014; Tachikawa et al., 2021; Yehudai et al., 2021).

The new findings of chapter 6 and 7 show a climate variability in the Atlantic Ocean basin endmember from the 900 ka event until the Holocene. The εNd data of all sites, regardless of their location, present a uniform picture in Nd isotope signatures during the MPT. Even the highly debated record from ODP 1063 from the Bermuda Rise gives the same impression despite strong millennial variability (Link, 2021). Thus, all εNd records of the different sites across the Atlantic show a synchronous behavior of the onset of the production and export of a strongly radiogenic glacial water

mass south of the Antarctic PF in the Atlantic during glacials from the 900 ka event onward. The observations of the interhemispheric gradient point to a balanced NSW and SSW export even throughout the MPT. The AMOC seems interrupted for the first time by a strong decrease in circulation strength during the 900 ka event, which recovers quickly in the following MIS. In summary this hints, that the 900 ka event was the fist time major changes in AMOC strength occurred. It likely indicates the high internal variability and bi-stability of the AMOC developing over the MPT.

With the aim to find a connection between changes in ocean circulation during the MPT and the occurrence of radiogenic εNd values, different studies modelled the first occurrence of the highly radiogenic Nd isotopic signatures during the 900 ka event and the following interglacials. Based on the assumption of a stable SSW εNd endmember, these studies suggest, that the radiogenic εNd signatures across the Atlantic during the 900 ka event are best explained by a reduced NSW export (Friedrich et al., 2014; Rempfer et al., 2011; Tachikawa et al., 2020). However, as already implied by different modelling studies (Arsouze et al., 2008; Menviel et al., 2020) and proxy reconstructions (Du et al., 2020; Gutjahr et al., 2008; Pöppelmeier et al., 2020; Zhao et al., 2019) endmember changes can also cause the shift to radiogenic values. Furthermore, Tachikawa et al. (2021) modelled the seawater εNd modification under different circulation conditions and endmember changes of NSW (+4 ε-units) across the 900 ka event. Depending on the model scenario they came to the conclusion, that an εNd endmember change as well as a reduced AMOC have the ability to cause a decline in εNd values across the Atlantic Ocean and the 900 ka event. A reduced AMOC causes a clear positive shift in εNd signatures in the southern Atlantic Ocean (Tachikawa et al., 2021). However, even in combination with an NSW εNd endmember change, the decrease in εNd is not as pronounced as recorded in ODP 1093. This can partly be explained by the combination of advective-diffusive processes accounting for the εNd at site ODP 1093. Further, the model does not implement possible changes in the SSW endmember, which have shown to be as likely as changes in NSW (chapter 6). Thus, the models' response to a variable SSW εNd endmember and a highly variable interhemispheric deep water exchange are beneficial for a full understanding the εNd signatures over the MPT.

8.4. εNd in ODP 1094 as Possible Tracer for Volcanic Activity

Site ODP 1094 is dominated by a different mechanism driving the εNd signature compared to site ODP 1093 (chapter 6.3). At site ODP 1094 the 900 ka event clearly

marks the change from a rather low εNd variability to the erratic system in the εNd signatures. The early-MPT phase is characterized by a low εNd variability with a trend toward radiogenic values of approximately $\varepsilon\text{Nd} = -4$. This behavior switches rather abruptly with the end of the 900 ka event to the highly variable system with random radiogenic excursions observed in the data before the 900 ka event (Fig. 8.1 b). However, the sortable silt at site PS97/093-3 (Toyos et al., 2020) still records similar ACC flow speeds in the early-MPT. This suggests, that the close relation between ACC speed at the Drake Passage and the erratic εNd signatures only starts with the 900 ka event. Possible explanations for the εNd changes at site ODP 1094 during the 900 ka event follow the hypothesis of hydrothermal vents or even volcanic sources changing the Nd budget. The course of the εNd signature during the MPT could imply a significant change in volcanic activity at site ODP 1094 originating from the region of the Bouvet triple junction.

The hypothesis of a local or regional change in climate caused by volcanism was investigated by several studies (Crowley et al., 2015; Huybers and Langmuir, 2009; Longman et al., 2024; Lund and Asimow, 2011; Tolstoy, 2015). It has been shown, that tephra layers in marine sediments occur more often during interglacials pointing to an increased volcanic activity during warm periods (Huybers and Langmuir, 2009). The periodicity of the occurrence of these layers also matches with the frequency of orbital parameters (Longman et al., 2024; Lund and Asimow, 2011). Hereby, the glacial changes in the cryosphere, especially its components on continents like ice sheets and glaciers, play a major role in re-distributing pressure on the Earth's mantle. This in turn leads to an increase of melting within the mantle and a following pressure rise in magma chambers (Crowley et al., 2015; Huybers and Langmuir, 2009). During terminations, characterized by abrupt deglaciations, the pressure on the continental crust and thus magma chambers is suddenly released, leading to more volcanism during the following warm period (Longman et al., 2024). These processes are assumed to occur globally, however, it is only investigated in certain areas of the planet (Longman et al., 2024; Lund and Asimow, 2011). Modelling the influence of sea level and thus ice volume changes on mantle melting leads to similar conclusions for hydrothermal activities near ocean ridges in the Atlantic and Pacific (Lund and Asimow, 2011). The observed εNd signatures at site ODP 1094 are in line with these hypotheses pointing to stronger volcanogenic Nd inputs in interglacials in the late and post-MPT. In the early-MPT, when εNd signatures at site ODP 1094 were less variable, there was no sign for enhanced volcanic activities. This suggests, that the ice sheets during the early-MPT were not sufficiently large enough to trigger a high pressure on the crust in this triple junction region.

The start of the erratic behavior in εNd signatures coincides with the end of the first pronounced glacial of the 100 ka cyclicity. The ice volume built up during the first strong glacial MIS 24, the missing deglaciation in MIS 23 and the following glacial MIS 22 were significantly larger in ice volume compared to the early-MPT (Elderfield et al., 2012). Assuming a pressure dependent impact of the cryosphere on the mantle and therefore magma chambers, the resulting ice sheet extent induces a larger pressure within the mantle and higher melting rates compared to the glacials before. Consequently, during the following deglaciation, termination X, the pressure release by volcanic activity must have been more severe. Thus, the whole process and volcanic activity might be crucial in setting the stronger glacial-interglacial variablity post-MPT. In summary, the findings of this study during the 900 ka event hypothesize the crossing of a threshold regarding the local pressure on the mantle due to ice sheet built up. Thus, leading to enhanced submarine volcanic activity in the vicinity of ODP 1094 and locally modifying the Nd isotopic composition of the bottom water. Altogether, site ODP 1094 might serve as a key location to investigate the response of volcanism to changes of cryosphere in the past. Nevertheless, the discussed hypotheses are based on only few observations and still remain statistically insignificant.

8.5. Conclusions

During the 900 ka event the recorded Nd isotopic signatures at site ODP 1093 show that for the first time a large ice cover around Antarctica significantly inhibited AABW export from the Weddell Sea and shifted the ACC fronts further to the North. This strengthened the Southern Ocean stratification and yielded an efficient ocean carbon storage. The drawn picture is coherent with data from across the whole Atlantic Ocean basin, resulting in an increase in the interhemispheric εNd gradient and accordingly a potential collapse of the deep convection. The findings, however, are difficult to interpret regarding full AMOC strength variability, since marine deep sea sediments only record the deep water masses. Moreover, large uncertainties stem from chronologies and the linear mixing concept, which neglects local fronts and concentration changes. Nevertheless, the gradient supports a variable North-South deep water exchange in the Atlantic during the 900 ka event. These results are in line with modelled results, showing that both a reduced AMOC and a change in εNd endmember have the potential to cause strong radiogenic εNd signatures across the Atlantic.

The new εNd data allows the conclusion, that the change in the climate system is equally strong reflected in both hemispheres. The pronounced glacials from the 900

ka event on were triggered by globally occurring processes. While in the North the removal of regolith, the formation of stable continental ice sheets and changes in NSW export may have played a large role in cooling the planet (Willeit et al., 2019; Birner et al., 2016; Kim et al., 2021; Yehudai et al., 2021), the South contributed to this process with enhanced carbon storage in a more stratified ocean, an extending sea ice cover and efficient deep water export in the Atlantic (Berends et al., 2021; Hönisch et al., 2009; Legrain et al., 2023). The data of this study supports the importance of the processes occuring in the South. Given the first occurrence of radiogenic εNd data in the Southern Hemisphere, both processes in the North and South went hand in hand rather than changes in the North triggering processes in the South.

9. Concluding Summary and Outlook

At the start of this thesis no authigenic Nd record was available, which reflects the SSW endmember in the Atlantic over more than two glacial cycle. Here, the first authigenic εNd data of millennial resolution deep sea sediment in the Southern Atlantic at site ODP 1093 was presented. A second site in close vicinity, ODP 1094, was analysed over terminations I, II, MIS 11 and the MPT. The εNd of ODP 1093 yielded the first 1 Ma εNd benchmark in the southern Atlantic Ocean, which shows a variable behavior synchronous with climate variability. The observed εNd point to an interplay of advective and diffusive processes influencing the εNd signatures preserved in the authigenic coating at site ODP 1093. The hypothesis of an enhanced carbon storage and weaker AABW export in the Southern Ocean during glacial times (e.g. Huang et al., 2020; Yu et al., 2020) is further extended back to the MPT. The data at site ODP 1094 highlights the importance of local Nd fluxes modifying the bottom water signature and hints a possible link between local volcanic activity and global ice volume changes.

Age Model Development for ODP 1093

The interpretation of the εNd data was initially limited by the lack of a suitable age model for the past 1 Ma. The correlation of εNd with climate could be proven for the past 150 ka, since the δ^{18}O record of ODP 1093 is sufficient to be tied to a climate record. The age model determined by Kemp et al. (2010) seemed doubtful for this time span and thus also for the past 1 Ma. The low abundance of foraminifera before 150 ka inhibited the tuning of benthic δ^{18}O to the LR04 (Lisiecki and Raymo, 2005). Under the assumption, that strong climate correlation is persistent over time, the issue of extending the age model could be addressed. A new approach was used, in which age tie points were assigned based on the strong climate signal of εNd to respective patterns in the LR04. The B/M boundary determined from the sedimentary intensity and inclination of the magnetization (Channell and Stoner, 2002) was used as an external age tie point, to evaluate the reliability of the new method. The 900 ka event was clearly determined as the timing, where the high εNd variability of $\sim$6 ε-units emerged. For post-MPT the uncertainty of the new age model was assumed to be 10 ka, which resulted from the difference between termination I and

II in the new age model and the one determined by Kemp et al. (2010). Prior to the 900 ka event, assigning tie points was difficult due to the lower resolution of the εNd data. Consequently, during this time only the relative changes of data were further evaluated.

In conclusion, finding a suitable age model for ODP 1093 remains challenging. However, the authigenic εNd could be used to overcome the lack of foraminifera in deeper sediment depths. It is important to note that the base for the new age model was the observation of the strong correlation of εNd with climate in the first 150 ka.

Extraction of the Authigenic Nd

Prior to the discussion of εNd signatures and their implications on water mass provenance, the elemental ratios and REE patterns in the leachates of the processed sediment samples were analysed. The multielement measurement of the carbonate depleted sediment leachates of ODP 1093 and 1094 point to a dominant authigenic source of the extracted Nd in both cases. Non-hydrogenetic and especially detrital influences on the authigenic εNd signatures were concluded for samples with greater than 1 ‰ in Sr/Ca. The higher Al contents of silicate rich sediments, required the rise to ∼300 of the limit for Al/Nd ratios compared to the limit of ∼100 in carbonate rich sediments (Blaser et al., 2016; Huang et al., 2020). Comparing the HREE/LREE and MREE/MREE* ratios, single samples outside the bounds of leached and seawater samples of Martin et al. (2010) were observed. In total 15 samples in the past 450 ka were excluded from the records.

To test the applicability of the here proposed limits for elemental ratios in other sediments South of the PF, further multielement measurements and investigation of leaching procedures in other silicate rich sediments are required. Thus, studies of REE and element ratios in silicate rich sediments are of high interest.

ODP 1093 - 1 Ma εNd Benchmark South of the Polar Front

The authigenic Nd isotope record of site ODP 1093 shows a clear climate influenced pattern. During interglacial times ODP 1093 is bathed in lower CDW and its signature becomes the most unradiogenic with values of approximately of -8.5 to -6.5, which reflects present day water mass signatures (Tachikawa et al., 2017; Stichel et al., 2018). During glacials the most radiogenic signatures are recorded, yielding values between -4 and even -2 in the LGM. These signatures are far more radiogenic than any water mass recorded in the modern Atlantic Ocean (Tachikawa et al., 2017). The high εNd dynamic is unlikely entirely caused by water mass provenance

changes, especially during glacials. To further test the hypothesis of PSW accounting for the glacial radiogenic signatures, εNd studies at sites in the Drake Passage should provide further evidence on whether or not such a pathway and intrusion of Pacific waters in the Atlantic is feasible. Note, that the drawn conclusions remain the same, even if PSW would account for the glacial radiogenic signatures.

In fact, a combination of three different processes influencing the Nd budget was inferred most likely. These processes are: Advective water mass changes, regionally altering pore water flux of Nd and modulation of the advection-diffusion balance by ACC volume and speeds. The sediment composition and Patagonian dust can be excluded as main driver of the εNd signatures. The results point to the important role of the strong mixing capacity of the ACC, which modulates the strength of the diffusive overprint on the εNd signature. Weaker ACC strength and diminishing AABW production and export during glacials allow benthic fluxes to dominate the Nd isotopic composition of the bottom water mass. With higher ACC strength, it is more likely that advection accounts for εNd signatures recorded in the authigenic coating of site ODP 1093. In summary, ODP 1093 depicts the variable southern Atlantic Ocean basin εNd endmember, which changes synchronously with climate and interacts with the Atlantic Ocean basin, when passing the PF.

However, the interpretation of the data from site ODP 1093 is partly limited by the age model uncertainties. Moreover, the exact sedimentary processes, which cause the diffusive term in the Nd budget of carbonate depleted sediments south of the PF requires further investigations. The influence of pore fluids modifying the authigenic coating of silicate sediments could give further insight in the complexity of sedimentary fluxes acting as Nd sources in the ocean. More investigations on authigenic εNd in the southern Atlantic Ocean could give insights to confine the spatial extend of radiogenic modified water during glacials.

Despite remaining questions on the Nd budget, ODP 1093 serves as an εNd benchmark South of the PF, which reflects the southern Atlantic Ocean basin endmember.

Carbon Storage South of the Polar Front

The εNd signatures observed in ODP 1093 highlight the crucial role of the ACC and ice volume changes on water mass dynamics in the Southern Ocean. The results support the occurrence of a respired carbon rich, poorly ventilated water mass in the southern Atlantic Ocean during glacials prior to the LGM (Yu et al., 2020). The deep water export of these carbon rich water masses and their upwelling and outgassing from the ocean, have the potential to significantly influence the atmospheric carbon

budget. Thus, especially during terminations these processes bear the potential to contribute significantly to the abrupt climate changes in the past.

The investigation of deep water carbonate ion concentrations and benthic $\delta^{13}C$ south of the PF, would further contribute to examine the extent of the proposed carbon rich water mass in the past.

Volcanogenic influences in ODP 1094

The εNd signature at site ODP 1094 shows a highly variable climate independent signature. The most radiogenic values of ~ -1 are far beyond any water mass signature in the modern global ocean (Tachikawa et al., 2017). Site ODP 1094 is situated close to an active volcanic and hydrothermal area. Thus, the surrounding water masses are likely influenced by punctual scavenging of Nd and relabelling due to volcanic isotope exchange processes. Similar to ODP 1093, ACC flow speed changes lead to recurring volcanogenic overprints of the water masses at site ODP 1094.

The 900 ka event clearly marks the change from a rather low εNd variability to the erratic system of the εNd signatures. The early-MPT phase is characterized by a low εNd variability with a trend toward radiogenic values of approximately εNd $= -4$. These observations coincide with and increase in the ice volume during the MPT (Bereiter et al., 2015; Legrain et al., 2023). It was hypotesized, that this led to the crossing of a threshold in the local pressure on the mantle and therefore magma chambers leading to submarine volcanic activity in the vicinity of ODP 1094. This in turn has the potential to locally modify the Nd isotopic composition of the bottom water.

Altogether, site ODP 1094 might serve as a key location to investigate the response of volcanism to changes of cryosphere in the past. However, the discussed hypotheses are based on few observations and may remain statistically insignificant. Thus, the completion of the εNd record at site ODP 1094 is of high interest. Additionally, further investigations are required on volcanic activity in the Bouvet region and the origin of volcanogenic εNd signatures.

Atlantic Interhemispheric Gradient

A comparison of εNd records from sites across the Atlantic Ocean, revealed a similar pattern of radiogenic glacial and unradiogenic interglacial signatures. The change of εNd signatures across the Atlantic Ocean over time was examined via the εNd gradient $\Delta\varepsilon$Nd. The $\Delta\varepsilon$Nd serves as an indicator for the sensitivity of water masses

in the Atlantic to changes in εNd. This opened up the possibility to review proposed changes in the strength of deep ocean circulation with a variable εNd endmember. For the northern εNd endmember the two sites IODP U1313/DSDP 607 and ODP 1063 were considered, since they are the only available εNd records for the past 1 Ma. However, neither of the εNd data sets are perfectly suitable for the gradient calculations due to low εNd resolution (IODP U1313/DSDP 607) or local modifications of the water mass Nd isotopic composition (ODP 1063). For the southern reference ODP 1093 was chosen.

The resulting gradient values were within the expected $\Delta\varepsilon$Nd range of 0.4 to 1.4, with high $\Delta\varepsilon$Nd indicating weaker circulation strength and vice versa. The gradient shows a high variability around a mean value of $\Delta\varepsilon\text{Nd} = 0.88 \pm 0.17$ and is in first order climate independent. This holds true over the last 1 Ma and is likely a hint for the operation of the AMOC. The distribution of the $\Delta\varepsilon$Nd data points to two different circulations states, which could hint to a circulation bi-stability, but it also imples that the circulation state itself is not the cause of climate change. There is no sign pointing to a persistent deep circulation weakening solely during glacial periods. Hence, for the past 1 Ma stable Atlantic deep water dynamics are proposed with a North-South pathway being the leading but variable AMOC pattern. These results support the findings from several other studies and modern observations, that suggest a stable Atlantic deep water mass structure during the past 100 ka and a high present day variability (Du et al., 2016; Hines et al., 2021; Howe et al., 2016a; Latif et al., 2022; Pöppelmeier et al., 2020, 2021a). Nevertheless, it would be of high interest to evaluate the results of modelling studies with a variable southern εNd endmember.

The mean gradient was used to predict the εNd signatures at central Atlantic site ODP 929. Taking the smoothing effects on the εNd signature within the basin into account, the prediction for central Atlantic signatures are in line with the measured εNd record. This further emphasizes the balanced export of SSW and NSW through time. The veiled water mass signal at site OPD 1063 could partly be decoupled from the overlying erratic unradiogenic signal with the prediction of the εNd signature using the εNd gradient.

The ongoing debate on AMOC changes, the discrepancies in the proxy and model results and the new southern εNd endmember give reason to further investigate the AMOC structure across the Atlantic Ocean basin in the past. The use of εNd gradients, as hint to AMOC strength variability, bears high potential to explore intra-basin deep circulation changes. However it could not be fully exploited yet, due to the lack of chronological constraints in the southern endmember and the solely two available

1 Ma records of millennial resolution. The extension of IODP U1313/DSDP 607 to a millennial resolution would offer an opportunity to overcome this. Additionally, south of the PF the circulation tracer of benthic δ^{13}C would be of high interest. The $\Delta\delta^{13}$C gradient across the Atlantic Ocean could provide further insight in the evolution of the AMOC and its different operation modes.

In summary and despite the limitations the $\Delta\varepsilon$Nd gradient shows, that today's AMOC is in an exceptional strong state. Today strong AMOC is still in the range of natural AMOC variability of the past, however it is likely that this circulation will return back toward a more frequently observed weaker circulation state. This is in line with modern observations and models of a weakening of the AMOC within its natural variability (e.g. Latif et al., 2022; Weijer et al., 2019; Pöppelmeier et al., 2021b, 2023).

Ocean Circulation over the Mid Pleistocene Transition

The observation of a lower climate variability in εNd prior to the 900 ka event at site ODP 1093 are interpreted as indication for the first large ice cover around Antarctica, which significantly inhibited AABW export from the Weddell Sea, shifted the ACC fronts further to the North and caused an enhanced Southern Ocean carbon storage. This is in line with ice volume reconstructions showing a threshold crossing in MIS 24, when the first 100 ka ice volume cycle emerged (Bereiter et al., 2015; Legrain et al., 2023). The interhemispheric gradient $\Delta\varepsilon$Nd hints the first severe weakening of the circulation in the following glacial-like interglacial of MIS 23. This is coherent, with studies from the North Atlantic, which propose a full collapse of the AMOC during the 900 ka event. This event further marks the start of the high gradient variability, while prior to the 900 ka event the gradient shows less variability, however with a similar mean gradient.

To answer the question of how and why the MPT was triggered, the here obtained results further prove, that the change in the climate system is reflected in both hemispheres. The pronounced glacials from the 900 ka event onward were triggered by globally occuring processes. The observations of the interhemispheric gradient point to a balanced NSW and SSW export even throughout the MPT. The AMOC seems interrupted for the first time by a strong decrease in circulation strength during the 900 ka event, which recovers quickly in the MIS after. In summary the 900 ka event was shown to be the fist time major changes in AMOC strength occurred. It likely points to the high internal variability and bi-stability in the operation of the AMOC, which develops over the MPT.

Final remarks

In summary, this study demonstrates the potential but also the limitations of authigenic Nd isotopes, which both are still not fully exploited. The advective-diffusive processes of Nd in the ocean and especially their preservation in carbonate depleted sediments requires further understanding, to realise the full potential of Nd isotopes in the Southern Ocean. High resolution εNd data across all ocean basins are of high importance to reconstruct the global ocean circulation. In accomplishing these tasks, εNd isotope studies will provide valuable information on the processes behind climate changes in the past. Supplementary modeling studies, which reach farther back in time and implement the variable southern εNd endmember, will extend our knowledge on the Nd cycle and changes in ocean circulation in the past and the future.

Bibliography

Abbott, A., Löhr, S., Payne, A., Kumar, H., and Du, J. (2022). Widespread lithogenic control of marine authigenic neodymium isotope records? Implications for paleoceanographic reconstructions. *Geochimica et Cosmochimica Acta*, 319:318–336.

Abbott, A. N., Haley, B. A., and McManus, J. (2015a). Bottoms up: Sedimentary control of the deep North Pacific Ocean's εNd signature. *Geology*, 43(11):1035–1035.

Abbott, A. N., Haley, B. A., McManus, J., and Reimers, C. E. (2015b). The sedimentary flux of dissolved rare earth elements to the ocean. *Geochimica et Cosmochimica Acta*, 154:186–200.

Abbott, A. N., Löhr, S., and Trethewy, M. (2019). Are clay minerals the primary control on the oceanic rare earth element budget? *Frontiers in Marine Science*, 6:504.

Abelmann, A., Gersonde, R., Knorr, G., Zhang, X., Chapligin, B., Maier, E., Esper, O., Friedrichsen, H., Lohmann, G., Meyer, H., and Tiedemann, R. (2015). The seasonal sea-ice zone in the glacial Southern Ocean as a carbon sink. *Nature Communications*, 6(1):8136.

Adkins, J. F. (2013). The role of deep ocean circulation in setting glacial climates. *Paleoceanography*, 28(3):539–561.

Adkins, J. F., McIntyre, K., and Schrag, D. P. (2002). The salinity, temperature, and δ^{18}O of the glacial deep ocean. *Science*, 298(5599):1769–1773.

Ai, X. E., Thöle, L. M., Auderset, A., Schmitt, M., Moretti, S., Studer, A. S., Michel, E., Wegmann, M., Mazaud, A., Bijl, P. K., Sigman, D. M., Martínez-García, A., and Jaccard, S. L. (2024). The southward migration of the Antarctic Circumpolar Current enhanced oceanic degassing of carbon dioxide during the last two deglaciations. *Communications Earth Environment*, 5(1):58.

Anderson, R. F., Ali, S., Bradtmiller, L. I., Nielsen, S. H., Fleisher, M. Q., Anderson, B. E., and Burckle, L. H. (2009). Wind-driven upwelling in the Southern Ocean and the deglacial rise in atmospheric CO_2. *Science*, 323(5920):1443–8.

Arsouze, T., Dutay, J. C., Kageyama, M., Lacan, F., Alkama, R., Marti, O., and Jeandel, C. (2008). A modeling sensitivity study of the influence of the Atlantic meridional overturning circulation on neodymium isotopic composition at the Last Glacial Maximum. *Clim. Past*, 4(3):191–203.

Basak, C., Fröllje, H., Lamy, F., Gersonde, R., Benz, V., Anderson, R. F., Molina-Kescher, M., and Pahnke, K. (2018). Breakup of last glacial deep stratification in the South Pacific. *Science*, 359(6378):900–904.

Bayon, G., German, C., Boella, R., Milton, J., Taylor, R., and Nesbitt, R. (2002). An improved method for extracting marine sediment fractions and its application to Sr and Nd isotopic analysis. *Chemical Geology*, 187(3-4):179–199.

Bayon, G., German, C. R., Burton, K. W., Nesbitt, R. W., and Rogers, N. (2004). Sedimentary Fe–Mn oxyhydroxides as paleoceanographic archives and the role of aeolian flux in regulating oceanic dissolved REE. *Earth and Planetary Science Letters*, 224(3-4):477–492.

Bereiter, B., Eggleston, S., Schmitt, J., Nehrbass-Ahles, C., Stocker, T. F., Fischer, H., Kipfstuhl, S., and Chappellaz, J. (2015). Revision of the EPICA Dome C CO_2 record from 800 to 600 kyr before present. *Geophysical Research Letters*, 42(2):542–549.

Berends, C. J., de Boer, B., and van de Wal, R. S. W. (2021). Reconstructing the evolution of ice sheets, sea level, and atmospheric CO_2 during the past 3.6 million years. *Clim. Past*, 17(1):361–377.

Birner, B., Hodell, D., Tzedakis, P., and Skinner, L. (2016). Similar millennial climate variability on the Iberian margin during two early Pleistocene glacials and MIS 3. *Paleoceanography*, 31(1):203–217.

Blaser, P. (2017). *The application of radiogenic neodymium isotopes as a palaeo water mass tracer in the subpolar North Atlantic*. Dissertation.

Blaser, P., Gutjahr, M., Pöppelmeier, F., Frank, M., Kaboth-Bahr, S., and Lippold, J. (2020). Labrador Sea bottom water provenance and REE exchange during the past 35,000 years. *Earth and Planetary Science Letters*, 542.

Blaser, P., Lippold, J., Gutjahr, M., Frank, N., Link, J. M., and Frank, M. (2016). Extracting foraminiferal seawater Nd isotope signatures from bulk deep sea sediment by chemical leaching. *Chemical Geology*, 439:189–204.

Blaser, P., Pöppelmeier, F., Schulz, H., Gutjahr, M., Frank, M., Lippold, J., Heinrich, H., Link, J., Hoffmann, J., and Szidat, S. (2019). The resilience and sensitivity of

Northeast Atlantic deep water Nd to overprinting by detrital fluxes over the past 30,000 years. *Geochimica et Cosmochimica Acta*, 245:79–97.

Bradtmiller, L. I., McManus, J. F., and Robinson, L. F. (2014). 231Pa/230Th evidence for a weakened but persistent Atlantic meridional overturning circulation during Heinrich Stadial 1. *Nature communications*, 5(1):5817.

Broecker, W. S. (1987). The biggest chill. *Global Climate Change Linkages; Acid Rain, Air Quality, and Stratospheric Ozone*, pages 13–22.

Broecker, W. S. (1991). The Great Ocean Conveyor. *Oceanography*.

Brovkin, V., Ganopolski, A., Archer, D., and Rahmstorf, S. (2007). Lowering of glacial atmospheric CO_2 in response to changes in oceanic circulation and marine biogeochemistry. *Paleoceanography*, 22(4).

Burke, A. and Robinson, L. F. (2012). The Southern Ocean's role in carbon exchange during the last deglaciation. *Science*, 335(6068):557–61.

Böhm, E., Lippold, J., Gutjahr, M., Frank, M., Blaser, P., Antz, B., Fohlmeister, J., Frank, N., Andersen, M. B., and Deininger, M. (2015). Strong and deep Atlantic meridional overturning circulation during the last glacial cycle. *Nature*, 517(7532):73–6.

Chalk, T. B., Hain, M. P., Foster, G. L., Rohling, E. J., Sexton, P. F., Badger, M. P. S., Cherry, S. G., Hasenfratz, A. P., Haug, G. H., Jaccard, S. L., Martínez-García, A., Pälike, H., Pancost, R. D., and Wilson, P. A. (2017). Causes of ice age intensification across the Mid-Pleistocene Transition. *Proceedings of the National Academy of Sciences*, 114(50):13114–13119.

Channell, J. and Stoner, J. (2002). Plio-Pleistocene magnetic polarity stratigraphies and diagenetic magnetite dissolution at ODP Leg 177 Sites (1089, 1091, 1093 and 1094). *Marine Micropaleontology*, 45(3-4):269–290.

Charles, C. D., Froelich, P. N., Zibello, M. A., Mortlock, R. A., and Morley, J. J. (1991). Biogenic opal in Southern Ocean sediments over the last 450,000 years: Implications for surface water chemistry and circulation. *Paleoceanography*, 6(6):697–728.

Clark, P. U., Archer, D., Pollard, D., Blum, J. D., Rial, J. A., Brovkin, V., Mix, A. C., Pisias, N. G., and Roy, M. (2006). The middle Pleistocene transition: characteristics, mechanisms, and implications for long-term changes in atmospheric pCO_2. *Quaternary Science Reviews*, 25(23):3150–3184.

Clark, P. U. and Pollard, D. (1998). Origin of the middle Pleistocene transition by ice sheet erosion of regolith. *Paleoceanography*, 13(1):1–9.

Colin, C., Frank, N., Copard, K., and Douville, E. (2010). Neodymium isotopic composition of deep-sea corals from the NE Atlantic: implications for past hydrological changes during the Holocene. *Quaternary Science Reviews*, 29(19-20):2509–2517.

Copard, K., Colin, C., Douville, E., Freiwald, A., Gudmundsson, G., De Mol, B., and Frank, N. (2010). Nd isotopes in deep-sea corals in the North-eastern Atlantic. *Quaternary Science Reviews*, 29(19-20):2499–2508.

Copard, K., Colin, C., Henderson, G. M., Scholten, J., Douville, E., Sicre, M. A., and Frank, N. (2012). Late Holocene intermediate water variability in the northeastern Atlantic as recorded by deep-sea corals. *Earth and Planetary Science Letters*, 313-314:34–44.

Crowley, J. W., Katz, R. F., Huybers, P., Langmuir, C. H., and Park, S.-H. (2015). Glacial cycles drive variations in the production of oceanic crust. *Science*, 347(6227):1237–1240.

Curry, W. B. and Oppo, D. W. (2005). Glacial water mass geometry and the distribution of δ^{13}C of $\sum CO_2$ in the western Atlantic Ocean. *Paleoceanography*, 20(1).

Detlef, H., Belt, S. T., Sosdian, S. M., Smik, L., Lear, C. H., Hall, I. R., Cabedo-Sanz, P., Husum, K., and Kender, S. (2018). Sea ice dynamics across the Mid-Pleistocene transition in the Bering Sea. *Nature Communications*, 9(1):941.

Du, J., Haley, B. A., and Mix, A. C. (2016). Neodymium isotopes in authigenic phases, bottom waters and detrital sediments in the Gulf of Alaska and their implications for paleo-circulation reconstruction. *Geochimica et Cosmochimica Acta*, 193:14–35.

Du, J., Haley, B. A., and Mix, A. C. (2020). Evolution of the Global Overturning Circulation since the Last Glacial Maximum based on marine authigenic neodymium isotopes. *Quaternary Science Reviews*, 241.

Duplessy, J., Shackleton, N., Fairbanks, R., Labeyrie, L., Oppo, D., and Kallel, N. (1988). Deepwater source variations during the last climatic cycle and their impact on the global deepwater circulation. *Paleoceanography*, 3(3):343–360.

Elderfield, H., Ferretti, P., Greaves, M., Crowhurst, S., McCave, I. N., Hodell, D., and Piotrowski, A. M. (2012). Evolution of Ocean Temperature and Ice Volume Through the Mid-Pleistocene Climate Transition. *Science*, 337(6095):704–709.

Farmer, J. R., Hönisch, B., Haynes, L. L., Kroon, D., Jung, S., Ford, H. L., Raymo, M. E., Jaume-Seguí, M., Bell, D. B., Goldstein, S. L., Pena, L. D., Yehudai, M., and Kim, J. (2019). Deep atlantic ocean carbon storage and the rise of 100,000-year glacial cycles. *Nature Geoscience*, 12(5):355–360.

Flanagan, F. J. and Gottfried, D. (1980). USGS rock standards; III, Manganese-nodule reference samples USGS-Nod-A-1 and USGS-Nod-P-1. Report 2330-7102, US Govt. Print Off.

Ford, H. L. and Raymo, M. E. (2019). Regional and global signals in seawater δ^{18}O records across the mid-Pleistocene transition. *Geology*, 48(2):113–117.

Ford, H. L., Sosdian, S. M., Rosenthal, Y., and Raymo, M. E. (2016). Gradual and abrupt changes during the mid-pleistocene transition. *Quaternary Science Reviews*, 148:222–233.

Foster, G. L. and Vance, D. (2006). In situ Nd isotopic analysis of geological materials by laser ablation MC-ICP-MS. *Journal of Analytical Atomic Spectrometry*, 21(3):288–296.

Foster, G. L., Vance, D., and Prytulak, J. (2007). No change in the neodymium isotope composition of deep water exported from the North Atlantic on glacial-interglacial time scales. *Geology*, 35(1):37–40.

Frank, M. (2002). Radiogenic isotopes: Tracers of past ocean circulation and erosional input. *Reviews of Geophysics*, 40(1).

Frank, N. and Hemsing, F. (2021). Dating of corals and other geological samples via the radioactive disequilibrium of uranium and thorium isotopes. *Paleoclimatology*, pages 89–100.

Friedrich, T., Timmermann, A., Stichel, T., and Pahnke, K. (2014). Ocean circulation reconstructions from Nd: A model-based feasibility study. *Paleoceanography*, 29(11):1003–1023.

Frölicher, T. L., Sarmiento, J. L., Paynter, D. J., Dunne, J. P., Krasting, J. P., and Winton, M. (2015). Dominance of the southern ocean in anthropogenic carbon and heat uptake in cmip5 models. *Journal of Climate*, 28(2):862–886.

Gebbie, G. (2014). How much did glacial North Atlantic water shoal? *Paleoceanography*, 29(3):190–209.

German, C. R., Petersen, S., and Hannington, M. D. (2016). Hydrothermal exploration of mid-ocean ridges: Where might the largest sulfide deposits be forming? *Chemical Geology*, 420:114–126.

Gersonde, R., Crosta, X., Abelmann, A., and Armand, L. (2005). Sea-surface temperature and sea ice distribution of the Southern Ocean at the EPILOG Last Glacial Maximum—a circum-Antarctic view based on siliceous microfossil records. *Quaternary Science Reviews*, 24(7):869–896.

Gersonde, R., Hodell, D. A., and Blum, Peter, e. a. e. (1999). Leg 177 summary: Southern Ocean paleoceanography. *Proceedings of the Ocean Drilling Program, Initial Reports*.

Goldstein, S. L., O'Nions, R. K., and Hamilton, P. J. (1984). A Sm-Nd isotopic study of atmospheric dusts and particulates from major river systems. *Earth and Planetary Science Letters*, 70(2):221–236.

Gordon, A. L. (1986). Interocean exchange of thermocline water. *Journal of Geophysical Research: Oceans*, 91(C4):5037–5046.

Gottschalk, J., Skinner, L. C., Lippold, J., Vogel, H., Frank, N., Jaccard, S. L., and Waelbroeck, C. (2016). Biological and physical controls in the Southern Ocean on past millennial-scale atmospheric CO_2 changes. *Nature Communications*, 7(1):11539.

Gray, A. L. and Date, A. R. (1983). Inductively coupled plasma source mass spectrometry using continuum flow ion extraction. *Analyst*, 108(1290):1033–1050.

Gu, S., Liu, Z., Oppo, D. W., Lynch-Stieglitz, J., Jahn, A., Zhang, J., and Wu, L. (2020). Assessing the potential capability of reconstructing glacial Atlantic water masses and AMOC using multiple proxies in CESM. *Earth and Planetary Science Letters*, 541.

Gutjahr, M., Frank, M., Stirling, C. H., Keigwin, L. D., and Halliday, A. N. (2008). Tracing the Nd isotope evolution of North Atlantic Deep and Intermediate Waters in the western North Atlantic since the Last Glacial Maximum from Blake Ridge sediments. *Earth and Planetary Science Letters*, 266(1):61–77.

Gutjahr, M., Frank, M., Stirling, C. H., Klemm, V., Van de Flierdt, T., and Halliday, A. N. (2007). Reliable extraction of a deepwater trace metal isotope signal from Fe–Mn oxyhydroxide coatings of marine sediments. *Chemical Geology*, 242(3-4):351–370.

Gutjahr, M., Hoogakker, B. A. A., Frank, M., and McCave, I. N. (2010). Changes in North Atlantic Deep Water strength and bottom water masses during Marine Isotope Stage 3 (45–35kaBP). *Quaternary Science Reviews*, 29(19-20):2451–2461.

Gutjahr, M. and Lippold, J. (2011). Early arrival of Southern Source Water in the deep North Atlantic prior to Heinrich event 2. *Paleoceanography*, 26(2).

Haley, B. A., Du, J., Abbott, A. N., and McManus, J. (2017). The impact of benthic processes on rare earth element and neodymium isotope distributions in the oceans. *Frontiers in Marine Science*, 4:426.

Haley, B. A., Klinkhammer, G. P., and McManus, J. (2004). Rare earth elements in pore waters of marine sediments. *Geochimica et Cosmochimica Acta*, 68(6):1265–1279.

Haley, B. A., Wu, Y., Muratli, J. M., Basak, C., Pena, L. D., and Goldstein, S. L. (2021). Rare earth element and neodymium isotopes of the eastern US GEOTRACES Equatorial Pacific Zonal Transect (GP16). *Earth and Planetary Science Letters*, 576:117233.

Hallberg, R. and Gnanadesikan, A. (2006). The role of eddies in determining the structure and response of the wind-driven Southern Hemisphere overturning: Results from the Modeling Eddies in the Southern Ocean (MESO) project. *Journal of Physical Oceanography*, 36(12):2232–2252.

Hallmaier, M., Rückert, E., Link, J., Lütkes, L., and Frank, N. (2023a). Authigenic neodymium isotope data of sediment cores from the deep South Atlantic [Dataset].

Hallmaier, M., Rückert, E., Link, J., Lütkes, L., and Frank, N. (2023b). Large-scale Pacific-sourced intrusion into the glacial South Atlantic [Preprint].

Hamilton, P., O'nions, R., Bridgwater, D., and Nutman, A. (1983). Sm-Nd studies of Archaean metasediments and metavolcanics from West Greenland and their implications for the Earth's early history. *Earth and Planetary Science Letters*, 62(2):263–272.

Hasenfratz, A. P., Jaccard, S. L., Martínez-García, A., Sigman, D. M., Hodell, D. A., Vance, D., Bernasconi, S. M., Kleiven, H. F., Haumann, F. A., and Haug, G. H. (2019). The residence time of Southern Ocean surface waters and the 100,000-year ice age cycle. *Science*, 363(6431):1080–1084.

Henry, L. G., McManus, J. F., Curry, W. B., Roberts, N. L., Piotrowski, A. M., and Keigwin, L. D. (2016). North Atlantic ocean circulation and abrupt climate change during the last glaciation. *Science*, 353(6298):470–474.

Hines, S. K., Bolge, L., Goldstein, S. L., Charles, C. D., Hall, I. R., and Hemming, S. R. (2021). Little change in ice age water mass structure from Cape Basin

benthic neodymium and carbon isotopes. *Paleoceanography and Paleoclimatology*, 36(11):e2021PA004281.

Hines, S. K. V., Thompson, A. F., and Adkins, J. F. (2019). The Role of the Southern Ocean in Abrupt Transitions and Hysteresis in Glacial Ocean Circulation. *Paleoceanography and Paleoclimatology*, 34(4):490–510.

Hodell, D. A., C. C. D. C. J. H. M. P. G. N. U. S. and Venz, K. A. (2003). *Data report: Oxygen isotope stratigraphy of ODP Leg 177 Sites 1088, 1089, 1090, 1093, and 1094,*, volume 177.

Homoky, W. B., Weber, T., Berelson, W. M., Conway, T. M., Henderson, G. M., Van Hulten, M., Jeandel, C., Severmann, S., and Tagliabue, A. (2016). Quantifying trace element and isotope fluxes at the ocean–sediment boundary: a review. *Philosophical Transactions of the Royal Society A: Mathematical, Physical and Engineering Sciences*, 374(2081):20160246.

Houk, R. S., Fassel, V. A., Flesch, G. D., Svec, H. J., Gray, A. L., and Taylor, C. E. (1980). Inductively coupled argon plasma as an ion source for mass spectrometric determination of trace elements. *Analytical Chemistry*, 52(14):2283–2289.

Howe, J. N. W. and Piotrowski, A. M. (2017). Atlantic deep water provenance decoupled from atmospheric CO_2 concentration during the lukewarm interglacials. *Nature Communications*, 8(1):2003.

Howe, J. N. W., Piotrowski, A. M., Noble, T. L., Mulitza, S., Chiessi, C. M., and Bayon, G. (2016a). North Atlantic Deep Water Production during the Last Glacial Maximum. *Nature Communications*, 7.

Howe, J. N. W., Piotrowski, A. M., and Rennie, V. C. F. (2016b). Abyssal origin for the early Holocene pulse of unradiogenic neodymium isotopes in Atlantic seawater. *Geology*, 44(10):831–834.

Hu, R. and Piotrowski, A. M. (2018). Neodymium isotope evidence for glacial-interglacial variability of deepwater transit time in the Pacific Ocean. *Nature Communications*, 9(1):4709.

Huang, H., Gutjahr, M., Eisenhauer, A., and Kuhn, G. (2020). No detectable Weddell Sea Antarctic Bottom Water export during the Last and Penultimate Glacial Maximum. *Nature Communications*, 11(1):424.

Huang, H., Gutjahr, M., Kuhn, G., Hathorne, E. C., and Eisenhauer, A. (2021). Efficient Extraction of Past Seawater Pb and Nd Isotope Signatures From Southern Ocean Sediments. *Geochemistry, Geophysics, Geosystems*, 22(3):e2020GC009287.

Hughes, P. D., Gibbard, P. L., and Ehlers, J. (2020). The "missing glaciations" of the Middle Pleistocene. *Quaternary Research*, 96:161–183.

Huybers, P. and Langmuir, C. (2009). Feedback between deglaciation, volcanism, and atmospheric CO_2. *Earth and Planetary Science Letters*, 286(3):479–491.

Huybers, P. and Tziperman, E. (2008). Integrated summer insolation forcing and 40,000-year glacial cycles: The perspective from an ice-sheet/energy-balance model. *Paleoceanography*, 23(1).

Hönisch, B., Hemming, N. G., Archer, D., Siddall, M., and McManus, J. F. (2009). Atmospheric Carbon Dioxide Concentration Across the Mid-Pleistocene Transition. *Science*, 324(5934):1551–1554.

Jaccard, S. L., Galbraith, E. D., Martínez-García, A., and Anderson, R. F. (2016). Covariation of deep Southern Ocean oxygenation and atmospheric CO_2 through the last ice age. *Nature*, 530(7589):207–210.

Jaccard, S. L., Hayes, C. T., Martinez-Garcia, A., Hodell, D. A., Anderson, R. F., Sigman, D. M., and Haug, G. (2013). Two modes of change in Southern Ocean productivity over the past million years. *Science*, 339(6126):1419–1423.

Jacobsen, S. B. and Wasserburg, G. J. (1980). Sm-Nd isotopic evolution of chondrites. *Earth and Planetary Science Letters*, 50(1):139–155.

Janecek, T. R. (2001). (Table T1) Biogenic opal concentrations, ODP Hole 177-1093B.

Jaume-Seguí, M., Kim, J., Pena, L. D., Goldstein, S. L., Knudson, K. P., Yehudai, M., Hartman, A. E., Bolge, L., and Ferretti, P. (2021). Distinguishing glacial AMOC and interglacial non-AMOC Nd isotopic signals in the deep western Atlantic over the last 1 Myr. *Paleoceanography and Paleoclimatology*, 36(1):e2020PA003877.

Jeandel, C. (2016). Overview of the mechanisms that could explain the 'Boundary Exchange' at the land-ocean contact. *Philos Trans A Math Phys Eng Sci*, 374(2081).

Jeandel, C., Delattre, H., Grenier, M., Pradoux, C., and Lacan, F. (2013). Rare earth element concentrations and Nd isotopes in the Southeast Pacific Ocean. *Geochemistry, Geophysics, Geosystems*, 14(2):328–341.

Jochum, M. and Eden, C. (2015). The Connection between Southern Ocean Winds, the Atlantic Meridional Overturning Circulation, and Indo-Pacific Upwelling. *Journal of Climate*, 28(23):9250–9257.

Kanfoush, S. L., Hodell, D. A., Charles, C. D., Janecek, T. R., and Rack, F. R. (2002). Comparison of ice-rafted debris and physical properties in ODP Site 1094 (South Atlantic) with the Vostok ice core over the last four climatic cycles. *Palaeogeography, Palaeoclimatology, Palaeoecology*, 182(3-4):329–349.

Keigwin, L. D. (2004). Radiocarbon and stable isotope constraints on Last Glacial Maximum and Younger Dryas ventilation in the western North Atlantic. *Paleoceanography*, 19(4).

Keigwin, L. D. and Swift, S. A. (2017). Carbon isotope evidence for a northern source of deep water in the glacial western North Atlantic. *Proceedings of the National Academy of Sciences*, 114(11):2831–2835.

Kemp, A. E. S., Grigorov, I., Pearce, R. B., and Naveira Garabato, A. C. (2010). Migration of the Antarctic Polar Front through the mid-Pleistocene transition: evidence and climatic implications. *Quaternary Science Reviews*, 29(17):1993–2009.

Kender, S., Ravelo, A. C., Worne, S., Swann, G. E. A., Leng, M. J., Asahi, H., Becker, J., Detlef, H., Aiello, I. W., Andreasen, D., and Hall, I. R. (2018). Closure of the Bering Strait caused Mid-Pleistocene Transition cooling. *Nature Communications*, 9(1):5386.

Kim, J., Goldstein, S. L., Pena, L. D., Jaume-Seguí, M., Knudson, K. P., Yehudai, M., and Bolge, L. (2021). North Atlantic deep water during Pleistocene interglacials and glacials. *Quaternary Science Reviews*, 269:107146.

Kitamura, A. and Kawagoe, T. (2006). Eustatic sea-level change at the Mid-Pleistocene climate transition: new evidence from the shallow-marine sediment record of Japan. *Quaternary Science Reviews*, 25(3):323–335.

Klunder, M. B., Laan, P., Middag, R., De Baar, H. J. W., and van Ooijen, J. C. (2011). Dissolved iron in the Southern Ocean (Atlantic sector). *Deep Sea Research Part II: Topical Studies in Oceanography*, 58(25-26):2678–2694.

Kobayashi, H., Abe-Ouchi, A., and Oka, A. (2015). Role of Southern Ocean stratification in glacial atmospheric CO_2 reduction evaluated by a three-dimensional ocean general circulation model. *Paleoceanography*, 30(9):1202–1216.

Kraft, S., Frank, M., Hathorne, E. C., and Weldeab, S. (2013). Assessment of seawater Nd isotope signatures extracted from foraminiferal shells and authigenic phases of Gulf of Guinea sediments. *Geochimica et Cosmochimica Acta*, 121:414–435.

Kuhlbrodt, T., Griesel, A., Montoya, M., Levermann, A., Hofmann, M., and Rahmstorf, S. (2007). On the driving processes of the Atlantic meridional overturning circulation. *Reviews of Geophysics*, 45(2).

Lacan, F. and Jeandel, C. (2005). Neodymium isotopes as a new tool for quantifying exchange fluxes at the continent–ocean interface. *Earth and Planetary Science Letters*, 232(3-4):245–257.

Lacan, F., Tachikawa, K., and Jeandel, C. (2012). Neodymium isotopic composition of the oceans: A compilation of seawater data. *Chemical Geology*, 300-301:177–184.

Lal, D., Charles, C., Vacher, L., Goswami, J. N., Jull, A. J. T., McHargue, L., and Finkel, R. C. (2006). Paleo-ocean chemistry records in marine opal: Implications for fluxes of trace elements, cosmogenic nuclides (10Be and 26Al), and biological productivity. *Geochimica et Cosmochimica Acta*, 70(13):3275–3289.

Lamy, F., Gersonde, R., Winckler, G., Esper, O., Jaeschke, A., Kuhn, G., Ullermann, J., Martínez-Garcia, A., Lambert, F., and Kilian, R. (2014). Increased dust deposition in the Pacific Southern Ocean during glacial periods. *Science*, 343(6169):403–407.

Lamy, F., Winckler, G., Arz, H. W., Farmer, J. R., Gottschalk, J., Lembke-Jene, L., Middleton, J. L., van der Does, M., Tiedemann, R., Alvarez Zarikian, C., Basak, C., Brombacher, A., Dumm, L., Esper, O. M., Herbert, L. C., Iwasaki, S., Kreps, G., Lawson, V. J., Lo, L., Malinverno, E., Martinez-Garcia, A., Michel, E., Moretti, S., Moy, C. M., Ravelo, A. C., Riesselman, C. R., Saavedra-Pellitero, M., Sadatzki, H., Seo, I., Singh, R. K., Smith, R. A., Souza, A. L., Stoner, J. S., Toyos, M., de Oliveira, I. M. V. P., Wan, S., Wu, S., and Zhao, X. (2024). Five million years of Antarctic Circumpolar Current strength variability. *Nature*, 627(8005):789–796.

Lang, D. C., Bailey, I., Wilson, P. A., Chalk, T. B., Foster, G. L., and Gutjahr, M. (2016). Incursions of southern-sourced water into the deep North Atlantic during late Pliocene glacial intensification. *Nature Geoscience*, 9(5):375–379.

Laskar, J., Fienga, A., Gastineau, M., and Manche, H. (2011). La2010: a new orbital solution for the long-term motion of the Earth. *Astronomy Astrophysics*, 532:A89.

Latif, M., Sun, J., Visbeck, M., and Hadi Bordbar, M. (2022). Natural variability has dominated Atlantic Meridional Overturning Circulation since 1900. *Nature Climate Change*, 12(5):455–460.

Lawrence, K. T., Sosdian, S., White, H. E., and Rosenthal, Y. (2010). North Atlantic climate evolution through the Plio-Pleistocene climate transitions. *Earth and Planetary Science Letters*, 300(3):329–342.

Lear, C. H., Billups, K., Rickaby, R. E. M., Diester-Haass, L., Mawbey, E. M., and Sosdian, S. M. (2016). Breathing more deeply: Deep ocean carbon storage during the mid-Pleistocene climate transition. *Geology*, 44(12):1035–1038.

Lee, H., Calvin, K., Dasgupta, D., Krinner, G., Mukherji, A., Thorne, P., Trisos, C., Romero, J., Aldunce, P., Barret, K., et al. (2023). IPCC, 2023: Climate Change 2023: Synthesis Report, Summary for Policymakers. Contribution of Working Groups I, II and III to the Sixth Assessment Report of the Intergovernmental Panel on Climate Change [Core Writing Team, H. Lee and J. Romero (eds.)]. IPCC, Geneva, Switzerland.

Legrain, E., Parrenin, F., and Capron, E. (2023). A gradual change is more likely to have caused the Mid-Pleistocene Transition than an abrupt event. *Communications Earth Environment*, 4(1):90.

Lenton, T. M., Held, H., Kriegler, E., Hall, J. W., Lucht, W., Rahmstorf, S., and Schellnhuber, H. J. (2008). Tipping elements in the Earth's climate system. *Proceedings of the National Academy of Sciences*, 105(6):1786–1793.

Li, J., Tang, S., Zhu, X., and Pan, C. (2017). Production and certification of the reference material GSB 04-3258-2015 as a 143Nd/144Nd isotope ratio reference. *Geostandards and Geoanalytical Research*, 41(2):255–262.

Ligi, M., Bonatti, E., Bortoluzzi, G., Carrara, G., Fabretti, P., Gilod, D., Peyve, A. A., Skolotnev, S., and Turko, N. (1999). Bouvet triple junction in the South Atlantic: Geology and evolution. *Journal of Geophysical Research: Solid Earth*, 104(B12):29365–29385.

Link, J. M. (2021). *Atlantic Deep Circulation During Marine Isotope Stage 11 and the Last One Million Years Inferred From Neodymium Isotopes*. Dissertation.

Lippold, J., Gutjahr, M., Blaser, P., Christner, E., de Carvalho Ferreira, M. L., Mulitza, S., Christl, M., Wombacher, F., Böhm, E., and Antz, B. (2016). Deep water provenance and dynamics of the (de) glacial Atlantic meridional overturning circulation. *Earth and Planetary Science Letters*, 445:68–78.

Lippold, J., Luo, Y., Francois, R., Allen, S. E., Gherardi, J., Pichat, S., Hickey, B., and Schulz, H. (2012). Strength and geometry of the glacial Atlantic Meridional Overturning Circulation. *Nature Geoscience*, 5(11):813–816.

Lippold, J., Pöppelmeier, F., Süfke, F., Gutjahr, M., Goepfert, T. J., Blaser, P., Friedrich, O., Link, J. M., Wacker, L., Rheinberger, S., and Jaccard, S. L. (2019). Constraining the Variability of the Atlantic Meridional Overturning Circulation During the Holocene. *Geophysical Research Letters*, 46(20):11338–11346.

Lisiecki, L. E. (2010). Links between eccentricity forcing and the 100,000-year glacial cycle. *Nature Geoscience*, 3(5):349–352.

Lisiecki, L. E. and Raymo, M. E. (2005). A Pliocene-Pleistocene stack of 57 globally distributed benthic 18O records. *Paleoceanography*, 20(1):n/a–n/a.

Longman, J., Gernon, T., Hincks, T., Panitz, S., and Palmer, M. (2024). Intensified global volcanism during Late Pleistocene glacial strength shift.

Luais, B., Telouk, P., and Albaréde, F. (1997). Precise and accurate neodymium isotopic measurements by plasma-source mass spectrometry. *Geochimica et Cosmochimica Acta*, 61(22):4847–4854.

Lund, D. C. and Asimow, P. D. (2011). Does sea level influence mid-ocean ridge magmatism on Milankovitch timescales? *Geochemistry, Geophysics, Geosystems*, 12(12).

Lynch-Stieglitz, J. (2003). Tracers of Past Ocean Circulation. *Treatise on Geochemistry*, 6:625.

Lynch-Stieglitz, J. (2017). The Atlantic Meridional Overturning Circulation and Abrupt Climate Change. *Annual Review of Marine Science*, 9(1):83–104.

Lynch-Stieglitz, J., Adkins, J. F., Curry, W. B., Dokken, T., Hall, I. R., Herguera, J. C., Hirschi, J. J.-M., Ivanova, E. V., Kissel, C., and Marchal, O. (2007). Atlantic meridional overturning circulation during the Last Glacial Maximum. *science*, 316(5821):66–69.

Marchitto, T. M. and Broecker, W. S. (2006). Deep water mass geometry in the glacial Atlantic Ocean: A review of constraints from the paleonutrient proxy Cd/Ca. *Geochemistry, Geophysics, Geosystems*, 7(12).

Marshall, J. and Speer, K. (2012). Closure of the meridional overturning circulation through southern ocean upwelling. *Nature Geoscience*, 5(3):171–180.

Martin, E. and Scher, H. (2004). Preservation of seawater Sr and Nd isotopes in fossil fish teeth: bad news and good news. *Earth and Planetary Science Letters*, 220(1-2):25–39.

Martin, E. E., Blair, S. W., Kamenov, G. D., Scher, H. D., Bourbon, E., Basak, C., and Newkirk, D. N. (2010). Extraction of Nd isotopes from bulk deep sea sediments for paleoceanographic studies on Cenozoic time scales. *Chemical Geology*, 269(3-4):414–431.

Martin, E. E. and Haley, B. A. (2000). Fossil fish teeth as proxies for seawater Sr and Nd isotopes. *Geochimica et Cosmochimica Acta*, 64(5):835–847.

Martínez-García, A., Sigman, D. M., Ren, H., Anderson, R. F., Straub, M., Hodell, D. A., Jaccard, S. L., Eglinton, T. I., and Haug, G. H. (2014). Iron fertilization of the subantarctic ocean during the last ice age. *Science*, 343(6177):1347–1350.

McCave, I., Thornalley, D., and Hall, I. R. (2017). Relation of sortable silt grain-size to deep-sea current speeds: Calibration of the 'Mud Current Meter'. *Deep Sea Research Part I: Oceanographic Research Papers*, 127:1–12.

McManus, J. F., Francois, R., Gherardi, J. M., Keigwin, L. D., and Brown-Leger, S. (2004). Collapse and rapid resumption of Atlantic meridional circulation linked to deglacial climate changes. *Nature*, 428(6985):834–837.

Menviel, L., Spence, P., Skinner, L., Tachikawa, K., Friedrich, T., Missiaen, L., and Yu, J. (2020). Enhanced Mid-depth Southward Transport in the Northeast Atlantic at the Last Glacial Maximum Despite a Weaker AMOC. *Paleoceanography and Paleoclimatology*, 35(2):e2019PA003793.

Middag, R. d., De Baar, H., Laan, P., Cai, P. v., and Van Ooijen, J. (2011). Dissolved manganese in the Atlantic sector of the Southern Ocean. *Deep Sea Research Part II: Topical Studies in Oceanography*, 58(25-26):2661–2677.

Milankovitch, M. (1941). Canon of insolation and the iceage problem. *Koniglich Serbische Akademice Beograd Special Publication*, 132.

Molina-Kescher, M., Frank, M., and Hathorne, E. C. (2014). Nd and sr isotope compositions of different phases of surface sediments in the south pacific: Extraction of seawater signatures, boundary exchange, and detrital/dust provenance. *Geochemistry, Geophysics, Geosystems*, 15(9):3502–3520.

Mudelsee, M. and Schulz, M. (1997). The Mid-Pleistocene climate transition: onset of 100 ka cycle lags ice volume build-up by 280 ka. *Earth and Planetary Science Letters*, 151(1):117–123.

Nance, W. B. and Taylor, S. (1976). Rare earth element patterns and crustal evolution—I. Australian post-Archean sedimentary rocks. *Geochimica et Cosmochimica Acta*, 40(12):1539–1551.

Ng, H. C., Robinson, L. F., McManus, J. F., Mohamed, K. J., Jacobel, A. W., Ivanovic, R. F., Gregoire, L. J., and Chen, T. (2018). Coherent deglacial changes in western Atlantic Ocean circulation. *Nature Communications*, 9(1):2947.

Nielsen, S. H., Hodell, D., Kamenov, G., Guilderson, T., and Perfit, M. (2007). Origin and significance of ice-rafted detritus in the Atlantic sector of the Southern Ocean. *Geochemistry, Geophysics, Geosystems*, 8(12).

Noble, T., Rohling, E., Aitken, A., Bostock, H., Chase, Z., Gomez, N., Jong, L., King, M. A., Mackintosh, A., and McCormack, F. (2020). The sensitivity of the Antarctic ice sheet to a changing climate: Past, present, and future. *Reviews of Geophysics*, 58(4):e2019RG000663.

Noble, T. L., Piotrowski, A. M., Robinson, L. F., McManus, J. F., Hillenbrand, C.-D., and Bory, A. J. M. (2012). Greater supply of Patagonian-sourced detritus and transport by the ACC to the Atlantic sector of the Southern Ocean during the last glacial period. *Earth and Planetary Science Letters*, 317-318:374–385.

O'nions, R., Carter, S., Evensen, N., and Hamilton, P. (1979). Geochemical and cosmochemical applications of Nd isotope analysis. *Annual Review of Earth and Planetary Sciences*, 7(1):11–38.

O'nions, R., Hamilton, P., and Evensen, N. (1977). Variations in 143Nd/144Nd and 87Sr/86Sr ratios in oceanic basalts. *Earth and Planetary Science Letters*, 34(1):13–22.

Orsi, A. H., Whitworth, T., and Nowlin, W. D. (1995). On the meridional extent and fronts of the Antarctic Circumpolar Current. *Deep Sea Research Part I: Oceanographic Research Papers*, 42(5):641–673.

Paillard, D., Labeyrie, L., and Yiou, P. (1996). Macintosh program performs time-series analysis. *Eos, Transactions American Geophysical Union*, 77(39):379–379.

Pena, L. D. and Goldstein, S. L. (2014). Thermohaline circulation crisis and impacts during the mid-Pleistocene transition. *Science*, 345(6194):318–322.

Petit, J. R., Jouzel, J., Raynaud, D., Barkov, N. I., Barnola, J. M., Basile, I., Bender, M., Chappellaz, J., Davis, M., Delaygue, G., Delmotte, M., Kotlyakov, V. M., Legrand, M., Lipenkov, V. Y., Lorius, C., PÉpin, L., Ritz, C., Saltzman, E., and Stievenard, M. (1999). Climate and atmospheric history of the past 420,000 years from the Vostok ice core, Antarctica. *Nature*, 399(6735):429–436.

Piepgras, D., Wasserburg, G., and Dasch, E. (1979). The isotopic composition of Nd in different ocean masses. *Earth and Planetary Science Letters*, 45(2):223–236.

Pin, C., Briot, D., Bassin, C., and Poitrasson, F. (1994). Concomitant separation of strontium and samarium-neodymium for isotopic analysis in silicate samples, based on specific extraction chromatography. *Analytica Chimica Acta*, 298(2):209–217.

Piotrowski, A. M., Goldstein, S. L., Hemming, S. R., and Fairbanks, R. G. (2004). Intensification and variability of ocean thermohaline circulation through the last deglaciation. *Earth and Planetary Science Letters*, 225(1-2):205–220.

Piotrowski, A. M., Goldstein, S. L., Hemming, S. R., and Fairbanks, R. G. (2005). Temporal relationships of carbon cycling and ocean circulation at glacial boundaries. *Science*, 307(5717):1933–1938.

Pöppelmeier, F., Blaser, P., Gutjahr, M., Jaccard, S. L., Frank, M., Max, L., and Lippold, J. (2020). Northern-sourced water dominated the Atlantic Ocean during the Last Glacial Maximum. *Geology*, 48(8):826–829.

Pöppelmeier, F., Gutjahr, M., Blaser, P., Schulz, H., Süfke, F., and Lippold, J. (2021a). Stable Atlantic Deep Water Mass Sourcing on Glacial-Interglacial Timescales. *Geophysical Research Letters*, 48(15):e2021GL092722.

Pöppelmeier, F., Jeltsch-Thömmes, A., Lippold, J., Joos, F., and Stocker, T. F. (2023). Multi-proxy constraints on Atlantic circulation dynamics since the last ice age. *Nature Geoscience*, 16(4):349–356.

Pöppelmeier, F., Lippold, J., Blaser, P., Gutjahr, M., Frank, M., and Stocker, T. F. (2022). Neodymium isotopes as a paleo-water mass tracer: A model-data reassessment. *Quaternary Science Reviews*, 279:107404.

Pöppelmeier, F., Scheen, J., Jeltsch-Thömmes, A., and Stocker, T. F. (2021b). Simulated stability of the Atlantic meridional overturning circulation during the last glacial maximum. *Climate of the Past*, 17(2):615–632.

Rahmstorf, S. (2002). Ocean circulation and climate during the past 120,000 years. *Nature*, 419(6903):207–214.

Rahmstorf, S. (2006). Thermohaline ocean circulation. *Encyclopedia of quaternary sciences*, 5.

Raymo, M., Oppo, D., and Curry, W. (1997). The mid-Pleistocene climate transition: A deep sea carbon isotopic perspective. *Paleoceanography*, 12(4):546–559.

Raymo, M. E., Lisiecki, L. E., and Nisancioglu, K. H. (2006). Plio-Pleistocene Ice Volume, Antarctic Climate, and the Global 18O Record. *Science*, 313(5786):492–495.

Rempfer, J., Stocker, T. F., Joos, F., Dutay, J.-C., and Siddall, M. (2011). Modelling Nd-isotopes with a coarse resolution ocean circulation model: Sensitivities to model parameters and source/sink distributions. *Geochimica et Cosmochimica Acta*, 75(20):5927–5950.

Rintoul, S. R. (2018). The global influence of localized dynamics in the Southern Ocean. *Nature*, 558(7709):209–218.

Roberts, N. L. and Piotrowski, A. M. (2015). Radiogenic Nd isotope labeling of the northern NE Atlantic during MIS 2. *Earth and Planetary Science Letters*, 423:125–133.

Roberts, N. L., Piotrowski, A. M., Elderfield, H., Eglinton, T. I., and Lomas, M. W. (2012). Rare earth element association with foraminifera. *Geochimica et Cosmochimica Acta*, 94:57–71.

Roberts, N. L., Piotrowski, A. M., McManus, J. F., and Keigwin, L. D. (2010). Synchronous deglacial overturning and water mass source changes. *Science*, 327(5961):75–78.

Robinson, L. F., Adkins, J. F., Frank, N., Gagnon, A. C., Prouty, N. G., Brendan Roark, E., and de Flierdt, T. v. (2014). The geochemistry of deep-sea coral skeletons: A review of vital effects and applications for palaeoceanography. *Deep Sea Research Part II: Topical Studies in Oceanography*, 99:184–198.

Robinson, L. F. and van de Flierdt, T. (2009). Southern Ocean evidence for reduced export of North Atlantic Deep Water during Heinrich event 1. *Geology*, 37(3):195–198.

Robinson, S., Ivanovic, R., van de Flierdt, T., Blanchet, C. L., Tachikawa, K., Martin, E. E., Cook, C. P., Williams, T., Gregoire, L., Plancherel, Y., Jeandel, C., and Arsouze, T. (2021). Global continental and marine detrital Nd: An updated compilation for use in understanding marine Nd cycling. *Chemical Geology*, 567.

Roy-Barman, M. and Jeandel, C. (2016). *Marine geochemistry: ocean circulation, carbon cycle and climate change*. Oxford University Press.

Rutberg, R. L., Hemming, S. R., and Goldstein, S. L. (2000). Reduced North Atlantic Deep Water flux to the glacial Southern Ocean inferred from neodymium isotope ratios. *Nature*, 405(6789):935–938.

Rückert, E. (2020). *Hochpräzisionsmessungen von Neodymisotopen an einem Massenspektrometer mit induktiv gekoppeltem Plasma*. Thesis for first state examination.

Schlitzer, R. (2019). *Ocean Data View. https://odv.awi.de*.

Schneider-Mor, A., Yam, R., Bianchi, C., Kunz-Pirrung, M., Gersonde, R., and Shemesh, A. (2005). Climate-L10704-Diatom stable isotopes, sea ice presence and sea surface temperature records of the past 640 ka in the Atlantic sector of the Southern Ocean. *Geophysical Research Letters*, 32(10).

Schneider-Mor, A., Yam, R., Bianchi, C., Kunz-Pirrung, M., Gersonde, R., and Shemesh, A. (2008). Nutrient regime at the siliceous belt of the Atlantic sector of the Southern Ocean during the past 660 ka. *Paleoceanography*, 23(3):n/a–n/a.

Shi, J.-R., Talley, L. D., Xie, S.-P., Peng, Q., and Liu, W. (2021). Ocean warming and accelerating Southern Ocean zonal flow. *Nature Climate Change*, 11(12):1090–1097.

Shoenfelt, E. M., Winckler, G., Lamy, F., Anderson, R. F., and Bostick, B. C. (2018). Highly bioavailable dust-borne iron delivered to the Southern Ocean during glacial periods. *Proceedings of the National Academy of Sciences*, 115(44):11180–11185.

Sigman, D. M., Hain, M. P., and Haug, G. H. (2010). The polar ocean and glacial cycles in atmospheric CO_2 concentration. *Nature*, 466(7302):47–55.

Singer, B. S., Jicha, B. R., Mochizuki, N., and Coe, R. S. (2019). Synchronizing volcanic, sedimentary, and ice core records of Earth's last magnetic polarity reversal. *Science Advances*, 5(8):eaaw4621.

Skinner, L. C., Scrivner, A. E., Vance, D., Barker, S., Fallon, S., and Waelbroeck, C. (2013). North Atlantic versus Southern Ocean contributions to a deglacial surge in deep ocean ventilation. *Geology*, 41(6):667–670.

Spooner, P. T., Thornalley, D. J., and Ellis, P. (2018). Grain size constraints on glacial circulation in the Southwest Atlantic. *Paleoceanography and Paleoclimatology*, 33(1):21–30.

Stichel, T., Frank, M., Rickli, J., and Haley, B. A. (2012). The hafnium and neodymium isotope composition of seawater in the Atlantic sector of the Southern Ocean. *Earth and Planetary Science Letters*, 317-318:282–294.

Stichel, T., Pahnke, K., Duggan, B., Goldstein, S. L., Hartman, A. E., Paffrath, R., and Scher, H. D. (2018). TAG Plume: Revisiting the Hydrothermal Neodymium Contribution to Seawater. *Frontiers in Marine Science*, 5.

Struve, T., Longman, J., Zander, M., Lamy, F., Winckler, G., and Pahnke, K. (2022). Systematic changes in circumpolar dust transport to the Subantarctic Pacific Ocean over the last two glacial cycles. *Proceedings of the National Academy of Sciences*, 119(47):e2206085119.

Struve, T., Pahnke, K., Lamy, F., Wengler, M., Böning, P., and Winckler, G. (2020a). A circumpolar dust conveyor in the glacial Southern Ocean. *Nature Communications*, 11(1):5655.

Struve, T., Wilson, D. J., van de Flierdt, T., Pratt, N., and Crocket, K. C. (2020b). Middle Holocene expansion of Pacific Deep Water into the Southern Ocean. *Proc Natl Acad Sci U S A*, 117(2):889–894.

Süfke, F., Pöppelmeier, F., Goepfert, T. J., Regelous, M., Koutsodendris, A., Blaser, P., Gutjahr, M., and Lippold, J. (2019). Constraints on the northwestern Atlantic deep water circulation from 231Pa/230Th during the last 30,000 years. *Paleoceanography and Paleoclimatology*, 34(12):1945–1958.

Tachikawa, K. (2003). Neodymium budget in the modern ocean and paleo-oceanographic implications. *Journal of Geophysical Research*, 108(C8).

Tachikawa, K., Arsouze, T., Bayon, G., Bory, A., Colin, C., Dutay, J.-C., Frank, N., Giraud, X., Gourlan, A. T., Jeandel, C., Lacan, F., Meynadier, L., Montagna, P., Piotrowski, A. M., Plancherel, Y., Pucéat, E., Roy-Barman, M., and Waelbroeck, C. (2017). The large-scale evolution of neodymium isotopic composition in the global modern and Holocene ocean revealed from seawater and archive data. *Chemical Geology*, 457:131–148.

Tachikawa, K., Jeandel, C., and Roy-Barman, M. (1999). A new approach to the Nd residence time in the ocean: the role of atmospheric inputs. *Earth and Planetary Science Letters*, 170(4):433–446.

Tachikawa, K., Piotrowski, A. M., and Bayon, G. (2014). Neodymium associated with foraminiferal carbonate as a recorder of seawater isotopic signatures. *Quaternary Science Reviews*, 88:1–13.

Tachikawa, K., Rapuc, W., Dubois-Dauphin, Q., Guihou, A., and Skonieczny, C. (2020). Reconstruction of ocean circulation based on neodymium isotopic composition. *Oceanography*, 33(2):80–87.

Tachikawa, K., Rapuc, W., Vidal, L., Dubois-Dauphin, Q., Westerhold, T., Guihou, A., Bickert, T., Pérez-Asensio, J. N., Deschamps, P., and Skonieczny, C. (2021). Eastern Atlantic deep-water circulation and carbon storage inferred from neodymium and carbon isotopic compositions over the past 1.1 million years. *Quaternary Science Reviews*, 252.

Talley, L. D. (2013). Closure of the Global Overturning Circulation Through the Indian, Pacific, and Southern Oceans: Schematics and Transports. *Oceanography*, 26(1):80–97.

Tanaka, T., Togashi, S., Kamioka, H., Amakawa, H., Kagami, H., Hamamoto, T., Yuhara, M., Orihashi, Y., Yoneda, S., Shimizu, H., Kunimaru, T., Takahashi, K.,

Yanagi, T., Nakano, T., Fujimaki, H., Shinjo, R., Asahara, Y., Tanimizu, M., and Dragusanu, C. (2000). JNdi-1: a neodymium isotopic reference in consistency with LaJolla neodymium. *Chemical Geology*, 168(3):279–281.

Thermo Fisher Scientific (2009). *Neptune Plus Hardware Manual*.

Tian, Q., Liu, D., Yuan, P., Li, M., Yang, W., Zhou, J., Wei, H., Zhou, J., and Guo, H. (2022). Occurrence of structural aluminium (Al) in marine diatom biological silica: visible evidence from microscopic analysis. *Ocean Science*, 18(2):321–329.

Toggweiler, J. R., Russell, J. L., and Carson, S. R. (2006). Midlatitude westerlies, atmospheric $\{CO_2, and climate change during the ice ages. Paleoceanography$, 21(2).

Tolstoy, M. (2015). Mid-ocean ridge eruptions as a climate valve. *Geophysical Research Letters*, 42(5):1346–1351.

Toyos, M. H., Lamy, F., Lange, C. B., Lembke-Jene, L., Saavedra-Pellitero, M., Esper, O., and Arz, H. W. (2020). Antarctic Circumpolar Current dynamics at the Pacific entrance to the Drake Passage over the past 1.3 million years. *Paleoceanography and Paleoclimatology*, 35(7):e2019PA003773.

van de Flierdt, T., Griffiths, A. M., Lambelet, M., Little, S. H., Stichel, T., and Wilson, D. J. (2016). Neodymium in the oceans: a global database, a regional comparison and implications for palaeoceanographic research. *Philos Trans A Math Phys Eng Sci*, 374(2081).

van de Flierdt, T., Robinson, L. F., and Adkins, J. F. (2010). Deep-sea coral aragonite as a recorder for the neodymium isotopic composition of seawater. *Geochimica et Cosmochimica Acta*, 74(21):6014–6032.

van de Flierdt, T., Robinson, L. F., Adkins, J. F., Hemming, S. R., and Goldstein, S. L. (2006). Temporal stability of the neodymium isotope signature of the Holocene to glacial North Atlantic. *Paleoceanography*, 21(4).

Vance, D. and Thirlwall, M. (2002). An assessment of mass discrimination in MC-ICPMS using Nd isotopes. *Chemical Geology*, 185(3):227–240.

Vogt-Vincent, N., Lippold, J., Kaboth-Bahr, S., and Blaser, P. (2020). Ice-rafted debris as a source of non-conservative behaviour for the Nd palaeotracer: insights from a simple model. *Geo-Marine Letters*, 40(3):325–340.

Wang, R., Williams, T. J., Hillenbrand, C.-D., Ehrmann, W., Larkin, C. S., Hutchings, A. M., and Piotrowski, A. M. (2022). Boundary processes and neodymium cycling along the Pacific margin of West Antarctica. *Geochimica et Cosmochimica Acta*, 327:1–20.

Weber, M. E., Bailey, I., Hemming, S. R., Martos, Y. M., Reilly, B. T., Ronge, T. A., Brachfeld, S., Williams, T., Raymo, M., and Belt, S. T. (2022). Antiphased dust deposition and productivity in the Antarctic Zone over 1.5 million years. *Nature Communications*, 13(1):2044.

Weijer, W., Cheng, W., Drijfhout, S. S., Fedorov, A. V., Hu, A., Jackson, L. C., Liu, W., McDonagh, E. L., Mecking, J. V., and Zhang, J. (2019). Stability of the atlantic meridional overturning circulation: A review and synthesis. *Journal of Geophysical Research: Oceans*, 124(8):5336–5375.

Well, R., Roether, W., and Stevens, D. P. (2003). An additional deep-water mass in Drake Passage as revealed by 3He data. *Deep Sea Research Part I: Oceanographic Research Papers*, 50(9):1079–1098.

Willeit, M., Ganopolski, A., Calov, R., and Brovkin, V. (2019). Mid-Pleistocene transition in glacial cycles explained by declining CO_2 and regolith removal. *Science Advances*, 5(4):eaav7337.

Williams, T. J., Martin, E. E., Sikes, E., Starr, A., Umling, N. E., and Glaubke, R. (2021). Neodymium isotope evidence for coupled Southern Ocean circulation and Antarctic climate throughout the last 118,000 years. *Quaternary Science Reviews*, 260.

Wilson, D. J., Struve, T., van de Flierdt, T., Chen, T., Li, T., Burke, A., and Robinson, L. F. (2020). Sea-ice control on deglacial lower cell circulation changes recorded by Drake Passage deep-sea corals. *Earth and Planetary Science Letters*, 544:116405.

Wolff, E. W., Fischer, H., Fundel, F., Ruth, U., Twarloh, B., Littot, G. C., Mulvaney, R., Röthlisberger, R., de Angelis, M., Boutron, C. F., Hansson, M., Jonsell, U., Hutterli, M. A., Lambert, F., Kaufmann, P., Stauffer, B., Stocker, T. F., Steffensen, J. P., Bigler, M., Siggaard-Andersen, M. L., Udisti, R., Becagli, S., Castellano, E., Severi, M., Wagenbach, D., Barbante, C., Gabrielli, P., and Gaspari, V. (2006). Southern Ocean sea-ice extent, productivity and iron flux over the past eight glacial cycles. *Nature*, 440(7083):491–496.

Wu, S., Kuhn, G., Diekmann, B., Lembke-Jene, L., Tiedemann, R., Zheng, X., Ehrhardt, S., Arz, H. W., and Lamy, F. (2019). Surface sediment characteristics related to provenance and ocean circulation in the Drake Passage sector of the Southern Ocean. *Deep Sea Research Part I: Oceanographic Research Papers*, 154:103135.

Wu, S., Lembke-Jene, L., Lamy, F., Arz, H. W., Nowaczyk, N., Xiao, W., Zhang, X., Hass, H. C., Titschack, J., Zheng, X., Liu, J., Dumm, L., Diekmann, B., Nurnberg, D., Tiedemann, R., and Kuhn, G. (2021). Orbital- and millennial-scale Antarctic Circumpolar Current variability in Drake Passage over the past 140,000 years. *Nature Communications*, 12(1):3948.

Wu, Y., Pena, L. D., Anderson, R. F., Hartman, A. E., Bolge, L. L., Basak, C., Kim, J., Rijkenberg, M. J., De Baar, H. J., and Goldstein, S. L. (2022). Assessing neodymium isotopes as an ocean circulation tracer in the Southwest Atlantic. *Earth and Planetary Science Letters*, 599:117846.

Xu, L., Yang, J., Ni, Q., Yang, Y., Hu, Z., Liu, Y., Wu, Y., Luo, T., and Hu, S. (2018). Determination of Sm-Nd Isotopic Compositions in Fifteen Geological Materials Using Laser Ablation MC-ICP-MS and Application to Monazite Geochronology of Metasedimentary Rock in the North China Craton. *Geostandards and Geoanalytical Research*, 42(3):379–394.

Yamamoto, M., Clemens, S. C., Seki, O., Tsuchiya, Y., Huang, Y., O'ishi, R., and Abe-Ouchi, A. (2022). Increased interglacial atmospheric CO_2 levels followed the mid-Pleistocene Transition. *Nature Geoscience*, 15(4):307–313.

Yehudai, M., Kim, J., Pena, L. D., Jaume-Seguí, M., Knudson, K. P., Bolge, L., Malinverno, A., Bickert, T., and Goldstein, S. L. (2021). Evidence for a Northern Hemispheric trigger of the 100,000-y glacial cyclicity. *Proceedings of the National Academy of Sciences*, 118(46):e2020260118.

Yehudai, M., Tweed, L. E., Ridge, S., Wu, Y., and Goldstein, S. L. (2023). Effects of Past Nd Seawater Concentrations on Nd-Isotope Paleocirculation Reconstructions: A Bayesian Approach. *Geophysical Research Letters*, 50(21).

Yu, J., Menviel, L., Jin, Z. D., Anderson, R. F., Jian, Z., Piotrowski, A. M., Ma, X., Rohling, E. J., Zhang, F., Marino, G., and McManus, J. F. (2020). Last glacial atmospheric CO_2 decline due to widespread Pacific deep-water expansion. *Nature Geoscience*, 13(9):628–633.

Yu, J., Oppo, D. W., Jin, Z., Lacerra, M., Ji, X., Umling, N. E., Lund, D. C., McCave, N., Menviel, L., and Shao, J. (2022). Millennial and centennial CO2 release from the Southern Ocean during the last deglaciation. *Nature Geoscience*, 15(4):293–299.

Zhao, N., Oppo, D. W., Huang, K.-F., Howe, J. N., Blusztajn, J., and Keigwin, L. D. (2019). Glacial–interglacial nd isotope variability of north atlantic deep water modulated by north american ice sheet. *Nature Communications*, 10(1):5773.

Appendix

A. Lists

A.1. List of Figures

A.2. List of Tables

A.3. Abbreviations

AABW	Antarctic Bottom Water
AAIW	Antarctic Intermediate Water
ACC	Antarctic Circumpolar Current
AMOC	Atlantic Meridional Overturning Circulation
B/M	Brunhes-Matuyama
bmDW	benthic modified Deep Water
BP	before present
CDW	Circumpolar Deep Water
CHUR	Chondritic Uniform Reservoir
DSDP	Deep Sea Drilling Program
DSOW	Denmark Strait Overflow Water
ESA	Electrostatic Analyzer
HH	hydroxylamine hydrochloride
ICP	Inductively Coupled Plasma
ICPMS	Inductively Coupled Plasma sourced Mass Spectrometry
IDW	Indian Ocean Deep Water
IODP	Integrated Ocean Drilling Program
IRD	Ice Rafted Debris
ISOW	Iceland Scottland Overflow Water
ka	thousand years
KDE	Kernel Density Estimation
KED	Kinetic Energy Discrimination
LGM	Last Glacial Maximum
LSW	Labrador Sea Water
Ma	million years
MC-ICPMS	Multi Collector Inductively Coupled Plasma Mass Spectrometry
MIS	Marine Isotope Stage
MPT	Mid Pleistocene Transition
NADW	North Atlantic Deep Water
NSW	Northern Sourced Water
ODP	Ocean Drilling Program
PAAS	Post Archaean Australian Shale
PDW	Pacific Deep Water
PF	Polar Front
ppb	parts per billion
ppm	parts per million
PSW	Pacific Sourced Water

REE	Rare Earth Elements
SACCF	Southern ACC Front
SAF	Subantarctic Front
SAO	Southern Atlantic Ocean
SEM	Secondary Electron Multiplier
SMOC	Southern Meridional Overturning Circulation
SSW	Southern Sourced Water
TIMS	Thermal Ionization Mass Spectrometry

B. Supplementary Material

Table B.1.: εNd data of Nod-P-1 reference material (Flanagan and Gottfried, 1980) measured at the Institute of Environmental Physics in Heidelberg in context with data from Foster and Vance (2006); Gutjahr et al. (2010); Xu et al. (2018).

Label	εNd	2SD
5592	−3.52	0.13
5678	−3.80	0.13
5693	−3.77	0.11
5827	−3.89	0.09
5893	−3.80	0.12
5954	−3.84	0.12
6028	−3.79	0.09
6114	−4.06	0.13
6264	−3.87	0.14
6329	−3.93	0.11
6370	−3.99	0.11
6510	−3.67	0.15
6624	−3.87	0.14
6752	−3.85	0.14
Foster & Vance	−4.25	0.43
Xu et al.	−3.57	3.71
Gutjahr et al.	−3.88	0.31

Table B.2.: Age tie points for ODP 1093. The first 150 ka are based on the age model determined from δ^{18}O in ODP 1093 (Hallmaier et al., 2023a; Hodell and Venz, 2003). The extension of the age model is based on the assignment of drastic changes in the εNd signature with terminations and times of deglaciation. Further details can be found in chapter 5.

Depth (mcd)	Age (ka BP)	Based on	Reference
0	0	δ^{18}O	Hallmaier et al.
2.8	5.76	”	”
9.48	14.58	”	”
19.44	79.00	”	”
29.24	114.85	”	”
31.14	127.09	”	”
34.04	131.68	”	”
38.46	144.47	εNd	This work
47.01	191	”	”
75.73	243	”	”
89.52	300	”	”
104.69	336.04	δ^{18}O	Hallmaier et al.
106.49	337	εNd	This work
119.4	374	”	”
132.36	424	”	”
140.91	478	”	”
152.88	533	”	”
157.38	563	”	”
187.43	621	”	”
194.31	676	”	”
204.69	712	”	”
209.04	761	”	”
215.01	790	”	”
216.51	814	”	”
223.24	866	”	”
226.39	900	”	”
229.9	917	”	”
233.95	936	”	”
241.39	959	”	”
242.71	982	”	”
244.4	1014	”	”
246.89	1081	”	”

C. Data

C.1. Site ODP 1093

Table C.1.: Authigenic εNd at site ODP 1093 with new age model (this study and Hallmaier et al. (2023a)). Samples marked with an asterisk were excluded from further discussion based on the multielement analysis.

Label	εNd	2SD	Depth (mcd)	Age (ka BP)			
5586	A1H1W	37	38	0.37	0.76	−8.19	0.16
5559	A1H1W	77	78	0.77	1.58	−8.43	0.15
5579	A1H2W	9	10	1.59	3.27	−8.31	0.18
5587	A1H2W	9	10	1.59	3.27	−8.50	0.14
5562	A1H2W	48	49	1.98	4.07	−8.39	0.14
5613	A1H2W	89	90	2.39	4.92	−8.32	0.13
5551	A1H2W	136	137	2.86	5.84	−8.51	0.17
5578	A1H3W	36	37	3.36	6.50	−8.25	0.12
5560	A1H3W	55	56	3.55	6.75	−8.53	0.13
5584	A1H3W	98	99	3.98	7.32	−8.42	0.14
5576	A1H3W	137	138	4.37	7.83	−8.59	0.13
5585	A1H4W	29	30	4.79	8.39	−8.61	0.14
5610	A1H4W	69	70	5.19	8.92	−8.73	0.15
5597	A1H5W	4	5	6.04	10.04	−8.41	0.19
5581	A1H5W	36	37	6.36	10.46	−8.52	0.15
5558	A1H5W	78	79	6.78	11.02	−8.15	0.17
5591	A1H5W	124	125	7.24	11.62	−7.86	0.18
5555	B1H2W	125	126	8.03	12.67	−7.08	0.20
5557	B1H3W	12	13	8.4	13.15	−7.10	0.20

Continued on next page

Table C.1 – *Authigenic εNd at site ODP 1093 – continued from previous page*

Label	Core	Depth top (cm)	Depth bottom (cm)	Depth (mcd)	Age (ka BP)	εNd	2SD
5567	B1H3W	12	13	8.4	13.15	−7.35	0.23
5554	B1H3W	52	53	8.8	13.68	−7.30	0.21
5571	B1H3W	92	93	9.2	14.21	−6.69	0.19
5599	B1H3W	132	133	9.6	15.36	−4.73	0.18
5697	B1H4W	24	25	10.02	18.07	−2.93	0.18
5580	B1H4W	24	25	10.02	18.07	−2.45	0.18
5604	A2H2W	25	26	10.43	20.72	−2.35	0.13
5714*	A2H2W	25	26	10.43	20.72	−2.64	0.16
5556	A2H2W	65	66	10.83	23.31	−3.57	0.25
5561	A2H2W	105	106	11.23	25.90	−3.64	0.16
5605	A2H2W	136	137	11.54	27.90	−5.33	0.12
5413	A2H3W	25	27	11.93	30.43	−6.22	0.12
5420	A2H3W	105	107	12.73	35.60	−4.87	0.12
5439	A2H4W	25	27	13.43	40.13	−5.88	0.17
5466	A2H4W	105	107	14.23	45.30	−5.22	0.14
5442	A2H5W	18	20	14.86	49.38	−5.51	0.23
5468	A2H5W	68	70	15.36	52.61	−6.14	0.13
5430	A2H5W	118	120	15.86	55.85	−5.78	0.13
5424	A2H6W	18	20	16.36	59.08	−6.65	0.17
5423	A2H6W	68	70	16.86	62.32	−5.61	0.15
5427	A2H6W	118	120	17.36	65.55	−4.37	0.12

Continued on next page

Table C.1 – *Authigenic εNd at site ODP 1093 – continued from previous page*

Label	Core	Depth top (cm)	Depth bottom (cm)	Depth (mcd)	Age (ka BP)	εNd	2SD
5840	B2H3	32	33	17.36	65.55	−4.65	0.08
5702	A2H7W	31	33	17.99	69.62	−4.01	0.14
5463	A2H7W	31	33	17.99	69.62	−4.17	0.12
5564	B2H3W	96	97	18	69.69	−5.86	0.15
5721	B2H3	136	137	18.4	72.28	−6.78	0.13
5716	B2H4	26	27	18.8	74.86	−7.21	0.12
5703	B2H4	66	67	19.2	77.45	−6.39	0.12
5467	A3H1W	18	20	19.56	79.44	−7.21	0.16
5707	B2H4	104	105	19.58	79.52	−6.91	0.14
5433	A3H1W	67	69	20.05	81.23	−7.46	0.15
5817	B2H5	5	6	20.09	81.38	−7.43	0.09
5853	B2H5	52	53	20.56	83.10	−7.69	0.12
5459	A3H1W	118	120	20.56	83.10	−7.81	0.15
5456	A3H2W	18	20	21.06	84.93	−7.76	0.15
5864	B2H5	105	106	21.09	85.04	−7.82	0.10
5432	A3H2W	67	69	21.55	86.72	−6.94	0.18
5863	B2H6	5	6	21.59	86.87	−7.08	0.11
5457	A3H2W	118	120	22.06	88.59	−6.53	0.13
5857	B2H6	52	53	22.06	88.59	−6.68	0.11
5443	A3H2W	118	120	22.06	88.59	−6.61	0.13
5458	A3H3W	18	20	22.56	90.42	−6.56	0.14

Continued on next page

Table C.1 – *Authigenic εNd at site ODP 1093 – continued from previous page*

Label	Core	Depth top (cm)	Depth bottom (cm)	Depth (mcd)	Age (ka BP)	εNd	2SD
5419	A3H3W	67	69	23.05	92.21	−7.12	0.15
5416	A3H3W	118	120	23.56	94.07	−7.33	0.13
5448	A3H4W	18	20	24.06	95.90	−7.13	0.12
5471	A3H4W	67	69	24.55	97.69	−7.42	0.15
5441	A3H4W	115.5	117.5	25.035	99.47	−7.44	0.16
5425	A3H5W	18	20	25.56	101.39	−7.61	0.13
5449	A3H5W	67	69	26.05	103.18	−7.43	0.14
5440	A3H5W	115.5	117.5	26.535	104.95	−7.20	0.13
5421	A3H6W	18	20	27.06	106.87	−6.99	0.14
5464	A3H6W	67	69	27.55	108.67	−7.04	0.15
5436	A3H6W	118	120	28.06	110.53	−6.96	0.17
5452	A3H7W	28	30	28.66	112.73	−6.76	0.14
5696	C3H2	13	14	29.27	115.04	−7.39	0.09
5708	C3H2	72	73	29.86	118.84	−7.46	0.11
5718	C3H2	132	133	30.46	122.71	−7.73	0.14
5695	C3H3	45	46	31.09	126.77	−7.61	0.09
5699	C3H3	45	46	31.09	126.77	−7.70	0.13
5450	A4H1W	18	20	31.66	127.92	−7.63	0.15
5691	C3H3	105	106	31.69	127.96	−7.44	0.11
5444	A4H1W	67	69	32.15	128.69	−7.50	0.14
5810	C3H4	5	6	32.19	128.75	−7.64	0.11

Continued on next page

Table C.1 – *Authigenic εNd at site ODP 1093 – continued from previous page*

Label	Core	Depth top (cm)	Depth bottom (cm)	Depth (mcd)	Age (ka BP)	εNd	2SD
5803	C3H4	52	53	32.66	129.50	−7.04	0.12
5445	A4H1W	118	120	32.66	129.50	−7.20	0.15
5829	C3H4	98	99	33.12	130.23	−7.53	0.09
5460	A4H2W	19	21	33.17	130.31	−7.64	0.13
5469	A4H2W	67	69	33.65	131.06	−7.07	0.15
5819	C3H5	3	4	33.67	131.10	−7.45	0.08
5431	A4H2W	118	120	34.16	132.03	−6.37	0.13
5815	C3H5	53	54	34.17	132.06	−6.57	0.09
5429	A4H3W	18	20	34.66	133.48	−5.02	0.15
5454	A4H3W	18	20	34.66	133.48	−5.22	0.16
5418	A4H3W	67	69	35.15	134.89	−4.38	0.15
5473	A4H3W	118	120	35.66	136.37	−4.02	0.14
5472	A4H4W	25	27	36.23	138.02	−4.12	0.17
5437	A4H4W	95	97	36.93	140.04	−3.40	0.15
5465	A4H5W	25	27	37.73	142.36	−3.18	0.15
5719	A4H5	98	100	38.46	144.47	−3.33	0.13
5851	F1H2	56	57	38.98	147.30	−4.80	0.09
5843	F1H2	106	107	39.48	150.02	−4.40	0.10
5835	F1H3	6	7	39.98	152.74	−4.49	0.21
5859	F1H3	56	57	40.48	155.46	−5.35	0.11
5814	C4H2	100	101	40.96	158.07	−4.40	0.10

Continued on next page

Table C.1 – *Authigenic εNd at site ODP 1093 – continued from previous page*

Label	Core	Depth top (cm)	Depth bottom (cm)	Depth (mcd)	Age (ka BP)	εNd	2SD
5818	C4H3	5	6	41.51	161.07	−4.49	0.14
5811	C4H3	53	54	41.99	163.68	−3.67	0.11
5854	C4H3	105	106	42.51	166.51	−4.28	0.13
5830	C4H3	105	106	42.51	166.51	−4.41	0.10
5807	C4H4	5	6	43.01	169.23	−5.16	0.11
5805	C4H4	52	53	43.48	171.79	−5.07	0.13
5844	C4H4	100	101	43.96	174.40	−4.80	0.08
5821	C4H5	5	6	44.51	177.39	−5.77	0.12
5825	A5H4	12	13	44.98	179.95	−5.77	0.11
5842	A5H4	59	60	45.45	182.51	−5.92	0.09
5841	A5H4	112	113	45.98	185.39	−5.13	0.10
5801	A5H5	16	17	46.52	188.33	−5.30	0.09
5856	A5H5	65	66	47.01	191.00	−6.21	0.12
5848	A5H5	112	113	47.48	191.85	−6.68	0.11
5850	A5H6	12	13	47.98	192.76	−7.25	0.09
5838	A5H6	65	66	48.51	193.72	−7.44	0.10
5846	B5H1	118	119	48.88	194.39	−6.98	0.10
5845	B5H2	19	20	49.39	195.31	−7.52	0.07
6639	B5H2	19	20	49.39	195.31	−7.41	0.19
5806	B5H2	69	70	49.89	196.21	−7.46	0.11
5824	B5H2	118	119	50.38	197.10	−7.80	0.09

Continued on next page

Table C.1 – *Authigenic εNd at site ODP 1093 – continued from previous page*

Label	Core	Depth top (cm)	Depth bottom (cm)	Depth (mcd)	Age (ka BP)	εNd	2SD
5804	B5H3	19	20	50.89	198.03	−7.59	0.11
5858	B5H3	69	70	51.39	198.93	−7.31	0.12
5837	B5H3	117	118	51.87	199.80	−7.13	0.08
5828	B5H4	19	20	52.39	200.74	−6.58	0.08
5834	A6H1	92	93	52.76	201.41	−6.51	0.09
5809	A6H1	138	139	53.22	202.24	−6.62	0.13
5816	A6H2	45	46	53.79	203.28	−6.68	0.09
5836	A6H2	92	93	54.26	204.13	−6.79	0.11
5833	A6H2	138	139	54.72	204.96	−6.98	0.09
6284	A6H3W	38	39	55.22	205.86	−7.34	0.13
5860	A6H3	92	93	55.76	206.84	−7.32	0.12
6001*	A6H3W	138	139	56.22	207.68	−7.21	0.11
5855	A6H3	138	139	56.22	207.68	−7.16	0.12
5823	A6H4	45	46	56.79	208.71	−7.16	0.08
5802	A6H4	92	93	57.26	209.56	−7.39	0.08
5832	A6H4	138	139	57.72	210.39	−7.30	0.09
5862	A6H5	38	39	58.22	211.30	−6.98	0.10
5812	A6H5	92	93	58.76	212.27	−6.95	0.08
5942	A6H5W	138	139	59.22	213.11	−7.03	0.11
5826	A6H5	138	139	59.22	213.11	−6.91	0.09
5813	A6H5	138	139	59.22	213.11	−6.98	0.10

Continued on next page

Table C.1 – *Authigenic εNd at site ODP 1093 – continued from previous page*

Label	Core	Depth top (cm)	Depth bottom (cm)	Depth (mcd)	Age (ka BP)	εNd	2SD
5831	A6H6	45	46	59.79	214.14	−6.80	0.09
5852	A6H6	92	93	60.26	214.99	−6.79	0.08
5948	B6H1W	99	100	60.75	215.88	−7.10	0.13
6002	B6H2W	4	5	61.3	216.87	−6.84	0.15
6021	B6H2W	4	5	61.3	216.87	−6.66	0.14
5957	B6H2W	49	50	61.75	217.69	−6.93	0.14
6000	B6H2W	97	98	62.23	218.56	−6.93	0.11
6004	B6H3W	5	6	62.81	219.61	−6.38	0.14
5984	B6H3W	49	50	63.25	220.40	−6.74	0.17
5953	B6H3W	99	100	63.75	221.31	−6.85	0.12
5956	B6H4W	4	5	64.3	222.31	−6.46	0.12
5961*	B6H4W	48	49	64.74	223.10	−6.02	0.10
5998	B6H4W	97	98	65.23	223.99	−5.07	0.10
6236	B6H5W	5	6	65.81	225.04	−4.49	0.22
5982	A7H3W	117	118	66.4	226.11	−5.35	0.11
5966	A7H4W	12	13	66.85	226.92	−5.85	0.09
5967	A7H4W	65	66	67.38	227.88	−5.44	0.09
5949	A7H4W	112	113	67.85	228.73	−5.32	0.10
6300	A7H5W	12	13	68.35	229.64	−6.42	0.11
6251	A7H5W	12	13	68.35	229.64	−6.30	0.12
5959	A7H5W	64	65	68.87	230.58	−6.06	0.15

Continued on next page

Table C.1 – *Authigenic εNd at site ODP 1093 – continued from previous page*

Label	Core	Depth top (cm)	Depth bottom (cm)	Depth (mcd)	Age (ka BP)	εNd	2SD
5941	A7H5W	112	113	69.35	231.45	−6.23	0.11
5980	A7H6W	12	13	69.85	232.35	−6.58	0.09
5947	A7H6W	65	66	70.38	233.31	−6.91	0.13
5990	A7H6W	112	113	70.85	234.16	−7.17	0.09
5997	A7H6W	112	113	70.85	234.16	−7.08	0.11
5945	C7H2W	56	57	71.37	235.11	−7.21	0.12
5972	C7H2W	105	106	71.86	235.99	−7.17	0.10
5986	C7H3W	6	7	72.37	236.92	−7.45	0.10
5952	C7H3W	56	57	72.87	237.82	−7.31	0.12
5965	C7H3W	106	107	73.37	238.73	−7.62	0.13
5962	C7H4W	6	7	73.87	239.63	−7.42	0.08
5968	C7H4W	56	57	74.37	240.54	−8.03	0.11
5979	C7H4W	106	107	74.87	241.44	−7.81	0.11
5950	C7H5W	6	7	75.37	242.35	−6.43	0.09
5991	C7H5W	56	57	75.87	243.58	−4.91	0.25
5970	C7H5W	106	107	76.37	245.65	−5.12	0.20
6003	C7H6W	6	7	76.87	247.71	−5.50	0.13
5969	C7H6W	56	57	77.37	249.78	−3.87	0.10
5943	A8H4W	36	37	77.89	251.93	−6.39	0.12
5996	A8H4W	85	86	78.38	253.95	−5.06	0.13
5992	A8H4W	134	135	78.87	255.98	−4.57	0.11

Continued on next page

Table C.1 – *Authigenic εNd at site ODP 1093 – continued from previous page*

Label	Core	Depth top (cm)	Depth bottom (cm)	Depth (mcd)	Age (ka BP)	εNd	2SD
5944	A8H5W	33	34	79.36	258.00	−3.85	0.11
5987	A8H5W	85	86	79.88	260.15	−3.95	0.10
5994	B8H2W	69	70	80.76	263.79	−3.05	0.11
5989	B8H3W	19	20	81.76	267.92	−3.84	0.09
6280	B8H3W	69	70	82.26	269.99	−4.60	0.12
5973	B8H3W	118	119	82.75	272.02	−4.69	0.10
5960	B8H4W	19	20	83.26	274.12	−4.04	0.11
5978	B8H4W	19	20	83.26	274.12	−4.06	0.13
5985	B8H4W	67	68	83.74	276.11	−4.93	0.16
5993	B8H4W	117	118	84.24	278.18	−4.94	0.13
5977	B8H5W	19	20	84.76	280.32	−4.55	0.11
5976	B8H5W	68	69	85.25	282.35	−5.32	0.10
5981	B8H5W	118	119	85.75	284.42	−5.89	0.11
5995	A9H3W	32	33	85.99	285.41	−5.10	0.12
5999	A9H3W	85	86	86.52	287.60	−5.44	0.12
6074	A9H3W	132	133	86.99	289.54	−5.79	0.13
5951	A9H3W	132	133	86.99	289.54	−6.01	0.12
5971	A9H4W	32	33	87.49	291.61	−6.19	0.09
6013	A9H4W	85	86	88.02	293.80	−6.55	0.08
6046	A9H4W	132	133	88.49	295.74	−6.46	0.12
6016	A9H5W	32	33	88.99	297.81	−4.74	0.12

Continued on next page

Table C.1 – *Authigenic εNd at site ODP 1093 – continued from previous page*

Label	Core	Depth top (cm)	Depth bottom (cm)	Depth (mcd)	Age (ka BP)	εNd	2SD
6042	A9H5W	85	86	89.52	300.00	−5.25	0.11
6065	A9H5W	85	86	89.52	300.00	−5.16	0.11
6073	A9H5W	133	134	90	301.14	−4.76	0.10
6025*	A9H6W	32	33	90.49	302.30	−5.21	0.14
6071*	B9H1W	117	118	90.86	303.18	−5.24	0.12
6031	B9H2W	19	20	91.38	304.42	−5.76	0.11
6062	B9H2W	69	70	91.88	305.61	−5.43	0.12
6063*	B9H2W	119	120	92.38	306.79	−4.65	0.15
6043	B9H3W	19	20	92.88	307.98	−4.56	0.14
6032	B9H3W	69	70	93.38	309.17	−5.22	0.11
6068	B9H3W	119	120	93.88	310.36	−5.45	0.13
6051	B9H4W	19	20	94.38	311.55	−5.38	0.13
6014	B9H4W	19	20	94.38	311.55	−5.54	0.10
6038	B9H4W	69	70	94.88	312.73	−6.14	0.11
6019	B9H4W	119	120	95.38	313.92	−5.63	0.10
6055	B9H5W	19	20	95.88	315.11	−6.47	0.12
6053*	B9H5W	69	70	96.38	316.30	−5.45	0.12
6036	B9H5W	119	120	96.88	317.49	−5.48	0.13
6250	B9H6W	19	20	97.38	318.67	−6.42	0.13
6106	B9H6W	19	20	97.38	318.67	−6.47	0.27
6658	B9H6W	19	20	97.38	318.67	−6.48	0.26

Continued on next page

Table C.1 – *Authigenic εNd at site ODP 1093 – continued from previous page*

Label	Core	Depth top (cm)	Depth bottom (cm)	Depth (mcd)	Age (ka BP)	εNd	2SD
6067	B9H6W	69	70	97.88	319.86	−6.91	0.11
6066*	A10H4W	35	36	98.38	321.05	−6.89	0.11
6064	A10H4W	85	86	98.88	322.24	−6.66	0.12
6034	A10H4W	132	133	99.35	323.35	−6.18	0.12
6026	A10H5W	35	36	99.88	324.61	−6.44	0.10
6056	A10H5W	85	86	100.38	325.80	−6.22	0.11
6090	A10H5W	85	86	100.38	325.80	−6.68	0.12
6059	A10H5W	135	136	100.88	326.99	−6.88	0.12
6020	A10H6W	35	36	101.43	328.30	−6.98	0.12
6616	A10H6W	35	36	101.43	328.30	−7.19	0.16
6070	A10H6W	85	86	101.93	329.48	−7.39	0.10
6023	B10H2W	144	145	102.51	330.86	−7.51	0.11
6015	B10H3W	44	45	103.01	332.05	−7.51	0.09
6030	B10H3W	93	94	103.5	333.21	−7.62	0.12
6045	B10H3W	144	145	104.01	334.42	−7.34	0.11
6040	B10H4W	39	40	104.46	335.49	−7.31	0.11
6060	B10H4W	92	93	104.99	336.20	−7.70	0.12
6027	B10H4W	144	145	105.51	336.48	−7.77	0.12
6011	B10H5W	45	46	106.02	336.75	−6.64	0.10
6012	B10H5W	92	93	106.49	337.00	−5.44	0.12
6041	B10H5W	144	145	107.01	338.49	−3.53	0.11

Continued on next page

Table C.1 – *Authigenic εNd at site ODP 1093 – continued from previous page*

Label	Core	Depth top (cm)	Depth bottom (cm)	Depth (mcd)	Age (ka BP)	εNd	2SD
6091	A11H3W	14	15	107.49	339.87	−3.25	0.14
6093	A11H3W	65	66	108	341.33	−4.02	0.13
6133	A11H3W	114	115	108.49	342.73	−4.49	0.17
6137	A11H4W	14	15	108.99	344.16	−4.74	0.17
6134	A11H4W	64	65	109.49	345.60	−4.59	0.13
6094	A11H4W	114	115	109.99	347.03	−4.54	0.14
6118	A11H5W	14	15	110.49	348.46	−4.04	0.11
6142	A11H5W	65	66	111	349.93	−3.59	0.12
6143	A11H5W	114	115	111.49	351.33	−3.70	0.11
6140	A11H6W	14	15	111.99	352.76	−3.82	0.13
6671	A11H6W	65	66	112.5	354.22	−4.72	0.17
6119	A11H6W	114	115	112.99	355.63	−4.47	0.11
6095	B11H2W	58	59	113.39	356.78	−4.73	0.13
6122	B11H2W	107	108	113.88	358.18	−4.26	0.12
6112	B11H3W	8	9	114.39	359.64	−4.42	0.14
6081	B11H3W	58	59	114.89	361.07	−4.26	0.12
6111	B11H3W	110	111	115.41	362.56	−4.77	0.11
6120	B11H4W	8	9	115.89	363.94	−3.92	0.14
6121	B11H4W	58	59	116.39	365.37	−4.17	0.20
6109	B11H4W	108	109	116.89	366.81	−4.12	0.21
6518	B11H5W	8	9	117.39	368.24	−4.28	0.39

Continued on next page

Table C.1 – *Authigenic εNd at site ODP 1093 – continued from previous page*

Label	Core	Depth top (cm)	Depth bottom (cm)	Depth (mcd)	Age (ka BP)	εNd	2SD
6135	B11H5W	58	59	117.89	369.67	−4.10	0.15
6113	B11H5W	110	111	118.41	371.16	−5.46	0.10
6637	A12H3W	77	78	118.9	372.57	−4.88	0.15
6144	A12H3W	77	78	118.9	372.57	−4.63	0.13
6084	A12H3W	127	128	119.4	374.00	−5.10	0.13
6136	A12H4W	27	28	119.9	375.93	−5.78	0.13
6082	A12H4W	77	78	120.4	377.86	−6.50	0.17
6098	A12H4W	127	128	120.9	379.79	−5.71	0.16
6129	A12H5W	27	28	121.4	381.72	−7.06	0.12
6102	A12H5W	77	78	121.9	383.65	−7.68	0.12
5933	A12H5W	126	127	122.39	385.54	−7.30	0.12
5910	A12H6W	13	14	122.76	386.96	−7.59	0.11
5914	A12H6W	77	78	123.4	389.43	−7.77	0.15
5920	B12H2W	73	74	123.88	391.28	−8.32	0.12
5900	B12H2W	127	128	124.42	393.37	−7.99	0.13
5930	B12H3W	23	24	124.88	395.14	−7.89	0.16
5891	B12H3W	73	74	125.38	397.07	−7.95	0.13
5904	A13H1W	123	124	125.9	399.08	−7.75	0.12
5908	A13H2W	21	22	126.38	400.93	−7.67	0.14
5881	A13H2W	72	73	126.89	402.90	−7.50	0.12
5925	A13H2W	121	122	127.38	404.79	−7.73	0.14

Continued on next page

Table C.1 – *Authigenic εNd at site ODP 1093 – continued from previous page*

Label	Core	Depth top (cm)	Depth bottom (cm)	Depth (mcd)	Age (ka BP)	εNd	2SD
5932	A13H3W	23	24	127.9	406.79	−7.28	0.14
5918	A13H3W	72	73	128.39	408.68	−7.17	0.12
5889	A13H3W	123	124	128.9	410.65	−7.06	0.13
5895	A13H4W	21	22	129.38	412.50	−6.21	0.16
5907	A13H4W	72	73	129.89	414.47	−6.12	0.14
5888	A13H4W	119	120	130.36	416.28	−6.56	0.14
5922	A13H5W	27	28	130.94	418.52	−6.72	0.12
5917	A13H5W	73	74	131.4	420.30	−6.86	0.12
5906	A13H5W	119	120	131.86	422.07	−5.77	0.18
5903	A13H6W	19	20	132.36	424.00	−5.06	0.14
5905	A13H6W	68	69	132.85	427.09	−3.48	0.13
5892	B13H3W	26	27	133.39	430.51	−2.80	0.11
5885	B13H3W	76	77	133.89	433.66	−3.70	0.12
5878	B13H3W	126	127	134.39	436.82	−2.42	0.15
5890	B13H3W	126	127	134.39	436.82	−2.65	0.13
5879	B13H4W	27	28	134.9	440.04	−2.69	0.13
5913*	B13H4W	76	77	135.39	443.14	−3.24	0.12
5921*	B13H4W	126	127	135.89	446.29	−3.82	0.13
5899	B13H5W	26	27	136.39	449.45	−3.66	0.13
6139	B13H5W	76	77	136.89	452.61	−4.33	0.13
6141	B13H5W	126	127	137.39	455.77	−4.29	0.13

Continued on next page

Table C.1 – *Authigenic εNd at site ODP 1093 – continued from previous page*

Label	Core	Depth top (cm)	Depth bottom (cm)	Depth (mcd)	Age (ka BP)	εNd	2SD
6125	B13H6W	26	27	137.89	458.93	−3.48	0.11
6330	B13H6W	26	27	137.89	458.93	−3.74	0.12
6127	B13H6W	76	77	138.39	462.08	−5.04	0.12
6096	B13H6W	126	127	138.89	465.24	−5.05	0.11
6132	A14H3W	146	147	139.39	468.40	−4.60	0.11
6104	A14H4W	46	47	139.89	471.56	−4.15	0.13
6097	A14H4W	96	97	140.39	474.72	−4.48	0.12
6110	A14H4W	138	139	140.81	477.37	−4.36	0.12
6117	A14H5W	46	47	141.39	480.21	−6.17	0.13
6088	A14H5W	96	97	141.89	482.50	−7.01	0.11
6087	B14H2W	32	33	142.39	484.80	−4.41	0.13
6099	B14H2W	84	85	142.91	487.19	−6.27	0.13
6126	B14H2W	132	133	143.39	489.40	−6.43	0.12
6085	B14H3W	32	33	143.89	491.69	−5.40	0.13
6115	B14H3W	84	85	144.41	494.08	−6.05	0.12
6128	B14H3W	132	133	144.89	496.29	−6.38	0.12
6083	B14H4W	32	33	145.39	498.58	−6.57	0.12
6092	B14H4W	79	80	145.86	500.74	−7.03	0.12
6101	B14H4W	79	80	145.86	500.74	−6.94	0.13
6089	B14H4W	132	133	146.39	503.18	−7.86	0.13
6123	B14H5W	32	33	146.89	505.48	−7.54	0.12

Continued on next page

Table C.1 – *Authigenic εNd at site ODP 1093 – continued from previous page*

Label	Core	Depth top (cm)	Depth bottom (cm)	Depth (mcd)	Age (ka BP)	εNd	2SD
6108	A15H3W	5	6	147.4	507.82	−6.77	0.13
6138	A15H3W	5	6	147.4	507.82	−6.76	0.11
6131	A15H3W	55	56	147.9	510.12	−6.34	0.13
6107	A15H3W	104	105	148.39	512.37	−6.53	0.12
6103	A15H4W	5	6	148.9	514.71	−6.69	0.12
6279	A15H4W	54	55	149.39	516.96	−6.37	0.14
6263	A15H4W	105	106	149.9	519.31	−6.79	0.15
6260	A15H5W	5	6	150.4	521.60	−6.88	0.12
6225	A15H5W	54	55	150.89	523.86	−6.89	0.13
6272	A15H5W	54	55	150.89	523.86	−7.11	0.24
6242	A15H5W	105	106	151.4	526.20	−6.82	0.12
6238	A15H6W	5	6	151.9	528.50	−6.72	0.14
6243	A15H6W	54	55	152.39	530.75	−6.98	0.14
6223	B15H2W	7	8	152.88	533.00	−6.48	0.14
6277	B15H2W	59	60	153.4	536.47	−6.26	0.17
6261	B15H2W	107	108	153.88	539.67	−6.22	0.17
6254	B15H3W	8	9	154.39	543.07	−5.66	0.20
6231	B15H3W	59	60	154.9	546.47	−6.35	0.16
6270	B15H3W	109	110	155.4	549.80	−6.05	0.16
6235	B15H4W	8	9	155.89	553.07	−6.00	0.20
6267	A16H2W	19	20	156.38	556.33	−5.89	0.17

Continued on next page

Table C.1 – *Authigenic εNd at site ODP 1093 – continued from previous page*

Label	Core	Depth top (cm)	Depth bottom (cm)	Depth (mcd)	Age (ka BP)	εNd	2SD
6274	A16H2W	69	70	156.88	559.67	−6.32	0.15
6256	A16H2W	119	120	157.38	563.00	−6.60	0.16
6273	A16H3W	19	20	157.88	563.97	−7.17	0.15
6259	A16H3W	69	70	158.38	564.93	−6.92	0.13
6278	A16H3W	119	120	158.88	565.90	−7.41	0.15
6227	A16H4W	19	20	159.38	566.86	−7.06	0.14
6241	A16H4W	69	70	159.88	567.83	−7.15	0.14
6244	A16H4W	119	120	160.38	568.79	−7.25	0.16
6239	A16H5W	18	19	160.87	569.74	−6.78	0.16
6232	A16H5W	68	69	161.37	570.70	−5.96	0.16
6249	A16H5W	119	120	161.88	571.69	−5.47	0.22
6283	A16H6W	19	20	162.38	572.65	−5.02	0.15
6268	B16H2W	116	117	162.91	573.67	−4.42	0.13
6222	B16H3W	16	17	163.41	574.64	−5.05	0.16
6276	B16H3W	66	67	163.91	575.60	−5.56	0.18
6226	B16H3W	116	117	164.41	576.57	−5.26	0.16
6234	B16H4W	16	17	164.91	577.53	−6.28	0.14
6269	B16H4W	66	67	165.41	578.50	−6.71	0.17
6229	B16H4W	116	117	165.91	579.46	−6.36	0.14
6247	A17H2W	104	105	166.47	580.54	−6.07	0.16
6246	A17H3W	5	6	166.98	581.53	−6.88	0.16

Continued on next page

Table C.1 – *Authigenic εNd at site ODP 1093 – continued from previous page*

Label	Core	Depth top (cm)	Depth bottom (cm)	Depth (mcd)	Age (ka BP)	εNd	2SD
6252	A17H3W	52	53	167.45	582.44	−7.29	0.12
6262	A17H3W	104	105	167.97	583.44	−7.58	0.14
6221	A17H4W	5	6	168.48	584.42	−8.08	0.11
6248	A17H4W	52	53	168.95	585.33	−8.01	0.15
6611	A17H4W	52	53	168.95	585.33	−7.89	0.16
6228	A17H4W	104	105	169.47	586.34	−7.97	0.13
6245	A17H5W	5	6	169.98	587.32	−7.64	0.14
6257	A17H5W	52	53	170.45	588.23	−7.92	0.15
6253	A17H5W	102	103	170.95	589.19	−7.62	0.15
6281	A17H6W	3	4	171.46	590.18	−7.77	0.16
6266	A17H6W	52	53	171.95	591.12	−7.05	0.18
6271	A17H6W	104	105	172.47	592.13	−6.97	0.12
6258	A17H7W	3	4	172.96	593.07	−6.04	0.16
6224	B17H2W	112	113	173.37	593.86	−5.86	0.18
6255	B17H3W	9	10	173.84	594.77	−6.26	0.13
6237	B17H3W	59	60	174.34	595.73	−6.63	0.18
6294	B17H3W	108	109	174.83	596.68	−7.35	0.15
6291	B17H4W	9	10	175.34	597.66	−6.97	0.15
6302	B17H4W	59	60	175.84	598.63	−7.31	0.18
6352	B17H4W	108	109	176.33	599.58	−7.84	0.19
6340	B17H5W	9	10	176.84	600.56	−7.55	0.11

Continued on next page

Table C.1 – *Authigenic εNd at site ODP 1093 – continued from previous page*

Label	Core	Depth top (cm)	Depth bottom (cm)	Depth (mcd)	Age (ka BP)	εNd	2SD
6327	B17H5W	59	60	177.34	601.53	−6.63	0.13
6304	B17H5W	112	113	177.87	602.55	−6.96	0.21
6315	B17H6W	9	10	178.34	603.46	−6.31	0.13
6344	A18H3W	82	83	178.43	603.63	−5.97	0.14
6341	A18H3W	132	133	178.93	604.59	−7.07	0.10
6316	A18H4W	32	33	179.43	605.56	−6.61	0.11
6299	A18H4W	82	83	179.93	606.52	−7.07	0.12
6296	A18H4W	132	133	180.43	607.49	−7.75	0.10
6331	A18H5W	32	33	180.93	608.45	−7.91	0.14
6295	A18H5W	82	83	181.43	609.42	−7.88	0.12
6306	A18H5W	82	83	181.43	609.42	−8.07	0.13
6320	A18H5W	132	133	181.93	610.38	−7.46	0.13
6348	A18H6W	33	34	182.44	611.37	−7.67	0.10
6339	A18H6W	82	83	182.93	612.31	−7.01	0.15
6335	D4H2W	30	31	183.43	613.28	−7.38	0.14
6310	D4H2W	80	81	183.93	614.24	−7.39	0.16
6303	D4H2W	130	131	184.43	615.21	−7.30	0.20
6350	D4H3W	30	31	184.93	616.17	−7.35	0.14
6432	D4H3W	30	31	184.93	616.17	−7.00	0.12
6309	D4H3W	80	81	185.43	617.14	−7.07	0.19
6346	D4H3W	130	131	185.93	618.10	−6.76	0.18

Continued on next page

Table C.1 – *Authigenic εNd at site ODP 1093 – continued from previous page*

Label	Core	Depth top (cm)	Depth bottom (cm)	Depth (mcd)	Age (ka BP)	εNd	2SD
6323	D4H4W	30	31	186.43	619.07	−6.12	0.15
6322	D4H4W	80	81	186.93	620.03	−6.35	0.18
6313	D4H4W	130	131	187.43	621.00	−5.94	0.10
6383	D4H4W	130	131	187.43	621.00	−5.97	0.09
6314	D4H5W	30	31	187.93	625.00	−4.18	0.12
6292	A19H2W	2	3	188.43	628.99	−3.31	0.12
6345	A19H2W	52	53	188.93	632.99	−3.33	0.12
6347	A19H2W	102	103	189.43	636.99	−4.63	0.15
6321	A19H3W	3	4	189.94	641.07	−4.88	0.13
6305	A19H3W	49	50	190.4	644.74	−4.22	0.21
6328	A19H3W	103	104	190.94	649.06	−4.76	0.11
6336	A19H3W	103	104	190.94	649.06	−4.69	0.13
6298	A19H4W	17	18	191.58	654.18	−4.92	0.17
6311	A19H4W	76	77	192.17	658.89	−4.91	0.10
6301	A19H4W	111	112	192.52	661.69	−4.53	0.13
6326	A19H5W	9	10	193	665.53	−7.44	0.13
6351	A19H5W	52	53	193.43	668.97	−6.66	0.13
6349	A19H5W	105	106	193.96	673.20	−4.89	0.13
6333	D5H2W	76	77	194.31	676.00	−6.82	0.13
6319	D5H2W	126	127	194.81	677.73	−7.12	0.11
6308	D5H3W	26	27	195.31	679.47	−7.62	0.11

Continued on next page

Table C.1 – *Authigenic εNd at site ODP 1093 – continued from previous page*

Label	Core	Depth top (cm)	Depth bottom (cm)	Depth (mcd)	Age (ka BP)	εNd	2SD
6318	D5H3W	76	77	195.81	681.20	−7.84	0.10
6307	D5H3W	126	127	196.31	682.94	−8.05	0.10
6338	D5H4W	26	27	196.81	684.67	−8.02	0.13
6337	D5H4W	76	77	197.31	686.40	−7.79	0.12
6332	D5H4W	126	127	197.81	688.14	−8.25	0.12
6353	D5H5W	26	27	198.31	689.87	−8.11	0.10
6312	D5H5W	76	77	198.81	691.61	−7.92	0.12
6324	D5H5W	126	127	199.31	693.34	−7.99	0.12
6297	A20H1W	132	133	199.69	694.66	−7.96	0.17
6342	A20H2W	33	34	200.2	696.43	−8.12	0.12
6627	A20H2W	83	84	200.7	698.16	−7.41	0.14
6334	A20H2W	83	84	200.7	698.16	−7.84	0.11
6354	A20H2W	132	133	201.19	699.86	−7.91	0.16
6664	A20H3W	33	34	201.7	701.63	−7.58	0.17
6653	A20H3W	83	84	202.2	703.36	−7.66	0.19
6507	A20H3W	83	84	202.2	703.36	−7.83	0.16
6663	A20H3W	132	133	202.69	705.06	−7.85	0.19
6504	A20H4W	32	33	203.19	706.80	−7.76	0.22
6511	A20H4W	82	83	203.69	708.53	−8.14	0.16
6651	A20H4W	132	133	204.19	710.27	−6.81	0.30
6513	A20H5W	32	33	204.69	712.00	−5.78	0.14

Continued on next page

Table C.1 – *Authigenic εNd at site ODP 1093 – continued from previous page*

Label	Core	Depth top (cm)	Depth bottom (cm)	Depth (mcd)	Age (ka BP)	εNd	2SD
6525	A20H5W	82	83	205.19	717.63	−4.40	0.16
6519	A20H5W	131	132	205.68	723.15	−4.96	0.24
6514	A20H6W	32	33	206.19	728.90	−6.28	0.12
6666	A20H6W	82	83	206.69	734.53	−6.57	0.18
6670	A20H6W	132	133	207.19	740.16	−6.55	0.17
6678	A20H7W	33	34	207.7	745.91	−5.05	0.16
6515	B20H2W	73	74	208.04	749.74	−3.91	0.17
6682	B20H2W	123	124	208.54	755.37	−4.55	0.18
6508	B20H3W	23	24	209.04	761.00	−4.57	0.15
6662	B20H3W	72	73	209.53	763.38	−5.70	0.21
6502	B20H3W	122	123	210.03	765.81	−6.92	0.16
6679	A21H1W	114	115	210.51	768.14	−7.74	0.14
6529	A21H2W	13	14	211	770.52	−7.81	0.17
6660	A21H2W	62	63	211.49	772.90	−7.56	0.18
6672	A21H2W	112	113	211.99	775.33	−8.05	0.16
6677	A21H3W	14	15	212.51	777.86	−8.19	0.22
6656	A21H3W	64	65	213.01	780.28	−7.86	0.19
6680	A21H3W	114	115	213.51	782.71	−7.91	0.15
6528	A21H4W	14	15	214.01	785.14	−7.39	0.13
6674	A21H4W	43	44	214.3	786.55	−6.22	0.19
6676	A21H4W	64	65	214.51	787.57	−5.43	0.28

Continued on next page

Table C.1 – *Authigenic εNd at site ODP 1093 – continued from previous page*

Label	Core	Depth top (cm)	Depth bottom (cm)	Depth (mcd)	Age (ka BP)	εNd	2SD
6531	A21H4W	89	90	214.76	788.79	−5.09	0.13
6509	A21H4W	114	115	215.01	790.00	−4.20	0.17
6520	A21H5W	14	15	215.51	798.00	−3.65	0.14
6532	A21H5W	64	65	216.01	806.00	−4.46	0.14
6526	A21H5W	114	115	216.51	814.00	−5.89	0.17
6522	A21H6W	14	15	217.01	817.86	−8.24	0.17
6675	A21H6W	64	65	217.51	821.73	−7.08	0.18
6665	B21H2W	22	23	217.99	825.44	−6.13	0.24
6503	B21H2W	72	73	218.49	829.30	−7.37	0.13
6622	B21H2W	72	73	218.49	829.30	−7.17	0.15
6681	B21H2W	122	123	218.99	833.16	−7.11	0.15
6523	B21H3W	22	23	219.49	837.03	−7.45	0.17
6657	B21H3W	74	75	220.01	841.04	−7.67	0.19
6521	B21H3W	122	123	220.49	844.75	−7.16	0.17
6659	B21H4W	22	23	220.99	848.62	−7.77	0.20
6652	B21H4W	72	73	221.49	852.48	−7.41	0.18
6517	B21H4W	118	119	221.95	856.03	−7.93	0.19
6512	B21H5W	22	23	222.49	860.21	−7.92	0.14
6439	B21H5W	72	73	222.99	864.07	−6.37	0.12
6374	A22H3W	143	144	223.24	866.00	−5.92	0.11
6377	A22H4W	42	43	223.73	871.29	−3.48	0.12

Continued on next page

Table C.1 – *Authigenic εNd at site ODP 1093 – continued from previous page*

Label	Core	Depth top (cm)	Depth bottom (cm)	Depth (mcd)	Age (ka BP)	εNd	2SD
6391	A22H4W	92	93	224.23	876.69	−3.18	0.12
6363	A22H4W	139	140	224.7	881.76	−2.97	0.17
6378	A22H4W	139	140	224.7	881.76	−3.11	0.12
6456	A22H5W	42	43	225.23	887.48	−4.00	0.07
6389	A22H6W	13	14	225.78	893.42	−2.84	0.09
6460	B22H1W	146	147	226.39	900.00	−4.73	0.10
6434	B22H2W	45	46	226.88	902.37	−5.40	0.10
6448	B22H2W	97	98	227.4	904.89	−5.95	0.11
6452	B22H2W	145	146	227.88	907.22	−5.94	0.09
6386	B22H3W	47	48	228.4	909.74	−4.76	0.14
6449	B22H3W	96	97	228.89	912.11	−5.97	0.10
6442	B22H3W	147	148	229.4	914.58	−5.40	0.12
6390	B22H4W	47	48	229.9	917.00	−5.16	0.12
6381	B22H4W	97	98	230.4	919.35	−3.37	0.11
6368	B22H4W	147	149	230.9	921.69	−3.95	0.11
6361	B22H5W	47	48	231.4	924.04	−4.40	0.11
6379	B22H5W	97	98	231.9	926.38	−4.03	0.10
6443	A23H3W	49	50	232.4	928.73	−4.64	0.11
6458	A23H3W	99	100	232.9	931.07	−6.31	0.12
6366	A23H4W	6	7	233.47	933.75	−6.53	0.17
6369	A23H4W	54	55	233.95	936.00	−5.98	0.11

Continued on next page

Table C.1 – *Authigenic εNd at site ODP 1093 – continued from previous page*

Label	Core	Depth top (cm)	Depth bottom (cm)	Depth (mcd)	Age (ka BP)	εNd	2SD
6444	A23H4W	101	102	234.42	937.45	−6.75	0.11
6628	A23H4W	101	102	234.42	937.45	−6.70	0.15
6384	A23H5W	3	4	234.94	939.06	−6.39	0.09
6453	A23H5W	52	53	235.43	940.58	−7.51	0.12
6376	A23H5W	102	102	235.93	942.12	−7.59	0.11
6454	A23H6W	5	6	236.46	943.76	−8.11	0.10
6382	A23H6W	48	49	236.89	945.09	−8.23	0.11
6387	A23H6W	97	98	237.38	946.60	−8.39	0.07
6446	B23H2W	52	53	237.89	948.18	−8.36	0.10
6506	B23H2W	102	103	238.39	949.73	−8.29	0.16
6524	B23H3W	5	6	238.92	951.36	−7.89	0.18
6530	B23H3W	52	53	239.39	952.82	−7.88	0.14
6516	B23H3W	102	103	239.89	954.36	−7.81	0.16
6661	B23H4W	6	7	240.43	956.03	−7.94	0.21
6668	B23H4W	54	55	240.91	957.52	−7.72	0.21
6654	B23H4W	102	103	241.39	959.00	−8.29	0.23
6501	B23H5W	7	8	241.94	968.58	−8.74	0.15
6669	B23H5W	36	37	242.23	973.64	−6.69	0.18
6673	B23H5W	57	58	242.44	977.30	−7.89	0.22
6738	B23H5W	84	85	242.71	982.00	−6.65	0.37
6736	B23H5W	112	113	242.99	987.30	−6.79	0.14

Continued on next page

Table C.1 – *Authigenic εNd at site ODP 1093 – continued from previous page*

Label	Core	Depth top (cm)	Depth bottom (cm)	Depth (mcd)	Age (ka BP)	εNd	2SD
6734	B23H6W	5	6	243.42	995.44	−7.76	0.17
6693	A24H4W	19	20	243.9	1004.53	−7.12	0.13
6751	A24H4W	69	70	244.4	1014.00	−8.31	0.26
6701	A24H4W	122	123	244.93	1028.26	−7.68	0.24
6716	A24H4W	122	123	244.93	1028.26	−7.20	0.18
6749	A24H5W	23	24	245.44	1041.98	−6.74	0.11
6707	A24H5W	68	69	245.89	1054.09	−6.54	0.12
6613	A24H5W	118	119	246.39	1067.55	−7.35	0.14
6695	A24H5W	118	119	246.39	1067.55	−7.30	0.14
6714	A24H6W	18	19	246.89	1081.00	−7.38	0.14

Table C.2.: Element ratios of the leachates at site ODP 1093

Label	Al/Nd	Sr/Ca (‰)	HREE/LREE	MREE/MREE*	Ce/Ce*	Eu/Eu*	$CaCO_3$ (%)
5551	62.43	4.32	1.13	1.41	0.47	1.15	20.75
5554	215.29	4.59	1.32	1.30	0.98	0.74	2.92
5555	176.22	4.27	1.42	1.28	0.90	0.94	5.64
5556	168.73	8.83	1.00	1.64	1.19	0.94	0.51
5557	202.53	4.39	1.59	1.31	1.00	0.79	4.59
5557	178.74	4.19	1.28	1.50	0.91	0.87	5.18
5557	221.91	4.82	1.39	1.38	1.06	2.20	4.62
5558	133.94	4.63	1.13	1.44	0.75	1.08	7.46
5559	29.31	4.23	1.01	1.50	0.45	1.17	42.82
5560	86.07	4.83	1.11	1.45	0.51	1.19	14.23
5561	166.86	9.82	1.25	1.75	1.66	1.04	0.53
5562	49.40	4.92	1.19	1.42	0.52	1.11	26.01
5567	183.67	4.91	1.44	1.25	0.94	0.81	4.77
5571	172.22	5.17	1.30	1.44	1.18	0.78	3.31
5576	90.40	4.75	1.26	1.42	0.54	0.93	15.96
5578	80.70	4.62	1.19	1.43	0.49	0.98	20.15
5579	47.25	4.34	1.15	1.42	0.50	0.92	28.10
5580	196.99	8.85	1.33	1.72	1.59	0.87	0.49
5581	99.50	4.97	1.18	1.38	0.67	0.97	9.87

Continued on next page

Table C.2 – *Element ratios of the leachates at site ODP 1093 – continued from previous page*

Label	Al/Nd	Sr/Ca (‰)	HREE/LREE	MREE/MREE*	Ce/Ce*	Eu/Eu*	$CaCO_3$ (%)
5584	89.70	4.73	1.17	1.35	0.46	0.90	18.92
5585	70.48	4.70	1.20	1.43	0.58	0.91	19.92
5586	32.51	4.36	0.98	1.53	0.46	0.99	32.76
5587	42.23	4.41	1.14	1.45	0.49	0.96	29.95
5591	105.16	4.44	1.16	1.51	0.80	0.85	15.45
5597	142.47	4.79	1.14	1.42	0.71	0.05	14.59
5599	164.23	6.20	1.24	1.74	2.01	1.37	1.31
5604	152.57	13.63	1.15	1.70	1.67	0.24	0.27
5605	151.28	4.63	1.24	1.66	1.67	1.24	3.16
5610	99.80	4.55	1.14	1.35	0.60	0.24	19.85
5613	95.38	4.45	1.13	1.38	0.50	0.44	19.35
5691	22.94	4.90	1.33	1.50	0.75	1.13	28.66
5695	18.37	4.88	1.35	1.47	0.53	1.01	31.26
5696	29.68	4.48	1.49	1.55	0.83	0.99	14.45
5697	109.72	7.73	1.45	1.77	1.56	1.08	0.44
5697	246.48	7.59	1.35	1.72	1.63	1.53	0.56
5699	12.44	4.63	1.35	1.43	0.54	1.01	35.44
5702	118.84	18.38	1.43	1.72	1.70	1.00	0.22
5703	52.86	6.07	1.82	1.60	0.74	1.04	12.10
5707	116.83	4.41	1.75	1.51	0.57	0.96	14.70
5708	29.23	3.89	1.45	1.58	0.72	0.86	21.78

Continued on next page

Table C.2 – *Element ratios of the leachates at site ODP 1093 – continued from previous page*

Label	Al/Nd	Sr/Ca (‰)	HREE/LREE	MREE/MREE*	Ce/Ce*	Eu/Eu*	$CaCO_3$ (%)
5714	127.77	12.34	1.38	1.87	1.64	0.91	0.26
5714	28.51	12.10	0.60	1.14	1.64	0.90	0.30
5714	111.44	16.73	1.69	1.73	1.61	1.24	0.20
5714	200.07	13.39	1.34	1.65	1.75	1.84	0.29
5714	120.48	10.73	1.37	1.82	1.71	1.08	0.30
5714	112.67	11.76	1.57	1.65	1.50	0.99	0.31
5716	31.60	4.23	1.55	1.53	0.66	1.07	16.73
5718	20.10	4.31	1.37	1.49	0.65	1.14	25.41
5719	79.08	12.36	1.43	1.64	1.62	1.02	0.26
5721	56.54	4.40	1.60	1.60	1.10	1.04	6.22
5801	222.82	15.09	1.51	1.57	1.54	0.86	0.11
5802	86.43	4.16	1.40	1.68	1.28	0.91	4.18
5803	33.49	4.59	1.46	1.48	0.60	0.78	12.41
5804	98.62	5.34	1.51	1.66	1.07	0.73	2.17
5805	214.36	13.81	1.23	1.71	1.63	0.85	0.11
5806	64.65	4.32	1.73	1.54	0.90	0.98	4.48
5807	194.08	11.94	1.32	1.56	1.65	0.72	0.11
5809	115.52	1.53	1.70	1.59	1.58	0.68	0.57
5810	23.95	4.23	1.41	1.47	0.57	1.02	22.08
5811	237.60	12.75	1.31	1.72	1.47	0.84	0.11
5812	73.94	3.95	1.80	1.41	1.25	0.75	4.82

Continued on next page

Table C.2 – *Element ratios of the leachates at site ODP 1093 – continued from previous page*

Label	Al/Nd	Sr/Ca (‰)	HREE/LREE	MREE/MREE*	Ce/Ce*	Eu/Eu*	$CaCO_3$ (%)
5813	62.24	4.12	1.91	1.43	1.20	0.81	4.26
5814	202.94	16.34	1.49	1.53	1.63	0.76	0.10
5815	56.14	4.55	1.91	1.40	1.24	0.77	6.37
5816	92.02	8.33	1.49	1.63	1.66	0.67	0.38
5817	59.53	4.31	1.52	1.48	0.56	0.84	13.90
5818	97.49	4.20	1.90	1.71	1.60	0.72	0.50
5819		4.40	1.45	1.33	0.63	0.84	44.65
5821	233.68	21.26	1.12	1.65	1.63	0.71	0.05
5823	79.27	4.57	1.75	1.43	1.22	0.69	4.57
5824	70.36	4.94	1.40	1.65	0.82	0.85	4.33
5825	248.49	24.30	1.51	1.47	1.65	0.87	0.05
5826	72.85	4.71	1.71	1.47	1.16	0.86	4.01
5828	84.07	8.98	1.17	1.71	1.64	0.86	0.27
5829	36.11	4.13	1.31	1.58	0.55	0.94	17.31
5830	298.23	9.27	1.48	1.54	1.54	0.75	0.13
5831	84.15	3.66	1.99	1.39	1.10	0.66	4.00
5832	59.36	3.63	1.41	1.51	1.19	0.88	5.70
5833	88.18	4.66	1.70	1.53	1.41	0.80	1.83
5834	123.00	9.22	1.58	1.75	1.66	0.80	0.32
5835	172.68	6.86	1.93	1.73	1.69	0.91	0.58
5836	132.20	6.14	1.41	1.75	1.60	0.85	0.76

Continued on next page

Table C.2 – *Element ratios of the leachates at site ODP 1093 – continued from previous page*

Label	Al/Nd	Sr/Ca (‰)	HREE/LREE	MREE/MREE*	Ce/Ce*	Eu/Eu*	$CaCO_3$ (%)
5837	60.54	14.13	1.12	1.60	1.61	0.92	0.29
5838	74.89	4.93	1.74	1.48	0.97	0.79	1.94
5840	73.86	11.03	1.18	1.85	1.65	0.73	0.23
5841	204.03	10.86	1.30	1.61	1.49	0.71	0.14
5842	214.57	11.82	1.53	1.56	1.50	0.78	0.10
5843	225.36	17.27	1.32	1.55	1.65	0.90	0.06
5844	137.65	13.39	1.35	1.52	1.65	0.85	0.16
5845	79.39	4.17	1.75	1.48	0.98	0.89	2.19
5846	123.89	7.71	1.61	1.59	1.12	0.67	0.38
5848	88.09	14.88	1.05	1.85	1.35	0.81	0.16
5850	45.65	4.89	2.10	1.38	1.10	0.83	2.21
5851	168.93	11.22	1.30	1.54	1.72	0.71	0.15
5852	81.87	4.24	1.71	1.50	1.08	0.66	3.79
5853	40.10	4.29	1.38	1.51	0.47	0.92	18.06
5854	262.27	12.94	1.44	1.49	1.34	0.73	0.09
5855	60.00	4.02	1.80	1.49	1.26	0.92	5.53
5856	102.33	16.76	1.31	1.81	1.30	0.83	0.13
5857		4.07	1.53	1.50	1.02	0.87	7.73
5858	143.66	4.57	1.91	1.39	1.20	0.88	3.33
5859	42.58	13.31	0.89	1.77	2.09	0.84	0.15
5860	65.18	3.91	1.63	1.58	1.30	0.83	4.70

Continued on next page

Table C.2 – *Element ratios of the leachates at site ODP 1093 – continued from previous page*

Label	Al/Nd	Sr/Ca (‰)	HREE/LREE	MREE/MREE*	Ce/Ce*	Eu/Eu*	$CaCO_3$ (%)
5862	85.88	3.83	1.72	1.50	1.17	0.69	3.69
5863	29.32	3.77	1.48	1.55	0.77	0.88	15.91
5864	41.61	4.24	1.40	1.50	0.43	0.89	18.04
5878	180.19	12.94	1.25	1.63	1.69	0.91	0.16
5879	218.77	13.46	1.30	1.63	1.73	0.91	0.11
5881		4.91	1.39	1.36	0.56	0.91	35.98
5885	164.25	11.84	1.39	1.62	1.61	0.90	0.16
5888		5.41	1.65	1.43	1.01	0.94	4.54
5889		5.26	1.55	1.37	0.73	0.85	8.16
5890	204.84	10.65	1.37	1.54	1.72	0.96	0.18
5891		5.26	1.30	1.26	0.36	0.94	52.82
5892	256.54	18.01	1.40	1.61	1.54	0.80	0.07
5895		5.64	1.73	1.41	0.90	0.99	4.48
5899	299.55	16.88	1.43	1.55	2.14	0.92	0.10
5900		5.39	1.73	1.40	0.22	0.89	50.35
5903		13.54	1.15	1.81	1.65	0.92	0.11
5904		4.99	1.35	1.36	0.49	0.91	35.42
5905	223.68	16.38	1.33	1.58	1.86	0.91	0.10
5906		5.62	2.15	1.22	1.10	0.77	0.95
5907		5.34	1.70	1.48	0.92	0.97	5.26
5908		4.76	1.44	1.39	0.51	0.97	41.85

Continued on next page

Table C.2 – *Element ratios of the leachates at site ODP 1093 – continued from previous page*

Label	Al/Nd	Sr/Ca (‰)	HREE/LREE	MREE/MREE*	Ce/Ce*	Eu/Eu*	$CaCO_3$ (%)
5910		5.06	1.50	1.46	0.57	1.02	12.06
5913	327.73	17.79	1.38	1.52	1.67	0.86	0.06
5914		5.70	1.31	1.52	0.39	0.98	19.67
5917		5.20	1.89	1.30	0.84	1.01	6.81
5918		5.04	1.54	1.49	0.71	0.93	13.33
5920		5.23	1.63	1.44	0.20	0.97	54.35
5921	312.79	9.95	1.38	1.61	1.70	0.87	0.11
5922		5.15	1.74	1.43	0.90	1.06	4.87
5925		4.70	1.48	1.34	0.48	0.99	22.97
5930		5.27	1.73	1.40	0.24	1.02	52.47
5932		5.05	1.65	1.34	0.61	0.96	12.97
5933		3.91	1.36	1.61	0.86	0.99	10.08
5941		7.26	1.40	1.67	1.31	0.94	0.54
5942		4.53	1.57	1.48	0.97	0.87	3.88
5943		4.26	1.88	1.47	0.97	0.95	4.82
5944	165.11	14.00	1.21	1.70	1.43	0.91	0.10
5945		4.32	1.53	1.49	0.66	0.97	5.82
5947		1.70	1.46	1.62	1.08	1.01	9.83
5948		4.44	1.65	1.35	1.02	1.07	5.68
5949	107.75	14.09	1.27	1.51	1.36	0.95	0.10
5950		4.77	1.71	1.57	1.10	0.99	2.85

Continued on next page

Table C.2 – *Element ratios of the leachates at site ODP 1093 – continued from previous page*

Label	Al/Nd	Sr/Ca (‰)	HREE/LREE	MREE/MREE*	Ce/Ce*	Eu/Eu*	$CaCO_3$ (%)
5951		8.49	1.43	1.52	1.01	0.84	0.32
5952		4.62	1.38	1.52	0.80	1.02	7.49
5953		4.75	1.60	1.46	0.86	0.94	3.21
5956		4.67	1.83	1.31	1.02	0.88	6.07
5957		4.48	1.69	1.38	0.92	0.81	4.34
5959		6.94	1.37	1.52	1.50	0.81	0.58
5960	248.95	19.89	1.25	1.46	1.25	0.99	0.06
5961		0.81	1.70	1.29	0.89	0.79	7.99
5962		4.59	1.34	1.41	0.49	1.02	23.37
5965	35.00	4.14	1.40	1.44	0.49	1.06	31.16
5966	80.31	14.42	1.21	1.64	1.85	0.93	0.15
5967	131.89	11.25	1.21	1.65	1.39	0.95	0.17
5968	24.35	3.74	1.24	1.46	0.42	1.04	62.51
5969	152.97	11.51	1.20	1.63	1.61	0.96	0.13
5970		4.85	1.55	1.68	1.48	1.17	1.72
5971		5.30	1.99	1.33	0.97	0.87	0.98
5972		4.60	1.36	1.48	0.54	0.86	3.67
5973	124.85	14.91	1.18	1.63	1.31	1.05	0.09
5976		11.49	1.48	1.54	1.18	0.99	0.21
5977	167.86	19.78	1.26	1.55	1.23	0.90	0.07
5978	208.89	16.54	1.21	1.66	1.33	1.01	0.09

Continued on next page

Table C.2 – *Element ratios of the leachates at site ODP 1093 – continued from previous page*

Label	Al/Nd	Sr/Ca (‰)	HREE/LREE	MREE/MREE*	Ce/Ce*	Eu/Eu*	$CaCO_3$ (%)
5979		3.80	1.43	1.27	0.43	0.91	48.88
5980		5.76	1.36	1.65	1.18	1.03	1.23
5981		7.54	1.67	1.56	1.32	0.86	0.46
5982		6.44	2.12	1.51	1.68	0.95	0.67
5984		4.70	1.50	1.55	0.77	0.90	2.77
5985		10.46	1.93	1.62	1.35	0.88	0.19
5986		4.21	1.45	1.40	0.62	1.01	7.85
5987	218.96	13.66	1.47	1.62	1.50	0.85	0.12
5989	187.92	14.01	1.61	1.45	1.89	0.99	0.14
5990		4.47	1.56	1.46	0.92	0.91	3.98
5991		4.99	1.30	1.74	1.64	1.05	1.73
5992		8.60	1.28	1.67	1.70	1.02	0.32
5993	182.14	12.16	1.41	1.57	1.38	0.95	0.16
5994	223.34	9.41	1.39	1.62	1.33	0.88	0.19
5995		13.08	1.44	1.67	1.13	1.00	0.19
5996		5.92	2.18	1.48	1.50	0.86	0.71
5997		4.30	1.47	1.53	0.90	0.89	2.80
5998		9.43	1.07	1.65	1.66	0.90	0.25
5999		6.83	1.83	1.56	1.13	1.04	0.39
6000	61.44	4.52	1.55	1.42	0.88	0.98	9.39
6001		4.06	0.21	0.43	0.87	0.95	1.96

Continued on next page

Table C.2 – *Element ratios of the leachates at site ODP 1093 – continued from previous page*

Label	Al/Nd	Sr/Ca (‰)	HREE/LREE	MREE/MREE*	Ce/Ce*	Eu/Eu*	$CaCO_3$ (%)
6002		4.52	2.20	1.04	0.24	0.90	0.74
6003		4.20	2.32	1.49	0.92	0.94	2.97
6004		4.47	1.82	1.23	0.95	0.99	8.65
6011	82.07	4.81	1.49	1.47	0.93	0.98	6.81
6012	116.44	5.03	1.42	1.61	1.36	1.03	2.10
6013	78.94	5.25	2.17	1.25	1.18	1.08	1.87
6014	292.14	15.23	1.05	1.58	1.55	0.92	0.08
6015	34.90	4.44	1.20	1.66	0.77	1.02	10.75
6016	156.46	10.36	1.20	1.60	1.37	1.04	0.17
6019	98.22	12.65	1.73	1.53	1.34	0.98	0.17
6020	69.91	6.20	1.23	1.56	1.55	1.11	0.81
6021	96.77	4.93	1.61	1.55	1.13	0.87	2.28
6023	29.58	3.84	1.26	1.69	0.93	1.08	11.39
6025	28.15	15.85	0.44	0.75	1.64	1.18	0.08
6026	87.94	12.81	1.41	1.61	1.75	1.13	0.14
6027		3.79	1.22	1.27	0.56	0.89	45.62
6030	34.46	4.24	1.32	1.55	0.69	1.08	14.11
6031	214.17	13.45	1.10	1.56	1.60	0.99	0.09
6032	67.12	11.82	1.21	1.49	2.27	0.88	0.12
6034	92.26	17.14	1.19	1.63	1.98	1.00	0.14
6036	228.63	20.06	1.53	1.52	1.61	0.86	0.10

Continued on next page

Table C.2 – *Element ratios of the leachates at site ODP 1093 – continued from previous page*

Label	Al/Nd	Sr/Ca (‰)	HREE/LREE	MREE/MREE*	Ce/Ce*	Eu/Eu*	$CaCO_3$ (%)
6038	136.98	11.25	1.50	1.48	1.77	1.06	0.14
6040	43.72	4.47	1.27	1.56	0.68	1.02	13.09
6041	248.39	11.46	1.08	1.70	1.98	0.96	0.14
6042	141.03	16.89	1.18	1.73	1.71	1.10	0.08
6043	226.76	11.85	1.26	1.66	1.35	0.85	0.09
6045	35.00	4.26	1.36	1.60	0.69	1.01	13.23
6046	74.13	4.80	2.92	1.23	1.26	1.00	1.97
6051	234.45	16.40	1.36	1.44	1.48	0.97	0.08
6053	303.18	11.19	1.59	1.53	1.52	0.81	0.11
6055	108.29	15.97	1.41	1.61	1.57	1.15	0.12
6056	93.59	17.78	1.32	1.60	1.58	1.01	0.14
6059	91.49	6.59	1.79	1.61	1.47	1.10	0.76
6060	37.94	4.71	1.44	1.46	0.60	1.03	15.27
6062	213.76	14.30	1.32	1.56	1.78	0.93	0.11
6063	366.99	12.05	1.61	1.61	1.65	0.89	0.08
6064	79.46	18.40	1.33	1.71	1.64	0.99	0.14
6065	193.61	19.11	1.33	1.76	1.69	1.21	0.08
6066	98.72	4.84	3.44	1.41	1.57	1.05	2.29
6067	77.06	12.58	1.17	1.72	1.66	1.10	0.21
6068	259.13	15.45	1.31	1.45	1.61	1.03	0.08
6070	68.06	5.12	1.41	1.61	1.18	0.95	2.42

Continued on next page

Table C.2 – *Element ratios of the leachates at site ODP 1093 – continued from previous page*

Label	Al/Nd	Sr/Ca (‰)	HREE/LREE	MREE/MREE*	Ce/Ce*	Eu/Eu*	$CaCO_3$ (%)
6071	317.03	15.50	1.34	1.52	1.66	0.88	0.08
6073	140.30	19.79	1.20	1.74	1.52	1.04	0.06
6074	116.24	8.09	1.73	1.51	1.63	0.90	0.35

C.2. Site ODP 1094

Table C.3.: Authigenic εNd at site ODP 1094 (this study and Hallmaier et al. (2023a)). Age model from Hasenfratz et al. (2019). Samples marked with an asterisk were excluded from further discussion based on the multielement analysis.

Label	εNd	2SD	Depth (mcd)	Age (ka BP)			
5570	A1H2W	19	20	1.69	3.20	−0.82	0.15
5701	A1H2W	37	38	1.87	3.51	−0.68	0.15
5601	A1H2W	37	38	1.87	3.51	−0.25	0.15
5569	A1H2W	87	88	2.37	4.40	−0.87	0.23
5572	A1H2W	97	98	2.47	4.58	−2.53	0.16
5563	C1H2W	88	89	2.66	4.91	−3.34	0.14
5573	C1H3W	7	8	3.35	6.13	−2.70	0.22
5606	C1H3W	37	38	3.65	6.66	−3.06	0.23
5607	C1H3W	59	60	3.87	7.06	−5.51	0.20
5574*	C1H3W	89	90	4.17	7.60	−2.97	0.32
5596	C1H3W	117	118	4.45	8.11	−4.53	0.22
5582*	C1H4W	7	8	4.85	8.83	−2.99	0.38
5614	C1H4W	7	8	4.85	8.83	−2.58	0.35
5575	C1H4W	37	38	5.15	9.38	−3.31	0.21
5603*	C1H4W	59	60	5.37	9.77	−2.86	0.29
5553*	C1H4W	89	90	5.67	10.32	−2.24	0.29
5583	C1H4W	119	120	5.97	10.86	−6.07	0.23
5608*	C1H5W	37	38	6.65	12.51	−1.53	0.25
5590	C1H5W	67	68	6.95	13.59	−0.99	0.21

Continued on next page

Table C.3 – *Authigenic εNd at site ODP 1094 – continued from previous page*

Label	Core	Depth top (cm)	Depth bottom (cm)	Depth (mcd)	Age (ka BP)	εNd	2SD
5588	C1H5W	97	98	7.25	14.67	−2.28	0.17
5612	C1H5W	118	119	7.46	15.42	−2.99	0.17
5566	C1H6W	7	8	7.85	16.83	−2.46	0.16
5589	C1H6W	36	37	8.14	17.87	−3.03	0.16
5709	C1H6W	67	68	8.45	18.99	−3.03	0.12
5594	C1H6W	95	96	8.73	20.68	−3.42	0.16
5602	A2H2W	146	147	9.1	24.13	−2.06	0.12
5600	A2H3W	27	28	9.41	27.01	−2.90	0.12
5598	A2H3W	27	28	9.41	27.01	−3.05	0.13
5565	A2H3W	106	107	10.2	35.12	−3.30	0.14
5595	A2H3W	127	128	10.41	35.88	−3.10	0.13
5593	A2H4W	16	17	10.8	37.29	−3.77	0.14
5628	A3H4	116	117	22.18	119.77	−2.24	0.22
5637	A3H4	142	143	22.44	120.59	−1.88	0.23
5639	A3H5	27	28	22.79	121.70	−2.65	0.23
5643	A3H5	67	68	23.19	122.96	−1.99	0.25
5664	A3H5	116	117	23.68	124.51	−1.88	0.18
5670	C3H3	74	75	23.9	125.20	−3.35	0.19
5713	C3H4	57	58	25.23	128.43	−3.98	0.21
5722	C3H4	78	79	25.44	128.84	−3.49	0.29
5706	C3H4	78	79	25.44	128.84	−3.12	0.32

Continued on next page

Table C.3 – *Authigenic εNd at site ODP 1094 – continued from previous page*

Label	Core	Depth top (cm)	Depth bottom (cm)	Depth (mcd)	Age (ka BP)	εNd	2SD
5712	C3H4	117	118	25.83	129.59	−2.82	0.32
5698	C3H4	146	147	26.12	130.15	−2.58	0.24
5711	C3H5	19	20	26.35	131.10	−1.89	0.23
5692	C3H5	48	49	26.64	132.71	−3.03	0.14
5717	C3H5	79	80	26.95	134.47	−3.16	0.19
5704	C3H5	116	117	27.32	139.99	−2.41	0.10
5710	C3H5	146	147	27.62	144.47	−2.54	0.17
6692	C6H6W	16	17	55.98	353.26	−4.41	0.16
6726	C6H6W	47	48	56.29	356.23	−4.11	0.11
6706	A7H2W	88	89	56.58	359.02	−3.90	0.15
6727	A7H2W	148	149	57.18	364.78	−3.10	0.11
6733	A7H3W	28	29	57.48	367.66	−1.91	0.15
6699	A7H3W	58	59	57.78	370.54	−3.73	0.13
6712	A7H3W	97	98	58.17	374.28	−1.47	0.08
6703	A7H3W	148	149	58.68	379.17	−2.62	0.13
6735	A7H4W	58	59	59.28	384.93	−4.11	0.11
5916	A7H4W	76	77	59.46	386.70	−1.86	0.13
5931	A7H4W	118	119	59.88	390.70	−1.93	0.26
5887	A7H5W	28	29	60.48	395.50	−4.68	0.12
5871	A7H5W	118	119	61.38	397.50	−5.12	0.15
5872	A7H6W	28	29	61.98	398.90	−4.93	0.13

Continued on next page

Table C.3 – *Authigenic εNd at site ODP 1094 – continued from previous page*

Label	Core	Depth top (cm)	Depth bottom (cm)	Depth (mcd)	Age (ka BP)	εNd	2SD
5880	A7H6W	96	97	62.66	400.40	−6.65	0.13
5934	A8H1W	9	10	63.83	403.10	−4.39	0.13
5919	A8H1W	59	60	64.33	404.20	−1.87	0.17
5923	A8H2W	9	10	65.33	406.50	−0.92	0.17
5929	A8H2W	67	68	65.91	407.80	−0.97	0.12
5873	A8H2W	136	137	66.6	409.30	−2.08	0.16
5877	A8H3W	38	39	67.12	411.80	−1.99	0.17
5897	A8H3W	58	59	67.32	414.10	−2.19	0.18
5902	A8H3W	97	98	67.71	418.40	−2.48	0.19
5927	A8H3W	136	137	68.1	420.70	−2.40	0.18
5909	A8H4W	9	10	68.33	421.40	−2.03	0.18
5874	A8H4W	38	39	68.62	422.30	0.17	0.14
5912	A8H4W	67	68	68.91	423.10	0.80	0.13
5898	A8H4W	98	99	69.22	424.00	0.21	0.12
5926	A8H4W	135	136	69.59	425.10	−0.42	0.16
5911	A8H4W	135	136	69.59	425.10	−0.44	0.11
5883	A8H5W	38	39	70.12	426.70	−3.04	0.32
5924	A8H5W	69	70	70.43	427.60	−2.19	0.17
5886	A8H5W	98	99	70.72	428.40	−0.79	0.13
5876	A8H6W	8	9	71.32	438.20	−2.96	0.13
5882	D6H3W	56	57	71.8	441.40	−2.86	0.12

Continued on next page

Table C.3 – *Authigenic εNd at site ODP 1094 – continued from previous page*

Label	Core	Depth top (cm)	Depth bottom (cm)	Depth (mcd)	Age (ka BP)	εNd	2SD
5896	D6H3W	97	98	72.21	444.10	−2.87	0.12
6698	A12H3W	88	89	105.06	850.32	−1.88	0.16
6743	A12H3W	118	119	105.36	853.28	−0.96	0.27
6745	A12H4W	9	10	105.77	857.32	−4.01	0.19
6728	A12H4W	28	29	106.25	861.86	−5.85	0.20
6719	A12H4W	88	89	106.56	864.52	−2.69	0.16
6718	A12H4W	123	124	106.91	867.52	−3.17	0.11
6696	A12H5W	3	4	107.21	870.09	−3.30	0.13
6723	D10H2W	9	10	107.53	872.83	−3.42	0.14
6700	D10H2W	48	49	107.92	876.17	−4.01	0.09
6729	D10H2W	78	79	108.22	880.69	−3.24	0.10
6694	D10H2W	108	109	108.52	886.55	−4.03	0.12
6702	D10H2W	138	139	108.82	892.41	−4.44	0.13
6753	D10H3W	27	28	109.21	900.42	−3.82	0.12
6747	D10H3W	47	48	109.41	904.91	−3.52	0.10
6740	D10H3W	79	80	109.73	912.10	−4.02	0.11
6725	D10H3W	79	80	109.73	912.10	−3.90	0.12
6722	D10H3W	98	99	109.92	915.89	−4.02	0.18
6739	D10H4W	48	49	110.92	919.37	−4.12	0.12
6754	A13H1W	59	60	112.13	924.68	−4.65	0.11
6737	A13H1W	119	120	112.73	928.76	−5.37	0.12

Continued on next page

Table C.3 – *Authigenic εNd at site ODP 1094 – continued from previous page*

Label	Core	Depth top (cm)	Depth bottom (cm)	Depth (mcd)	Age (ka BP)	εNd	2SD
6710	A13H2W	28	29	113.32	932.77	−4.80	0.10
6720	A13H2W	58	59	113.62	935.06	−4.64	0.16
6741	A13H2W	117	118	114.21	939.63	−4.41	0.10
6711	A13H2W	149	150	114.53	942.11	−5.08	0.15
6709	A13H3W	59	60	115.13	945.62	−3.83	0.15
6697	A13H3W	59	60	115.13	945.62	−3.63	0.14
6731	A13H3W	144	145	115.98	950.09	−3.78	0.18
6705	A13H4W	58	59	116.62	956.60	−6.00	0.33
6744	A13H5W	4	5	117.22	960.91	−4.92	0.12
6708	D11H2W	68	69	117.82	965.21	−4.56	0.12
6715	D11H2W	128	129	118.42	969.52	−4.69	0.16
6748	D11H3W	39	40	119.03	973.90	−4.84	0.12
6750	D11H3W	68	69	119.32	975.98	−4.91	0.14
6742	D11H3W	99	100	119.63	978.32	−4.84	0.12
6721	D11H4W	9	10	120.23	983.25	−5.19	0.10
6704	D11H4W	38	39	120.52	986.69	−5.12	0.13
6724	D11H4W	72	73	120.86	990.72	−4.74	0.08
6746	D11H4W	72	73	120.86	990.72	−4.56	0.10
6717	D11H4W	98	99	121.12	993.81	−4.79	0.08

Table C.4.: Element ratios of the leachates at site ODP 1094

Label	Al/Nd	Sr/Ca (‰)	HREE/LREE	MREE/MREE*	Ce/Ce*	Eu/Eu*	$CaCO_3$ (%)
5553	304.64	15.42	1.09	1.47	0.98	−0.52	0.24
5563	135.58	7.81	1.10	1.53	0.97	0.82	1.03
5566	179.55	11.22	1.35	1.50	1.52	0.87	0.62
5569	129.35	15.14	0.98	1.65	0.94	0.74	0.30
5570	90.80	18.40	0.88	1.61	1.00	0.73	0.26
5570	112.51	15.71	0.83	1.64	1.03	0.23	0.30
5570	85.29	20.11	0.90	1.55	1.01	0.85	0.24
5572	124.91	11.15	1.04	1.63	1.01	0.68	0.47
5573	154.21	7.05	1.09	1.51	0.93	0.76	1.49
5574	359.41	16.74	1.30	1.39	0.95	−0.52	0.22
5575	192.52	12.57	0.98	1.51	0.95	0.46	0.34
5582	360.98	19.16	1.07	1.53	1.00	−0.22	0.18
5583	197.69	6.22	1.90	1.15	1.07	0.35	1.22
5588	193.35	10.76	0.93	1.54	1.28	0.55	0.44
5589	141.89	11.59	1.05	1.73	1.70	0.83	0.60
5590	204.00	15.52	1.05	1.62	1.23	0.38	0.27
5594	133.64	14.61	0.88	1.77	1.87	0.83	0.40
5596	157.90	6.31	1.06	1.49	1.18	0.52	1.20
5598	151.88	17.85	0.97	1.71	1.77	0.67	0.31

Continued on next page

Table C.4 – *Element ratios of the leachates at site ODP 1094 – continued from previous page*

Label	Al/Nd	Sr/Ca (‰)	HREE/LREE	MREE/MREE*	Ce/Ce*	Eu/Eu*	$CaCO_3$ (%)
5600	149.09	17.85	0.93	1.79	1.78	0.44	0.31
5601	140.33	11.73	0.87	1.72	0.99	1.49	0.45
5602	140.15	17.46	0.97	1.75	1.77	0.75	0.34
5603	466.04	17.29	1.16	1.49	1.08	7.00	0.21
5606	238.24	8.01	1.11	1.48	1.06	2.31	0.83
5607	209.08	4.81	1.51	1.35	0.95	0.99	4.26
5608	370.43	11.20	1.03	1.51	1.24	1.56	0.44
5612	221.55	8.80	1.22	1.50	1.30	2.63	0.62
5614	457.97	16.51	1.05	1.59	1.04	5.65	0.23
5692	74.55	8.59	1.39	1.72	1.56	1.07	0.52
5698	85.77	7.70	1.59	1.44	1.10	1.05	0.40
5701	130.52	11.95	0.89	1.67	0.96	0.80	0.41
5701	46.75	7.57	1.00	1.88	0.98	1.03	0.36
5701		10.36	1.06	1.88	0.94	1.17	0.31
5701	75.14	9.87	1.07	1.80	0.91	1.01	0.31
5701	57.55	13.59	1.11	1.87	0.93	0.89	0.28
5701		10.44	1.07	1.67	0.85	0.94	0.31
5704	118.59	13.27	1.70	1.88	1.51	1.01	0.45
5706	121.73	8.33	2.71	1.05	1.29	0.74	0.33
5709	131.80	11.52	1.38	1.79	1.81	1.05	0.38
5709	161.57	11.53	1.04	1.67	1.85	0.69	0.56

Continued on next page

Table C.4 – *Element ratios of the leachates at site ODP 1094 – continued from previous page*

Label	Al/Nd	Sr/Ca (‰)	HREE/LREE	MREE/MREE*	Ce/Ce*	Eu/Eu*	$CaCO_3$ (%)
5710	127.35	10.60	1.46	1.84	1.55	1.10	0.44
5711	133.54	9.50	1.80	1.64	1.27	0.91	0.29
5712	69.56	6.08	1.93	1.45	1.17	0.96	1.26
5713	148.78	5.73	1.59	1.46	1.17	1.13	1.03
5717	136.46	5.05	1.65	1.68	1.72	1.08	2.08
5722	190.49	7.39	1.75	1.22	1.10	1.70	0.32
5871		4.57	1.70	1.32	0.86	1.05	7.12
5872		4.35	1.53	1.38	0.68	1.06	6.45
5873		4.90	1.53	1.42	1.00	1.15	1.14
5874		8.17	1.41	1.47	1.01	0.92	0.35
5876	61.91	12.39	1.12	1.79	1.79	0.99	0.28
5877		5.40	1.40	1.58	1.00	1.07	0.98
5880		4.74	1.52	1.43	0.43	0.91	14.08
5882	77.22	16.32	1.34	1.73	1.66	1.05	0.20
5883		10.92	2.68	1.11	1.18	2.92	0.12
5886		6.81	1.64	1.52	1.29	0.98	0.48
5887		4.63	2.14	1.37	0.70	0.93	3.02
5896	117.73	5.00	1.72	1.78	1.56	1.07	1.42
5897		5.21	1.92	1.29	1.06	1.02	1.77
5898		8.27	1.19	1.67	1.19	1.01	0.32
5902		5.17	1.52	1.48	1.15	0.99	1.06

Continued on next page

Table C.4 – *Element ratios of the leachates at site ODP 1094 – continued from previous page*

Label	Al/Nd	Sr/Ca (‰)	HREE/LREE	MREE/MREE*	Ce/Ce*	Eu/Eu*	$CaCO_3$ (%)
5909		8.68	2.91	1.08	0.97	0.92	1.20
5911		11.27	1.31	1.60	1.18	0.83	0.24
5912	96.16	3.58	1.16	1.67	1.11	0.99	1.03
5916	67.77	12.78	1.28	1.74	1.12	1.03	0.21
5919		4.27	1.48	1.42	0.80	0.92	0.51
5923		6.11	1.21	1.69	0.90	1.12	0.66
5924		3.08	2.07	1.28	1.26	1.06	1.12
5926		4.67	1.38	1.54	1.22	1.00	0.67
5927		4.60	2.25	1.99	0.99	0.94	2.27
5929		4.25	1.64	1.47	0.97	0.87	1.60
5931		4.13	0.98	1.78	1.07	0.92	0.57
5934		6.12	1.75	1.36	0.79	0.79	0.66

Acknowledgements

Ganz am Schluss dieser Dissertation möchte ich mich bei allen Menschen bedanken, die direkt oder indirekt dazu beigetragen haben.

An erster Stelle möchte ich Norbert danken, der mich schon während meiner Staatsexamensarbeit ermutigt hat den Weg in Richtung Promotion einzuschlagen. Der Erfolg dieser Arbeit wäre unmöglich gewesen ohne deinen Enthusiasmus, das Austauschen gemeinsamer Ideen und dem großen Spaß an diesem gemeisamen Projekt! Danke für deine Unterstützung bei dieser Arbeit! Danke besonders für deine uneingeschränkte Unterstützung in unzähligen inhaltlichen Diskussion, aber auch mit praktischen Tipps in den Laboren! Danke auch für dein Vertrauen in der Betreuung der Studis, den Laboren und der Nd Messungen! Danke für die Erfahrungen und meine wissenschaftliche aber auch persönliche Entwicklung, die ich in deiner Gruppe gemacht habe!

Ich möchte mich auch bei all den Hiwis danken, die mich unermüdlich bei der Aufbereitung aller Proben unterstützt haben und die Multielementmessungen durchgeführt haben. Danke Mareike, Celine, Moritz und Riccardo. Danke für die Diskussion der Bachelorarbeiten von Riccardo, Selina, Mareike, Clara und Moritz, die alle in diese Arbeit miteingeflossen sind. Und danke auch an die weiteren Arbeiten von Louisa, Laura, Carmen, Buhar, Sina, Achim und Moritz, bei deren Betreuungen ich meine εNd- und Massenspektrometriefähigkeiten weiter entwickeln konnte.

Die unzählgen Messungen an der ICAP und der Neptune wären nicht möglich gewesen ohne René. Danke dir, dass du mir immer mit Rat und Tat geholfen hast optimale Messergebnisse zu erzielen und mich Geduld und Fingerspitzengefühl an der Neptune gelehrt hast. Dank gilt auch Andrea für ihr offenes Ohr und die große Hilfe bei der Betreuung vieler der genannten Studis!

Danke an all die PhDs der Gruppe, von denen ich viel lernen konnte! Danke Jasmin, Steffen, Evan, Marleen, Thomas, Julius, Inga, Elvira, Sahra, Nils, Aaron und Yao! Und natürlich auch Danke an alle Mitglieder der PUAs - ihr seid mir über die Jahre sehr ans Herz gewachsen. Der Austausch mit meinem Büro 308 über Wissenschaft

aber auch die Optimierung des Pflanzenhaushalts haben mir jeden Tag großen Spaß gemacht - Danke Eva, Karo und Leon. Danke an die PhDs des Instituts für witzige Mittagspausen, Spieleabende und die nötige Ablenkung von der Arbeit - ihr habt meinen Alltag am IUP stark geprägt! Danke hier also stellvertretend für die PhDs an die PhD reps: Eva, Marvin, David und Robert. Die Arbeit mit euch als PhD reps hat immer viel Spaß gemacht!

Ich danke besonders allen Korrekturleser*innen dieser Arbeit, die die Arbeit mit ihren Kommentaren signifikant verbessert haben. Danke Moritz, Sahra, Nils, Karo, Eva und meinen Eltern. Und danke Elvia, Julia und Leon für die produktiven Schreibsessions. Danke an Norbert, Werner und Katharina für die Betreuung der Arbeit und André als Zweitgutachter.

Mein ganz besonderer Dank gilt Moritz - ich weiß gar nicht wo ich anfangen soll... Am Anfang? Danke, dass du mir gezeigt hast, wie man Sediment mörsert ;) Danke, dass daraus eine so schöne Freundschaft geworden ist! Danke für deine bereichernden Kommentare und Diskussionen von Anfang an, aber besonders jetzt am Schluss! Danke dir für unzählige geniale Arbeitstage im Labor und an der Neptune! Danke dir für die beste Teamarbeit und größten Spaß bei der Arbeit - ohne dich wären so manche Experimente im Labor und damit diese Arbeit nicht so erfolgreich geworden! Danke dir auch für die erholsamsten Kaffee- und Rennradpausen! Danke für Quitscheenten und Goldschweinchen und noch mehr Kaffee! Danke Mo einfach für alles! Auf uns - wie immer!!

Danke an alle meine Freunde aus der Schule, dem Studium, der WG, dem Stall und dem Bert und allen, die sich nicht in eine der Gruppen zuordnen lassen - die Namensliste wäre zu lang... Danke, dass ihr mich immer supportet und mich daran erinnert, was wirklich wichtig ist!

Abschließend möchte ich mich bei meinen allerwichtigsten Menschen bedanken für eigentlich alles: Danke Mama, Papa, Ariane und Flavia!!!